Universidad Autónoma de Madrid
Facultad de Ciencias

Departamento de Química

Photophysics and photochemistry of singlet oxygen precursor chromophores: insights from static calculations and molecular dynamics

A Thesis submitted for the degree of Doctor.

Candidate: Lara Martínez Fernández

Supervisor: Dr. Inés Corral Perez

Madrid, September 2014

A Dami,

Agradecimientos

A mi directora Inés Corral, por enseñarme, por entenderme y por cuidarme desde el primero día hasta último. Te agradeceré siempre las incalculables horas dedicadas a mi y a esta tesis. Ha sido un honor y un placer que me hayas sido mi directora y espero volver a trabajar a tu lado muy pronto.

Agredecer también al Prof. Manuel Yáñez Montero y la Prof. Otilia Mó Romero por aceptarme en su grupo y por todo el tiempo que han dedicado para que este trabajo salga adelante. También agradecer al Departamento de Química por todos los recursos, así como al Centro de Computación Científica por el tiempo de cálculo concedido.

Al Prof. Crespo-Hernández gracias acogerme en su grupo, ayudarme a entender los experimentos y hacer la estancia en el frío Cleveland mucho más llevadera. Vorrei anche ringraziare profondamente per l'aiuto datomi il Prof. Maurizio Persico e Giovanni Granucci. Grazie mille per essere sempre lì per qualsiasi cosa.

A toda la gente que ha pasado por el departamento desde que llegué hasta hoy, todos dispuestos a ayudar siempre con cualquier cosa. En especial a los miembros del 501-A desde los compañeros al inicio (Ane, Jose, Pablito ..), a los pasajeros (Alvarito) y hasta a los que os toco vivir la época más dura. Ori siempre ahí para intentar hacerme reír, no hay nadie mas buena y con mas paciencia que tu. Tefi se te echa de menos. Serra y JuanP gracias por aportar cordura al despacho. Thanks also to Marvin Pollum and Huijuan Huang for the support during my stay in Cleveland. E anche Grazie Vale per il tuo aiuto à Pisa. A José Manuel Segovia gracias por enseñarme y ayudarme con la parte gráfica de la tesis.

Also thanks to Maurizio Persico, Jesús González-Vázquez, Mar Reguero, Daniel Roca Sanjuan, Martial Boggio-Pasqua, Pedro Braña Coto and Emilio Martinez Nuñez for accepting taking part of this thesis as members of the tribunal.

Finalmente, me gustaría agradecer a mi familia en especial a mis padres por su por todo su dedicación y esfuerzo. Mami por saber cuando dejarme en paz porque no hay quien me hable y por saber cuando contarme bobadas para animarme. A Dami, espero que estés donde estés, estés orgulloso de la "*renaquaja*". A Iván, por su paciencia infinita y su incondicional apoyo que han hecho posible esta tesis. No se que habría hecho si en estas semanas tan duras no hubiera estado al llegar a casa para hacerme reír y desconectar. Gracias!!!!

Index

Abbreviations

FC	Franck-Condon
GS	Ground State
MEP	Minimum Energy Path
PES	Potential Energy Surface
PEC	Potential Energy Curves
CI	Conical Intersection
ISC	Intersystem Crossing
SOC	Spin Orbit Coupling
IC	Internal Conversion
HOMO	Highest Occupied Molecular Orbital
LUMO	Lowest Unoccupied Molecular Orbital
BO	Born-Oppenheimer
TDM	Transition Dipole Moment
A	Adenine
G	Guanine
C	Cytosine
T	Thymine
U	Uracil
AZG	8-AZaGuanine
AZA	8-AZaAdenine
AZC	5-AZaCytosine
AZU	6-AZaUracil
5AU	5-AminoUracil
6AU	6-AminoUracil
2AP	2-AminoPurine
2,6DAP	2,6-DiAminoPurine
3MU	3-MethylUracil
6MU	6-MethylUracil

1,5DMU	1,5-DiMethylUracil
6DMA	6-N,N-DiMethylAdenine
TT	4-ThioThymine
TU	4-ThioUracil
TG	6-ThioGuanine
TC	2-ThioCytosine
CHDEPO	CycloHexaDieneEndoPerOxide
APO	AnthraceneendoPerOxide
P	Purine
9MP	9-MethylPurine
VR	Vibrational Relaxation
ROS	Reactive Oxygen Species
PDT	PhotoDynamic Therapy
QM/MM	Quantum Mechanics/Molecular Mechanics
PCM	Polarizable Continuum Model

List of Tables

List of Figures

List of Schemes

Resumen

Aunque especies reactivas oxigenadas (oxígeno singlete ($^1O_2$) y ROS) han sido identificadas como las principales responsables del proceso de fotoxidación de la piel, sus propiedades oxidativas se han usado también con fines terapéuticos en tratamientos contra el cáncer. Por ello, muchos esfuerzos se han centrado en el descubrimiento de cromóforos capaces de producir $^1O_2$ después de ser tratados con luz y así eliminar las células tumorales. Entender el mecanismo por el cual estos cromóforos producen $^1O_2$ y ROS es fundamental para el diseño de nuevos sistemas capaces de maximizar las propiedades beneficiosas y eliminar sus efectos nocivos para la salud.

Dos tipos de cromóforos han sido estudiados durante esta tesis perimiendo obtener mayor información a cerca de su mecanismo de acción. Bases de ADN en las que un carbonilo a sido sustituido por un azufre, tiobases, han sido usadas como fotosensibilizadores durante décadas pero los efectos nocivos descubiertos en pacientes tratados con estas bases a largo plazo (alta incidencia de cáncer) han abierto la búsqueda de nuevas generaciones de fotosensibilizadores. Se conoce que estas tiobases son capaces de generar $^1O_2$ cuando son activadas con luz y en presencia de oxígeno molecular en la zona a tratar. El segundo tipo de sistemas estudiados son los endoperoxidos, sistemas aromáticos con un puente O-O. Este tipo de sistemas han sido propuestos como eficientes fotosensibilizadores bajo su excitación con luz incluso en ausencia de oxígeno molecular en el medio.

Es en el contexto arriba descrito en el que se enmarca esta tesis cuyo principal objetivo es el estudio de dichos mecanismos desde un punto de vista estático y también dinámico. Los mecanismos elucidados en la primera parte de esta tesis se comprobarán mediante estudios dinámicos que permiten una resolución temporal de los mismos así como obtener rendimientos para los distintos fotoproductos, en otras palabras, permiten obtener información acerca de los tiempos y la eficiencia de dichos fotosensibilizadores para obtener $^1O_2$.

Finalmente, las propiedades fotofísicas de la base libre purina han sido investigadas tratando de revelar como los diferentes sustituyentes alteran dichas propiedades y como pueden cambiar la fotoestabilidad de las bases de ADN hacia la fototoxicidad de algunos derivados.

Abstract

Despite reactive oxygen species (ROS and $^1O_2$) have been identified as responsible for the skin photo-oxidation processes, their oxidative properties have been also used with therapeutically anticancer effects. Thereby, tons of efforts have been done towards finding chromophores able to produce $^1O_2$ after being treated with light and then destroy tumoral cells. Understanding, the mechanism by which this chromophores produce $^1O_2$ and ROS is fundamental for the design of new systems that ideally will only present beneficial properties but not detrimental effects.

Two types of chromophores have been studied along this thesis providing important information about their mechanism of action. DNA bases where a carbonyl oxygen atom has been substituted by a sulfur, thiobases, have been used as therapeutical photosensitizers during decades. However, detrimental effects have been discovered in patients after years of treatment with this bases (high skin cancer incidence) and have led to the search of new generation of photosensitizers. These thiobases generate $^1O_2$ after being activated with light and in presence of molecular oxygen in the media.

The second type of studied systems is endoperoxides, aromatic systems carrying an O-O bridge. These systems have been proposed as prototype of effective photosensitizers, which are able to produce $^1O_2$ even in the absence of molecular oxygen in the media.

In the above context this Thesis aims to elucidate the photodeactivation mechanism of the mentioned systems both from static high-level multiconfigurational calculations and semiclassical dynamics. This approach allows knowing at molecular level all energetically possible competing relaxation mechanism and evaluating their relative importance according to the outcome of the time resolved picture provided by the dynamics.

Moreover, the combined static and dynamic analysis allows a more reliable interpretation of the experimental results od the systems considered in this thesis by estimating photoproduct yields and time scales for different processes.

Finally, the photophysical and photochemistry of purine free base have also been investigated aiming to provide insight on how the nature and position of different substituents affect the absorption properties and the photostability of these systems.

Chapter 1

Introduction

Ultraviolet light (UV) is absorbed by RNA and DNA nucleobases (adenine, cytosine, guanine, thymine and uracil, see scheme 1.1) leading to its electronic excitation. However, commonly these excitations do not lead to DNA photolesions, being the lesions provoked by UV absorption less than 1%. Photostability is thereby an extremely important characteristic of DNA behaviour since it rules the non-damage of the genetic material and the livelihood of organisms exposed to solar UV light.

Tons of efforts have been focused on understanding nucleobases' photochemistry for over 50 years, from both experimental and theoretical points of view. Spectroscopic studies have registered intense UV absorption joined to low emission and fluorescence quantum yield, which may be responsible for the DNA photostability. Furthermore, the modern powerful computational techniques allow for more complete and exhaustive studies that provide an insight about how excited DNA release its excess of electronic energy at molecular level.[1-6] These deactivations mechanisms have established that nucleobases are able to decay back to their ground state on ultrafast time scales. The faster and more efficient this decay is the lower is the DNA lesions probability. Then, DNA photostability can also be rationalised in terms of its ultrafast ground state recovery measured in experimental studies and inferred from static and dynamic calculations. Nevertheless, usually different photochemical/photophysical pathways can be mapped to relax to the ground state, leading to highly complicated deactivation mechanisms for these nucleobases (see Chapter 2).

Disruption of DNA nucleobases' original skeleton alters its electronic structure and consequently can also induce different photochemical behaviour. The interest on these derivatives has grown within the last decades due to their capability to replace the

natural nucleobase into the DNA but also due to the possibility that these compounds were present in the early stages of the earth. The interchange between DNA nucleobases and one derivative can dramatically affect DNA structure altering its photostability and leading to DNA damage. In fact this is, for instance, the case of thiobases (where a sulphur atom has replaced the original oxygen atom from the carbonyl group), which have been related with high rate of skin cancer in patients treated with drugs containing these derivatives (see section 1.3). Other structural changes, such as removing a NH_2 group from the nucleobase skeleton, can also alter the base photochemical properties and excited lifetimes.

In the following further details about DNA nucleobases and its derivatives photochemistry will be discussed.

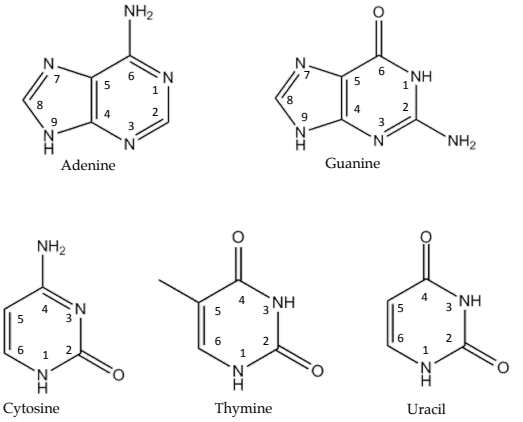

Scheme 1.1. Five RNA nucleobases with their corresponding labelling.

1.1 DNA nucleobases

The changes experimented by DNA nucleobases upon UV light absorption and its ensuing relaxation processes can be comprehended by following the photochemical reaction paths. Modern quantum chemical methods can be used for this purpose. By means of minimum energy paths (MEP) calculations (see section 2.4 in Chapter 2) it is possible to statically predict the potential energy profile connected to the more plausible deactivation mechanism. By computing these MEPs, starting from the nucleobase ground state equilibrium geometry, and following the gradient of the singlet excited state mainly populated after excitation (see section 2.1 in Chapter 2) it is possible to rationalize how this excited state decays back to the ground state. In general, two main prototypes (see Scheme 1.2) of decay pathways have been found for DNA nucleobases and its derivatives: (1) those presenting a minimum before reaching the conical intersection (CI) (see section 2.3 in Chapter 2) between the singlet excited and the ground state and/or (2) those where the CI is directly reached following the MEP showing no minimum along the pathway.

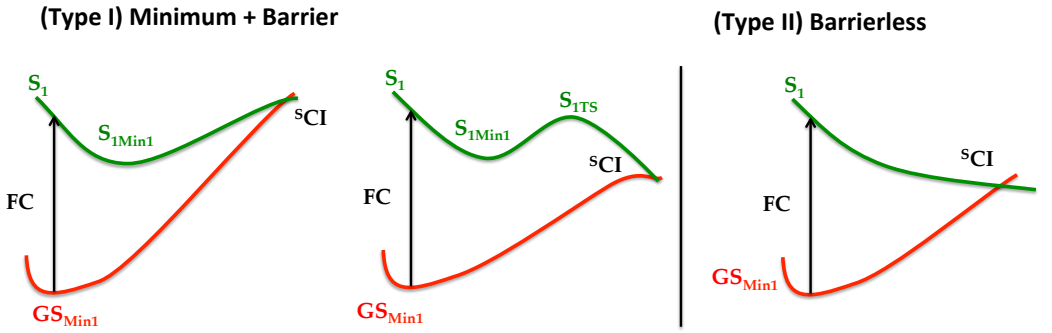

Scheme 1.2. Two main prototypes of decay pathways have been found for DNA nucleobases and its derivatives.

DNA nucleobases' photostability has been explained in terms of barrierless MEPs. For all the natural DNA bases (guanine, adenine, cytosine, uracil and thymine), no energy barriers have been computed to access the CI between the spectroscopic and the ground state (decay pathways type 2). However, the photochemistry of some DNA derivatives has been characterized by decay pathways type 1 (2aminopurine). The former static predictions have also been supported by several dynamic studies carried out with different approaches and by different groups. The theoretically predicted deactivation rates and lifetimes can be summarized and compared with the experimental measurements to define a global mechanistic picture of the nucleobases' deactivation. There are hundreds of original works and multiple reviews published on the topic. In the following, the main ideas regarding the DNA nucleobases photochemistry are summarized trying to extract the main conclusions, which lay the foundations to understand the photochemistry of substituted DNA bases that will be discussed during the next section.

Up to now, only singlet excited states have been discussed, however, after the population of a singlet excited state triplet states can also be populated through intersystem crossing processes (see section 2.5 in Chapter 2). Triplet states are usually longer lived species compared to the singlet since their decay to the ground state is spin forbidden although it can occur if large spin orbit couplings (SOC) are present. Due to their longer lifetimes, excited triplet states can be precursors of other excited species, such as singlet molecular oxygen (see section 1.4), which can be detrimental to DNA inducing its oxidation. In this sense, triplet potential energy surfaces (PES) of the nucleobases are also of interest and have been computed for all of them.[7] Of particular interest are the singlet/triplet crossings, which are responsible for the transfer of population from the excited singlet state to the triplet manifold. The topology of the PES around these crossings as well as the size of the spin orbit couplings terms at these points can anticipate the probability for triplet population. Again, dynamic simulations are extremely useful to confirm the population if the triplet manifold as well as to estimate triplet yields and lifetimes, but until now only few theoretical dynamic studies on DNA nucleobases have been performed within this framework.[8] Experimental excited state dynamic studies have contributed to shed some light on the triplet manifold population both in gas phase and in solvent.[9] As for the singlet

PESs, nucleobases derivatives differ from their canonical counterparts in the mechanism and the efficiency with which they populate the triplet manifold. This specially holds for the thiosubstituted (see section 1.3) nucleobases that present large SOC due to the heavy atom effect.

Purine Bases

Although several theoretical groups have studied the photochemistry of these nucleobases for simplicity we will focus on the results obtained by the group of Serrano-Andrés.[4] Despite this group have shown that some of these nucleobases present several stable tautomers, we will only focused on the biologically relevant ones.

Before revising **adenine's** photochemistry we will start by analysing its vertical absorption spectrum at the ground state equilibrium geometry, the so-called Franck-Condon (FC) region. The low energy region of the absorption spectrum of 9H-adenine tautomer calculated at the CASPT2//CASSCF(16,13)/6-31G(d,p) level of theory[4] is composed by one $n\pi^*$ (S_1) followed by two $\pi\pi^*$ (S_2 and S_3) states. The first $n\pi^*$ singlet excited state is placed vertically at 4.96 eV and presents low oscillator strength, 0.0037 (see section 2.1 in Chapter 2). The two $\pi\pi^*$ excitations are placed at 5.16 eV ($\pi\pi^* L_b$) and 5.35 eV ($\pi\pi^* L_a$) with 0.0042 and 0.1747 oscillator strengths, respectively. The L_a assignment corresponds to an HOMO (H)->LUMO (L) transition following Platt's nomenclature, while L_b corresponds to a linear combination of H->L+1 and H->1-L configurations. In view of the oscillator strengths, the authors assign the spectroscopic state to the S_3 $\pi\pi^* L_a$ state. Regarding the triplet states, three triplet excitations (4.00, 4.91 and 4.95 eV) can be found below the S_1 state. The state ordering for these triplet transitions are $\pi\pi^* L_a$, $n\pi^*$ and another $\pi\pi^*$ (with no correspondence with Platt's nomenclature).[7]

For a complete description of the adenine's photochemistry, regions beyond the FC structure should also be explored. The MEP starting at the FC region and following the spectroscopic S_3 $\pi\pi^* L_a$ state leads directly to a CI with the ground state ($gs/^1\pi\pi^* L_a$), see Figure 1.1.[4] This CI is characterised by the combined stretching and twisting of the C_2-N_3 bond, respect to the GS equilibrium geometry. The accessibility of the CI explains the experimentally determined low fluorescence quantum yields and rapid deactivation decay times for adenine (see below). Along this MEP, the spectroscopic state crosses the two low-lying singlet excited states and also the three triplet states.

The three possible optimized ISC (see Figure 1.1) are energy accessible and present modest SOC values, then at least from this static point of view, the authors suggest that an efficient population of the triplet manifold in adenine upon UV irradiation can take place.[4,7]

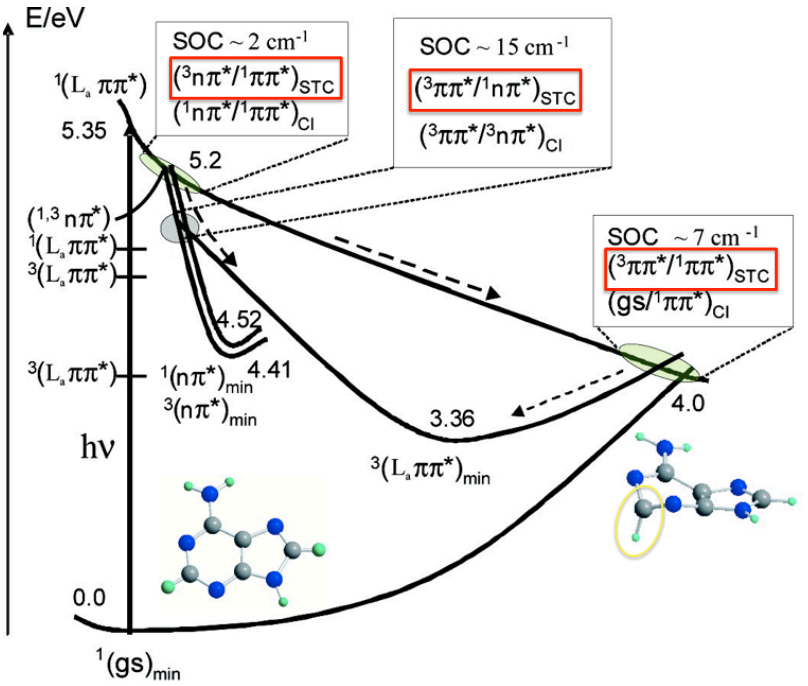

Figure 1.1. CASPT2 singlet and triplet profiles (energies in eV) describing the deactivation of adenine extracted for Ref [4]. Framed in red possible ISC funnels along the MEP and highlighted in yellow main geometrical distortion undergone by the system at the position of the CI compared to the FC structure.

Dynamic insight into the deactivation mechanism of 9H-adenine was achieved by Barbatti et al. through mixed quantum-classical dynamics simulations at the multireference configuration interaction (MR-CIS) level.[10] These authors optimized several S_1/S_0 minima on the crossing seam for adenine, besides the ones found in the literature. Among these it is worth mentioning those that involve pyrimidine ring deformation (envelope ^2E and screw-boat conformations $^1S_6$), imidazole ring puckering (E_8) or even bond breakings ($^4H_3$). Several of these CIs were computed to be lower in energy than the FC vertical excitation energy. The mechanism observed during the dynamic simulations follows the scheme S_3-> S_2->S_1, being the former an ultrafast process taking place in ~22fs. Then adenine remains trapped close to the ^2E region, accessing the CI as early as 1 ps. Despite being energetically accessible, the other alternative $^1S_6$ CI involving pyrimidine deformation was never found to be accessed during the dynamics, which the authors attributed to the great deformation that adenine must undergo to reach this CI. This is in agreement with the static calculations of Serrano-Andrés that suggests that the ground state is mainly reached through a barrierless funnel corresponding to the ^2E conical intersections within 100 fs, being the $^1S_6$ CI an alternative residual funnel for deactivation.

Femtosecond experiments show a biexponential decay with τ_1=40-100 fs and τ_2= 0.75-1.1 ps, depending on the selected excitation energy within the range 250-277 nm, that are in very good agreement with the simulated times computed by Barbatti, τ_1= 22 fs and τ_2= 1ps.[11,12] Although Bisgaard et al. experimentally measure similar deactivation times for adenine, 0.75 ps, these authors conclude that the population of the ground

state mostly takes place through the singlet $n\pi^*$ relaxation funnel. [13]
Regarding triplet state population, few experimental data are available, however a very little quantum yield for triplet population (0.0023) was measured by Nikogosyan et al. [14] and Bishop et al. registered modest singlet oxygen yield (0.03).[15] These results are consistent with the ultrafast decay to the ground state from the singlet manifold described above, which prevents the wavepacket from visiting regions of the PES for ISC for enough time to populate the triplets. Unfortunately, no dynamics simulations considering the triplet state population for adenine have been performed, being not possible to corroborate the assumptions made based on static quantum calculations.

The other natural purine DNA nucleobase is **guanine**. Similar analysis for the main deactivation mechanism for excited guanine base can be made in terms of static and dynamic calculations. Additionally, numerous experiments were performed for this base. As for adenine, although there are several possible tautomers for the guanine, on the following only the 9H-guanine will be considered for being the biological relevant. Guanine's calculated (CASPT2//CASSCF(14,12)/6-31G(d,p))[3] absorption spectrum presents significant differences compared to adenine's. The S_3 $\pi\pi^* L_a$ state in adenine, becomes the first excited state, S_1 $\pi\pi^* L_a$ state, in guanine placed at 4.93 eV and with an oscillator strength of 0.158. This state is followed by the S_2 $n\pi^*$ (0.002) and S_3 $\pi\pi^* L_b$ (0.145) excitations located at 5.54 and 5.72 eV respectively. Then, for guanine, the S_1 $\pi\pi^* L_a$ state corresponds to the spectroscopic state due to its large roscillator strength and its lower energy compared to the S_3 $\pi\pi^* L_b$.

The computed MEP from the spectroscopic state performed along the S_1 state for guanine in Ref [3], is presented in Figure 1.2. Since the spectroscopic state is the first excited state no crossings with lower-lying singlet state are found, except from the one with the ground state. The shape of the MEP profile is quite similar from the one computed for adenine, something reasonable if one takes into account that both bases share the same spectroscopic state. Again the MEP reaches the CI with the S_0 barrierless from the FC region, recall Figure 1.2. Reaching the ($gs/^1\pi\pi^* L_a$) CI requires both the twisting of the C_2-N_3 bond and a envelope puckered ^2E geometry, which involves the out of plane movement of the NH_2 group, see Figure 1.2. The geometries of both CIs for adenine and guanine are quite similar except for the intrinsic differences of both bases geometries. The authors connect the existence of this barrierless paths connecting the FC with the ground state, with favourable and ultrafast internal conversion processes.[3] Two triplet excited states were computed below the spectroscopic state at the FC region, lying at 4.11 and 4.76 eV above the GS and presenting $\pi\pi^* L_a$ and $\pi\pi^*$ characters. The next two triplet states, $\pi\pi^*$ (5.14 eV) and $\pi\pi^*$(5.30 eV), can be found between the S_1 and S_2 states. Then along the MEP, the S_1 $\pi\pi^* L_a$ state crosses with the two low-lying triplet states.[7] Almost at the beginning of the MEP, the $^3\pi\pi^*/^1\pi\pi^* L_a$ intersystem crossing is found, however the SOC terms were calculated to be < 0.1 cm^{-1} which turns the triplet population not very likely to occur. The crossing of the spectroscopic state with the lowest triplet is located almost at the end of the MEP, presenting larger SOC and therefore being a more efficient ISC funnel to the triplet manifold, see Figure 1.2. Although other singlet/triplet intersections were found with similar SOC values, their location far from the MEP renders them less favourable for triplet population.

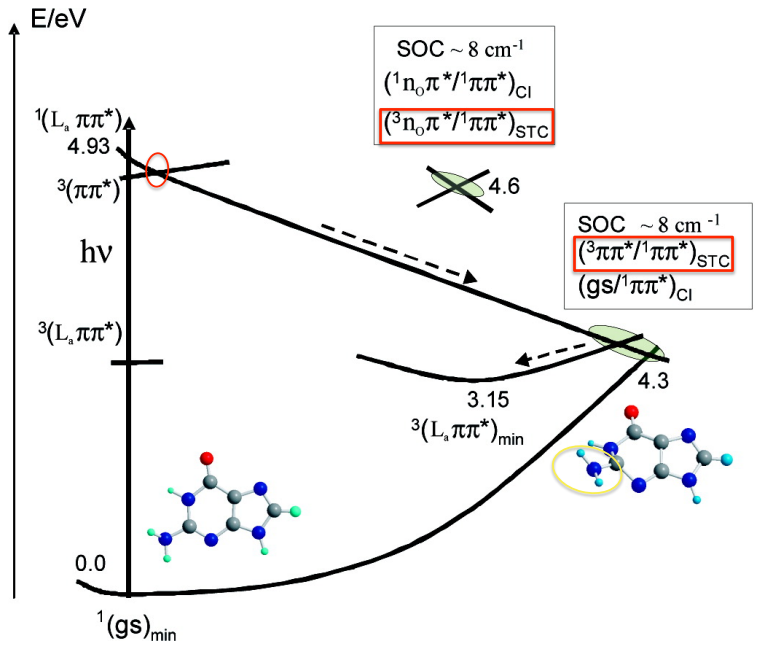

Figure 1.2. CASPT2 singlet and triplet profiles (energies in eV) describing the deactivation of guanine extracted from Ref [3]. Framed in red possible ISC funnels along the MEP and highlighted in yellow main geometrical distortion undergone by the system at the position of the CI compared to the FC structure.

Gas phase experiments show a biexponential decay with τ_1=0.15 ps and τ_2= 0.36 ps after 267 nm excitation.[11] The same behaviour was found for excited state dynamics of guanine in water with τ_1=0.22 ps and τ_2= 0.90 ps in the probe region 400-900 nm and triexponential with τ_1=0.25 ps, τ_2=1.00 ps and τ_3=2.50 ps between 270 and 400nm.[16] These authors relate τ_1 with the time that the system needs to reach the flatter parts of the PES from the FC region. Once in this region, the system can undergo IC to the ground state, τ_2, and then hot ground-state guanine molecules can undergo vibrational cooling, τ_3. This ultrafast decay of guanine is in good agreement with the existence of a barrierless pathway connecting the spectroscopic state at FC region with the GS, previously described. Although other studies[17] postulate the existence of a minimum preceding the CI to the ground state, its energy barrier to reach the CI is not high enough to avoid fast internal conversion. Three different CIs have been proposed to be responsible for the deactivation to the ground state in the basis of quantum chemical studies, and have also been observed in molecular dynamic simulations.[18] Two of them, ethylenic I and ethylenic II are characterized by the puckering of the C2 atom, while the third one, oop-O, requires the out of plane movement of the O atom. Nonadiabatic dynamics simulations performed in gas phase using MR-CIS level of theory conclude that the population of the ground state takes place in 0.224 ps through the ethylenic CIs (I and II) (almost 95 % trajectories show the puckering of the C2 atom), which perfectly matches with the experimental measurements described above (τ_2= 0.36 ps).

As for the adenine base, it has only been recently that the population of triplet manifold in guanine has gained interest from a dynamic point of view. Some

experimental measures have also reported a very low quantum yield for triplet population, 0.0012.[14] Again these low rates can be rationalised looking at the short lifetimes found for the S_1 state on its decay to the S_0, in both experimental and theoretical studies.

	ΔE (eV) (*f*)	τ_1^{S2-S1} (exp)	τ_1^{S2-S1} (theor)	τ_2^{S1-S0} (exp)	τ_2^{S1-S0} (theor)
Adenine					
$^1n\pi^*$	4.96 (0.004)				
$^1\pi\pi^*$ L_b	5.16 (0.004)	40-100fs	22fs	0.75-1.1ps	1ps
$^1\pi\pi^*$ L_a	5.35 (0.175)				
Guanine					
$^1\pi\pi^*$ L_a	4.93 (0.158)				
$^1n\pi^*$	5.54 (0.002)	0.15ps	-	0.36ps	0.22ps
$^1\pi\pi^*$ L_b	5.72 (0.145)				

Table 1.1. Summary of the main data characterizing adenine and guanine spectroscopic properties.

The fundamental theoretical and experimental information regarding absorption and deactivation of purine bases, adenine and guanine, are summarized in Table 1.1. From the existing experimental and theoretical literature it is possible to ascribe the ultrafast deactivation of guanine and adenine from their spectroscopic states S_1 and S_3 of $\pi\pi^*L_a$ nature to a barrierless pathway from the FC region towards the GS. The excited state lifetimes are shorter for guanine deactivation due to the lower number of internal conversion funnels it has to traverse on its way to the GS. Regarding triplet manifold population, both bases present ISC along the MEP but with modest computed SOC, being the experimentally measured quantum yield low.

Pyrimidine Bases

Thymine absorption spectrum has been widely studied using different computational methods,[2,19,20] concluding that the spectroscopic state of this base is the second excited state, S_2. For consistency, if the data obtained by means of CASPT2//CASSCF (14,10)/ANO-S are analysed[2], the low-lying singlet excited states of thymine are S_1 ($n\pi^*$) S_2 ($\pi\pi^*L_a$) and S_3 ($\pi\pi^*$) computed vertically at 4.77, 4.89 and 5.94 eV, see Table 1.2. The oscillator strengths for these excitations are respectively 0.004, 0.167 and 0.114. In view of these values, the S_2 $\pi\pi^*L_a$ state is considered the spectroscopic state for thymine. Although the state ordering differs from purine bases (compare Tables 1.1 and 1.2), the character of the spectroscopic states coincides for all the natural bases examined so far. Two triplet states, $\pi\pi^*L_a$ and $n\pi^*$, were computed

below S_2 presenting an energy difference between them of 1.2 eV. The triplet state pattern of thymine is quite similar to the one found for adenine (same state ordering and large energy gap between them, 0.9 eV in adenine), while both differ from the one recorded for guanine (the first two triplet states present $\pi\pi^*$ character and lye closer in energy 0.4 eV). The third triplet state lies within the spectroscopic state and the next singlet excited state.[7] Apparently, in view of the picture regarding state ordering at the FC region, a behaviour similar to the one of adenine is expected for the deactivation of excited thymine along the minimum energy path evolving along the $\pi\pi^* L_a$ state.

As previously described for the purine bases, the computed MEP from the spectroscopic state in thymine also reaches the $(gs/^1\pi\pi^* L_a)$ CI without non energy barriers. As thymine deactivated, the heterocycle moves out of the plane the CH_3 group, in position 5, see Figure 1.3. Close to the FC region, the spectroscopic state crosses the low-lying first $n\pi^*$ singlet state. If the system is able to populate this state, it can evolve to a minimum in this potential. Up to now the described region of the PES is very similar at the one found for the adenine base.[2] Three different ISC mechanisms for triplet population can take place. Close to the FC region, the system can populate the triplet manifold via $^3n\pi^*/^1\pi\pi^* L_a$ crossing point.[7] As the MEP evolves, another region with non-negligible ISC probability is found close to the CI with the ground state, see Figure 1.3. Both singlet/triplet crossing points are characterised by modest spin orbit coupling terms ~8 cm^{-1}.

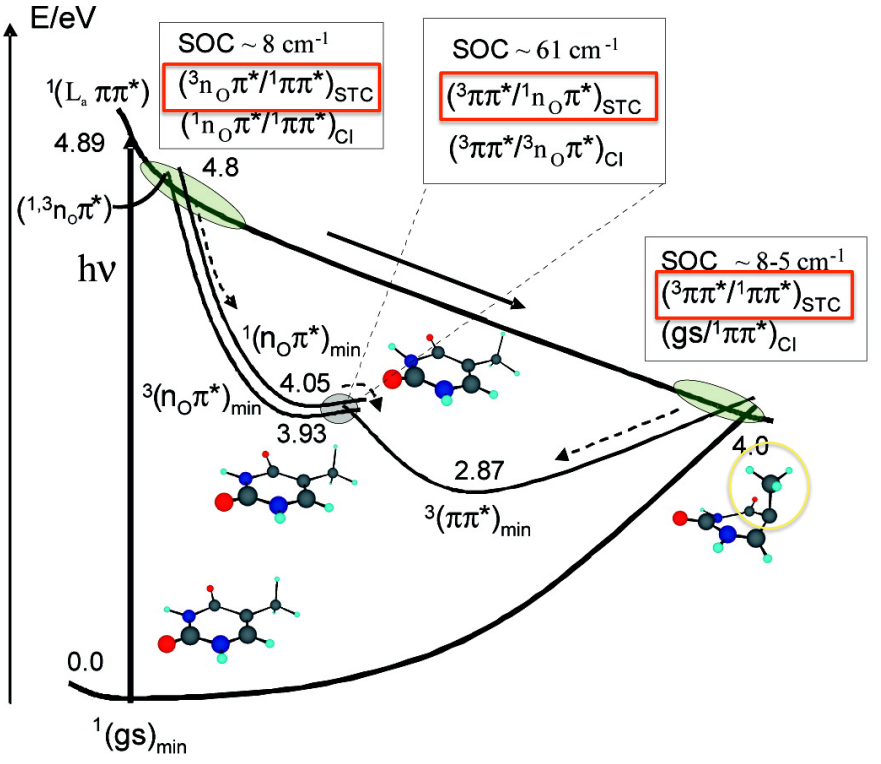

Figure 1.3. CASPT2 singlet and triplet profiles (energies in eV) describing the deactivation of thymine extracted from Ref [2]. Framed in red possible ISC funnels along the MEP and highlighted in yellow main geometrical distortion undergone by the system at the position of the CI compared to the FC structure.

A third mechanism for triplet population can take place from the $^1n\pi^*$ singlet state through a $^1n\pi^*$ / $^3\pi\pi^*$ crossing with much more larger SOCs amounting to 61 cm^{-1}, suggesting that it is the most important one. The three ISC paths are similar to those computed for the adenine base, however the last one presents also modest SOC in adenine. Then, the first difference between adenine and thymine can be established in base of the preferable intersystem crossing for triplet population (compare Figures 1.1 and 1.3).
Dynamic experiments and theoretical simulations on thymine base have led to quite different results. The existence of both a short-lived singlet state and a long-lived dark state have been experimentally demonstrated both in gas phase and in solution.[21-23] However, Buker et al maintain that in water solution internal conversion to the ground state takes place so fast that the dark state is not populated anymore, being possible to increase its lifetime under careful control of the water pressure.[23] These works assign this dark state either to an $n\pi^*$ state or a triplet state. The later possibility has been supported by fs pump probe spectroscopic studies, in acetonitrile solution, which measure the lifetime for triplet population to be < 10ps.[21,24,25] This triplet state cannot be reached from the $n\pi^*$ state since its population takes place in 3ns. However, hot molecules of the $n\pi^*$ can be precursors of the triplet state in solution. In fact, thymine and its analogue uracil have been reported to present larger yield for triplets (0.012 and 0.014)[14] and singlet oxygen generation (0.07 and 0.13)[15] than purine bases. Unfortunately no dynamic simulations considering the triplet states have been performed so far for thymine, which would be very useful to understand the actual role of the triplet states in the experimental lifetimes.

Nonadiabatic dynamics performed along the singlet manifold demonstrate that thymine has the longest lifetime for the S_2-> S_1 decay, 2.6 ps,[26] among the five natural nucleobases, which in view of the absorption energies at FC region is not very reasonable since both states are as closer in energy as for instance in adenine (22fs). Then, this long time measured for the S_2-S_1 decay has been reasoned in terms of three possible scenarios: (1) Perun et al[27] suggest that this long time can be attributed to direct population of the dark $n\pi^*$ state, trapping the population on its minimum (2) Hudock et al[28] show that within the first 500 fs only a small number of the trajectories will decay to S_1 and (3) Merchán et al[29] predict that S_2 molecules would undergo IC to the GS through a barrierless pathway in the fs scale, while alternative mechanisms involving the S_2 trapping will take place at longer times. Regarding the decay to the ground state, dynamic simulations performed during 3 ps were not able to obtain enough trajectories decaying to the ground state to be statistically relevant.[26] These authors attribute the longer lifetimes observed for thymine to both S_2 and S_1 minima trapping. Interestingly, the MEP in Figure 1.3 based on CASPT2 calculations shows no minimum before the CI for accessing the S_1 or the S_0, however the shape of the potential is very flat in this region of the surface. In fact, the energy difference between the FC excitation energy and the S_1/S_0 CI is small (0.8 eV) compared to adenine (1.4 eV). Is the topology of the PES along the MEP able to explain the longer S_1-> S_0 and the S_2-> S_1 decay times? Are there other states involved in those traps? Further calculations on similar derivatives could be useful on providing an answer to these questions.

The last part of this section is dedicated to **cytosine** DNA base. As for the other bases, its absorption spectrum at the FC region will be analysed in first instance.[6] The first excited state is the $^1\pi\pi^*$ L_a with an excitation energy of 4.41 eV and an oscillator strength of 0.069. This state is followed by two $^1n\pi^*$ states placed at 4.95 and 5.06 eV presenting both of them very small intensities. Taking into account the much higher excitation energy of the $^1\pi\pi^*$ L_b state (5.89 eV) which correspond to the fourth singlet excited state in cytosine, despite its larger oscillator strength (0.106) the S_1 has been traditionally taken as the spectroscopic state.[6] Then, the situation is similar to the guanine base where also the S_1 $^1\pi\pi^*$ L_a is the bright state, although some differences are found considering the position of the triplets at the FC region. In fact there is only one triplet state, the $^3\pi\pi^*$ L_a, below the S_1 while other three triplet states are placed between S_1 and S_2 (one $^3\pi\pi$ plus two $^3n\pi$ states).

The singlet decay for cytosine is more complicated, since it presents a $^1\pi\pi^*$ L_a minimum in the proximity of the (gs/$^1\pi\pi^*$ L_a) CI. The CI is of the ethane-like type and is placed at 3.6 eV relative to the GS.[6] The existence of this minimum opens other possible competitive deactivation mechanisms, as for instance, fluorescence from this minimum. However, the computed energy barrier from the $^1\pi\pi^*$ L_a to the CI amounts to 2.5 kcal/mol and therefore the MEP could in practice be considered barrierless, being in principle more favourable to reach the ground state radiationless through the CI. Intersystem crossing to the triplet manifold can compete with IC to the ground state.[7] Again, the $^3\pi\pi^*/^1\pi\pi^*$ L_a crossing which is close to the (gs/$^1\pi\pi^*$ L_a) CI, presents a non-negligible value for spin orbit coupling terms (6 cm^{-1}).

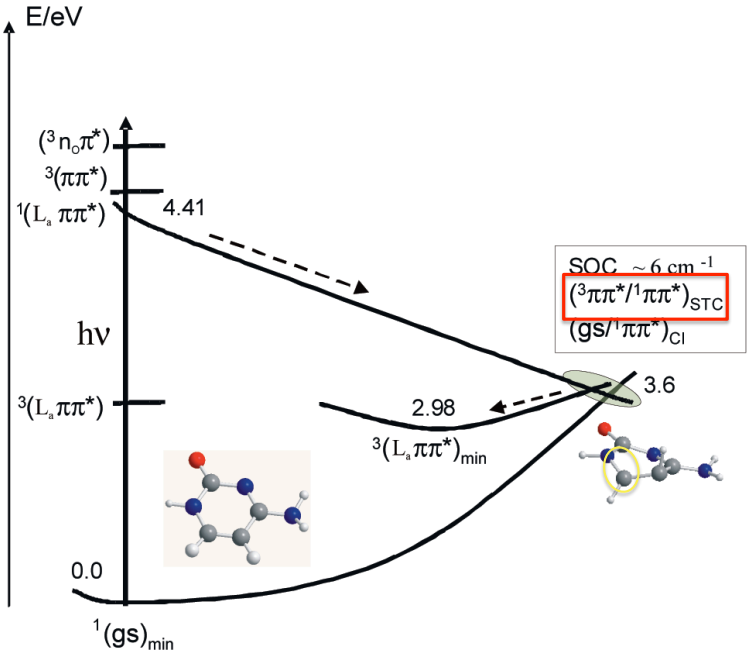

Figure 1.4. CASPT2 singlet and triplet profiles (energies in eV) describing the deactivation of cytosine extracted from Ref [6] Framed in red possible ISC funnels along the MEP and highlighted in yellow main geometrical distortion undergone by the system at the position of the CI compared to the FC structure.

Ultrafast excited state decay time constants of <50 fs, 820 fs and 3.2ps upon 250 nm excitation have been measured for cytosine.[30] Barbatti et al[31] found three different accessible CI for accessing the ground state. One of them is semi-planar, while the other two imply out-of-plane movements of the NH_2 (oop-NH_2) and the C6 (C6-puckered) atom respectively. Merchán et al[32] gave more importance to the C6 CI due to the barrierless connection between the FC region and this region of the PES. Different results have arisen from dynamic simulations depending on the selected level of theory used for the calculations. CASSCF(2,2)[33] and AM1/Configuration Interaction. [34] dynamics simulations found the CI oop-NH_2 to be preferred for most of the trajectories. However, more recent CASSCF dynamics using a larger active space (12,9)[8] attribute more importance to the semi-planar CI in the deactivation mechanism of excited cytosine. Baribatti et al., performing CASSCF(14,10) dynamics, arrive to similar results finding a 62% of the trajectories deactivating through this CI, opposed to the remaining 18% which reach either C6 or oop-NH_2 CIs.[31] All these dynamic studies predict internal conversion to take place in the sub-picosecond scale, but they differ on the proposed deactivation pathway. Experiments on cytosine registered similar triplet population yields as for the other pyrimidine bases. However, for this base, recent ab initio surface hopping dynamic simulations considering the triplet manifold have been performed.[8] This study shows that although a large percentage of the trajectories, 60%, decays back to the ground state within the first 500 fs also some population, 25%, is transferred to the triplet manifold within the same time scale. These results confirm that, although cytosine presents modest spin orbit coupling terms, the main deactivation mechanism based on IC to the ground state competes with ISC, in concordance with the experimental results.[8]

Conclusions: (1) For the four DNA bases (A,G,C and T) the spectroscopic state is the $^1\pi\pi^* L_a$. This state corresponds to the S_1 for G and C, S_3 for A and S_2 for T. (2) Barrierless paths are found for all of them connecting the FC region with the ground state (3) Non negligible but modest probability for triplet population are found for all of them through $^3\pi\pi^*/^1\pi\pi^* L_a$ and the $^3\pi\pi^*/^1n\pi^*$ (for T) crossings.

	ΔE (eV) (*f*)	τ_1 S2-S1 (exp)	τ_1 S2-S1 (theor)	τ_2 S1-S0 (exp)	τ_2 S1-S0 (theor)
Thymine					
$^1n\pi^*$	4.77 (0.004)	-	2.6ps	0.5-30ps (assigned to $^1n\pi^*$) 0.15-0.20ps (assigned to $^1\pi\pi^*$)	> 3ps
$^1\pi\pi^* L_a$	4.89 (0.167)				
$^1\pi\pi^*$	5.94 (0.114)				
Cytosine					
$^1\pi\pi^* L_a$	4.41 (0.069)	50-100fs	7-40fs	160-820fs	270-800fs
$^1n\pi^*$	4.95 (0.001)				
$^1n\pi^*$	5.06 (0.003)				
$^1\pi\pi^* L_b$	5.89 (0.106)				

Table 1.2. Summary of the main data characterizing thymine and cytosine spectroscopic properties.

1.2 DNA Derivatives

Structural DNA bases analogues have gained importance during the last decades. This interest relies in their biochemical properties. In fact some of these derivatives have been found to be useful for medical purpose, such as anticancer therapies. Examples of these derivatives are, for instance, the aza bases, where an extra nitrogen atom has been inserted into the purine's skeleton, which are well-known for their antineoplastic and fungistatic properties, as well as for their biological effects. Amino derivatives, as 2-aminopurine, which is a constitutional derivative of the adenine base is also a quite interesting case due to its strong fluorescence compared to the nonfluorescent behavior of adenine. Also methylation has been taken as a strategy to shed light into the deactivation mechanism of the nucleobases by comparing their decay with the one found for the natural bases. However, oxygen-by-sulfur substitution has been proved to present one of the strongest effects on the DNA photostability, being the study of these thiobases one of the main aims of this thesis.

1.2.1 Aza bases

As already mentioned the interest of aza-substituted bases relies in their application as drugs for the treatment of several diseases, including cancer. The dramatical change in the excited dynamics of the natural bases when aza substitution of a carbon atom within the six-membered ring takes place, has been widely studied by Kobayashi et al.[35,36] High level quantum chemical calculations have been also performed for some of the aza-substituted bases.

CASPT2//CASSCF/ANO-L-VDZP calculations performed by Gobbo et al.[37] on the 8-**azaadenine** (AZA) base show already differences at the FC absorption spectrum compared to adenine. Although the two bases have in common the character of the first excited state, ($n\pi^*$), the spectroscopic $\pi\pi^*$ excited state is the second excited state in AZA but it corresponds to the third excited state in adenine. The spectroscopic state of AZA peaks at 4.63 eV (~0.5 eV lower in energy than adenine) with an oscillator strength of 0.284. The MEP starting from this state at the FC region, leads barrierless to a minimum in this potential, being the CI with $S_1(n\pi^*)$ state close to this minimum. Then, two different singlet minima $S_2(\pi\pi^*)_{min}$ and $S_1(n\pi^*)_{min}$ can be easily accessed barrierless from the FC region.

Regarding triplet population of AZA, efficient mechanisms towards the triplet manifold were found from any of the above described singlet minima. If the $S_2(\pi\pi^*)_{min}$ is reached, there is a non negligible probability that the wavepacket explores the region of a crossing with the $T_2(n\pi^*)$ very close to it. Relaxation to the $T_1(\pi\pi^*)$ would be then achieved through a CI between the two triplet states. On the other hand, if the $S_1(n\pi^*)$ minimum is populated through the S_2/S_1 CI, the triplet manifold would be populated through an ISC with the $T_1(\pi\pi^*)$ lying close to this $S_1(n\pi^*)_{min}$, (see Figure 1.5). The presence of minima along the MEP together with the existence of energy barriers preventing the decay to the ground state is in good agreement with the

experimental findings where they are able to measure a fluorescence quantum yield of 3.2×10^{-3}.[35] Transient absorption spectrum after 248nm irradiation shows a peak at 455 nm, which has been associated to the absorption of AZA triplet states for its lifetime of submicroseconds and its effective quencher by O_2. Sensitized singlet oxygen formation in AA was also observed with quantum yields of 0.15±0.02, which again suggests a very efficient triplet population.[35]

Interestingly, the computed spin orbit coupling at both ISC presented above were found to be modest SOC ~10 cm^{-1}. A careful inspection of similar calculations performed for **6-azauracil** (AZU) reveal similar pathways as the ones characterized for the deactivation of AZA, but however, for AZU larger SOC terms, ~60 cm^{-1}, were found at the $^3\pi\pi^*/^1n\pi^*$ crossing.[38] Experimentally, only a weak emission was observed after excitation with 308 nm light, presenting a fluorescence quantum yield of 4.2×10^{-3}.[36] The transient absorption spectrum is characterized by an intense absorption band placed at 320 nm that decays within the microsecond timescale. The transient was effectively quenched by O_2, with a singlet oxygen formation quantum yield of 0.63±0.03.[36] The larger singlet oxygen yields obtained for AZU are perfectly consistent with the larger SOCs calculated for this system.

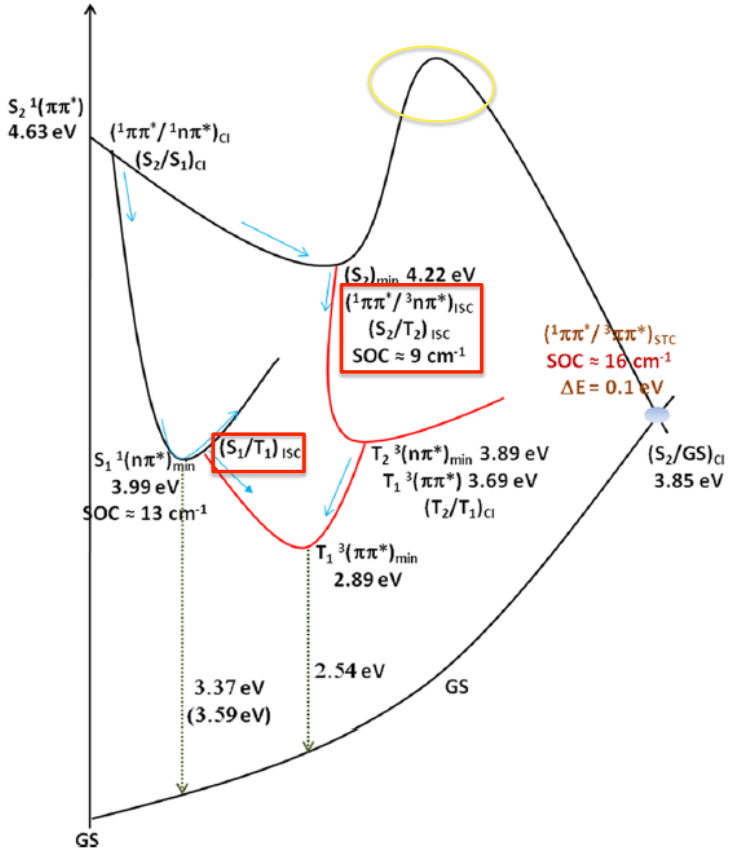

Figure 1.5. CASPT2 singlet and triplet profiles (energies in eV) describing the deactivation of azaadenine extracted from Ref [37] Framed in red possible ISC funnels along the MEP and yellow circles indicate the energy barrier that needs to be surmounted for accessing the CI for decaying to the ground state.

Experimental and computational data suggest that relaxation mechanisms in the natural (U and A) and aza-substituted bases (AZA and AZU) are very different. While relaxation to the ground state is the main deactivation channel in excited U and A, singlet-triplet intersystem crossing (ISC) seems to be the most important process in excited AZA and AZU.

Similar experimental studies have been performed by Kobayashi et al.[36] for the aza derivatives of guanine and cytosine bases, but no theoretical studies far from the FC region are available. The absorption spectrum of **8-azaguanine** (AZG) presents an intense band peaking around 260 nm (as AZA and AZU), whereas a very weak band was found in this region for **5-azacytosine** (AZC).[35] TD-DFT calculations of the absorption spectrum reported by the same authors attribute the absorption band of AZG to the first excited state $S_1(\pi\pi^*)$ peaking at 267 nm and with large oscillator strength (0.1482). On the contrary, the TD-DFT computed absorption spectrum for AZC predict the first two excited state $S_1(\pi\pi^*)$ and $S_2(\pi\pi^*)$ in the energy region (266 and 248 nm) but presenting significantly lower oscillator strength (0.0034 and 0.0145), in agreement with the weak experimentally recorded band.

In order to investigate the role of triplet states in AZG and AZC, Kobayashi et al.[36] recorded the transient absorption spectra for both azabases. A weak and broad band in the region from 300 to 700 nm characterized these spectra for AZG and AZC. However, the authors do not connect these results with the evidence of triplet states since they were no quenched by O_2. The formation of triplet species in AZG and AZC was not observed, revealing that they should present a low triplet yield.

Considering the previous experimental findings and supported by computational results, Kobayashi et al. conclude that the aza derivatives can be divided into two main categories. Type A bases (AZA and AZU) that present significant intersystem crossing quantum yields, becoming potentially photosensitizers, and Type B derivatives (AZG and AZC) for which ISC was found to be negligible. These differences are explained in terms of the character of the first excited states: Type A molecules present a dark $S_1(n\pi^*)$ state below the spectroscopic $S_2(\pi\pi^*)$ state, whereas in the case of Type B bases both S_1 and S_2 state present $\pi\pi^*$ character. This fact is expected to influence the relaxation mechanism of the aza analogues leading to different excited state dynamics. However, further computational studies including minimum energy paths, the optimization of singlet/singlet and singlet/triplet minimum energy crossing points and the computation SOC at these points are required (for AZG and AZC) to corroborate this hypothesis, which allows the classification of azabases as potential photosensitizers.

1.2.2 Amino and methyl substitution effects

Studies carried out by Gustavsson et al. show that **amino substitution** in **uracils** affects their photochemistry, in a greater or lesser extent, depending on the position where substitution takes place.[39] First, the absorption spectra of U, 5aminouracil (5AU) and 6aminouracil (6AU) will be examined from both experimental and theoretical

points of view. The absorption spectrum of 5AU is extremely different compared to the one recorded for U: (1) the first absorption band of 5AU peaks at 290 nm, which is substantially red-shifted with respect to U (259 nm)[39,40] and (2) a more intense band higher in energy was recorder for 5AU at 221 nm, which is present for U but it is a very weak band. Interestingly, the absorption spectrum of 6AU resembles the one recorded for U: (1) presents the lowest energy band at 262nm, which means a red-shift of only 0.08 eV respect to U and (2) the band at 220 nm is of the same intensity for both U and 6AU. These results suggest that 5-amino substitution has a much greater effect in the absorption spectrum, compared to amino substitution in the 6-position that does not lead to important changes. Theoretical calculated absorption energies at CASPT2/CASSCF(14,10)-ANOL level, agrees with the experimental findings, being the energies for the $S_1(\pi\pi^*)$ (which can be described as a HOMO-LUMO excitation) state much more affected (1 eV) by the substitution at 5 position: 5.22 eV (U) < 5.42 eV (6AU) < 4.42 eV (5AU). The authors explain the decrease of the HOMO-LUMO energy gap for 5AU in terms of the shape of the frontier orbitals, which show that the contribution of the lone pair of the amino substituent is antibonding with respect to the C_5 atom. The stabilization of the S_1 state at the FC region justifies the red-shift of the absorption energy.

Fluorescence quantum yields of 5-aminouracil $6x10^{-4}$ (5AU), 6-aminouracil $5x10^{-5}$ (6AU) and uracil $3.5x10^{-5}$ (U) seem to confirm that the excited-state behavior of amino derivatives are much more sensitive to the 5-substitution.[39,40] Computational studies rationalize this fluorescence behavior in terms of the shape of the S_1 PES (1) the absence of a minimum in the barrierless path connecting FC to the CI with the GS for U and 6AU explains the low fluorescence yields, whereas (2) the presence of a true minimum in the S_1 potential for 5AU could explain the low fluorescence yield, since the system could remain trapped in this minimum before reaching the conical intersections with the ground state.[39,40]

Regarding **purine** bases, similar excited state dynamics has been shown for 2-aminopurine (2AP) and 2,6-diaminopurine (2,6DAP) differing from the one previously described for adenine (A=6AP).[41,42] For instance, their experimental recorded decay lifetimes to the ground state are around 6 ns for both 2AP and 2,6DAP, much more longer that the ones found for A (1 ps). These differences have been rationalized in terms of the geometrical changes that the system needs to undergo for accessing their deactivation funnels. It has been demonstrated that the CI for accessing the ground state is characterized by the twisting of the C_5=C_6 bond together with the C_2 puckering. Both structural changes were assumed to be harder to achieve in substituted AP on these positions (2, 5 and 6), resulting in slower excited state dynamics in these derivatives.[41] CASSCF/MRMP2 calculations performed by Mburu et al. at the FC equilibrium geometry conclude that substitution at the C_2 position leads to a great stabilization of the $\pi\pi^*$ state, whereas introducing an amino group at the C_6 has much lower effect. [43]

Recently, transient absorption experiments have investigated the role of intersystem crossing in 2AP excited state dynamics.[44] Three transient absorption bands were recorded, peaking at 330, 410 and 540 nm in acetonitrile which were

associated to ππ* states absorption. Measured lifetimes are strongly dependent on the solvent, varying from 0.3 ps in acetonitrile to 12 ps in ethanol. As the ππ* state signal decays, a new transient absorption band appears with a maximum at 425 nm. This new band, which is quenched by O_2, indicates that the transient corresponds to a triplet state. The relative triplet yield also depends on the polarity of the solvent being 0.2±0.1 and 0.4±0.1 in ethanol and acetonitrile, respectively.[44] For the studied solvents, the sum of fluorescence and triplet yields amounts to ~0.7, suggesting that only 30% of the initial state decays to the ground state. The authors suggest the following nonradiative relaxation pathway for this system: $^1\pi\pi^*$-> $^1n\pi^*$-> $^3\pi\pi^*$.

Serrano-Andrés et al.[5] have also examined the photochemistry of 2AP from a theoretical perspective aiming to explain the differences between this system and its analogue, adenine, as well as the rationalization of the experimental findings described above. Based on CASPT2//CASSCF (16,13)/6-31g(d,p) calculations, they found that the substitution of the purine's skeleton with an amino group affects also to the absorption spectrum of the base. In this respect, the low lying excited states of 2AP at the FC region show $\pi\pi^*L_a$, $n\pi^*$ and $\pi\pi^*L_b$ character, peak at 4.33, 4.46 and 5.33 eV and present 0.070, 0.008 and 0.148 oscillator strengths, respectively. At difference, A absorption spectrum is characterised by one $n\pi^*$ (S_1) followed by two $\pi\pi^*$, S_2 ($\pi\pi^*L_b$) and S_3($\pi\pi^*L_a$), with the later considered as the spectroscopic state. Thus, although both bases have in common the spectroscopic state (S_1 in 2AP and S_3 in A), the FC ordering if the electronic state is different. Other differences arise when comparing the MEPs of both bases.

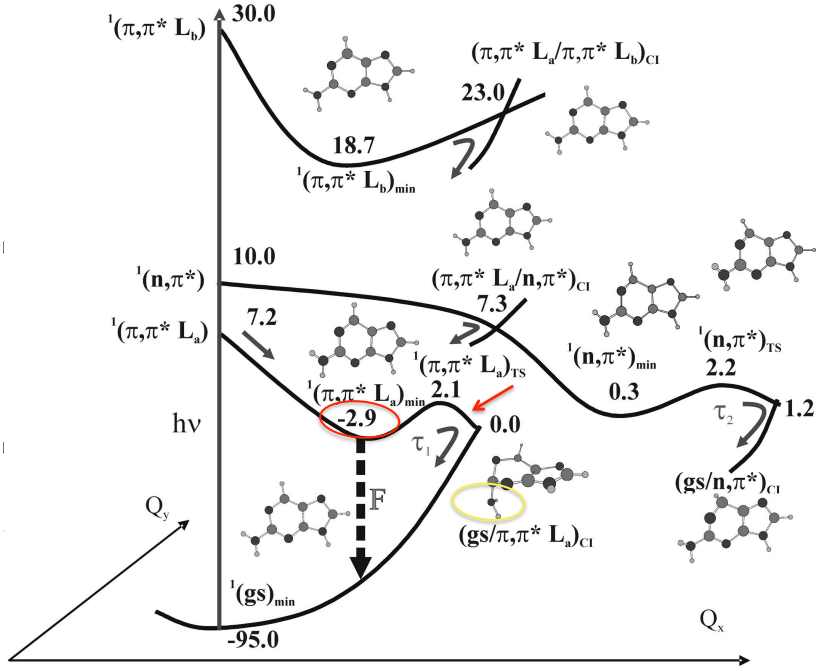

Figure 1.6. CASPT2 singlet and triplet profiles (energies in kcal/mol) describing the deactivation of 2aminopurine extracted from Ref [5] Framed in red differences in the profile compared to adenine and highlighted in yellow main geometrical distortion undergone by the system at the position of the CI compared to the FC structure.

In 2AP the MEP from the FC region[5] along the $\pi\pi^*$ L_a state arrives at a minimum on this potential (see Figure 1.6). This is in contrast with A, where the MEP directly leads to the CI with the ground state (recall Figure 1.1). The absence/presence of this minimum would explain why adenine efficiently quenches fluorescence, while experimental studies are able to measure fluorescence for 2AP. From the minimum, after surmounting a small energy barrier it is possible to reach the deactivation funnel to the ground state. As already mentioned above, the geometrical distortion of the substituted purine ring would be responsible for the small energy barrier separating the minimum and the CI. This profile would as well explain the longer lifetimes found for 2AP decay to the ground state compared to adenine, where the CI is accessed barrierless along the MEP. 2AP is one of the derivatives with a minimum along the MEP of the spectroscopic state, most of them evolve without energy barriers and/or minimum towards the CI facilitating deactivation to the ground state. Nevertheless, it is important to highlitgh that the height of the energy barrier is very low.

In the following, we will summarize the effect of introducing **methyl group**s into the purines' skeleton.

Methylation of **uracil** in positions 1 and 5 shifts the absorption maxima ca. 8 nm and 6 nm, respectively, to the red.[45] Taking into account that this shift for 1,5DMU (1,5-dimethyuracil) is almost twice the former value, a first glance to it could conclude that the effect of methylation is additive. For substitution in position 6 6MU (6-methyluracil) and 3 3MU (3-methyluracil), however, no significant changes were observed in the absorption spectra with respect to the no substituted base. TD-DFT calculations show that methylation in position 1 or 5 induces antibonding character to the HOMO orbital, increasing its energy, at the same time decreasing the HOMO-LUMO energy gap.[45] This could be and explanation for the red-shift in the absorption spectrum of 5 methyl-compounds and it is in good agreement with the results found in combined experimental-theoretical studies performed by Bányász et al for the 5-aminouracil (5AU) derivative.[40]

Although the Stokes shifts in the fluorescence spectra do not show a constant trend, it was found to be larger for 5-substituted derivatives. In view of the fluorescence behavior the authors conclude then, that even if methylation in position 5 leads to changes in the ground and excited state electronic structure, these effects could be similar but not the same. The fluorescence decay time for U, 1MU (1-methyluracil), 3MU, 6MU and 1,3DMU (1,3-dimethyluracil) were estimated to amount to about 100 fs. Again, position 5 is the only one showing slower decay of the fluorescence. In fact, 5MU and 1,5DMU decay biexponentially four times slower than other methyl derivatives. The optimized S_1/S_0 conical intersection at the CASSCF level of theory, presents a pyramidalization of the C_5 atom. The access of this CI in derivatives substituted at the C_5 position would be more difficult, leading to longer excited-state lifetimes.[45]

Excited state dynamics of 6-N,N-dimethyl**adenine** (6DMA) was found to be very

different from that of adenine. 6DMA presents dual fluorescence due to the presence of two ππ* states, which can be connected through the motion of the methylamino group through a twisted mode. Both studies[46,47] ascribed S_1 state to an intramolecular charge transfer (ICT) state, while the higher excited state, is a localized state (LE), mostly centered within the purine ring. LE is predicted to rapidly decay via ISC to the triplets, which eventually could experiment a non-radiative deactivation to the ground state. [46,47]

In view of the all above presented studies some conclusion can be extracted: (1) Substitution at different positions does not affect to the same extent the photochemistry of natural bases. In fact, the positions leading to the greater changes were found to be system dependent, being for instance 6 and 1 in uracil and 2 in the purine ring. Why these numbers? These positions have been proven to change their electron density upon excitation and to be involved in the geometrical changes that the system undergoes in its way to the GS (2) The effect of amino substitution was found to strongly influence nucleobase's photophysical properties, while methylation was suggested to affect their photophysics in a lesser extent.

Calculations in other DNA derivatives as the free purine base can be useful on understanding how the substituents affect the photochemistry of these bases, see Chapter 6.

1.3 ThioBases

Other interesting derivatives to be studied are those arisen from the incorporation of heavy (second row) atoms in the system. This is the case of thiobases where the oxygen from the carbonyl group has been substituted by sulfur atoms. Thiopurines have been extensively used as immunosuppressant after organ transplantation and prescribed as effective anti-inflammatory and anticancer agents.[48] The anticancer properties were first found for 6-mercaptopurine (6-MP), which was shown to inhibit tumor growth in rodents and to dramatically increase the improvement in the survival of children suffering from leukemia. Some years later, 6-MP was also found to present immunosuppressant pharmacological properties. Since their introduction in 1960s their use has been widely extended due to increase in patients' survival following organ transplantation, after treatment with this drugs. These prodrugs have been progressively replaced by a newer generation of immunosuppressant, for instance mycophenolate acid, which is actually prescribed for 80% of renal transplant patients in the United States hospitals.

Although still thiopurines' use remains widespread caution must be exerted since their potential carcinogenic consequences have been associated to their prolonged use. In fact, long-term treatment with thiopurines has been associated with acute skin sensitivity to UVA radiation, increasing the risk of suffering from skin cancer. Sunlight exposure has been proven to be a cofactor in this increased cancer risk. Despite UVA comprises more than the 95% of the ultraviolet radiation in incident sunlight, it has been considered less harmful than UVB radiation. That is because

DNA weakly absorb in this region of the spectrum (see previous section), in contrast to thiopurines that do absorb in this region. Thereby, after their incorporation into patient's DNA thiopurines can act as UVA photosensitizers. Upon UVA absorption, thiopurines can react generating singlet oxygen, $^1O_2$, as a major product and other reactive oxygen species (ROS). ROS can cause DNA damage and can also oxidize thiopurine themselves, being a major source of mutation. Oxidized forms of thiopurines can also cause problems during the replication process. Furthermore, $^1O_2$ can strongly affect proteins involved in DNA metabolism causing protein damage and DNA-protein cross linking.[49] Cross-linked and/or aggregated proteins would later react with aromatic (alanine, tryptophan…), basic (arginine, lysine and histidine) and sulfur containing (methionine and cysteine) amino acids.

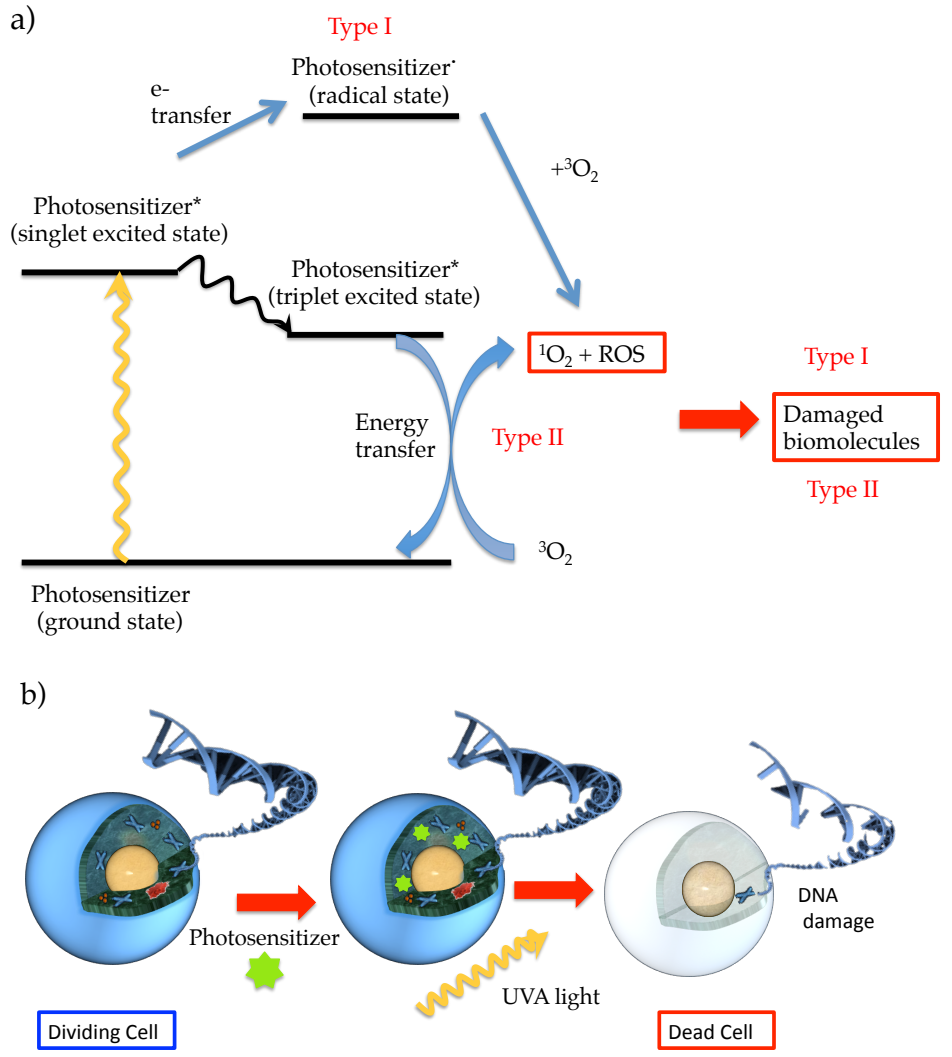

Figure 1.7. a) Jablonski Diagram describing Type I and Type II reactions, which relates the photosensitizer excitation with biomolecules damaging. b) PhotoDynamic Therapy. The photosensitizer is incorporated into the target cell killing it after UVA light absorption.

Then, in summary, photochemical reactions of thiopurine substituted DNA are hazardous for two reasons, first it is a potential UVA photosensitizer which can lead to damage when exposed to sunlight and second, subsequent ROS and $^1O_2$ formation which can lead to proteins mutation and cell death.

Nevertheless, those harmful properties have been used with medical purposes in Photodynamic Therapy (PDT) of cancer, where drugs (as thiopurines) are combined with light to destroy tumoral cells (see Figure 1.7b). Depending on the part of the body being treated, the drug is incorporated to the patients' body either through the bloodstream or into the skin. Light is applied into the affected area once the has been absorbed by the cancer cells. By the above-described mechanism, $^1O_2$ is produced destroying the cancer cells. Despite presenting many pros, as being a less invasive treatment, PDT also has limitations depending on the used drug. When thiopurines are employed the patient remains very sensitive to light for some time, so caution must be taken they are put in or on the body.

Understanding the mechanism responsible for the carcinogenic properties of these drugs, which leads to the cytotoxic products upon UVA absorption, could be very useful to design new functional drugs not presenting these dangerous collateral effects. In this sense, many efforts have been done in the last decades for describing the excited state dynamics and the role of triplet states in thiobases' photochemistry.

6-Thioguanine

6-Thioguanine (6-TG) is one of the most effective thiopurine prodrugs and its unusual photochemical properties are responsible for its damaging effects after incorporation into patients DNA.[50] As other thiobases, 6-TG absorbs within the UVA range, making 6-TG substituted-DNA susceptible to UVA damage and to Type I and Type II reactions (see Figure 1.7a). In Type I mechanisms, the excited sensitizer reacts with any substrate in the environment abstracting hydrogen and generating free radicals. These radicals would react with molecular oxygen, leading to ROS. Type II mechanisms in turn involve an energy transfer between the excited sensitizer in its triplet state (T_1) and environmental molecular oxygen ($^3O_2$), producing $^1O_2$. This oxygen form has a longer lifetime compared to other ROS and react with other biomolecules. Thus, both Type I and Type II reactions of 6-TG substituted-DNA can be considered a potential risk for the damage that can induce to biomolecules, such as proteins. Moreover, the oxidation of 6-TG itself leading to guanine-6-sulphinate (G^{SO2}) and guanine-6-sulphonate (G^{SO3}) can also involve DNA damage. These products have been found to inhibit replication and transcription of polymerases since they, for instance, significantly destabilizes double-stranded oligonucleotides, being these processes irreversible at high doses of 6-TG/UVA. Recent, combined experimental and computational studies based on density functional theory calculations, have located the intermediate products generated during the mechanism of $^1O_2$ production from 6-TG.[51] The potential energy profiles show that the mechanism leading to G^{SO2} occurs almost barrierless (see Scheme 1.3) since the optimized transition states are lower in energy than the reactants or at the same energy. Competing with this pathway, another mechanism was computed, which involves the recovering of the

natural base guanine G, however the energy barrier calculated for this mechanism, was found to be larger than the previous one, explaining that G is only obtained as a minor product. Further oxidation of G^{SO2} can also occur, leading to G^{SO3} due to the high oxidative power of $^1O_2$. Three different mechanism were reported for this latter oxidation processes although one of them seems to be preferred due to small energy barriers involved and the high stability of the final product placed ~90 kcal/mol below in energy than the reactants (see Scheme 1.3). This last mechanism is in concordance with the fast rate constant measured experimentally. The capability of 6-TG to induce Type I and Type II reactions upon light absorption, added to the possibility to generate harmful oxidized products, would explain the increase of skin sensitivity experienced by patients undergoing treatments with this substances. These photophysical/photochemical properties are in contrast with those observe for its canonical DNA nucleobase analogue, guanine.

Differences between 6-TG and G have been widely studied form an experimental point of view using ultrafast transient absorption techniques. Special attention has been paid to the triplet state rate formation and its lifetimes due to its importance in Type II reactions, as well as, the comparison of the lifetime decays to the GS of both systems, much slower in the thiosubstituted derivatives.

Steady state spectroscopy of 6TG shows that the lowest-energy absorption band has a maximum at ~340 nm, which has been connected with its second excited state.[52] Regarding emission spectra, no emission was detected within the sensitivity of the spectrometer.

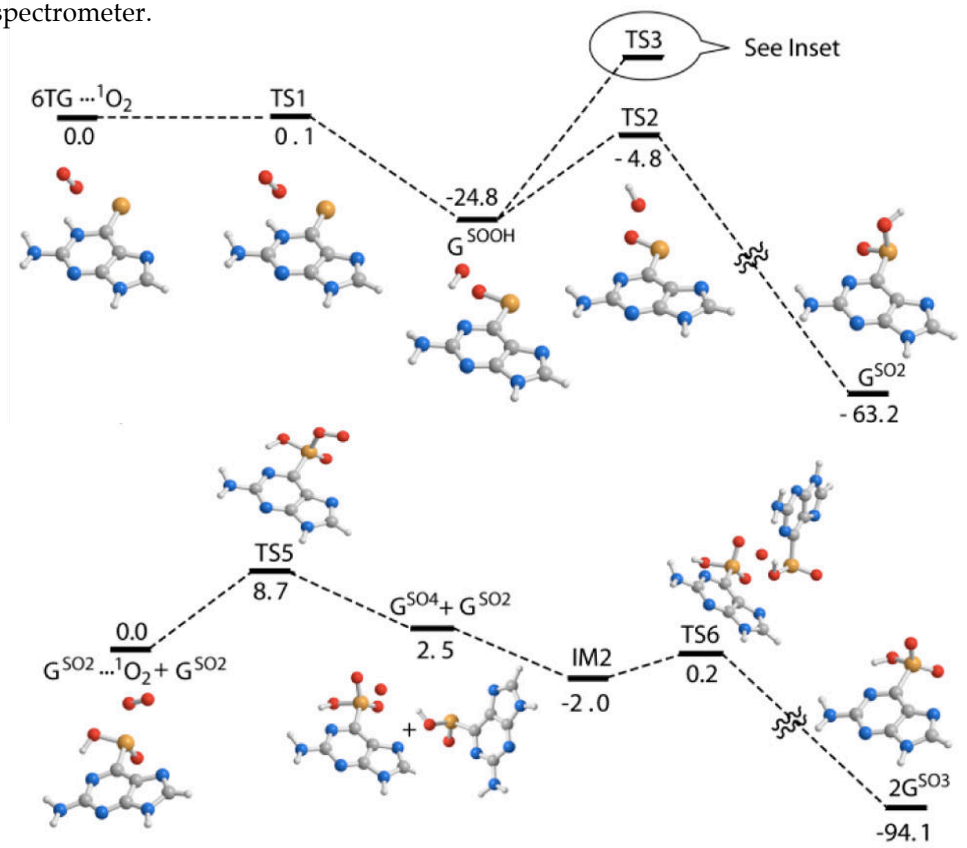

Scheme 1.3 Potential energy profiles leading to GSO2 (upper panel) and GSO3 (lower panel) products. Extracted from Ref [51].

Transient absorption spectra in aqueous buffer solution upon 340 nm excitation present two main bands: a negative band below 350 nm, which is assigned to ground state depopulation, and a positive band with a maximum in the 375-600 nm region (see Chapter 7). The globally fitted lifetimes are 0.31±0.05 ps and 80±15 ps in aqueous solution. The first lifetime is assigned to the ultrafast population of the triplet state, which decays back to the ground state 720±10 ns. A second, minor decay channel is also populated within 0.3 ps and it corresponds to IC from S_2 to the S_1 state. Via these mechanisms, experiments measure the repopulation of the ground state in tens of picoseconds.[52] These results involve differences with the photophysical properties of the canonical G bases, since they were governed by short time scales to reach the GS due to barrierless access to this funnels (recall Figure 1.2). The different topology of the PES along the deactivation global reaction coordinate is ultimately behind the very different photophysics of both systems.

The recovery of the GS population in the ps timescale points to an energetically unfavorable deactivation mechanism to the GS, which is consistent with the fact that the system remains in the excited state enough time to experience an intersystem crossing to the triplet manifold, leading to a high triplet quantum yield (0.8±0.2).[53] Efficient $^1O_2$ production (Φ_Δ=0.58±0.08)[53] joined to the rapidly deactivation founded for excited 6-TG in presence of oxygen molecules and light, suggest that 6TG is and effective photosensitizer.

4-Thiothymine

The sulfur substituted pyrimidine base, 4-thiothymine, (4-TT) has been demonstrated to be a very promising photochemotherapeutic drug due to its capacity to inhibit tumor growth. Other known photochemotherapies have been also found to present important drawback; for instance psolaren plus UVA radiation (PUVA) has been associated with an increased skin cancer risk, while photodynamic therapy, see Figure 1.7b is not completely selective and can be very painful. Recent studies have been focused on the use of alternative therapies, which involve lower radiation doses and improved selectivity.[54] 4-TT and irradiation with UVA have been combined to treat rat carcinoma finding quite interesting results.[54] During the rat treatment effective levels of 4-TT substituted-DNA where achieved in target cells, while incorporation into normal skin was found to be very low, suggesting that this treatment will selectively accumulate in tumor cell not affecting the normal ones. Furthermore, these studies attribute 4-TT a low mutagenicity. In fact, the activation of 4-TT with UVA does not lead to ROS production. At least within the detectable limits, activation of 4-TT DNA does not either produce single-strand breaking or guanine oxidation, in contrast to the 6-TG. In addition, a very important property of 4-TT is its extremely low toxicity also in absence of light, also at difference from 6-TG. All these properties suggest that 4-TT can be effective and safety used as photochemotherapeutic drug.[54]

Experimental have been also shed some light into the photophysics of 4-thiouracil **(**4-TU**)** and its methylated form, 4-thiothymine (4-TT).

For instance, the absorption and emission spectra of 4TU and its derivatives (1,3-

dimethyl-4-thiouracil (DMTU)) have been explained in terms of two different regions, related to the S_0->S_2 ($\pi\pi^*$) electronic transition and S_0->S_1 ($n\pi^*$) excitation. S_2-S_0 fluorescence signal (λ_{max}~420 nm) decays in a complex way and is characterized by the presence of three different emitting species with lifetimes of τ_1 = 4 ps, τ_2 = 60 ps and τ_3 = 590 ps.[55,56] The authors suggest that "this behavior of 4TU revealed by picosecond laser spectroscopy studies can be accounted for by assuming phototautomerism of this molecule in the S_2 excited state". Regarding the rate of triplet in the photophysics of these systems, both 4TU and DMTU were found to efficiently populate T_1 with a triplet quantum yields of 0.9±0.1 and 1±0.1, respectively.[57] These could a priori be in contrast with the low production of ROS founded by Karran et al. during their studies regarding 4-TT cytotoxicity.

The photophysics of other thiouracil derivative, **4TT** has been widely studied from the experimental point of view. While its absorption spectrum seems to be well characterized presenting a λ_{max} in the region 340-370 nm contradictory results were found for 4TT emission and excited state dynamics.[58-61] 4TT emission has been explained in terms of dual emission[60,61] consisting on fluorescence (maximum at ~400 nm) plus phosphorescence (maximum at ~540 nm) or as only phosphorescence with two bands at 494 and 521 nm.[59] Based on transient spectra (upon 263 nm excitation) Harada *et al.* conclude that the relaxation process is completed within the first 10 ps, being the time scale in which singlet-triplet ISC takes place for excited 4TT. These authors also observed a sub 10 ps relaxation pathway, which they ascribe to two possible mechanisms: vibrational cooling in the T_1 state or slow internal conversion from the S_2 to the S_1.[58] Parallel, femtosecond transient absorption spectra (after 340 excitation) performed by Reichardt *et al* registered two bands with negative amplitudes at short delay times (assigned to ground state depopulation and stimulated emission), plus a second one with small positive amplitude (ascribed to triplet state population). The stimulated emission signal decays with a lifetime of 0.24 ps, while the triplet T_1 band increases above 520 nm. A fraction (~15%) of this triplet state population decays back to the ground state with a lifetime of ~80 ps.[60,61] Triplet state reacts with molecular oxygen generating $^1O_2$, with a quantum yield for this production to 0.50±0.10.[59] These experimental results do not find any signal, which could be assigned to vibrational cooling on the triplet manifold and/or slow S_2->S_1 internal conversion. Then, despite both works are in qualitative agreement about the time scale and the very high quantum yield connected to ISC 1.0±0.1,[59] they however differ in the mechanism proposed the T_1 population.

Other thiosubstituted analogue of natural T, 2TT, shows similar photophysical characteristics with an intense absorption band centered at 300 nm, a low fluorescence quantum yield and phosphorescence observed in 2-methyltetrahydrofuran glassy matrix at 77 K.[62] Transients measured after 308 nm laser excitation for 2TT were fitted to a single lifetime of 2.7±0.5 μs. Since this transient was efficiently quenched by dissolved oxygen, it was assigned to the lowest triplet excited state of 2TT. The Φ_{ISC} values were determined to be 1.00±0.05, so 2TT could also in principle act as an effective photosensitizer. Interestingly, similar experiments performed on an aza derivative, ATT, showed a substantial high yield for $^1O_2$ formation, 0.69±0.02 in oxygen-saturated acetonitrile solution, being the highest value found for a DNA/RNA

base derivatives.[62]

The rationalization of these experimental findings with high level ab initio calculations and the comparison between the canonical and thioubstituted nucleobases is one of the main aims of this thesis, see Chapter 7. In particular, our aim is to model the absorption spectrum and the deactivation mechanism through the calculation of minimum energy paths, the location of singlet/singlet and singlet/triplet minimum energy crossing points for these thiobases. Furthermore, in order to compare with experimental lifetimes, also semiclassical dynamic simulations were also performed for these bases (see section X.4 in Chapter 4).

1.4 Singlet Molecular Oxygen and Endoperoxides

The use of thiobases as photosensitizers leading to Type II reactions is restricted to environments where ground state molecular oxygen is present. Due to this limiting factor, other precursors of $^1O_2$ have been explored to ensure the photosensitizing activity in the absence of molecular oxygen. In this sense, molecules bearing an O-O bridge have been considered as potential effective photosensitizers to be used in anaerobic environments. For instance, several experiments have proven that aromatic endoperoxides can cyclorevert and generate $^1O_2$ when irradiated with the correct wavelength. Moreover, these systems have a photochemical interest due to their dual photochemistry: two different products, O-O homolysis and cycloreevrsion, can be obtained depending on the excitation wavelength. The particular electronic configuration of $^1O_2$ and its reactivity confer this molecule a very rich chemistry, which can be detrimental, as is the case of photodegradation of polymers, but can also be beneficial.[63] Beyond its use in PDT as described above, the toxic effect of $^1O_2$ can be employed for controlling plant growing and pests. Furthermore, due to its high and specific reactivity, $^1O_2$ turns out to be a very important reagent in *organic synthesis and wastewater treatments*. Its capability to undergo Diels-Alder reaction or to oxidize phenols, sulphides and amines are examples of its multiples uses in the synthesis industry. The great versatility of singlet oxygen heads the interest of many works towards the study of systems which are able to deliver this reagent by Type II reactions and/or by intramolecular rearrangements.

In this respect, due to the capability of aromatic **endoperoxides** for generating $^1O_2$, the photophysics and photochemistry of these aromatic endoperoxides have been widely studied since the 70's by many groups reaching to contradictory conclusions. Kearns and Khan, using orbital correlation diagrams, assign a $\pi^*_{OO}\sigma^*_{OO}$ character to the first excited state (S_1) of oxygenated olefins.[64] These correlation diagrams for the model cyclopentadiene endoperoxide reveal a smooth correlation between $\pi^*_{OO}\sigma^*_{OO}$ states and diradical products and between $\pi^*_{OO}\sigma^*_{CO}$ excitations and cycloreversion products. They also predict that both cycloreversion (from $\pi^*_{OO}\sigma^*_{CO}$ transitions) and O-O homolysis (from $\pi^*_{OO}\sigma^*_{OO}$ states) are preceded by energetic barriers.[64]

During the 80's, experimental studies performed on anthracene endoperoxide, support the competition between O-O homolysis and cycloreversion reaction, and

conclude that the first process occurs from the S_1, $\pi^*_{OO}\sigma^*_{OO}$ state while $^1O_2$ production takes place from higher excited states (S_n n≥2). [65] However other experiments and calculations, the S_1 state is assigned to a $\pi^*_{OO}\pi^*_{CC}$ excitation and no $\pi^*_{OO}\sigma^*_{OO}$ state is found among the low-lying excited states of these endoperoxides.[66]

This controversy encouraged a recently revision of the photochemical behaviour of these systems from both a theoretical and experimental points of view.[67,68] The new computational results, based on reliable MS-CASPT2//CASSCF (multi-state second order perturbation theory on complete active space self-consistent-field wave functions) calculations, allow for a new assignment of the absorption spectrum of APO, which confirms that the S_1 state corresponds to a $\pi^*_{OO}\sigma^*_{OO}$ absorption, whereas high lying excited states present $\pi\pi^*$ character. The first excited state would be connected to O-O homolysis while $^1O_2$ production would take place from higher excited states.

This dual photochemistry (see Figure 1.8) has been as well investigates by means of femtosecond UV pump-supercontinuum probe experiments. These studies concluded that after 282 nm excitation, cycloreversion generates singlet oxygen and vibrationally excited anthracene (AC) in its singlet ground state with 25% quantum yield. Only 1-2 % of this AC is generated in its triplet excited state, while anything was found in its singlet excited state. The hot AC is formed within the first 3ps, while the subsequent cooling takes 18 ps more. Competing with AC production, O-O homolysis leads to biradicals, that evolve to electronically excited diepoxides (DE), which are the major products. DE are formed with a time constant of 1.5 ps followed by another constant of 21 ps corresponding to their vibrational cooling. In summary, although both processes (cycloreversion and O-O homolysis) seem to take place within the same timescale, experimental reveal that DE are the most favourable productsobtained from APO relaxation upon 282 nm excitation, while singlet oxygen is only formed as a minor product.

The different nature of the hydrocarbon moiety supporting the endoperoxide bridge has been found to strongly influence the FC absorption spectrum of the endoperoxide and, as a consequence, also its photochemistry. For instance the S_1 state for the smaller endoperoxide, cyclohexadieneendoperoxide (CHDEPO),[69] has been calculated to be of $\pi^*_{OO}\pi^*_{CC}$ nature, while the $\pi^*_{OO}\sigma^*_{OO}$ absorption was found to be S_3 excited state. It can, then, be concluded that while in APO O-O homolysis takes place from the S_1, in CHDEPO it would occur from the S_3. Consistently, $^1O_2$ production is expected from higher lying excited states in APO but from the S_1 in CHDEPO.

Despite these differences, these two endoperoxides also share some similarities, for instance, both present a four singlet plus four triplet state degeneracy point (4+4 CI) which allows the efficient deactivation of the excited endoperoxide to the ground state from excited $\pi^*_{OO}\sigma^*_{OO}$ states.[70,71]

Other of the main goals of this thesis is to investigate at molecular level the mechanism leading to $^1O_2$ both from an static and a dynamic perspective, see Chapter 5. For this, we will investigate the minimum energy deactivation pathways from the corresponding spectroscopic states and we will obtain (for the smaller endoperoxide) a time resolved picture of the latter that will also provide important information about timescales and yields of $^1O_2$ generation.

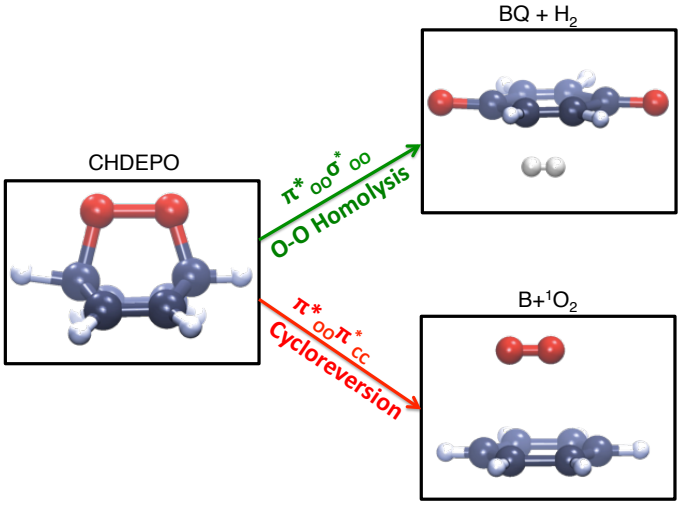

Figure 1.8. Dual photochemistry of a model endoperoxide Cyclohexadieneendoperoxide (CHDEPO). Excitation of $\pi^*_{OO}\sigma^*_{OO}$ states generates benzoquinone (BQ) and H_2 as products, whereas $\pi^*_{OO}\pi^*_{CC}$ excitations are connected with singlet oxygen generation.

Bibliography

(1) Climent, T.; González-Luque, R.; Merchán, M.; Serrano-Andrés, L. *Chem. Phys. Lett.* **2007**, *441*, 327.

(2) Serrano-Pérez, J. J.; González-Luque, R.; Merchán, M.; Serrano-Andrés, L. *J. Phys. Chem. Lett. B* **2007**, *111*, 11880.

(3) Serrano-Andrés, L.; Merchán, M.; Borin, A. C. *J. Am. Chem. Soc* **2008**, *130*, 2477.

(4) Serrano-Andrés, L.; Merchán, M.; Borin, A. C. *Chem. Eur. J.* **2006**, *12*, 6559.

(5) Serrano-Andrés, L.; Merchán, M.; Borin, A. C. *Proceedings of the National Academy of Sciences* **2006**, *103*, 8691.

(6) Merchán, M.; Serrano-Andrés, L.; Robb, M. A.; Blancafort, L. *J. Am. Chem. Soc.* **2005**, *127*, 1820.

(7) González-Luque, R.; Climent, T.; González-Ramírez, I.; Merchán, M.; Serrano-Andrés, L. *J. Chem. Theory Comput.* **2010**, *6*, 2103.

(8) Mai, S.; Marquetand, P.; Richter, M.; González-Vázquez, J.; González, L. *Chem. Phys. Chem.* **2013**, *14*, 2920.

(9) Middleton, C. T.; La Harpe, K. d.; Su, C.; Law, Y. K.; Crespo-Hernández, C. E.; Kohler, B. *Annu. Rev. Phys. Chem.* **2009**, *60*, 217.

(10) Barbatti, M.; Lischka, H. *J. Am. Chem. Soc.* **2008**, *130*, 6831.

(11) Canuel, C.; Mons, M.; Piuzzi, F.; Tardivel, B.; Dimicoli, I.; Elhanine, M. J. *J. Chem. Phys* **2005**, *122*, 074316.

(12) Ullrich, S.; Schultz, T.; Zgierski, M. Z.; Stolow, A. *J. Am. Chem. Soc.* **2004**, *126*, 2262.

(13) Bisgaard, C. Z.; Satzger, H.; Ullrich, S.; Stolow, A. *Chem. Phys. Chem.* **2004**, *10*, 101.

(14) Nikogosyan, D. N.; Letokhov, V. S. *Riv. Nuovo Cimento Soc. Ital. Fis* **1983**, *6*, 1.

(15) Bishop, S. M.; Malone, M.; Phillips, D.; Parker, A. W.; Symons, C. R. *J. Chem. Soc., Chem. Commun.* **1994**, 871.

(16) Karunakaran, V.; Kleinermanns, K.; Improta, R.; Kovalenko, S. A. *J. Am. Chem. Soc.* **2009**, *131*, 5839.

(17) Chen, H.; Li, S. *J. Chem. Phys* **2006**, *124*, 154315.

(18) Barbatti, M.; Szymczak, J. J.; Aquino, A. J. A.; Nachtigallová, D.; Lischka, H. *J. Chem. Phys* **2011**, *134*, 014304.

(19) Improta, R.; Barone, V. *Theor. Chem. Acc.* **2008**, *120*, 491.

(20) Asturiol, D.; Lasorne, B.; Robb, M. A.; Blancafort, L. *J. Phys. Chem. A* **2009**, *113*, 10211.

(21) Hare, P. M.; Crespo-Hernández, C. E.; Kohler, B. *Proceedings of the National Academy of Sciences* **2007**, *104*, 435.

(22) He, Y.; Wu, C.; Kong, W. *J. Phys. Chem. A* **2004**, *108*, 943.

(23) Busker, M.; Nispel, M.; Haber, T.; Kleinermanns, K.; Etinski, M.; Fleig, T. *Chem. Phys. Chem.* **2008**, *9*, 1570.

(24) Hare, P. M.; Middleton, C. T.; Mertel, K. I.; Herbert, J. M.; Kohler, B. *Chem. Phys.* **2008**, *347*, 383.

(25) Etinski, M.; Fleig, T.; Marian, C. M. *J. Phys. Chem. A* **2009**, 11809.

(26) Szymczak, J. J.; Barbatti, M.; Soo Hoo, J. T.; Adkins, J. A.; Windus, T. L.; Nachtigallová, D.; Lischka, H. *J. Phys. Chem. A* **2009**, *113*, 12686.

(27) Perun, S.; Sobolewski, A. L.; Domcke, W. *J. Phys. Chem. A* **2006**, *110*, 13238.

(28) Hudock, H. R.; Levine, B. G.; Thompson, A. L.; Satzger, H.; Townsd, D.; Gador, N.; Ullrich, S.; Stolow, A.; Martinez, T. J. *J. Phys. Chem. A* **2007**, *111*, 8500.
(29) Merchán, M.; González-Luque, R.; Climent, T.; Serrano-Andrés, L.; Rodriguez, E.; Reguero, M.; Pelaez, D. *J. phys. Chem. B* **2006**, *110*, 26471.
(30) Ullrich, S.; Schultz, T.; Zgierski, M. Z.; Stolow, A. *Phys. Chem. Chem. Phys.* **2004**, *6*, 2796.
(31) Barbatti, M.; Aquino, A. J. A.; Szymczak, J. J.; Nachtigallová, D.; Lischka, H. *Phys. Chem. Chem. Phys.* **2011**, *13*, 6145.
(32) Merchán, M.; Serrano-Andrés, L. *J. Am. Chem. Soc.* **2003**, *125*, 8108.
(33) Hudock, H. R.; Martinez, T. J. *Chem. Phys. Chem.* **2008**, *9*, 2486.
(34) Alexandrova, A. N.; Tully, J. C.; Granucci, G. *J. Phys. Chem. B* **2010**, *114*, 12116.
(35) Kobayashi, T.; Harada, Y.; Suzuki, T.; Ichimura, T. *J. Phys. Chem. A* **2008**, *112*, 13308.
(36) Kobayashi, T.; Kuramochi, H.; Harada, Y.; Suzuki, T.; Ichimura, T. *J. Phys. Chem. A* **2009**, *113*, 12088.
(37) Gobbo, J. P.; Borin, A. C. *J. Phys. Chem. B* **2012**, *116*, 14000.
(38) Gobbo, J. P.; Borin, A. C.; Serrano-Andrés, L. *J. Phys. Chem. B* **2011**, *115*, 6243.
(39) Gustavsson, T.; Improta, R.; Banyasz, A.; Vaya, I.; Markovitsi, D. *J. Photochem. Photobiol. A: Chem* **2012**, *234*, 37.
(40) Banyasz, A.; Mercier, S. K.; Reguero, M.; Gustavsson, T.; Markovitsi, D.; Improta, R. *J. Phys. Chem. B* **2010**, *114*, 12708.
(41) Gengeliczki, Z.; Callahan, M. P.; Svadlenak, N.; Pongor, I.; Sztáray, B.; Meerts, L.; Nachtigallová, D.; Hobza, P.; Barbatti, M.; Lischka, H.; S. de Vries, M. *Phys. Chem. Chem. Phys.* **2010**, *12*, 5375.
(42) Larsen, O. F. A.; van Stokkum, I. H. M.; -L., G. M.; Kennis, J. T. M.; van Grondelle, R.; van Amerongen, H. *Chem. Phys. Lett.* **2003**, *371*, 157.
(43) Mburu, E.; Matsika, S. *J. Phys. Chem. A* **2008**, *112*, 12485.
(44) Reichardt, C.; Wen, C.; Vogt, R.; Crespo-Hernández, C. E. *Photochem. Photobiol. Sci* **2013**, *12*, 1341.
(45) Gustavsson, T.; Banyasz, A.; Lazzarotto, E.; Markovitsi, D.; Scalmani, G.; Frisch, M. J.; Barone, V.; Improta, R. *J. Am. Chem. Soc.* **2006**, *128*, 607.
(46) Parusel, A. B. J.; Rettig, W.; Rotkiewicz, K. *J. Phys. Chem. A* **2002**, *106*, 2293.
(47) Schwalb, N. K.; Temps, F. *Phys. Chem. Chem. Phys.* **2006**, *128*, 607.
(48) O'Donovan, P.; Perrett, C. M.; Zhang, X.; Montaner, B.; Xu, Y.-Z.; Harwood, C. A.; McGregor, J. M.; Walker, S. L.; Hanaoka, F.; Karran, P. *Science* **2005**, *309*, 1871.
(49) Brem, R.; Li, F.; Karran, P. *Nucl. Acids Res.* **2009**, *37*, 1951.
(50) Brem, R.; Karran, P. *Photochem. and Photobiol.* **2012**, *88*, 5.
(51) Zou, X.; Zhao, H.; Yu, Y.; Su, H. *J. Am. Chem. Soc.* **2013**, *135*, 4509.
(52) Reichardt, C.; Guo, C.; Crespo-Hernández, C. E. *J. Phys. Chem. B* **2011**, *2011*.
(53) Zhang, Y.; Zhu, X.; Smith, J.; Haygood, M. T.; Gao, R. *J. Phys. Chem. B* **2011**, *115*, 1889.
(54) Reelfs, O.; Macpherson, P.; Ren, X.; Xu, Y.-Z.; Karran, P.; Young, A. R. *Nucleic Acids Research* **2011**, *39*, 9620.
(55) Wenska, G.; Taras-Goslinska, K.; Skalski, B.; Maciejewski, A.; Burszinski, G.; Karolczak, J. *J. Photochem. and Photobiol. A: Chemistry* **2006**, *181*, 12.
(56) Wenska, G.; Taras-Goslinska, K.; Łukaszewicz, A.; Burdziński, G.; Koput, J.; Maciejewski, A. *Photochem. and Photobiol. Sci.* **2011**, *10*, 1294.
(57) Taras-Goślińska, K.; Wenska, G.; Skalski, B.; Maciejewski, A.; Burdziński, G.; Karolczak, J. *Photochem. and Photobiol.* **2002**, *75*, 448.
(58) Harada, Y.; Okabe, C.; Kobayashi, T.; Suzuki, T.; Ichimura, T.; Nishi, N.; Xu, Y.-Z. *J. Phys. Chem. Lett.* **2010**

, *1*, 480.
(59) Harada, Y.; Suzuki, T.; Ichimura, T.; Xu, Y.-Z. *J. Phys. Chem. B* **2007**, *111*, 5518.
(60) Reichardt, C.; Crespo-Hernández, C. E. *J. Phys. Chem. Lett.* **2010**, *1*, 2239.
(61) Reichardt, C.; Crespo-Hernández, C. E. *Chem. Commun.* **2010**, *46*, 5963.
(62) Kuramochi, H.; Kobayashi, T.; Suzuki, T.; Ichimura, T. *J. Phys. Chem. B* **2010**, *114*, 8782.
(63) DeRosa, M. C.; Crutchley, R. J. *Coord. Chem. Rev.* **2002**, *233/234*, 351.
(64) Kearns, D. R. *J. Am. Chem. Soc.* **1969**, *19*, 6554.
(65) Schmidt, R.; Schaffner, K.; Trost, W.; Brauer, H.-D. *J. Phys. Chem* **1984**, *88*, 956.
(66) Klein, A.; Kalb, M.; Gudipati, M. S. *J. Phys. Chem. A* **1999**, *103*, 3843.
(67) Corral, I.; González, L. *J. Comput. Chem.* **2008**, *29*, 1982.
(68) Corral, I.; González, L.; Lauer, A.; Freyer, W.; Fidder, H.; Heyne, K. *Chem. Phys. Lett.* **2008**, *452*, 67.
(69) Corral, I.; González, L. *Chem. Phys. Lett.* **2007**, *446*, 262.
(70) Corral, I.; González, L. *Chem. Phys. Lett.* **2010**, *499*, 21.
(71) Mollenhauer, D.; Corral, I.; González, L. *J. Phys. Chem. Lett.* **2010**, *1*, 1036.

Chapter 2

Introducing Photochemistry

Photochemical processes occur from the electronically excited molecules upon the absorption of suitable radiation. This branch of chemistry has gained relevance through the ages since many biological processes and technological advances rely on their applications. The aim of this chapter it to summarize the fundamental steps involved in photochemical reactions, including the excitation and deactivation of molecules.

The absorption of a photon having energy equal to the energy difference between two electronic states causes the promotion of an electron from a lower energy occupied orbital to a higher unoccupied one, Figure 2.1.

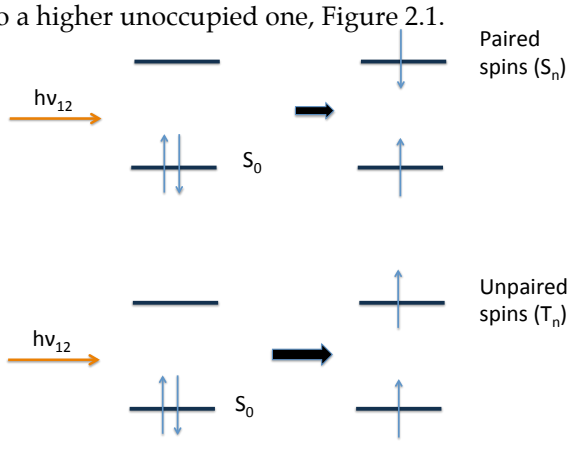

Figure 2.1. Representation of electrons (arrows) distribution within the energy levels before and after light absorption.

When electron excitation takes place from a singlet ground state, S_0, of a molecule, the most probable event is that the process occurs maintaining the spin multiplicity of the system, that is, that the system reaches another singlet state, S_n (upper panel of Figure 2.1). Thus, transitions from the ground state to a triplet excited state, T_n, are spin forbidden (lower panel of Figure 2.1). After light absorption, the final exited states present an excess of energy, which can be released through different processes. When the molecule relaxes to the starting ground state this can be understood as a photophysical process, alternatively it can also undergo photochemical reactions as quenching and electron energy transfer. The photophysical processes can be classified as radiative or radiationless depending on whether they involve the emission of a photon as the molecule relax to the ground state or not. The most important of those relaxation processes can be summarized through the Jablonski diagram (Figure 2.2) and are described in more detail in the following.

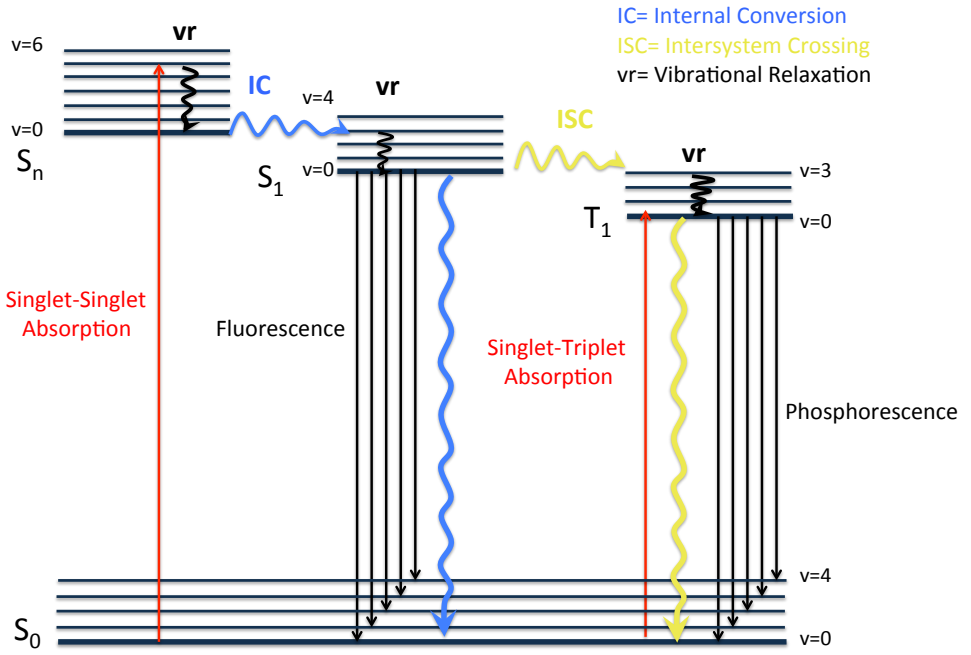

Figure 2.2. Jablonski diagram containing the main excited state radiative (straight arrows) and radiationless (wavy arrows) photophysical processes. S_1, S_2, … S_n and T_1, T_2,…T_n denote singlet and triplet excited states, respectively. Vibrational energies are represented by v=0,...,6.

Vibrational Relaxation

Light absorption generally leads to vibrationally excited electronic excited states, unless when 0-0 absorption takes place and the population reaches the lowest vibrational level of the excited state. This excess of energy can be

dissipated via vibrational relaxation (VR), which involves transitions between different vibrational states within the same electronic state. Vibrational relaxation in vacuum is very slow, since the excess of energy cannot be dissipated by collision with other molecules. However, in solution VR can take place within the picosecond timescale since the excess of energy can be transfer to other molecules of the environment. These molecules can be other solute molecules and then intramolecular vibrational relaxation takes place (0.1-10 ps) or solvent molecules leading to intermolecular vibrational relaxation process (10-100 ps). Time resolved spectroscopy allows the study of vibrational relaxation process being able to measure decay constants for this events.

Radiationless processes

- **Internal Conversion** occur when the system relaxes radiationless from an upper excited state relax to a lower excited state of the same multiplicity (singlet-singlet or triplet-triplet). Even, if the excitation energy is enough to excite higher excited states, S_n, molecules quickly deactivate to the lowest state S_1. Internal conversion takes place between isoenergetic vibronic, for instance in Figure 2.1 from S_n (v=0) to S_1 (v=3). Due to this small energy difference, the S_n-> S_1 transition takes places within the first 10^{-14}-10^{-11} s, whereas due to usually large energy gaps between the S_1 and S_0, IC is not always possible between these two states. In these cases, excited molecules trapped on the S_1 have two alternatives, (1) either a radiatively decay to the ground state by fluorescence (see radiative processes) or (2) experience a non-radiative transition to a triplet excited state by intersystem crossing (see below). Because of the rapid IC between high lying excited state, usually other radiative and radiationless process do not take place from them, but from the S_1.

- **Intersystem Crossing** involves the radiationless transition between isoenergetic vibrational states belonging to electronic states of different spin manifold, for instance S_1 (v=0) -> T_1 (v=3). Most relevant intersystem crossing transitions in photochemistry take place between S_1->T_1 and T_1->S_0 electronic states. Since direct population of the triplets is forbidden, the S_1->T_1 transition is the most probable way to populate T_1. As for IC, the energy difference between S_1 and T_1 is normally much smaller than the T_1->S_0 gap, what leads to a great difference, up to 10^9 factor, between the rate constants of both processes, κ_{ISC} (S_1->T_1) and κ_{ISC}^{T} (T_1->S_0). In some molecules other higher triplets, T_n, can as well participate in the deactivation mechanism. These states after being accessed from the singlet would undergo internal conversion to T_1. In those cases, the energy difference between S_1 and T_n the controlling step. Intersystem crossing (S_1->T_1) can take place within the range 10^{-11}-10^{-6}s, and the radiationless decay to the ground state from the triplet manifold will compete with phosphorescence (see below).

Radiative processes

- **Fluorescence** involves photon emission between states of same multiplicity. Accordingly to Kasha's rule this process generally takes place from the lowest vibrational level of the lowest excited singlet state, S_1, to the singlet ground state S_0. In the presence of other competitive process, with rate constants κ_i, the fluorescence lifetime is: $\tau_f = 1/(\kappa_f + \sum \kappa_i)$, where the rate constant of fluorescence κ_f is defined as a function of the natural radiative lifetime τ_N, $\kappa_f = 1/\tau_N$. Typical values for fluorescence lifetimes are in the range of picoseconds to microseconds.
  Fluorescence is not an efficient process for a large number of compounds, being generally observed in organic molecules with rigid framework and/or bearing particular substituents. For instance, electron-donating groups (as –OH and $–NH_2$) and conjugated systems with double bonds enhance fluorescence yields, while electron-withdrawing groups can even completely inhibit it. Fluorescence quantum yield, ϕ_f, can be defined as the ratio between emission and absorption rate: $\phi_f = \kappa_f[S_1]/I_a$, with $[S_1]$ being the concentration of the lowest singlet excited state and I_a the absorption intensity.

- **Phosphorescence** is the spin forbidden emission between states of different multiplicity. It usually takes place from the lowest triplet excited state, T_1, to the singlet ground state, S_0. Since this triplet state always lies below in energy than S_1, phosphorescence takes places at longer wavelengths than fluorescence. Due to the spin forbidden character of the transition, phosphorescence is less intense and less fast than fluorescence. Phosphorescence lifetime can be expressed as $\tau_p = 1/(\kappa_p + \kappa_{ISC}^T)$, where κ_{ISC}^T is the rate constant for intersystem crossing from the triplet to the ground state, being usually in the range τ_f, 10^{-3}-10^2 s. Phosphorescence quantum yield can also be written as a function of the triplet concentration and the absorption intensity: $\phi_p = \kappa_p[T_1]/I_a$. The forbidden nature of the T_1->S_0 transition leads to long lived T_1 and low quantum yields for phosphorescence emission being not observed under ordinary conditions, except for a few cases. However, the transition probability can be enforced by spin-orbit coupling interactions, in the presence of paramagnetic molecules (O_2) or in solvents carrying heavy atoms.

2.1 Light Absorption

Photochemical reactions start with the absorption of a photon, which results in molecule excitation from its ground state. The fundamental requirements for this transition to take place are: (i) the energy of the absorbed photon (hν) must be resonant to the energy difference between the ground and the excited state (ΔE) and

that (ii) the transition dipole moment (TDM) created by the interaction of the electron with the electromagnetic field must be finite.

$$\mathrm{TDM}_{m\to n} = \sum_{\alpha=x,y,z} \langle \psi_m | \hat{\mu}_\alpha | \psi_n \rangle$$

where $\hat{\mu}$ is the dipole moment operator for the α component. The transition probability for the m-> n transition is determined by the square of the module of the TDM. Then, the excited state at which the population arrives, S_n, is selected by the available energy and the value of TDM. This quantum mechanical magnitude can be related with the classical concept of the oscillator strength (f) by the formula:

$$f = \frac{2}{3}\Delta E \ |TDM|^2$$

Regarding vibrational transitions, the relative population of vibrational states within the excited electronic states is defined by the Franck-Condon principle. This principle is relies in the BO approximation, which state that since the nuclei are more massive than electrons when an electronic transition takes place from an orbital to another the nuclei remain stationary. In other words, when the transition takes place between ψ_m and ψ_n the nuclear geometry of the massive nuclei remains momentarily fixed while the new electron configuration readjusted from that of ψ_m to that of ψ_n. Then, the nuclei experienced the new electronic negative force field of ψ_n and start to move from the ψ_m geometry until they adjust their geometry to that of ψ_n. For transition between states of the same multiplicity but with different nuclear geometries, this later step would be the rate-determining step.

Expressed in quantum mechanical terms, the FC principle states that 'the most probable transitions between electronic states occur when the wave function of the initial vibrational state χ_m most resembles the wave function of the final vibrational state χ_n'. Analogue to the integral defining the overlap between two given electronic wave functions $\langle \psi_m | \psi_n \rangle$, an overlap integral between a pair of vibrational wave functions can be defined:

$$\langle \chi_m | \chi_n \rangle$$

These integrals are the so-called FC integrals and can be used to estimate the probability of a given vibronic transition: the more the two vibrational wave functions resemble, that is these integrals given values close to 1, the more probable the transition is. The rate constant for a given transition is proportional to the so-called FC factors $\langle \chi_m | \chi_n \rangle^2$.

Then, within the BO framework, the transition probability for a global transition can be written as:

$$P \approx \mathrm{TDM}_{m\to n} \langle \chi_m | \chi_n \rangle$$

Figure 2.3 represents the most probable vibrational transition in two different situations, (a) for both electronic states sharing similar nuclear geometries and (b) for the opposite case.

The FC principle described above for absorption (radiative transitions) can also be applied to radiationless processes. The basis ideas are (1) transitions are favoured if they imply small changes between the initial and final nuclear structure and momentum and (2) energy must be considered during the transition. For radiative transition these conditions are ensured by the absorption or emission of a photon, which has the same energy than thee energy difference between the initial and final states. In case of radiationless transitions, the initial and final states must present similar energies and nuclear geometry, that is, they must resemble both in energy and structure. Then, in contrast to radiative transitions, vertical jumps between states separated by large energy difference are improbable because of the need to conserve the energy during these radiationless processes.

2.2 Photochemical Reaction Pathways

Once the molecule has reached an excited state, it can undergo many photophysical or photochemical processes (fluorescence, phosphorescence, internal conversion, intersystem crossings…) both of which can involve starting structural changes. Considering a fixed nuclear geometry, the pathway along a particular reaction coordinate, for both the ground and the excited state, can be schematized using a 2D potential energy curves (PEC) (Figure 2.4). However, as detailed along the next section PE surfaces (PES) are extremely complicated objects usually difficult to visualize.

PEC represent the possible ways to go from the reactants (R) to the products (P) exploring both the ground and excited state surfaces (Figure 2.4). After excitation (1), R* molecules can decay back to the ground state (2) or the can evolve on the excited state surface to a funnel region (3). On this region of the PES, the ground and excited electronic states (R and R*) are close in energy existing a non-negligible probability of exchanging population between these two electronic states (4). Therefore, some molecules will be able to remain in the excited state and overcome the energy barrier to reach an excited state product P* (6). The rest of the population will decay back to the ground state and the population will be divided between R and P regions (5).

Some general conclusions for the photochemical behavior of a molecule can be extracted from the above picture:

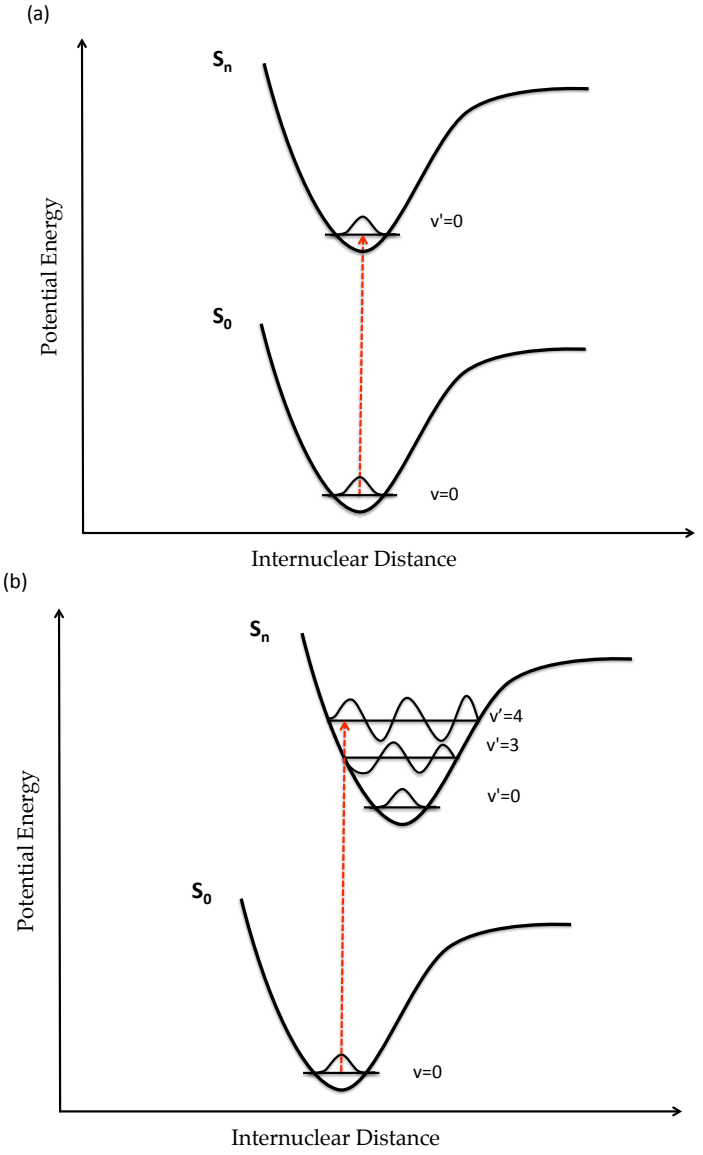

Figure 2.3. Most Probable vibronic transition from S_0 (v=0) (a) when both electronic states present similar geometries S_n (v=0) and (b) when both states present very different equilibrium internuclear distances S_n (v=4).

- Absorption and emission of light are preferred to occur from geometries corresponding to a minimum either in the ground or in the excited state. In general, when emission from an excited state minimum takes place, energy barriers separate this minimum from other point of the PES. Those barriers allow the molecule to remain traped in the region of the minimum for enough time to return to the ground state by fluorescence or internal conversion.

- At those geometries where the two PECs are close in energy, radiationless jumps between them are most likely to happen. Those funnels connecting both PES can be classified as true o avoided crossings. Crossings will be described in more detail in the following.
- The most probable mechanism can be predicted in view of the presence of energy barriers in a given PES and their magnitude. Barrierless mechanisms tend to be preferred in contrast to those presenting high energy barriers.
- Photochemical reactions must be understood as complicated mechanisms where photophysical and photochemical processes compete.

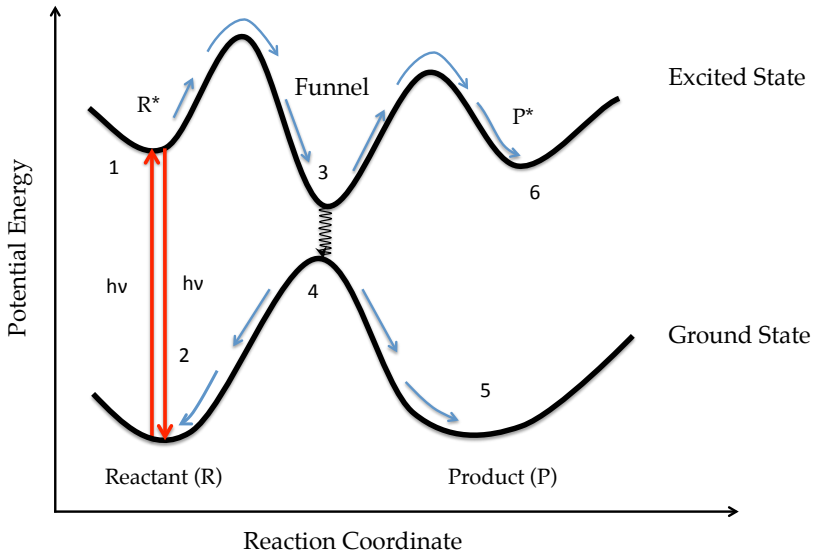

Figure 2.4. Potential energy curves, as a function of the reaction coordinate, for the ground and the excited state. Arrows show the possible pathways the molecule can follow along this coordinate. Adapted from Turro. [1]

2.3 Reaction Pathways Modelling

2.3.1 Conical Intersections

Excited state PESs can be defined as a sequence of several minima, transition states and surface crossings. Their connection through reaction path calculations can elucidate the photochemical reactivity from the excited state. Surface crossings play an important role in the deactivation mechanism from excited to the ground state.

Although the mathematic description of surface crossing as conical intersection will be given in Chapter 3, a qualitative brief description will be given in the following. *Adiabatic potential energy surfaces* are constructed under the adiabatic (or Born-

Oppenheimer, Chapter 3, allowing the separation of nuclei and electron movements) approximation: the nuclear motion is treated classically and, then, the electronic potential energy is evaluated for every nuclear configuration. If one of these nuclear configurations involves exploring a region where two states are mixed, the nuclear motion is not well described by a single surface anymore. Within the adiabatic approximation, the crossing of two surfaces is strictly forbidden, so the crossings are weakly or strongly avoided (see Figure 2.5).

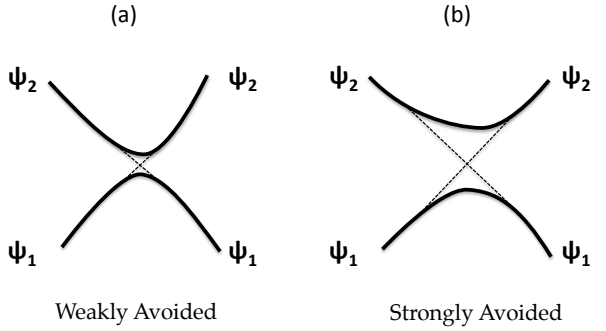

Figure 2.5. (a) Perfect crossing forbidden within the adiabatic approximation, (b) weakly avoided crossing and (c) strongly avoided crossing. Adapted from Turro. [1]

When the nuclear motion is so fast that the electrons cannot be treated using the adiabatic approach, the potential energy surface may be described within the *diabatic or nonadiabatic* frame. In this representation, the surface's nature does not dramatically change along or through the crossing region. Then, whereas in the adiabatic representation at both sides of the crossing the two surfaces (upper and lower ones) will be described by very similar wave functions (each surface is represented by the same wave function before and after the crossing, see Figure 2.6a), in the diabatic representation these wave functions will significantly change for both surfaces (different colors before and after the crossing, see Figure 2.6b). If nuclear motion is so fast that the electrons cannot instantaneously adapt to the new configuration of the nuclei the molecule will follow the diabatic PES, which is equivalent to undergo a jump in the adiabatic representation. In this regions the non-adiabatic coupling effects need to be taken into account for a correct description of the molecular motion of the system (see section 3.10).

A lot of computational effort has been done to develop algorithms for the location of conical intersection in polyatomic molecules (more than two degrees of freedom). Although in some previous figures (Figure 2.4 and 2.5) the PEC have been used to describe photochemical reactions, two coordinates are at least needed to define a 2-states degeneracy point or conical intersection (Figure 2.6 and 2.7). These two directions (x_1 and x_2) define the so-called "branching space" and it can be demonstrated that they are given by the gradient difference vector:

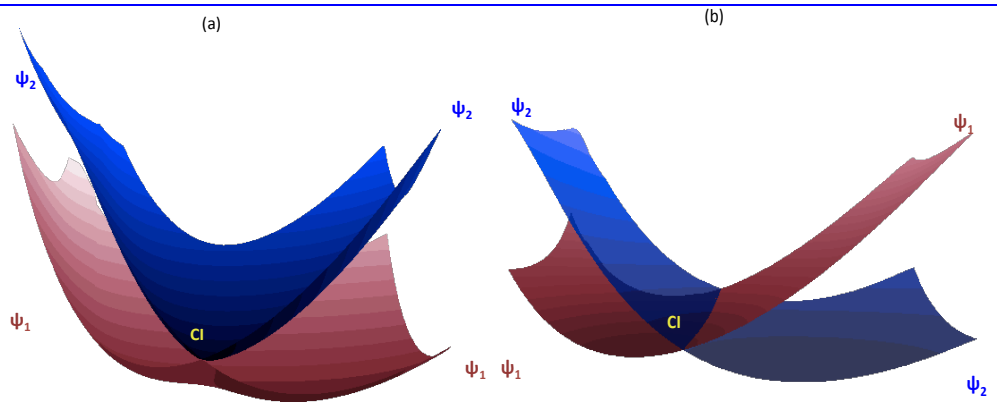

Figure 2.6. (a) Adiabatic and (b) Diabatic Potential energy surfaces

$$Gradient\ Difference\quad x_1 = \frac{\delta(E_1 - E_2)}{\delta q}$$

and the gradient of the interstate coupling vector,

$$Interstate\ Coupling\ x_2 = \left\langle \psi_1 \middle| \frac{\delta H}{\delta q} \middle| \psi_2 \right\rangle$$

The first coordinate defines the largest difference between the slopes of the upper and lower surfaces, while the second coordinate indicated the direction along which nuclear motion mixes the two electronic states, ψ_1 and ψ_2.

Different algorithms have been developed with the purpose of locating a conical intersection optimization or the lowest point of a degeneracy region, in other words, the lowest energy point of the funnel. A conical intersection optimization can be understood as a constrained optimization in the space orthogonal to the two coordinates, x_1 and x_2. The optimization of the lowest point of the degeneracy seem (the conical intersection) can be located by requiring the energy difference $E_1 - E_2$ between the states of interest to be zero in this orthogonal space. The procedure implemented by Robb et al.[2] in Gaussian use for the minimization of $E_1 - E_2$ the following condition:

$$\frac{\delta}{\delta q}\,(E_1 - E_2\,)^2 = 2(E_2 - E_1)\,x_1 = 0$$

where x_1 is the gradient difference vector. These authors use $(E_1 - E_2\,)^2$due to its smoother variation in regions close to the conical intersection. Using this procedure the conical optimization takes places by minimizing the energy difference between the states within the first steps, while the energy of the states is raised. Then, when this difference is small, the optimization minimizes the energy of the crossing in the intersection space.

Conical Intersection Structure

The relative orientation of the two potential curves in the vicinity of their crossing region has been used to characterized the topology of the conical intersections in peaked or sloped, see Figure 2.7. This classification was first considered by Atchity et al.[3] taking into account the relative gradient directions at the crossing and minima of the involved states. The so-called peaked crossings (Figure 2.7a) present orthogonal gradients and the crossing point is the lowest energy point in the excited state surface. In fact, the corresponding minimum of the two states (min_1 and min_2) are placed both on the same surface (S_0).[4,5] Some peaked intersections also show an intermediate minimum followed by a transition state in the excited state surface before reaching the conical intersection, but still the former is the lowest point in energy of the excited state surface. Sloped funnels (Figure 2.7b) present almost parallel gradients and there is a minimum on the excited state surface, which is lower in energy than the crossing point. Therefore, for both states the minima are located before reaching the crossing, in other words, one minimum in each surface (min_1 at S_0 potential and min_2 at S_1).

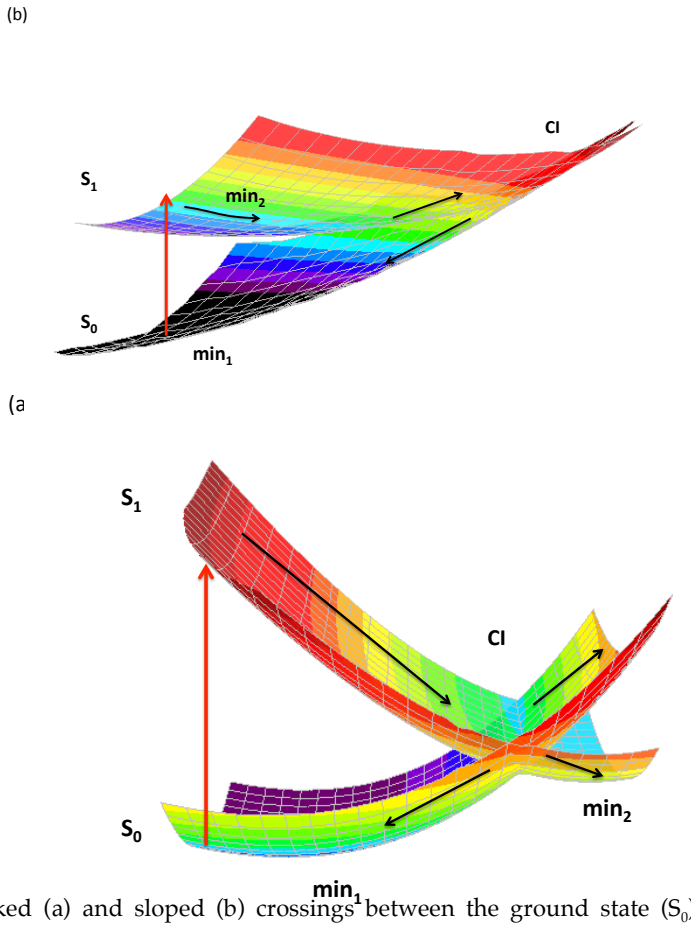

Figure 2.7. Peaked (a) and sloped (b) crossings between the ground state (S_0) and the first singlet excited state (S_1).

A very simple analysis of photochemical reactions can be done distinguishing between sloped and peaked crossings. As a general rule, peaked crossings are the most efficient funnels followed by the excited molecule to deactivate to the ground state. In this kind of crossings once in the S_0 potential the molecule can follow different channels, that it is, it can either populate the min_1 (reactants) or the min_2 (products) (see Figure 2.4 and 2.7) and its ratio could be estimated by performing molecular dynamic simulations. On the other hand, if a sloped intersection is reach, most of the population will be in min_1 (reactants) (specially if the crossing geometry is not far from the reactants). However, in this type of funnels, energy barriers can trap the molecule at the min_2 preventing the decay to the lower state. Unfortunately, predicting the outcome of a photophysical or photochemical reactions is usually not as easy as applying these reasoning since other variables such as the crossing's energy or the connection of these crossings with the FC needs also to be considered.

Conical Intersection Location

Regarding practical issues, the location of conical intersection can be one of the hardest tasks in the study of a photochemical problem, depending on its topology. Peaked conical intersections (see Figure 2.7a) are normally found during minima optimization or reaction path (next section 2.4) calculations, which fail due to degeneracy problems. These geometries can be a good starting point for the conical intersection optimization. Although this procedure does not guarantee the success of the optimization, they are usually promising starting points since the energy difference between the two involved states is almost minimized. In contrast, sloped conical intersections (see Figure 2.7b) are more difficult to localize, and several problems can arise during their optimization. First, this kind of critical points are not easily found along other calculations, especially if they are located high in energy and/or far from the reaction paths. Then, the best starting point can sometimes be the optimized excited state minima (min_2 in Figure 2.7b. As it can be seen from Figure 2.7b, these conical intersections are characterized by parallel gradient vectors that can lead to convergence problems during their optimization. In these cases, x_1 becomes very small and can cause inaccuracies during its projection. In order overcome these problems, it is possible to minimize the stepsize of the optimization and if the former does not work, the convergence thresholds could be reduced until safe values. Especially in these later cases, where conical intersection are hard to be optimized and lay far from the reaction paths, but in general for all the cases, it is important to connect them with the corresponding minima at each side of the crossing. This step is essential to ensure that the particular CI are or not accessible from any minima and that the minima correspond to the minima of interest.

Although some of the located conical intersections may not be involved in a photochemical reaction, some of them play a very important role as effective photophysical funnels. Especially attention has been paid to conical intersections that connect the excited state and ground state surfaces, since, for instance, have been used to rationalize the photostability of canonical DNA bases (see Chapter 1).

2.3.1 Minimum Energy Paths

The most common strategy used in computational photochemistry to map the photochemical reaction path consists on computing the Minimum Energy Paths (MEPs). These MEPs are used for connecting the initial populated excited state at the Franck-Condon structure to the final products passing through, for instance, minima or conical intersections.

Since MEPs focused on the minimum energy pathways they also locate intermediates, transition states and conical intersections that are directly accessible by the system. Other stationary points that can be optimized may be placed far from the followed reaction channels by the MEP. Although this can be seen as an advantage to limit the part of the PES that must be explored (the one revealed by MEP calculations), caution must be exerted since regions far from the PES can also become important for the deactivation mechanisms of some systems.

The computing of MEPs is widely used since it can be connected to methods that use wave packet or semi-classical trajectories on potential energy surfaces to describe photochemical processes. However, since during dynamic studies the molecule also has some kinetic energy available, a trajectory can also explore regions of the PES far from the MEP. If those regions become important the local static analysis of the PES based on MEPs must be completed with dynamic simulations, which will provide a more global and complete analysis of the photochemical reaction.

MEP algorithm

The algorithm used by MOLCAS, which (if not otherwise specified) has been the one used for MEPs calculations in this thesis, minimizes the energy within an hypersphere with a fixed radius, where the center of the sphere is the geometry of the structure optimized in the previous step (see Figure 2.8). The calculation ends when the energy found in a later step is higher than the previous one, and then an energy minimum is found on this PES.

The hypersphere is optimized using mass weighted Cartesian coordinates:

$$\boldsymbol{R}(q) = \left(\sqrt{m_1}\boldsymbol{r}_1(\boldsymbol{q}), \sqrt{m_2}\boldsymbol{r}_2(\boldsymbol{q}), \dots, \sqrt{m_n}\boldsymbol{r}_n(\boldsymbol{q})\right)$$

where the constrain is:

$$r_1 = \frac{\sqrt{(\boldsymbol{R}(\boldsymbol{q}) - \boldsymbol{R}(\boldsymbol{q}_{ref}))^2} - R}{\sqrt{M_{tot}}}$$

being R the radius of the hypersphere, M_{tot} the total mass of the system, $R(q_{ref})$ the origin of the hypersphere and $R(q)$ the coordinates of the current structure.

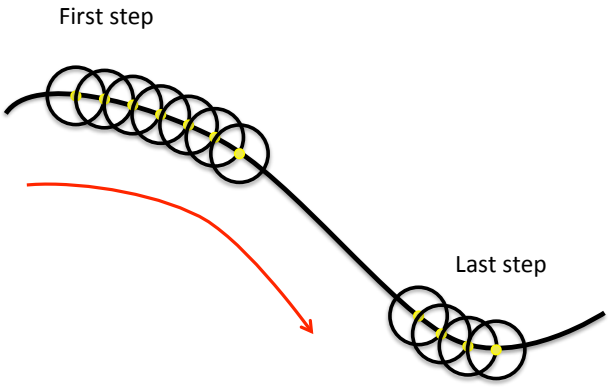

Figure 2.8. Minimum Energy Path Algorithm used by Molcas. Adapted from Molcas documentation at http://www.molcas.org

Practical issues: MEPs from FC and for the Locating Decay Paths from a Conical Intersection.

The most common procedure to obtain a qualitative idea of the most probable deactivation pathways of a particular system consists on the following steps.

The first step (1), is to perform MEP calculation from the FC structure along the gradient of the spectroscopic state (see light absorption section 2.1). This MEP usually ends up in a minimum on this potential (Figure 2.9a and b) or alternatively reaches barrierless a CI with the lower state (Figure 2.9c).

-When the MEP starting from FC reaches a minimum the location of a CI with the lower state can be started from it (recall previous section). Once the minimum (1 in Figure 2.9 a and b) and the CI are optimized, the next step is to connect them. Two possible scenarios can be possible, the CI is higher in energy respect to min_1 (Figure 2.9 a) or the CI and min_1 present similar energies and they are separated by a TS (Figure 2.9 b). In the first case new MEPs need to be performed started from the degeneracy point structure in order to connect the CI with the min_1 and min_2 (2 and 3 in Figure 2.9 a). However, in the second case, although the MEP from the CI towards min_2 can still be performed, the MEP connecting to min_1 will not work due to the an energy increase (2 and 3 in Figure 2.9 b). Therefore, the TS must be, optimized and then from it min_1 and the CI can then be connected.

-The MEP from the FC region in the other studied case leads directly to a CI with the lower state (1 in Figure 2.9 c). From this CI, the same MEP connecting it with the min_2 (3 in Figure 2.9 b) following the lower path can be performed. However, the other

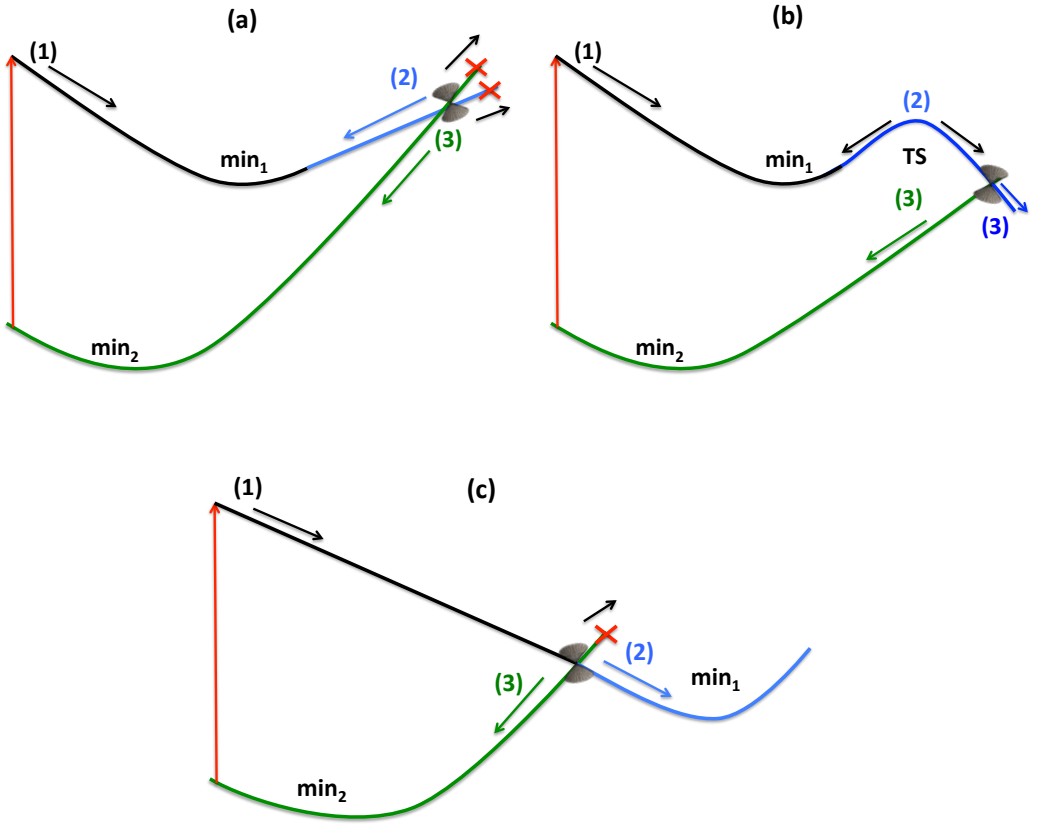

Figure 2.9. Minimum Energy Path of three hypothetical situations.

MEP needs now to follow the gradient of the upper root but after the CI, in other words, another MEP along the lower root but with different character (2 in Figure 2.9 b). In summary, two MEPs from the CI following the lower path but with different character should be carried out. For this, the CI structure can be slightly modified in order to achieve the correct state ordering at both sides of the CI before launching the MEPs.

Following this procedure a connected pathway including all the stationary and critical points along the MEP would be obtained elucidating the most probable mechanism, at least from a static point of view.

2.4 Spin Orbit Coupling and Intersystem Crossings

As discussed before intersystem crossing is a spin forbidden transition. Assuming the Zero Order approximation, which states that for a fixed nuclear geometry the electronic state is define by a single orbital configuration and spin, intersystem crossings are strictly forbidden. Within this approximation, if a molecule is initially in a singlet excited state, it will remain always in the singlet manifold and the same would occur for triplets. However, introducing spin orbit couplings make the exchange of population between different multiplicities more likely to occur. These interactions allow the mixing of states presenting different spins, for a given structure.

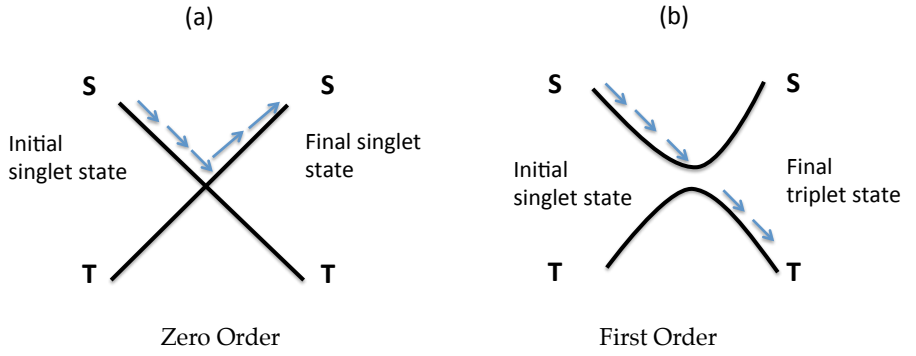

Figure 2.10. (a) Perfect forbidden intersystem crossing within the Zero Order approximation, (b) Allowed Intersystem crossing due to spin orbit couplings. Adapted from Turro. [1]

Spin orbit couplings can be defined as the field arising from the molecule which is able to provide the magnetic torque (generated by an electron's orbital promotion) required to flip the electron's spin magnetic moment, keeping at the same time the total momentum (coupling the spin-flip with an orbital promotion). Since the movement of any charged particle generates magnetic fields, $\boldsymbol{H_e}$, both the orbital and the spin motion of the electron generate magnetic moments. When an electron moving around the nucleus following a trajectory, which, for instance, describes the shape of a p_y orbital shape comes close to the nucleus, induces magnetic momenta ($\boldsymbol{H_e}$) that can act as a torque on the spin momenta ($\boldsymbol{\mu_s}$) causing the spin flipping. However, as it has been said before, the total momenta must be conserved, so the initial p_y orbital is transformed into a p_x orbital. Some general rules can be established regarding spin-orbit interactions:

- Spin orbit couplings are defined by an energy equal to:

$$\boldsymbol{E_{SO} = \pm H_e \mu_s}$$

- Intersystem crossings are more probable when an **orbital promotion** takes place, for instance, from a p_y orbital to a p_x one.

- If the orbital promotion takes place within the same atom (**one-center** effect), the spin flipping is also most likely to occur.
- Intersystem Crossing is most probable if the spin flipping takes place within a **heavy atom** (high value of Z). That is because for a given orbit, the acceleration of the force increases as the nuclear charge Z increases.

These conditions allow settling down some general selection rules for intersystem crossing. Taking a carbonyl group as an example the singlet states can be either of $^1n\pi^*$ or $^1\pi\pi^*$ character and the same for the triplet states ($^3n\pi^*$ or $^3\pi\pi^*$). Following the selection rules (1) the most probable transition involves a change of the orbital character and (2) if the transition takes place within orbitals of the same atom, the most probable singlet->triplet intersystem crossings are:

$$^1n\pi^* \rightarrow {}^3\pi\pi^* \quad \text{and}$$

$$^1\pi\pi^* \rightarrow {}^3n\pi^*$$

These rules are known as the El-Sayed's rules[6] and applicable to organic compounds. Furthermore, they can also be used to predict the probability for decaying to the ground state from a triplet state (T_1-> S_0), being those transitions:

$^3n\,\pi^* \rightarrow S_0$ (n(2e-)) Allowed

$^3\pi\,\pi^* \rightarrow S_0$ (π(2e-)) Forbidden

These probabilities can be understood attending to the characters of the orbitals involved in the transition to the ground state. In the first case the transition takes place from a π^* orbital to an n orbital, while in the second this transition involves two orbitals of the same π nature.

2.5 Summary

Within this chapter a brief description of the topology of the excited PESs (conical intersections and intersystem crossings) has been given, providing a general overview on how to face a general photochemical problem using the available computational methods.

Bibliography

(1) Turro, N. J. *Modern Molecular Photochemistry. Copyright 1991 Science Books* **1991**.

(2) Bearpark, M. J.; Robb, M. A.; Schlegel, H. B. *Chem. Phys. Lett.* **1994**, *223*, 269.

(3) Atchity, G. J.; Xantheas, S. S.; Ruedenberg, K. *J. Chem. Phys* **1991**, *95*, 1862.

(4) Boggio-Pasqua, M.; Bearpark, M. J.; Hunt, P. A.; Robb, M. A. *J. Am. Chem. Soc.* **2002**, *124*, 1456.

(5) Boggio-Pasqua, M.; Ravaglia, M.; Bearpark, M. J.; Garavelli, M.; Robb, M. A. *J. Phys. Chem. A* **2003**, *107*, 11139.

(6) El-Sayed, M. A. *J. Chem. Phys.* **1963**, *38*, 2834.

Chapter 3

Quantum Chemical Methodology

This chapter pretends to give an overview on the theoretical methods used throughout this master thesis.

One of the main interests of Quantum Chemistry is to find approximate solutions for the Schrödinger equation[1]

$$\hat{H}\Psi = E\Psi \qquad 3.1$$

where Ψ is the wave function, and contains all the information for a given system and $\hat{H}$ is the Hamiltonian operator, which contains kinetic ($\hat{T}$) and coulomb potential ($\hat{V}$) energy terms for all particles.

$$\hat{H} = \hat{T} + \hat{V} = -\frac{\hbar^2}{2m}\nabla^2 + \hat{V} \qquad 3.2$$

The kinetic energy operator $\hat{T}$ depends on the second order derivative ∇^2 and when $\hat{V}$ involves more than one particle equation (3.2) has no analytical solution. However, in order to solve it, some approximations can be taken into account. For instance, since the nuclei are much heavier, for a great number of physical problems, it is safe to neglect the coupling between nuclei and electronic velocities (Born-Oppenheimer approximation). Labelling nuclei (n) coordinates with R and electron (e) coordinates with r, nuclear and electronic variables can be separated

$$\hat{H}_{tot} = \underbrace{\hat{T}_e + \hat{V}_{Ne} + \hat{V}_{ee} + \hat{V}_{NN}}_{\hat{H}_e} + \hat{T}_N \qquad 3.3$$

$$\Psi_{tot}(R,r) = \Psi_N(R)\Psi_e(r,R) \qquad 3.4$$

$$\hat{H}_e\Psi_e(r,R) = E_e(R)\,\Psi_e(r,R) \qquad 3.5$$

where $\hat{T}_e$and $\hat{T}_N$ represent the kinetic and nuclei electronic energy, $\hat{V}_{Ne}$ the potential nuclei-electron attraction energy, $\hat{V}_{ee}$ the potential electron-electron repulsion energy and , $\hat{V}_{NN}$ the potential nuclei-nuclei repulsion energy. The procedure followed to calculate Ψ_{tot} and E_{tot} is now described. First, the equation involving the electrons movement is solved, keeping fixed the nuclei coordinates. The electronic energy is used to build the potential suffered by the nuclei, find the nuclei energy, and therefore the total final energy.

There are several approximations to solve the electronic Schrödinger equation (3.2). The main of them are wave function methods and density functional theory (DFT) methods. The first part of this chapter will summarize the basis of HF and pots HF methods (CI and CASSCF/ /MS-CASPT2).

3.1 Multi particle wave function: Slater determinants

The spin orbitals, χ, formed by a spatial component ψ and a spin function α or β, describe properly the wave function of a single electron. The electronic wave function, however, depends on the N electrons of the system. The easiest way to represent the electronic wave function as a function of spin orbitals is using the Hartree product

$$\Psi(x_1, x_2, \dots, x_N) = \chi_i(x_1)\chi_j(x_2) \dots \chi_k(x_N) \qquad 3.6$$

In equation 3.6, χ_i, are wave functions describing single electrons, the orbitals, and although this model was used in the early times of the quantum mechanics it present some deficiencies. Since electrons are identical particles and no change should be detectable in any of the observable properties of the system if two of them are interchanged, this equation does not reflect that statement. In other words, the Hartree product does not satisfy the Pauli exclusion principle, which states that no more than one electron can occupy the same spin orbital, or in other words, the wave function must be antisymmetric with respect to the interchange of spin and space of two electrons. Considering two electrons occupying the spin orbitals χ_i and χ_j, a function which satisfies this principle is a linear combination of the two possible Hartree products

$$\Psi\,(x_1, x_2) = \; 2^{-1/2}\,\left(\chi_i(x_1)\chi_j(x_2) - \chi_j(x_1)\chi_i(x_2)\right) \qquad 3.7$$

where the $2^{-1/2}$ is a normalization factor. The minus sing ensures the condition of antisymmetry with respect to the interchange of coordinates of the two electrons. Generalizing for any N-electron system, the previous expression can be written

$$\Psi(x_1, x_2, \dots, x_N) = (N)^{-1/2} \begin{vmatrix} \chi_i(x_1) & \chi_j(x_1) & \cdots & \chi_k(x_1) \\ \chi_i(x_2) & \chi_j(x_2) & \cdots & \chi_k(x_2) \\ \vdots & \vdots & & \vdots \\ \chi_i(x_N) & \chi_j(x_N) & \dots & \chi_k(x_N) \end{vmatrix} \qquad 3.8$$

This determinant is called the Slater determinant and represents the occupation of N spin orbitals by N electrons without specifying which orbital is occupied by which electron. Electrons label the rows while columns are labelled by spin orbitals. Since if there were two electrons in the same spin orbitals the determinant will be zero, the Slater determinants satisfy the Pauli exclusion principle. In sort, the Slater determinants can be written showing its diagonal elements

$$\Psi(x_1, x_2, \dots, x_N) = (N)^{-1/2}\,|\chi_i\chi_j \dots \chi_k\rangle \qquad 3.9$$

where $(N)^{-1/2}$ factor guarantees the function to be normalized.

3.2 Hartree-Fock Theory

The Hartree[2] Fock[3,4] (HF) theory is the simplest approximation to solve the Schrödinger equation, and is the starting point for more accurate ab initio methods. The HF wave function is described by a single Slater determinant formed by a set of spin orbitals, $\boldsymbol{\chi_a}$, depending on a single electron.

$$|\Psi_0\rangle = \; |\chi_1\chi_2 \dots \chi_a\chi_b \dots \chi_N\rangle \qquad 3.10$$

The Scrödinger equation that needs to be solved, can be written as

$$E_0 = \langle\Psi_0|\mathcal{H}|\Psi_0\rangle \qquad 3.11$$

were $\mathcal{H}$ is the full electronic Haniltonian and Ψ_0 represents the best approximation to the ground state of a N-electron system

Using Slater[5]-Condon[6] rules, the energy expression can be evaluated as a function of the spin orbitals $\{\chi_a\}$which form the Ψ determinant

$$E_0 = \sum_a^N \langle \chi_a | h | \chi_a \rangle + \frac{1}{2} \sum_{ab}^N \langle \chi_a \chi_b || \chi_a \chi_b \rangle \qquad \text{or} \qquad 3.12a$$

$$E_0 = \sum_a^N h_{aa} + \frac{1}{2} \sum_{ab}^N (J_{ab} - K_{ab}) \qquad 3.12b$$

where J_{ab} and K_{ab} are the Coulomb and Exchange operators, which will be defined later on. The HF theory seeks obtaining the minimum value for E_0 optimizing the spin orbitals $\{\chi_a\}$. This procedure is known as the variational principle.

3.3 The variational principle

The variational principle is one of the most important theorems in quantum mechanics (allows to obtain an approximation of the ground state energy). The variational principle states that, given a normalized wave function, φ, the expectation value of the Hamiltonian is an upper bound to the exact energy of the ground state

$$\langle \phi | \mathcal{H} | \phi \rangle \geq E_0 \qquad 3.13$$

Different guess functions are tried in order to find the best wave function that defines the ground state. The quality of the guess function is associated to its energy, the lower the energy the better the guess function. The basis of the variational methods rely on varying the parameters on which depend the wave function, until the expectation value $\langle \phi | \mathcal{H} | \phi \rangle$ is minimized. This minimum value is the variational estimate to the ground state energy.

3.4 Hartree-Fock equations

According to the variational principle, the Hartree-Fock equations, which determine the optimal spin orbitals, are obtained minimizing E_0. During the minimization the spin orbitals are constrained to remain orthonormal, $\langle \chi_a | \chi_b \rangle = \delta_{ab}$. The HF equation for a single electron is

$$h(1)\chi_a(1) + \sum_{b\neq a}\left[\int d\vec{x}_2|\chi_b(2)|^2\, r_{12}^{-1}\right]\chi_a(1) - \sum_{b\neq a}\left[\int d\vec{x}_2\chi_b^*(2)\chi_a(2)\, r_{12}^{-1}\right]\chi_b(1)$$

$$= \varepsilon_a\chi_a(1) \qquad 3.14$$

where ε_a is the orbital energy of the spin orbital χ_a and h(1) is the sum of the kinetic and potential energy (nuclei attraction) of a single electron, (1)

$$h(1) = -\frac{1}{2}\nabla_1^2 - \sum_A \frac{Z_A}{r_{1A}} \qquad 3.15$$

The two last terms in equation (3.14) represent electron-electron interactions. The first of them is the Coulomb term, which depicts the repulsive potential in $\vec{x}_1$ originated by an electron in χ_b. The *coulomb operator* acting on a spin orbital $\chi_a(1)$ can be defined as

$$J_b(1)\chi_a(1) = \left[\int d\vec{x}_2\chi_b^*(2)\, r_{12}^{-1}\,\chi_b(2)\right]\chi_a(1) \qquad 3.16$$

The second two-electron interaction is named as the Exchange term. Despite no classical interpretation can be extract from it, it is known to arise from the antisymetric nature of the single determinantal wave function. As well as the coulomb, the *exchange operator* is written on the spin orbital χ_a as

$$K_b(1)\chi_a(1) = \left[\int d\vec{x}_2\chi_b^*(2)\, r_{12}^{-1}\chi_a(2)\right]\chi_b(1) \qquad 3.17$$

The Hartree-Fock equation can be now rewritten as a function of J_b and K_b

$$\left[h(1) + \sum_{b\neq a} J_b\,(1) - \sum_{b\neq a} K_b\,(1)\right]\chi_a(1) = \varepsilon_a\chi_a(1) \qquad 3.18$$

The operator in brackets seems to be different for every spin orbital χ_a on which operates. However, considering that $[J_a(1) - K_a(1)]\chi_a(1) = 0$ the restriction in the summation can be deleted, defining the *Fock operator*

$$\mathrm{f}(1) = h(1) + \sum_b J_b\,(1) - K_b\,(1) \qquad 3.19$$

The Fock operator can be also expressed as the sum of the *core-Hamiltonian* operator $h(1)$ and an effective one electron potential, *the Hartree-Fock potential*, $v^{HF}(1)$

$$f(1) = h(1) + v^{HF}(1) \qquad 3.20$$

where

$$v^{HF}(1) = \sum_{b} J_b(1) - K_b(1) \qquad 3.21$$

Finally the Hartree-Fock equation

$$f|\chi_a\rangle = \varepsilon_a |\chi_a\rangle \qquad 3.22$$

is a pseudo-eigenvalue equation due to the dependence of the fock operator on the solutions $\{\chi_a\}$ of the pseudo-eigenvalue equation through the coulomb and exchange operators. Since a guess of spin orbital is needed to build the fock operator, the HF equations are non linear and should be solved iteratively. This iterative procedure is known as *Self Consistent Field* (SCF). Normally, a set of basis functions is introduced for the expansion of the spin orbitals and the matrix equations are solved. The idea of SCF is simple, using the initial guess of spin orbitals, the averaged field seen by each electron is calculated in order to find a new set of spin orbitals. With the new orbitals, new fields are obtained and the procedure is repeated until self-consistency is reached. Once the spin orbital are converged, a Slater determinant representing the wave function of the system is constructed.

3.5 Restricted Hartree-Fock: The Roothaan equations

The restricted Hartree-Fock formalism describes close-shell systems with N electrons doubly occupying n=N/2 spatial orbitals. Within this formalism α () and β ()spin orbitals are constrained to take the same spatial functions. Open-shell ground and excited states need to be described by the unrestricted formalism, which will be discussed in the next section.

The general spin orbital Hartree-Fock equation can be converted into a spatial eigenvalue equation where each spatial molecular orbital is doubly occupied. This transition can be easily carried out considering that the N spin orbitals can be written as a sum of N/2 spin α functions and N/2 spin β functions

$$\sum_{a}^{N} \chi_a = \sum_{a}^{N/2} \psi_a + \sum_{a}^{N/2} \bar{\psi}_a \qquad 3.23$$

where

$$\psi_a(x) = \psi_a(r)\alpha(\omega) \qquad 3.24$$

$$\overline{\psi}_a(x) = \psi_a(r)\beta\ (\omega) \qquad 3.25$$

The Hartree-Fock energy of a close-shell system, for the closed shell determinant $|\psi_0\rangle = |\psi_1\overline{\psi}_1 \dots \psi_{N/2}\overline{\psi}_{N/2}\rangle$ is given by

$$E_0 = 2\sum_{a}^{N/2} h_{aa} + \sum_{ab}^{N/2}(2J_{ab} - K_{ab}) \qquad 3.26$$

Once the spin has been eliminated, the Hartree-Fock equation can be seen as a spatial-integro differential problem

$$f(r_1)\psi_i(r_1) = \varepsilon_i\psi_i(r_1) \qquad 3.27$$

However, this equation has no analytical solution for molecules, since the molecular orbitals which are needed to start the procedure have no analytical form.

Roothaan solved this problem, introducing a set of known spatial basis functions to define the molecular orbitals

$$\psi_i = \sum_{\mu=1}^{k} C_{\mu i}\phi_\mu \qquad i = 1,2,\dots,k \qquad 3.28$$

If the basis set was complete, the expansion would be exact. Unfortunately the computational cost limits the basis set to a finite set of K basis functions.
Substituting this expansion in the Hartree-Fock equation

$$f(1)\sum_{\nu} C_{\nu i}\phi_\nu\ (1) = \varepsilon_i \sum_{\nu} C_{\nu i}\phi_\nu\ (1) \qquad i = 1,2,\dots,k \qquad 3.29$$

Multiplying by ϕ_μ^* (1) on the left and integrating, a matrix equation is obtained

$$\sum_{\nu} F_{\mu\nu}\ C_{\nu i} = \varepsilon_i \sum_{\nu} S_{\mu\nu}C_{\nu i} \qquad i = 1,2,\dots,k \qquad 3.30$$

where $F_{\mu\nu}$ is the Fock matrix and $S_{\mu\nu}$ is the overlap matrix

$$F_{\mu\nu} = \int d\vec{r}_1\phi_\mu^*\ (1)f(1)\phi_\nu\ (1) \qquad \text{and} \qquad S_{\mu\nu} = \int d\vec{r}_1\phi_\mu^*\ (1)\phi_\nu\ (1) \qquad 3.31$$

The Roothaan[7]-Hall[8] equations can be written in a matrix equation

$$\mathbf{FC} = \mathbf{SC\varepsilon} \qquad 3.32$$

The **C** matrix is a K x K matrix containing the expansion coefficients, which describe the molecular orbtials. Meanwhile, the ε matrix is a diagonal matrix collecting the orbital energies. The form of the **F** is the matrix representation of the Fock operator with the set of basis functions $\{\phi_u\}$

$$F_{\mu\nu} = \int d\vec{r}_1 \phi_\mu^* (1) f(1) \phi_\nu (1)$$

$$= \int d\vec{r}_1 \phi_\mu^* (1) h(1) \phi_\nu (1) + \sum_a^{N/2} d\vec{r}_1 \phi_\mu^* (1) [2J_a(1) - K_a(1)] \phi_\nu (1)$$

$$= H_{\mu\nu}^{core} + \sum_a^{N/2} 2(\mu\nu|aa) - (\mu a|a\nu) \qquad 3.33$$

where the $H_{\mu\nu}^{core}$ matrix contains the integrals involved in the one-electron operator h(1) equation (3.15). The physical nomenclature for the integrals has been introduced

$$(\mu a|a\nu) = \int d\vec{r}_1 d\vec{r}_2 \phi_\mu^* (1) \phi_a^* (2) \frac{1}{r_{12}} \phi_a(1) \phi_\nu (2) \qquad 3.34$$

Introducing the linear expansion for the molecular orbitals into the two electrons terms of the Fock matrix

$$F_{\mu\nu} = H_{\mu\nu}^{core} + \sum_a^{N/2} \sum_{\lambda\sigma} C_{\lambda a} C_{\sigma a}^* [2(\mu\nu|\sigma\lambda) - (\mu\lambda|\sigma\nu)] \qquad 3.35$$

Defining the density matrix as

$$P_{\lambda\sigma} = 2 \sum_a^{N/2} C_{\lambda a} C_{\sigma a}^* \qquad 3.36$$

then

$$F_{\mu\nu} = H_{\mu\nu}^{core} + \sum_{\lambda\sigma} P_{\lambda\sigma} [(\mu\nu|\sigma\lambda) - \tfrac{1}{2}(\mu\lambda|\sigma\nu)] \qquad 3.37$$

$$F_{\mu\nu} = H_{\mu\nu}^{core} + G_{\mu\nu} \qquad 3.38$$

The Fock matrix is now divided into two new matrixes: $\boldsymbol{H}^{core}$ which defines the one-electron part of the **F** matrix, being fixed given a basis set, and **G** which is the two-electron part of **F**, which depends on the density matrix. Due to the dependence of **F** on the coefficients matrix through **P**, the Roothaan equations are nonlinear and must be calculated iteratively. While the **H** matrix is fixed, **G** must be calculated for each iteration.

The expansion coefficients could be obtained directly diagonalizing the Fock matrix, if the basis set was orthonormal. Although the basis functions are normalized, they are not orthonormal to each other. This problem must be solved to evaluate the Roothaan´s equation in the usual matrix eigenvalue form. The more efficient solution is to consider a new coefficient matrix **C´** related with the old one

$$\boldsymbol{C'} = \boldsymbol{X}^{-1}\boldsymbol{C} \qquad \boldsymbol{C} = \boldsymbol{X}\boldsymbol{C'} \tag{3.39}$$

The **X** matrix is able to transform the initial basis set into an orthonormal one if it satisfies

$$\boldsymbol{X}^{\dagger}\boldsymbol{S}\,\boldsymbol{X} = \mathbf{1} \tag{3.40}$$

Introducing **C´** into the Roothaan equation and multiplying by $\boldsymbol{X}^{\dagger}$ on the left

$$(\boldsymbol{X}^{\dagger}\boldsymbol{F}\boldsymbol{X})\,\boldsymbol{C'} = (\boldsymbol{X}^{\dagger}\boldsymbol{S}\boldsymbol{X})\boldsymbol{C'}\boldsymbol{\varepsilon} \tag{3.41}$$

Defining,

$$\boldsymbol{F'} = (\boldsymbol{X}^{\dagger}\boldsymbol{F}\boldsymbol{X}) \tag{3.42}$$

The transformed Roothaan equations can be written as

$$\boldsymbol{F'}\boldsymbol{C'} = \boldsymbol{C'}\boldsymbol{\varepsilon} \tag{3.43}$$

Given a coefficient matrix **C, C´** can be easily obtained by the transformation matrix, obtained by diagonalizing **F´**. Another solution to the non orthogonalized problem, is for instance, to orthogonalize the initial basis set obtaining a new set of orthonormalized basis. This solution implies the recalculation of the two electron integrals which is computationally expensive.

The computational procedure for obtaining closed-shell Hartree-Fock wave function is now described.

(1) Define the molecule (number of electrons N, nuclear coordinates $\{R_A\}$, atomic numbers Z_A) and the basis set $\{\varphi_\mu\}$.

(2) Calculate the one-electron integrals $H_{\mu\nu}^{core}$ and the two electron ones $S_{\mu\nu}$ and $(\mu\nu|\sigma\lambda)$ integral, which will remain constant during the SCF procedure.

(3) Find the transformation matrix **X** by diagonalizing the overlap matrix **S**.

(4) Calculate all the necessary matrixes (**P,G**) to obtain the Fock matrix, **F**.

(5) Use the transformation matrix to generate **F´**.

(6) Diagonalize the transformed Fock matrix **F´** to obtain a new set of improved expansion coefficients, **C´**.

(7) Calculate **C** from **C´**, $\boldsymbol{C} = \boldsymbol{X}\boldsymbol{C'}$.

(8) Evaluate the new density matrix **P** from **C**. The procedure is converged if the new density matrix is the same as the previous one within a certain criteria. If the two densities are different, return to step four and repeat the cycle until converged.

(9) Once the procedure is converged, use **C,P,F**..etc to build the wave function and evaluate the properties of interest of the system.

3.6 Unrestricted Hartree-Fock: The Pople-Nesbet Equations

Many chemical problems as free radicals, excited states or stretched bonds can not been described by close-shell formalism. Two main approaches are used to deal with open-shell problems. In the first one, open-shell restricted Hartree-Fock (OSRHF) all electrons occupy close-shell orbitals, except those explicitly required to remain unpaired. The second approach, however, unrestricted Hartree-Fock (UHF), does not restrict the spin orbitals α and β to have identical spatial functions anymore. The important advantage of OSRHF is that the constructed wave function is an eigenfunction of the spin operator S^2. But occupying orbitals in pairs raises the variational energy.

The general Hartree-Fock equation can be also obtained in terms of unrestricted spin orbitals. An unrestricted set of spin orbitals takes the form

$$\chi_i = \begin{cases} \psi_j^{\alpha}(\vec{r})\alpha(\omega) \\ \psi_j^{\beta}(\vec{r})\beta(\omega) \end{cases} \qquad 3.44$$

The α electrons are described by the set of spatial orbitals $\{\psi_j^{\alpha} \mid j = 1,2,\ldots,k\}$ while the electrons β are described by a different one $\{\psi_j^{\beta} \mid j = 1,2,\ldots,k\}$. Since the spatial parts of the spin orbitals are different they also have different energies

$$f^{\alpha}(1)\psi_j^{\alpha}(1) = \varepsilon_j^{\alpha}\psi_j^{\alpha}(1) \qquad 3.45$$

$$f^{\beta}(1)\psi_j^{\beta}(1) = \varepsilon_j^{\beta}\psi_j^{\beta}(1) \qquad 3.46$$

The expression for the Fock operator is slightly different from that of the restricted case. For α electrons, it includes the kinetic energy, nuclei attraction and the effective interactions (coulomb and exchange) of the α electron with the rest of the same spin, but only the coulomb interaction with the β electrons

$$f^{\alpha}(1) = h(1) + \sum_{a}^{N\alpha}[J_a^{\alpha}(1) - K_a^{\alpha}(1)] + \sum_{a}^{N\beta} J_a^{\beta}(1) \qquad 3.47$$

For β electrons the corresponding Fock operator is

$$\mathfrak{f}^{\beta}(1) = h(1) + \sum_{a}^{N\beta}[J_a^{\beta}(1) - K_a^{\beta}(1)] + \sum_{a}^{N\alpha} J_a^{\alpha}(1) \qquad 3.48$$

The coulomb and exchange operator have the same description than in the restricted formalism

$$J_a^{\alpha}(1) = \int d\vec{r}_2 \psi_a^{\alpha *}(2) r_{12}^{-1} \psi_a^{\alpha}(2) \qquad 3.49$$

$$K_a^{\alpha}(1)\psi_i^{\alpha}(1) = \left[\int d\vec{r}_2 \psi_a^{\alpha *}(2) r_{12}^{-1} \psi_i^{\alpha}(2)\right] \psi_a^{\alpha}(1) \qquad 3.50$$

The operators $J_a^{\beta}(1)$ and $K_a^{\beta}(1)$ are defined identically. From the expressions of the Fock operator, it can be deduced that both equations are coupled, $\mathfrak{f}^{\alpha}(1)$depends on the β electrons trough $J_a^{\beta}(1)$ as the same way that $\mathfrak{f}^{\beta}(1)$ depends on the α electrons through $J_a^{\alpha}(1)$. Due to this dependency, both equations cannot be solved independently, and therefore require a simultaneous iterative solution. The total energy for unrestricted systems can be now written as

$$E_0 = \qquad 3.51$$
$$= \sum_{a}^{N^{\alpha}} h_{aa}^{\alpha} + \sum_{a}^{N^{\beta}} h_{aa}^{\beta} + \frac{1}{2}\sum_{a}^{N^{\alpha}}\sum_{b}^{N^{\alpha}} (J_{ab}^{\alpha\alpha} - K_{ab}^{\alpha\alpha}) + \frac{1}{2}\sum_{a}^{N^{\beta}}\sum_{b}^{N^{\beta}} (J_{ab}^{\beta\beta} - K_{ab}^{\beta\beta}) + \sum_{a}^{N^{\alpha}}\sum_{b}^{N^{\beta}} J_{ab}^{\alpha\beta}$$

where some terms need to be defined, for example, the Coulomb interaction between electrons of identical and different spin

$$J_{ij}^{\alpha\alpha} = \left(\psi_i^{\alpha}\middle|J_j^{\alpha}\middle|\psi_i^{\alpha}\right) = \left(\psi_j^{\alpha}|J_i^{\alpha}|\psi_j^{\alpha}\right) = \left(\psi_i^{\alpha}\psi_i^{\alpha}\middle|\psi_j^{\alpha}\psi_j^{\alpha}\right) \qquad 3.52$$

$$J_{ij}^{\beta\beta} = \left(\psi_i^{\beta}\middle|J_j^{\beta}\middle|\psi_i^{\beta}\right) = \left(\psi_j^{\beta}\middle|J_i^{\beta}\middle|\psi_j^{\beta}\right) = \left(\psi_i^{\beta}\psi_i^{\beta}\middle|\psi_j^{\beta}\psi_j^{\beta}\right) \qquad 3.53$$

$$J_{ij}^{\alpha\beta} = J_{ji}^{\beta\alpha} = \left(\psi_i^{\alpha}\middle|J_j^{\beta}\middle|\psi_i^{\alpha}\right) = \left(\psi_j^{\beta}|J_i^{\alpha}|\psi_j^{\beta}\right) = \left(\psi_i^{\alpha}\psi_i^{\alpha}\middle|\psi_j^{\beta}\psi_j^{\beta}\right) \qquad 3.54$$

As in the restricted case, to solve the unrestricted HF equations the unrestricted molecular orbitals must be expanded into a basis set $\{\phi_{\mu}\}$

$$\psi_i^{\alpha} = \sum_{\mu=1}^{K} C_{\mu i}^{\alpha}\phi_{\mu} \quad i = 1,2,\dots,k \qquad 3.55$$

$$\psi_i^{\beta} = \sum_{\mu=1}^{K} C_{\mu i}^{\beta}\phi_{\mu} \quad i = 1,2,\dots,k \qquad 3.56$$

Substituting those expressions into the equations (3.45 and 3.46) and multiplying by ϕ_μ^* on the left

$$\sum_\nu F_{\mu\nu}^\alpha C_{\nu j}^\alpha = \varepsilon_j^\alpha \sum_\nu S_{\mu\nu} C_{\nu j}^\alpha \qquad i = 1,2,\dots,k \tag{3.57}$$

$$\sum_\nu F_{\mu\nu}^\beta C_{\nu j}^\beta = \varepsilon_j^\beta \sum_\nu S_{\mu\nu} C_{\nu j}^\beta \qquad j = 1,2,\dots,k \tag{3.58}$$

where **S** is the overlap matrix and **F** represents the fock operator in the basis set $\{\phi_\mu\}$. Writing this equation into matrix form, the Pople-Nesbet[9] equations are obtained

$$\boldsymbol{F^\alpha C^\alpha = S C^\alpha \varepsilon^\alpha} \tag{3.59}$$

$$\boldsymbol{F^\beta C^\beta = S C^\beta \varepsilon^\beta} \tag{3.60}$$

$\boldsymbol{C^\alpha}$ and $\boldsymbol{C^\beta}$ matrixes are the k x k matrixes containing the expansion coefficients of the unrestricted orbitals. The orbital energies are contained in $\boldsymbol{\varepsilon^\alpha}$ and $\boldsymbol{\varepsilon^\beta}$. These equations are solved in a procedure very similar to the followed with the Roothaan-Hall equations, except that, here both equations must be solved simultaneously.
To find the explicit form of the Fock matrixes, it is important to define the α and β density matrixes. Considering N^α electrons of spin α, the charge density, or probability of finding this electron in a volume element $\vec{r}$ is

$$\rho^\alpha(r) = \sum_a^{N^\alpha} |\psi_a^\alpha(r)|^2 \tag{3.61}$$

$$\rho^\beta(r) = \sum_a^{N^\beta} \left|\psi_a^\beta(r)\right|^2 \tag{3.62}$$

The total charge density $\boldsymbol{\rho^T}$ and the spin density $\boldsymbol{\rho^S}$ can also be defined

$$\boldsymbol{\rho^T = \rho^\alpha + \rho^\beta} \tag{3.63}$$

$$\boldsymbol{\rho^S = \rho^\alpha - \rho^\beta} \tag{3.64}$$

The basis set expansion can be introduced in the density matrixes expressions

$$\boldsymbol{\rho^\alpha}(r) = \sum_a^{N^\alpha} |\boldsymbol{\psi_a^\alpha}(\boldsymbol{r})|^2 = \sum_\mu \sum_\nu \boldsymbol{P_{\mu\nu}^\alpha\ \phi_\mu}(\boldsymbol{r})\boldsymbol{\phi_\nu^*} \tag{3.65}$$

$$\boldsymbol{\rho^{\beta}}(r) = \sum_{\boldsymbol{a}}^{\boldsymbol{N^{\beta}}} \left|\boldsymbol{\psi_a^{\beta}}\,(\boldsymbol{r})\right|^2 = \sum_{\boldsymbol{\mu}}\sum_{\boldsymbol{\nu}} \boldsymbol{P_{\mu\nu}^{\beta}}\ \boldsymbol{\phi_{\mu}}(\boldsymbol{r})\boldsymbol{\phi_{\nu}^{*}} \qquad 3.66$$

where the matrix $\mathbf{P}^{\alpha}$ and the matrix $\mathbf{P}^{\beta}$ are defined by

$$\boldsymbol{P_{\mu\nu}^{\alpha}} = \sum_{a}^{N^{\alpha}} C_{\mu a}^{\alpha}(C_{\nu a}^{\alpha})^{*} \qquad 3.67$$

$$\boldsymbol{P_{\mu\nu}^{\beta}} = \sum_{a}^{N^{\beta}} C_{\mu a}^{\beta}(C_{\nu a}^{\beta})^{*} \qquad 3.68$$

Using these expressions, the Fock matrix **F** can be obtained as a function of the density matrix

$$\boldsymbol{F_{\mu\nu}^{\alpha}} = \int d\vec{r}_1 \phi_{\mu}^{*}(1) f^{\alpha}(1)\phi_{\nu}(1) \qquad 3.69$$

$$= H_{\mu\nu}^{core} + \sum_{a}^{N^{\alpha}}\left[\left(\phi_{\mu}\phi_{\nu}\middle|\psi_a^{\alpha}\psi_a^{\alpha}\right) - \left(\phi_{\mu}\psi_a^{\alpha}\middle|\psi_a^{\alpha}\phi_{\nu}\right)\right] + \sum_{a}^{N^{\beta}}\left(\phi_{\mu}\phi_{\nu}\middle|\psi_a^{\beta}\psi_a^{\beta}\right)$$

$$\boldsymbol{F_{\mu\nu}^{\beta}} = \int d\vec{r}_1 \phi_{\mu}^{*}(1) f^{\beta}(1)\phi_{\nu}(1) \qquad 3.70$$

$$= H_{\mu\nu}^{core} + \sum_{a}^{N^{\beta}}\left[\left(\phi_{\mu}\phi_{\nu}\middle|\psi_a^{\beta}\psi_a^{\beta}\right) - \left(\phi_{\mu}\psi_a^{\beta}\middle|\psi_a^{\beta}\phi_{\nu}\right)\right] + \sum_{a}^{N^{\alpha}}\left(\phi_{\mu}\phi_{\nu}\middle|\psi_a^{\alpha}\psi_a^{\alpha}\right)$$

Substituting the basis set expansion of ψ_a^{α} and ψ_a^{β}

$$\boldsymbol{F_{\mu\nu}^{\alpha}} = \qquad 3.71$$

$$= H_{\mu\nu}^{core} + \sum_{\lambda}\sum_{\sigma}\sum_{a}^{N^{\alpha}} C_{\lambda a}^{\alpha}(C_{\sigma a}^{\alpha})^{*}[(\mu\nu|\sigma\lambda) - (\mu\lambda|\sigma\nu)] + \sum_{\lambda}\sum_{\sigma}\sum_{a}^{N^{\beta}} C_{\lambda a}^{\beta}(C_{\sigma a}^{\beta})^{*}\,(\mu\nu|\sigma\lambda)$$

$$\boldsymbol{F_{\mu\nu}^{\alpha}} = H_{\mu\nu}^{core} + \sum_{\lambda}\sum_{\sigma} \boldsymbol{P_{\lambda\sigma}^{T}}(\mu\nu|\sigma\lambda) - \boldsymbol{P_{\lambda\sigma}^{\alpha}}\,(\mu\lambda|\sigma\nu) \qquad 3.72$$

$$\boldsymbol{F}_{\mu\nu}^{\beta} = \qquad 3.73$$

$$= H_{\mu\nu}^{core} + \sum_{\lambda}\sum_{\sigma}\sum_{a}^{N^{\beta}} C_{\lambda a}^{\beta}(C_{\sigma a}^{\beta})^{*}[(\mu\nu|\sigma\lambda) - (\mu\lambda|\sigma\nu)] + \sum_{\lambda}\sum_{\sigma}\sum_{a}^{N^{\alpha}} C_{\lambda a}^{\alpha}(C_{\sigma a}^{\alpha})^{*}\,(\mu\nu|\sigma\lambda)$$

$$\boldsymbol{F}_{\mu\nu}^{\beta} = H_{\mu\nu}^{core} + \sum_{\lambda}\sum_{\sigma} \boldsymbol{P}_{\lambda\sigma}^{T}(\mu\nu|\sigma\lambda) - \boldsymbol{P}_{\boldsymbol{\lambda\sigma}}^{\beta}\,(\mu\lambda|\sigma\nu) \qquad 3.74$$

The procedure to solve these equations is identical to the explained for the RHF method, except for the fact that two coefficients matrixes are needed to diagonalize $\mathbf{F}^{\alpha}$ and $\mathbf{F}^{\beta}$.

3.7 Hartree-Fock limitations: The correlation energy

Electron correlation is not included since the electron-electron repulsion is treated in an average way. This treatment considers that each electron moves in an averaged potential arising from the N-1 electrons in the other spin orbitals. The HF approximation would provide the lowest expectation value to HF energy if the expansion basis set was complete. However, an infinite number of basis functions are, computationally, impossible to obtain. The bigger is the basis set, the more flexible becomes the wave function so the more accurate the calculation is. Nevertheless, once a certain number of basis functions has been reached, the energy does not improve if this number is increased. This set can be considered a complete basis set, and the energy it provides is the HF limit.

The correlation energy is defined as the difference between the exact non-relativistic energy ($\mathcal{E}_0$) of the system and the HF limit (E_0)

$$E_{corr} = \mathcal{E}_0 - E_0 \qquad 3.75$$

Since the HF energy is an upper bound of the exact energy, the correlation energy is always negative. The limitations of the HF method regarding to this correlation energy can be divided into two different effects.

The first arises from the r_{ij}^{-1} term in the Hamiltonian operator. One electron, in the HF method, is supposed to move in an average potential created by the rest of the electrons. However, the movement of the electrons is correlated, when one electron moves the rest of them are affected. This fact constitutes the *dynamical correlation*. Post HF methods as Configuration Interaction (CI), Coupled-Custer (CC) and Møller-Plesset (MP) are focused on solving this correlation drawback of the HF method. CI, for instance, generate a list of configurations and use them in a linear combination way (see section 3.8). MP perturbation theory partitions the Hamiltonian into the Fock operator for the SCF treatment and expanding the energy as perturbation series of V.

Due to the mono configurational nature of the HF method, systems where more than one configurations are important cannot be correctly accurately described. In situation of near degeneracy effects, the HF method introduces an error known as *non dynamical correlation*. The most popular way to account this correlation is to explicitly include more than one configuration in the SCF procedure. Non dynamic correlation energy is often small in closed-shell molecules close to the equilibrium geometry, but becomes really important in distorted molecules when bonds are created or broken. It is also essential for treatment of open-shell molecules like excited states or transition metals.

Post HF methods overcome the limitations of HF theory by including one or both types of electronic correlation.

3.8 Configuration Interaction (CI)

Similarly to the HF approximation, the CI method is based on the variational principle. The configuration-interaction (CI) wave function consists of a linear combination of Slater determinants whose coefficients are variationally determined by requiring the energy to be a minimum. If the basis set was complete, CI method would provide the exact solution of the many-electron problem.

However, the use of an infinite set of determinants is not possible and CI wave function must be truncated providing an upper bound to the exact energy.

Considering the Hartree-Fock determinant formed from the N-electron lowest energy spin orbitals is $|\Psi_0\rangle = |\chi_1\chi_2 \dots \chi_a\chi_b \dots \chi_r\chi_s\rangle$ where $\chi_1\chi_2 \dots \chi_a\chi_b$ represent occupied orbitals while $\chi_r\chi_s$ are empty virtual orbitals. There is a set of possible determinants exciting from $|\Psi_0\rangle$:

$|\Psi_a^r\rangle$ are singly excited determinants, where an electron has been promoted from an occupied spin orbital *a* to one of the virtual spin orbitals *r*.

$|\Psi_{ab}^{rs}\rangle$ are douply excited determinants, where two electrons have been promoted from occupied spin orbitals *a* and *b* to virtual spin orbitals *r* and *s*.
For a system of N electrons and given an arbitrary basis set of 2K one-electron orbitals, the number of different Slater determinants we can construct is $\binom{2K}{N}$ which are named according to the number of electrons that have been moved to virtual orbitals: singly, doubly, … N-excited determinants. The full CI wave function takes the form

$$|\Phi_0\rangle = c_0|\Psi_0\rangle + \sum_{ar} c_a^r|\Psi_a^r\rangle + \sum_{\substack{a<b \\ r<s}} c_{ab}^{rs}|\Psi_{ab}^{rs}\rangle + \sum_{\substack{a<b<c \\ r<s<t}} c_{abc}^{rst}|\Psi_{abc}^{rst}\rangle + \cdots \qquad 3.76$$

Due to the fact that wave functions with different spin do not mix some of these determinants can be neglected. The remaining ones can be combined linearly leading to *configuration state functions (CSF).*

Full CI method is based on finding the corresponding energies of equation (3.76) function using the linear variational method. When the ground state is reasonably approximated to $|\Psi_0\rangle$, the c_0 coefficient will be larger than any other and $|\Phi_0\rangle$ is more conveniently written in the intermediate normalized form

$$|\Phi_0\rangle = |\Psi_0\rangle + \sum_{ct} c_c^t |\Psi_c^t\rangle + \sum_{\substack{c<d \\ t<u}} c_{cd}^{tu} |\Psi_{cd}^{tu}\rangle + \sum_{\substack{c<d<e \\ t<u<v}} c_{cde}^{tuv} |\Psi_{cde}^{tuv}\rangle + \cdots \qquad 3.77$$

Since

$$\langle\Phi_0|\Phi_0\rangle = 1 + \sum_{ar} (c_a^r)^2 + \sum_{\substack{a<b \\ r<s}} (c_{ab}^{rs})^2 + \cdots \qquad 3.78$$

$|\Phi_0\rangle$ is not normalized, but it satisfies an important property,

$$\langle\Psi_0|\Phi_0\rangle = 1 \qquad 3.79$$

The Schrödinger equation for the $|\Phi_0\rangle$ wave function can be written as

$$\mathcal{H}|\Phi_0\rangle = \mathcal{E}_0|\Phi_0\rangle \qquad 3.80$$

where $\mathcal{E}_0$ is the exact energy of the system in its ground state. Correlation energy, E_{corr} can be calculated by subtracting the HF energy (E_0) to equation (3.80)

$$(\mathcal{H} - E_0)|\Phi_0\rangle = E_{corr}|\Phi_0\rangle \qquad 3.81$$

Using the expression of $|\Phi_0\rangle$ obtained in equation (3.77) we obtain

$$\langle\Psi_0|\mathcal{H} - E_0|\Phi_0\rangle = \langle\Psi_0|\mathcal{H} - E_0\left(|\Psi_0\rangle + \sum_{ct} c_c^t|\Psi_c^t\rangle + \sum_{\substack{c<d \\ t<u}} c_{cd}^{tu}|\Psi_{cd}^{tu}\rangle + \cdots\right)\rangle \qquad 3.82$$

Applying Brillouin's theorem, which states that the matrix elements with the form $\langle\Psi_0|\mathcal{H}|\Psi_c^t\rangle$ are equal to 0, and considering that excitations which differ from $|\Psi_0\rangle$ in more than two spin orbitals do not mix, we can write E_{corr} as follows

$$E_{corr} = \sum_{\substack{a<b \\ r<s}} c_{ab}^{rs}\langle\Psi_0|\mathcal{H}|\Psi_{ab}^{rs}\rangle \qquad 3.83$$

Although E_{corr} seems to depend only on the doubly excitations coefficients, this does not mean that only doubly excitations need to be included for the exact description of the ground state, since c_{ab}^{rs} are affected by higher excitations. In fact, the coupling between singles, doubles, triples … coefficients leads to a large set of coupled equations too expensive to be solved, except for very small systems. Full CI method can be hardly ever used and it must be truncated at some excitation level. If only double excitations are considered a CID calculation is performed, however including single excitations does not increase the computational cost too much. Higher excitations are usually not included because they imply a huge number of determinants for most systems. There are cases where CID is not enough to describe de correlation energy properly and further excitations must be included which results in an increase of the computational cost.

The main drawback of truncated CI is that it is not a *size-consistent* method since it is not able to describe with the same precision molecules with different number of electrons. Size-consistency is essential to correctly describe dissociation processes. Some corrections can be considered in order to eliminate this problem, the Davidson correction is, probabily, the simplest and most popular approach. [10]
It is based on a perturbation treatment (once the E^{SD} energy has been calculated) which allows for the correction the correlation energy (DCI) so that it becomes size consistent

$$E_{corr} = E_{corr}(DCI) + \Delta E_{Davidson} \quad 3.84$$

$$\Delta E_{Davidson} = (1 - c_0^2)E_{corr}(DCI) \quad 3.85$$

where c_0 is the coefficient of the Hartree-Fock wave function in the DCI wave function. The inclusion of the correction is denoted by the suffix +Q, so the correlation energy could be expressed as

$$E_{corr+Q} = E_{corr}(DCI) + (1 - c_0^2)E_{corr}(DCI) \quad 3.86$$

$$= (2 - c_0^2)E_{corr}(DCI)$$

Further correction has been made to the Davidson's correction. For instance, Ahlrichs[11] gives an alternative derivation of the original one providing an additional insight. Writing the CID correlation energy as an expectation value, the original Davidson correction is

$$\Delta E_{Davidson} = E_{corr}(DCI)\ (\langle \Psi_{DCI}|\Psi_{DCI}\rangle - 1) \quad 3.87$$

and by inserting the correlation energy,

$$E_{corr+Q} = \langle \Psi_{DCI}|\mathcal{H} - E_0|\Psi_{DCI}\rangle \quad 3.88$$

what represents the energy functional $\langle\Psi_0|\mathcal{H}-E_0|\Psi_0\rangle$ evaluated with the DCI wave function.

Both the original and the normalized Davidson's correction behave inappropriately in the limit of small number of electrons, since they give size-extensivity correction for a two-electron system where there is none one. Pople and co-workers derived another corrections taking into account that this effect may be vanished.

Those corrections can also be extended to the multireference approach of the CI method, but this explanation can be found within following sections.

3.9 Multiconfigurational Approaches

The aim of this section is to describe how to determine molecular orbitals in cases where the wave function is not well described by the Hartree Fock approximations. Several examples can be described to illustrate the break down of the HF model. Maybe the simplest one is the dissociation of the single bond of the hydrogen molecule. The molecular orbitals for this molecule can be written as

$$\psi_i = N_i(\phi_A \pm \phi_B) \qquad 3.89$$

where ϕ_A and ϕ_B are two functions localized at the nuclei A and B and N is a normalization constant. The ground state wave functions for the H2 equilibrium geometry is dominated by the configuration $(\psi_1)^2$, where the molecular orbital ψ_1 is a bonding orbital doubly occupied built from two atomic orbitals ϕ_{1A} and ϕ_{1B}. The main contribution to these orbitals is from the 1s orbital from the hydrogen. Then,

$$\psi_1 = N_1(1s_A + 1s_B) \qquad 3.90$$

This molecular orbital is doubly occupied in the RHF model leading to reasonable good description of H2 in the regions close to the equilibrium geometry.

$$\Psi_1 = \psi_1(r_1)\psi_1(r_2)\Theta_{2,0} \qquad 3.91$$

being the $\Theta_{2,0}$ the singlet (S=0) spin function for two electrons. If this function is expanded into the atomic orbitals $1s_A$ and $1s_B$:

$$\Psi_1 = N_1^2\,[1s_A(r_1)1s_A(r_2) + 1s_A(r_1)1s_B(r_2) + 1s_B(r_1)1s_A(r_2) + 1s_B(r_1)1s_B(r_2)] \qquad 3.92$$

This wave function contains terms where both electrons are located in the same atom, which is unphysical at large bond distances since corresponds with a dissociating

situation H^+ and H^-. Consequently, RHF methods cannot be used to describe dissociating processes resulting in open shell products.

The easiest solution to this problem is to rewrite the above equation with coefficients in front of the different terms:

$$\Psi_1 = C_{ION}\Psi_{ION} + C_{COV}\Psi_{COV} \qquad 3.93$$

where the ionic and covalent terms are

$$\Psi_{ION} = N_{ION}[1s_A(r_1)1s_A(r_2) + 1s_B(r_1)1s_B(r_2)]\Theta_{2,0} \qquad 3.94$$

$$\Psi_{COV} = N_{COV}[1s_A(r_1)1s_B(r_2) + 1s_B(r_1)1s_A(r_2)]\Theta_{2,0} \qquad 3.95$$

The coefficients C_{ION} and C_{COV} can be modified to obtain an appropriate behaviour of the wave function at the separated limit ($C_{ION} = 0$) and at the equilibrium ($C_{ION} \approx C_{COV}$).

Further from bond breakings, the multiconfigurational treatment of the wave function becomes also essential in situations where different electronic configurations have similar energies. This degeneracy effects are very usual in the description of the excited states of molecular systems. When those configurations present the same symmetry, a small interaction between them can lead to strong mixing. Typical cases are unsaturated planar molecules, as for instance, benzene. The treatment of the π orbitals result in electronic configurations that are generated in pairs with equal weights.

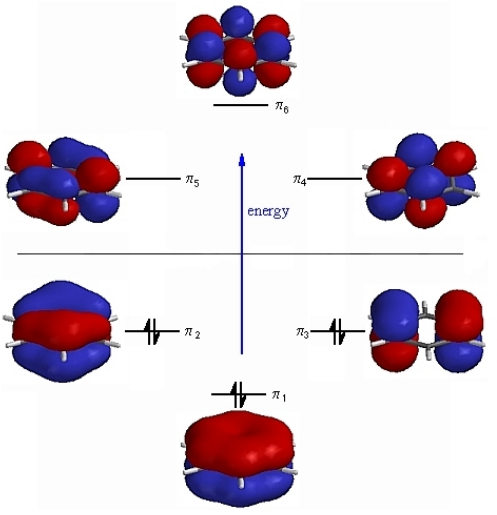

Figure 3.1 Benzene molecular orbitals.

Other important cases where degeneracy occurs are compounds containing transition metal atoms. Usually, these molecules present weak bonds with an important occupation of the antibonding orbital. This effect joined to the fat that the electronic configuration of these metals are often dominated by multiplets with very similar energies leads to a strong multiconfigurational character of this molecules.

During this section, the tools needed to treat problems, where several electronic configurations are close in energy and as a consequence where a single configuration description is not valid any more, are described. Not only the consideration of several configurations is necessary but also to provide an optimized set of molecular orbitals.

Caution must be taken since if only a CI calculation is performed with a set of predetermined orbitals those orbitals could not be appropriated to describe the chemical problem. If the previous case of H_2 molecule dissociation is analysed, it can be seen that the molecular orbitals from an SCF calculation will not lead to hydrogen atomic orbitals at large distances. Thereby, it is also necessary to optimize the orbital using a correct wave function, since multiconfigurational effects also tend to modify the involved molecular orbitals.
The ***Multi-Configuration Self-Consistent Field*** (MCSCF) method represents a flexible solution to handle chemical problems (bond breaking, quasi-degenerate states, surface crossings…) where more than one slater determinant is important. The MCSCF wave function is a truncated CI expansion

$$|\Psi_{\mathrm{MCSCF}}\rangle = \sum_{\mathrm{I}} \mathrm{c_I}\,|\Psi_{\mathrm{I}}\rangle \qquad 3.96$$

where Ψ_{I} represent the slater determinants built from ψ_{i} and $\overline{\psi}_i$, which are orthonormal orbitals occupied by α and β electron respectively and the index (I) runs over the different configurations

$$|\Psi_{\mathrm{I}}\rangle = |\psi_{\mathrm{A}}\overline{\psi}_A\psi_{\mathrm{B}}\overline{\psi}_{\mathrm{B}}\ldots\rangle \qquad 3.97$$

Those orbitals can be in turn expanded in a basis of atomic orbitals as

$$\psi_{\mathrm{i}} = \sum_{\mu} \mathrm{c}_{\mu\mathrm{i}}\phi_{\mathrm{i}} \qquad i = A, B \qquad 3.98$$

Aiming to further detailed the MCSCF method most formulations are based on second quantization formalism. During the derivation of the MCSCF equations derivation it will be assumed that the Hamiltonian does not contain spin-dependent terms, being possible to formulate the theory in terms of spin summed excitation operators $\hat{E}_{ij}$

$$\hat{E}_{ij} = \hat{a}^{\dagger}_{i\alpha}\hat{a}_{j\alpha} + \hat{a}^{\dagger}_{i\beta}\hat{a}_{j\beta} \qquad 3.99$$

being $\hat{a}^{\dagger}_{i}$ the creation operator which adds an electron in the *i* orbital and $\hat{a}_i$ the annihilation operator which removes an electron from the *i* orbital. When $\hat{E}_{ij}$ acts on a ket where *j* is unoccupied the result is zero and the same when *i* is doubly occupied, if *i* differes form *j*. However, if the i=j the result is two times the ket. In general,

$$\hat{E}^{\dagger}_{ii}\,|m\rangle = n_i|m\rangle \qquad 3.100$$

where n_i is the occupation number (0,1 or 2) of the molecular orbital.

A one-electron operator using this nomenclature is written as:

$$\hat{F} = \sum_{i,i} F_{ij}\,\hat{a}^{\dagger}_{i} \qquad 3.101$$

where F_{ij} is the matrix element of this operator in the spin-orbital basis and in the space and spin coordinates, x:

$$F_{ij} = \int \chi^{*}_{i}(x)\hat{F}(x)\chi_j(x)dx \qquad 3.102$$

For a spin independent operator and using equation 3.99,

$$\hat{F} = \sum_{i,i} F_{ij}\,\hat{E}_{ij} \qquad 3.103$$

where the sum is over the molecular orbitals and the integrals are defined in the molecular basis set. A matrix element of this operator between two Slater determinants, |m> and |n> is defined

$$\langle m|\hat{F}|n\rangle = \sum_{i,i} F_{ij}\,\langle m|\hat{E}_{ij}|n\rangle \qquad 3.104$$

where $\langle m|\hat{E}_{ij}|n\rangle = D^{nm}_{ij}$ are the one electron coupling coefficients, with values -1, 0, 1 or 2 (if i=j), so the diagonal elements are equal to the occupation number of orbital *i* if n=m. For a given wave function, $|\Psi\rangle = \sum_m C_m|m\rangle$, these couplings are related with the first order reduced density matrix

$$D_{ij} = \langle\Psi|\hat{E}_{ij}|\Psi\rangle = \sum_{m,n} C^{*}_{m}C_n\,D^{nm}_{ij} \qquad 3.105$$

Next step is to find the expression for the two-electron operators starting from a general one

$$\hat{G} = \frac{1}{2}\sum_{i,j,k,l} g_{ijkl}\,\hat{a}_i^{\dagger}\hat{a}_k^{\dagger}\hat{a}_l\hat{a}_j \qquad 3.106$$

where

$$g_{ijkl} = \int \chi_i^*(x_1)\chi_k^*(x_2)\hat{G}(x_1,x_2)\chi_j(x_1)\chi_l(x_2) \qquad 3.107$$

Within the present representation only the inter-electronic repulsion, $1/r_{12}$, presents this form and since it is spin independent, the previous expression can be sum over the spin variables

$$g_{ijkl} = \int \phi_i^*(r_1)\,\phi_j(r_1)\,1/r_{12} \int \phi_k^*(r_2)\,\phi_l(r_2)dV_1dV_2 \qquad 3.108$$

Using equation 3.99 and the anti-commutator rules:

$$\hat{G} = \frac{1}{2}\sum_{i,j,k,l} g_{ijkl}\,(\hat{E}_{ij}\hat{E}_{kl} - \delta_{jk}\hat{E}_{il}) \qquad 3.109$$

As for the one-electron operator, the matrix elements between Slater determinants are defined as

$$\langle m|\hat{G}|n\rangle = \sum_{i,j,k,l} g_{ijkl}\,P_{ijkl}^{mn} \qquad 3.110$$

where the two electron coupling coefficients are,

$$P_{ijkl}^{mn} = \frac{1}{2}\langle m|\hat{E}_{ij}\hat{E}_{kl} - \delta_{jk}\hat{E}_{il}|n\rangle \qquad 3.111$$

Then the second order reduced density matrix is

$$P_{ijkl}^{mn} = \sum_{m,n} C_m^* C_n\,P_{ijkl}^{nm} \qquad 3.112$$

Using all the above definitions, the Hamiltonian can be constructed in base of the excitation operators, $\hat{E}_{ij}$

$$\hat{H} = \sum_{ij} h_{ij}\hat{E}_{ij} + \frac{1}{2}\sum_{i,j,k,l} g_{ijkl}\,(\hat{E}_{ij}\hat{E}_{kl} - \delta_{jk}\hat{E}_{il}) \qquad 3.113$$

with h_{ij} being the one-electron integrals, including the kinetic energy and the electron-nuclear terms and the g_{ijkl} the two electron repulsion integrals. These summation is extended all over the molecular orbital basis, and for a normalized wave function, the MCSCF energy can be obtained as the expectation value of the Hamiltonian

$$E = \langle \Psi | \hat{H} | \Psi \rangle = \sum_{ij} h_{ij} D_{ij} + \sum_{ijkl} g_{ijkl} P_{ijkl} \qquad 3.114$$

The information about the molecular orbital coefficients are determined by the one and two electron integrals, while the density matrix D and P contain the information about the CI coefficients.

The iterative optimization of both the orbitals and CI coefficients is not easy to converge so the configurations´ expansion must be truncated selecting a suitable configuration space. Two kinds of techniques can be used to help the MCSCF iterative procedure to converge. First-order methods are based on the calculation of the energy and its first derivative respect to the vibrational parameters while second-order methods also calculated the expansion of the energy up to second order. Although higher order methods can be achieved by including more terms to the energy expansion, those have been demonstrated to slightly improve the convergence, so that the most extended methods are the second order ones, and within them the **Newton-Raphson Method**. The method selection should be done in terms of the time needed for each convergence iteration and the convergence capability. Since Newton-Raphson seems to give the best compromise between them it is one of the most extended selected methods nowadays to achieve MCSCF convergence.

The Newton-Raphson procedure defines the energy as a function of a set of parameters, p_i, which are arrange as a column vector $\boldsymbol{p}$, $E = E(\boldsymbol{p})$. If a Taylor expansion around a point (p_0) is performed,

$$E(\boldsymbol{p}) = E(\boldsymbol{0}) + \sum_i \left(\frac{\partial E}{\partial p_i}\right)_0 p_i + \frac{1}{2}\sum_{ij} p_i \left(\frac{\partial^2 E}{\partial p_i \partial p_j}\right)_0 p_j + \cdots \qquad 3.115$$

or using matrix notation:

$$E(\boldsymbol{p}) = E(\boldsymbol{0}) + \boldsymbol{g}^\dagger \boldsymbol{p} + \frac{1}{2}\boldsymbol{p}^\dagger \boldsymbol{H}\, \boldsymbol{p} + \cdots \qquad 3.116$$

where **g** is the energy gradient vector:

$$\boldsymbol{g} = \left(\frac{\partial E}{\partial p_i}\right)_0 \qquad 3.117$$

and **H** is the Hessian matrix:

$$\boldsymbol{H} = \left(\frac{\partial^2 E}{\partial p_i \partial p_j}\right)_0 \qquad 3.118$$

The stationary points of the energy surface are obtained by imposing the first derivative of the energy to be equal to zero $\left({}^{\partial E}/_{\partial p_i}\right) = 0$, then starting form eq 3.116 and setting this derivative to be zero it can be obtained that:

$$\boldsymbol{g} + \boldsymbol{Hp} = 0 \quad or \quad \boldsymbol{p} = -\boldsymbol{H}^{-1}\boldsymbol{g} \qquad 3.119$$

Then the Newton-Raphson iterations are obtained by solving this equation, defining the new point as the new zero point, recalculating $\boldsymbol{g}$ and $\boldsymbol{H}$ and repeating this iterative process.

Applying the gradient vector and the Hessian matrix to the MCSCF energy expression 3.114 the equations for the variation of the CI coefficients and for orbital rotations can be obtained. First, it is necessary to introduce the unitary operator $e^{\hat{S}}$ and the orbital rotations operator $e^{\hat{T}}$. The unitary operator is defined by

$$\hat{S} = \sum_{K\neq 0} S_{K0}(|K\rangle\langle 0| - |0\rangle\langle K|) \qquad 3.120$$

where $|0\rangle$ is the expansion of the MCSCF wave function as a function of the CI coefficients C_{m0}

$$|0\rangle = \sum_m |m\rangle C_{m0} \qquad 3.121$$

since the variation of the CI coefficients need to be normalized, a variational space , $|K\rangle$, which is orthogonal respect to the state $|0\rangle$ and is expanded in the same basis set

$$|K\rangle = \sum_m |m\rangle C_{mK} \qquad 3.122$$

On the other hand the orbital rotation operator is

$$\hat{T} = \sum_{i>j} T_{ij}\left(\hat{E}_{ij} - \hat{E}_{ji}\right) \qquad 3.123$$

where T_{ij} describes the unitary rotation if the molecular orbitals through $\boldsymbol{U} = e^{-\boldsymbol{T}}$, being U the unitary matrix.

If those operators are applied now to the MCSCF energy expression, a variation of an MCSCF state can be written as

$$|0'\rangle = e^{\hat{T}}\, e^{\hat{S}}\, |0\rangle \qquad 3.124$$

The energy of the new state is a function of the parameters in the above operators

$$E(\boldsymbol{T},\boldsymbol{S}) = \langle 0 \big| e^{-\hat{S}}\, e^{-\hat{T}}\, \hat{H} e^{\hat{T}}\, e^{\hat{S}} \big| 0 \rangle \qquad 3.125$$

and can be calculated expanding the operators to its second order

$$E(\boldsymbol{T},\boldsymbol{S}) = \langle 0|\, \hat{H} + \left[\hat{H},\hat{T}\right] + \left[\hat{H},\hat{S}\right] \qquad 3.126$$

$$+\frac{1}{2}\left[\left[\hat{H},\hat{T}\right],\hat{T}\right] + \frac{1}{2}\left[\left[\hat{H},\hat{S}\right],\hat{S}\right]$$

$$+\left[\left[\hat{H},\hat{T}\right],\hat{S}\right] + \cdots |0\rangle$$

The first term of this equation correspond to the zeroth order energy E(0,0) . The second and third terms are the first derivative with respect to the rotation T and S parameters, which are:

$$\langle 0 \big| \left[\hat{H},\hat{T}\right] \big| 0 \rangle = \sum_{i>j} T_{ij} \langle 0 \big| \hat{E}_{ij} - \hat{E}_{ji} \big| 0 \rangle \qquad 3.127$$

with its derivative being

$$g^0_{ij} = \langle 0 \big| \hat{E}_{ij} - \hat{E}_{ji} \big| 0 \rangle = \langle 0 \big| \hat{E}^{-}_{ij} \big| 0 \rangle \qquad 3.128$$

and

$$\langle 0 \big| \left[\hat{H},\hat{S}\right] \big| 0 \rangle = \sum_{K\neq 0} S_{K0} \left(\langle 0 \big| \hat{H} \big| K \rangle + \langle K \big| \hat{H} \big| 0 \rangle \right) \qquad 3.129$$

with its derivative being

$$g^c_{ij} = 2 \langle K \big| \hat{H} \big| 0 \rangle \qquad 3.130$$

The forth, fifth and sixth terms in equation 3.126 correspond to the second derivatives and for an easier analysis the Hessian matrix is divided into three parts, the orbital-orbital (oo), the configuration-configuration part (cc) and the CI coupling with the orbitals (co) one.

The $\left[\left[\hat{H},\hat{S}\right],\hat{S}\right]$ term is associated with the Hcc part and using eq 3.130 it can be obtained:

$$H_{KL}^{cc} = 2\left(\langle K|\hat{H}|L\rangle - \delta_{KL}\langle 0|\hat{H}|0\rangle\right) \qquad 3.131$$

The configuration-configuration part is related with the term $\left[\left[\hat{H},\hat{T}\right],\hat{T}\right]$ and using equation 3.128 can be defined as

$$H_{ij,kl}^{oo} = \langle 0|\hat{E}_{ij}^{-}\hat{E}_{kl}^{-}\hat{H}|0\rangle + \langle 0|\hat{H}\hat{E}_{ij}^{-}\hat{E}_{kl}^{-}|0\rangle + 2\langle 0|\hat{E}_{ij}^{-}\hat{H}\hat{E}_{kl}^{-}|0\rangle \qquad 3.132$$

and the last part corresponding with the term $\left[\left[\hat{H},\hat{T}\right],\hat{S}\right]$:

$$H_{K,ij}^{co} = H_{ij,K}^{oc} = 2\langle K|\hat{H},\hat{E}_{ij}^{-}|0\rangle \qquad 3.133$$

Those equations define the Hessian and the gradient in terms of the excitation operators. They can be evaluated by including the Hamiltonian into them and using one and two electron integrals and first and second order reduced density matrices, $\boldsymbol{P}^{K0}$ and $\boldsymbol{D}^{K0}$. These Newton-Raphson equations can be also written in matrix form:

$$\begin{pmatrix} \boldsymbol{a} & \boldsymbol{b} \\ \boldsymbol{b}^{\dagger} & \boldsymbol{c} \end{pmatrix}\begin{pmatrix} \boldsymbol{S} \\ \boldsymbol{T} \end{pmatrix} = -\begin{pmatrix} \boldsymbol{v} \\ \boldsymbol{w} \end{pmatrix} \qquad 3.134$$

where

$$\boldsymbol{a} = \frac{1}{2}\boldsymbol{H}^{\boldsymbol{cc}} \quad \boldsymbol{b} = \frac{1}{2}\boldsymbol{H}^{\boldsymbol{co}} \quad \boldsymbol{c} = \frac{1}{2}\boldsymbol{H}^{\boldsymbol{oo}} \quad \boldsymbol{v} = \frac{1}{2}\boldsymbol{g}^{\boldsymbol{c}} \quad \boldsymbol{w} = \frac{1}{2}\boldsymbol{g}^{\boldsymbol{o}} \qquad 3.135$$

The computational procedure for obtaining the rotation parameters $\boldsymbol{S}$ and $\boldsymbol{T}$ is not trivial and the above expression can be rewritten using several transformation operations. But as a summary the MCSCF procedure is the following, the parameter set $\boldsymbol{T}$ is obtained, as a solution of the above equations, and from them the orbital rotations can be determined. Then the CI coefficients are then obtained through the unitary matrix $e^{\boldsymbol{S}}$. Although the fully Newton-Raphson method described as in 3.134 presents satisfactory global convergence is however computationally complex becoming very time consuming for large orbital spaces. The direct solution of this equation is called as one-step model since both $\boldsymbol{S}$ and $\boldsymbol{T}$ are updated at the same time, however a two-step model can be rewritten from it where $\boldsymbol{S}$ is solved first. From the first row in the equation 3.134, it can be obtained

$$\boldsymbol{aS} + \boldsymbol{bT} = -\boldsymbol{v} \tag{3.136}$$

then

$$\boldsymbol{S} = -\boldsymbol{a}^{-1}\boldsymbol{v} - \boldsymbol{a}^{-1}\boldsymbol{bT} \tag{3.137}$$

If now this formula is inserted into the equation coming from the second row of 3.134

$$\boldsymbol{b}^{\dagger}\boldsymbol{S} + \boldsymbol{cT} = -\boldsymbol{w} \tag{3.138}$$

substituting $\boldsymbol{S}$

$$-\boldsymbol{b}^{\dagger}\boldsymbol{a}^{-1}\boldsymbol{v} - \boldsymbol{b}^{\dagger}\boldsymbol{a}^{-1}\boldsymbol{bT} + \boldsymbol{cT} = -\boldsymbol{w} \tag{3.139}$$

$$(\boldsymbol{c} - \boldsymbol{b}^{\dagger}\boldsymbol{a}^{-1}\boldsymbol{b})\boldsymbol{T} = -\boldsymbol{w} + -\boldsymbol{b}^{\dagger}\boldsymbol{a}^{-1}\boldsymbol{v} \tag{3.140}$$

However, this equation is not very practical since it involves the inverse of the CI part of the Hessian. But working in a configurational basis $(|0\rangle, |K\rangle)$ where $\boldsymbol{a}$ matrix is then diagonal with matrix elements $a_{KK} = (E_k - E_0)$ and the gradient vector $\boldsymbol{v}$ with lements $\langle 0|\widehat{H}|K\rangle$ is zero, the previous equation can be written as

$$\sum_{r>s}\left(c_{pq,rs} + \sum_{K}\frac{b_{pq,K}b_{K,rs}}{E_0 - E_K}\right)T_{rs} = -w_{pq} \tag{3.141}$$

This equation represent the basis of the two-step Newton-Raphson algorithm, but it is nor very practical since the eigenvalues E_K cannot be calculated for large multiconfigurational expansions. An approximation is to neglect the coupling between the CI rotations and the orbitals one since they are nor large expect for soecial cases (for instance in excited states). Then the final equations for these methods are

$$(\boldsymbol{H} - E_0\boldsymbol{1})\boldsymbol{C} = 0 \;\; and \;\; \boldsymbol{cT} = -\boldsymbol{w} \tag{3.142}$$

Although this method is nor quadratically convergent is used since it is much simpler than the general approach being possible to be solved for large MC expansions with efficient CI procedures, as for the CASSCF type wave functions (see below). Equation 3.142 can be used to obtain the so called Augmented Hessian Method (AM) secular problem, which cane be solved iteratively or it can be programmed to be a direct procedure, being the latest more independent in the size of the molecular orbital basis set.

$$\begin{pmatrix} 0 & \boldsymbol{w}^{\dagger} \\ \boldsymbol{w} & \boldsymbol{c} \end{pmatrix}\begin{pmatrix} 1 \\ \boldsymbol{T} \end{pmatrix} = -\epsilon_{AM}\begin{pmatrix} 1 \\ \boldsymbol{T} \end{pmatrix} \tag{3.143}$$

Other strategies have been investigated trying to simplify the second order Newton-Raphson approach. For instance the **Super-CI** method annihilates the single excited

configurations (Brillouin states) in an iterative procedure to achieve MCSCF convergence. Defining these Single excited or Brillouin states according to

$$\left|pq\right\rangle = \hat{E}_{pq}^{-}|0\rangle \qquad 3.144$$

The super-CI wave function is defined as a combination of these states

$$|SCI\rangle = |0\rangle + \sum_{p>q} t_{pq}|pq\rangle \qquad 3.145$$

The super-CI method solves the secular (equation 3.143) problem using t_{pq} as the exponential factors for orbital rotations. But it can also construct the first order reduced density matrix, diagonalize it and then use natural orbitals as new trail ones $|0\rangle$. t_{pq} are expected to decrease within each iteration and at convergence they will vanish, being equivalent to accomplish the condition $\langle 0|\hat{H}|pq\rangle = 0$.

The matrix elements of the Hamiltonian in the super-CI formalism (using equation 3.143) have the form

$$H_{0,pq} = \langle 0|\hat{H}|pq\rangle = \langle 0|\hat{H}\hat{E}_{pq}^{-}|0\rangle = w_{pq} \qquad 3.146$$

$$H_{pq,rs} = \langle pq|\hat{H}|rs\rangle = \langle 0|\hat{E}_{pq}^{-}\hat{H}\hat{E}_{rs}^{-}|0\rangle = d_{pq,rs} \qquad 3.147$$

where w_{pq} is a component of the gradient vector $\boldsymbol{w}$. It might be considered that the single excited states

$$S_{pq,rs} = \langle 0|\hat{E}_{pq}^{-}\hat{E}_{rs}^{-}|0\rangle \neq \delta_{pq,rs} \qquad 3.148$$

are not normalized ($S_{pq,pq} \neq 1$) but they are orthogonal to the reference state, $\langle 0|\hat{E}_{pq}^{-}|0\rangle = 0$.

Using the above equations 3.146, 3.147 and 3.148 the AM secular equation can be rewritten for the super-CI method

$$\begin{pmatrix} 0 & \boldsymbol{w}^{\dagger} \\ \boldsymbol{w} & \boldsymbol{d} - E_0\boldsymbol{S} \end{pmatrix}\begin{pmatrix} 1 \\ \boldsymbol{t} \end{pmatrix} = -(E_{SCI} - E_0)\begin{pmatrix} 1 & 0 \\ 0 & \boldsymbol{S} \end{pmatrix}\begin{pmatrix} 1 \\ \boldsymbol{t} \end{pmatrix} \qquad 3.149$$

being the super–CI energy

$$E_{SCI} = \frac{\langle SCI|\hat{H}|SCI\rangle}{\langle SCI||SCI\rangle} \qquad 3.150$$

The super-CI method can be considered as an approximation of the AM method. Both the AM and the super-CI methods present better convergence and always converge to a minimum, while the original Newton-Raphson is more difficult to converge and can converge to a saddle point or a maximum. Computationally, the super-CI method is more complicated since it works with the matrix **d,** which deals with the overlaps involving double excitations, instead of the **c** hessian matrix used by AM methods. This matrix involves high order terms of the reduced density matrix, which makes the super-CI to be not better than the original Newton-Raphson method.

New updated super-CI methods try to simplify the **d** matrix and also introduce the CI coupling terms into the Hessian leading to good approached to the full super-CI Hamiltonian. These methods are easier to implement from a computational point of view and also generally improves the MCSCF convergence. Both the original super-CI method and the newest updated ones have been used by the MOLCAS software in order to achieve CASSCF convergence.

Most commercial available programs are able to perform both closed shell SCF and/or UHF calculations for molecules and the user only need to provide its structural information and the desired basis set. Although they can be used as black-box methods without much information about the underlying theory, caution must be taken about the appropriate size for the basis set and also for the importance of correlation corrections for a relative study case. What is the situation for the MCSCF methods? Performing MCSCF is not so easy and the user needs to present some knowledge about the molecule under study and its electronic structure. This is required since for MCSCF methods the orbitals are not determined through the optimization process, as for the SCF cases, and the user needs to decide about the mots important electronic configurations to include in the MCSCF calculations. The most common procedure for this selection is to combine chemical intuition based on the studied case and the performance of several attempts to find the convenient orbitals to include into the MCSCF calculation.

Complete Active Space Self-Consistent Field (CASSCF)

The most widely used MCSCF method is the Complete Active Space Self-Consistent Field (CASSCF) approach. This method was first introduced by Roos[12] and coworkers and its based on the idea of obtaining a multiconfigurational wave function where both the CI coefficients and the molecular orbitals are optimized. The unitary and the orbital rotation operator are used to obtain the new state as well as its energy, recall equations from 3.120 to 3.125. Then by imposing that the first derivative of the energy

is equal to zero, a linear set of equations in terms of $\boldsymbol{S}$ and $\boldsymbol{T}$ are obtained. Those equations are optimized using any of the above mentioned optimization procedure in order to obtain the stationary value of the energy.

CASSCF method is based on dividing the orbitals into subsets depending on how they are use to build the wave function: primary and secondary orbitals:

- ✓ Primary space is in turn partitioned in active and inactive orbitals. Active orbitals can have any occupation between 2 and 0 electrons, while inactive orbitals are always doubly occupied and can be considered as core orbitals.
- ✓ Secondary, also called external or virtual, orbitals remain unoccupied.

A common notation is CASSCF(N,n), where N electrons are distributed in n orbitals. The CASSCF wave function is built with all the possible configurations involving the active electrons and the active orbitals. In other words, a full CI is performed with the active orbitals and all the resulting determinants are included in a MCSCF calculation, recovering non-dynamical correlation. Inactive orbitals are also optimized but within the RHF approach. Thus, the inactive orbitals have occupation numbers exactly equal to two, while the occupation numbers of the active orbitals varies between zero and two. The selection of the active and inactive orbitals totally condition the wave function, and they must be selected taking into account that the inactive orbitals must not be expected to contribute to correlation effects. One could think to perform a CASSCF calculation where all the orbitals are considered as active, however one of the main drawback of this method is the rapidly increase of the CI expansion size,N_{CAS} , as a function of the selected active orbitals. This can be estimated using the Weyl formula for n active orbitals, N electrons and total spin S

$$N_{CAS} = \frac{2S+1}{n+1}\binom{n+1}{N/2-S}\binom{n+1}{N/2+S+1} \qquad 3.151$$

Due to the increase of N_{CAS} as a function of n, it is strictly necessary to limit the number of active orbitals to around 16 orbitals. The choice of the most adequate active space is an extremely important but sometimes very difficult task from which depend the properties of the CASSF wave function. When such large active spaces lead to an extremely large number of CSFs or more active orbitals are needed in order to properly describe the chemical process some solutions can be considered.

One strategy is for instance to impose constrains on the CSF space, especially when it does not lead to degradation of the resulting wave function. For instance, an active space of 18 electrons within six π plus six σ orbitals for the N_2O_4 molecule gives 7910 CFs, while the constrained calculation where 10 electrons were imposed to occupy the σ orbitals and the other 8 electrons to be distributed between the π ones leads to 976

terms. This deletion of specific configuration is expected to arise small loss of accuracy. Another recent extension of the CASSCF method is to divide the active space in several subactive spaces and restrict the number of electrons in each of them. In the Restricted Active space (RASSCF) method the active orbitals (or RAS2 space) is divided into three spaces, the RAS1, RAS2 and RAS3. The RAS2 is still a space where a full CI calculation is performed allowing all the possible occupations as for the CASSCF case. The RAS1 space is formed by doubly occupied orbitals where a maximum number of holes (selected by the user) can be created. Finally, the RAS3 space contains unoccupied orbitals except for a number of electrons allowed to in this subspace. The RASSCF combines features of the CAS wave functions and more advanced CI ones, being able to recover some dynamical correlation (which is not present for the CASSCF method) giving more accurate treatments. However, RASSCF in no longer complete in the active orbital space, being necessary to introduce orbital rotation between the three spaces, which makes RASSCF method very difficult to achieve convergence in mots cases. The orbital convergence is performed using super-CI method and a quasi Newton updated can also be used to improve convergence.

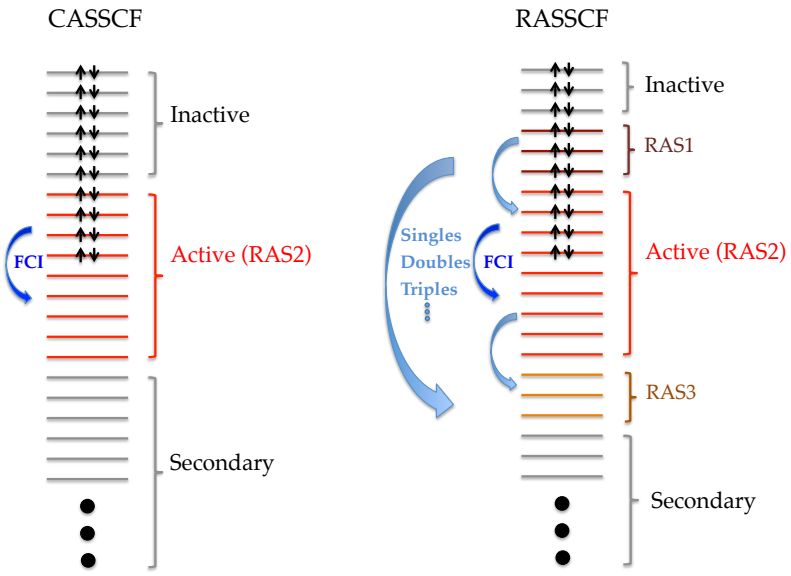

Figure 3.2. CASSCF and RASSCF schemes with the corresponding different spaces, with arrows illustrating the excitation possibilities within them. Dark blue arrows represent Full Configuration Iteration procedure within the RAS2 space, while light blue arrows represent single, double, triple .. etc excitations, within the RAS1, RAS2 and RAS3 spaces.

Active Space Selection

Although there is no general rule, which can ensure an appropriate selection, some guidelines can be followed.

- ✓ If an occupied orbital (e.g. π orbital) correlates with a virtual orbital (e.g. π* orbital), both should be included into the active space.
- ✓ Orbital energies can be another criteria to select orbitals. Occupied orbitals with the highest energy and virtual orbitals with the lowest energy must take part into the active space. This is a consequence of the second-order energy correction, the smaller the orbital energy difference is, the larger is its contribution to the correlation energy.
- ✓ The choice of the orbitals can also be made according to their occupations. In this respect natural orbitals, which are the orbitals that diagonalize the density matrix are very useful. The eigenvalues of the natural orbitals are the occupation numbers. Orbitals with zero or two occupation numbers should not be considered as part of the active space. The most important orbitals to include are those with occupation number between 1.98 and 0.2. MP2 or CISD calculation can be carried out to check orbital occupation numbers before the MCSCF calculation.
- ✓ Finally, orbitals that are essential to describe the chemical problem cannot be excluded from the active space.

Since they are not general, these rules can fail. Each system and its reactivity must be carefully studied before selecting the active space.

CASSCF calculations have been performed traditionally using a common set of orbitals for all the calculated states. This approach is known to solve two main problems, first, using common orbitals for all the states, these states are orthogonal between them, and second, the transition properties calculations are enormously simplified by this method.

In a **state average** calculation a functional of the energy is defined as an average of the different states energy.

$$E_{average} = \sum_{I} \omega_I E_I \qquad 3.152$$

where ω_I is the relative weight of each state. If equation 3.114 is inserted into the above formula replacing E, the result is the same except for the single state density matrices that are averaged matrices now. The optimization formalism is the same described above but taking into account that now more than one CI vector need to be optimized, obtaining M CI wave functions. The obtained averaged orbitals are usually a good set of starting orbitals. One can try to use these orbitals for a new

singlet state calculation where only the orbitals for the desired state are optimized. However, usually the position of this state can be altered respect to the state average calculation, a **root flipping** has occurred. This a very typical problem in ingle state calculations which leads to lots of convergence problems, since for instance the root one is asking to be optimized (third root) is now one state below in energy (second root). A possible solution is to try to perform a state average calculation between the second and the third root (for this example) assigning larger weights to the desired state. However, this procedure can be dangerous and the best option to avoid root flipping problems is to perform a state average calculation with equal weights for all the asked roots.

As said before using state average methodology implies a simplification in the calculation of the transition properties between state, which is one of the main aims on photochemical studies (see Chapter 2). If the formalism applied before when describing the MCSCF procedure is used, a one electron operator describing the transition matrix elements is obtained by

$$\langle i|\hat{A}|j\rangle = \sum_{pq} D_{pq}^{ij} A_{pq} \qquad 3.153$$

representing the sum of the matrix elements A_{pq} over all pairs of occupied molecular orbitals for two electronic states i and j. The transition density matrix elements are obtained

$$D_{pq}^{ij} = \langle i|\hat{E}_{pq}|j\rangle \qquad 3.154$$

These transition matrices can be computed from the CI coefficients of the two involved states and the CI-coupling coefficients. For the two electron operators can be obtained in an equivalent way but using second order transition density matrix. This simple formalism can be used only when the two electronic states are given in terms of common orthonormal molecular orbital basis. When this is not the case, and different set of orbitals defines the electronic states the matrix must be applied between Slater determinants.

Although MCSCF should be considered instead of HF method for cases where the wave function is composed by more than one determinant is, as an extension of HF method, the problem of dynamic correlation remain still untreated. Several attempts have been formulated in order to include this correlation and achieve more accurate results.

Multi-Reference CI

This approach expand the wave function as an expansion in all singly and doubly excited configurations with respect to chosen configurations:

$$\Psi = \sum_{I} (C_I \Phi_I + \sum_{i,a} C_{I\,ia}\, \Phi_{I\,ia} \sum_{i,a,j,b} C_{I\,ia\,jb}\, \Phi_{I\,ia\,jb}) \qquad 3.155$$

Where I indicates a set of reference configurations Φ_I and the other terms contains the configurations where one or two occupied orbitals i,j are replaced by one or two occupied or virtual orbitals a,b. This method gives quite accurate results for small molecules, presenting a reasonable number of reference functions and when using no very large basis set. However, nowadays it is limited to this kind of molecules, being very computing demanding for large systems.

Complete Active Space and Second order Perturbation Theory (CASPT2)[13]

Other alternatives, based on second order perturbation theory (CASPT2) have been shown to give also quite accurate results using a given CASSCF reference function and adding the remaining correlation effects using this perturbation theory. This approach has been widely used for lots of applications, especially in photochemistry.

Second order perturbation theory assume that the Hamiltonian can be divided into a zeroth order reference Hamltonian $\hat{H}^0$ and a small perturbation $\hat{H}'$ which strength is governed by the λ parameter

$$\hat{H} = \hat{H}_0 + \lambda \hat{H}_1 \qquad 3.156$$

The energy and the wave function can also be expanded as a Taylor series in powers of the perturbation parameter λ

$$\Psi = \Psi_0 + \lambda \Psi_1 + \lambda^2 \Psi_2 \qquad 3.157$$

$$E = E_0 + \lambda E_1 + \lambda^2 E_2 \qquad 3.158$$

If those expressions are inserted into the Schrödinger equation

$$\begin{aligned} (\hat{H}_0 + \lambda \hat{H}_1)(\Psi_0 + \lambda \Psi_1 + \lambda^2 \Psi_2) &= \\ = (E_0 + \lambda E_1 + \lambda^2 E_2)(\Psi_0 + \lambda \Psi_1 + \lambda^2 \Psi_2) & \end{aligned} \qquad 3.159$$

Grouping the different terms with the same power of λ ,

$$\hat{H}_0 |\Psi_0\rangle = E_0 |\Psi_0\rangle \qquad 3.160$$

$$(\hat{H}_0 - E_0)|\Psi_1\rangle = (E_1 - \hat{H}_1)|\Psi_0\rangle \qquad 3.161$$

$$\left(\widehat{H}_0 - E_0\right)|\Psi_2\rangle = (E_1 - \widehat{H}_1)|\Psi_1\rangle + E_2|\Psi_0\rangle \quad 3.162$$

Considering now the intermediate normalization of the total wave function $\langle\Psi|\Psi_0\rangle = 1$, the expressions for the energies are

$$E_0 = \langle\Psi_0|\widehat{H}_0|\Psi_0\rangle \quad 3.163$$

$$E_1 = \langle\Psi_0|\widehat{H}_1|\Psi_0\rangle \quad 3.164$$

$$E_2 = \langle\Psi_0|\widehat{H}_1|\Psi_1\rangle \quad 3.165$$

For solving the second order energy, the first order wave function is required. Møller-Plesset perturbation theory use HF as a reference, then let's assume that Ψ_0 is a HF determinant and construct the $\widehat{H}_0$

$$\widehat{H}_0 = \hat{P}_0\hat{F}\hat{P}_0 + \hat{P}_X\hat{F}\hat{P}_X \quad 3.166$$

being $\hat{P}_0 = |\Psi_0\rangle\langle\Psi_0|$ the projection operator onto the reference function, $\hat{P}_X$ the corresponding operator for the rest of the configurations space, and $\hat{F}$ the Fock operator, which is usually assumed to be diagonal in the orbital space:

$$\hat{F} = \sum_p \epsilon_p \hat{E}_{pp} \quad 3.167$$

where ϵ_p are the HF eigenvalues.

The zeroth order energy is obtained by the sum of the eigenvalues of the occupied spin-orbitals and the perturbation part of the Hamiltonian is the difference between the full one and $\widehat{H}_0$. In order to obtain the E_2value, the first order equation must be solved.

$$\Psi_1 = \sum_\mu C_\mu \Phi_\mu \quad 3.168$$

where the sum is over all the possible Slater determinants in the CI space generated by the spin orbitals, except the HF determinant. Inserting this equation into the Ψ_1 expression and multiplying by Φ_μ on the left:

$$\sum_{\mu} C_{\mu} \langle \Phi_{\mu} | (\hat{H}_0 - E_0) | \Phi_{\mu} \rangle = \langle \Phi_{\mu} | ((E_1 - \hat{H}_1)) | \Psi_0 \rangle \qquad 3.169$$

Taking into account that all the Φ_{μ} functions are eigenfunctions of $\hat{H}$ with eigenvalues equal to the sum of the orbital energies of the spin orbitals occupied in the given determinant, E_{μ}

$$C_{\mu} = -\frac{\langle \Phi_{\mu} | \hat{H}_1 | \Psi_0 \rangle}{E_{\mu} - E_0} \qquad 3.170$$

The numerator represents the interaction between the configurations Φ_{μ} and the reference HF function Ψ_0. This numerator can be expressed using either $\hat{H}_1$ or $\hat{H}$ since only the doubly excited configurations need to be included in this term (the singlet ones will not contribute due to the Brillouin theorem).

Those expressions can now be translated to the multiconfigurational case were the reference function Ψ_0 is now the CASSCF wave function. The analogue zeroth order Hamiltonian will be

$$\hat{H}_0 = \hat{P}_{CASSCF} \hat{F} \hat{P}_{CASSCF} + \hat{P}_K \hat{F} \hat{P}_K + \hat{P}_{SD} \hat{F} \hat{P}_{SD} + \hat{P}_X \hat{F} \hat{P}_X \qquad 3.171$$

where the CI space has been divided into four different spaces, CASSCF the reference function, K the rest of the CAS CI space, SD the single and doubly excited CSFs with respect to the CASSCF reference function, and X the rest of the CI space not interacting with the CASSF space.

The choice of the Fock operator is now more complicated and in this case, it is going to be defined as for the super-CI method being such as that for the inactive and external orbitals the diagonal elements correspond to orbital energies as for the Koopmans theorem:

$$\hat{F} = \sum_{pq} \mathfrak{f}_{pq} \hat{E}_{pq} \qquad 3.172$$

where

$$\mathfrak{f}_{pq} = h_{pq} + \sum_{rs} D_{rs} \left[(pq|rs) - \frac{1}{2} (pr|qs) \right] \qquad 3.173$$

This Fock operator has the property that when the orbital p is doubly occupied f_{pq} is the ionization potential but when it is empty it estimates the electron affinity. The CASSCF wave function must be independent to the rotation between inactive, active and external orbitals. If those considerations are taken and $\hat{F}$ is divided now into three set of orbitals such that the matrix is diagonal within it set:

$$\hat{F} = \sum_i \epsilon_i \hat{E}_{ii} + \sum_t \epsilon_t \hat{E}_{tt} + \sum_a \epsilon_a \hat{E}_{aa} \qquad 3.174$$

$$+ \sum_{it} f_{ti}[\hat{E}_{it} + \hat{E}_{ti}] + \sum_{ia} f_{ai}[\hat{E}_{ia} + \hat{E}_{ai}] +$$

$$\sum_{ta} f_{at}[\hat{E}_{ta} + \hat{E}_{at}]$$

where i are the inactive orbitals, t the active ones and a external ones.

Again, only the configurations interacting with the reference wave function must be included into the first order wave function.

$$\Psi_1 = \sum_{pqrs} C_{pqrs} \, |pqrs\rangle \qquad 3.175$$

$$|pqrs\rangle = \hat{E}_{pq}\hat{E}_{rs}|\Psi_{CASSCF}\rangle \qquad 3.176$$

neither of the four indices p, q, r or s can be active since the generated function belong to the space K. The space defined in the previous equation cover all the interacting space that contributes to the first order wave function, being each $|pqrs\rangle$ formed by many CSFs. In fact, they are linear combinations of CSFs with coefficients from the reference function. All the single and double (V_{SD} space) are included in the above wave function, except of those where all p,q,r and s are active orbitals.

The matrix form of the Fock operator is rather complicated since it need to know the first, second, third and forth order density matrices for the CASSCF reference function. In fact, the calculation of those matrices takes the most part of the computing time for a CASSCF calculation.

An even bigger concern is the presence of intruder state during the CASPT2 calculation. If the intermediate normalization is taken into account, the normalized wave function can be expressed as

$$\Psi = \sqrt{\omega}|\Psi_0\rangle + \sqrt{1-\omega}|1\rangle \qquad 3.177$$

where $\omega = 1/(1+S)$ is the weight of the reference wave function and $|1\rangle$ is the normalized first order wave function. Since the CASPT2 method is size-extensive, the weight of the reference function depends on the number of electrons:

$$\omega = (1+\alpha)^{-N/2} \qquad 3.178$$

where N is the number of electrons and α constant represent the correlation energy for a pair of electrons. The obtained value for the reference weight, ω, for an specific calculation can be used as an idea for the validity of the computed results. For instance, using $\alpha = 0.02$ the obtained ω should be between 0.90 (for 10 electrons) and 0.60 (for 50 electrons). Values lower than those could indicate that intruder states are taking part in our CASPT2 calculations.

Intruder states are states, which belong to the V_{SD} space but they have a zeroth order energy close to the reference energy. They could be weakly occupied orbitals presenting energies close to secondary orbitals and/or highly occupied ones, which are close in energy to the inactive ones. In these situations the coefficient in front of the $|1\rangle$ function no longer small, and then the perturbation treatment can not be applied anymore. If the intruder state strongly couples with the reference function it should be included expanding the active space. However, this solution is not always feasible, for instance in cases of large molecules, and/or when quite large active spaces are being already used. If the expansion of the as is not possible, the perturbative treatment can no be used and other strategies need to be applied. Nevertheless, the most common situation is that those intruder states slightly interact with the reference wave function and can be "removed" using the well-known Level-Shift CASPT2 method. A constant is added to the zero order Hamiltonian modifying the first order equation

$$\left(\hat{H}_0 - E_0 + \varepsilon\right)\left|\tilde{\Psi}_1\right\rangle = (E_1 - \hat{H}_1)|\Psi_0\rangle \qquad 3.179$$

and assuming that the zeroth order Hamiltonian is diagonal in the expansion space, the second order energy as a function of the shifted Hamiltonian can be written as

$$\tilde{E}_2 = -\sum_{i=1} \frac{\left|\langle\Psi_0|\hat{H}|\Phi_i\rangle\right|^2}{\epsilon_i - E_0 + \varepsilon} \qquad 3.180$$

From this equation, it can be extracted that the level shift parameter avoids the vanishing of the denominator and then the divergence in the perturbation treatments for those intruder orbitals, that, as said before, present a energy very close to E_0.

Multistate CASPT2 (MS-CASPT2)[14]

Represents an extension of the CASPT2 method, which is essential to describe correctly chemical situations where the CASSCF is not an adequate reference function and two or more reference states are required. This is for instance the case of

- Avoided Crossings
- Rydberg states
- Conical intersections

MS-CASPT2 performs as many calculations as reference functions are considered $\Phi_i \quad i = 1, \dots, N$. A set of Ψ_i orbitals, obtained through *N* average CASSCF states, is used for describing each reference function. CASPT2 calculations are performed for those reference wave functions. An effective Hamiltonian is constructed were the diagonal elements are the CASPT2 energies and the off-diagonal ones correspond with coupling up to the second order. This Hamiltonian is computed perturbatively and diagonalized in a multidimensional reference space, P expanded by the CASSCF states.

The final MS-CASPT2 wave function can be written as

$$\Psi_p^{MS-CASPT2} = \sum_i c_{pi}|i\rangle + \Psi_p{}^{(1)} \qquad 3.181$$

where $|i\rangle$ are the CASSCF reference functions and Ψ_p is the first order function of the p state. This function can be rewritten defining a model state $|i_p\rangle$ which is constructed from a linear combination of the CASS functions involved in the MS-CASPT2 calculation and which can be considered as a new reference function for the p state. $|i_p\rangle$ are also known as the Perturbation Modified CASS (PMCAS) reference functions:

$$\Psi_p^{MS-CASPT2} = \Psi_p^{PMCAS} + \Psi_p{}^{(1)} \qquad 3.182$$

which are computed to obtain transition properties and expectation values when the CASSCF method fails.

3.10 Basis sets

The use of any *ab initio* method requires the introduction of a basis set. If this basis set was complete, molecular orbitals composing the wavefunction could be described as a set of the known functions introducing no approximations. However, a

complete basis set involves a infinite number of functions which, unfortunately, is not possible to handle because of the current computational limits. The type and size of the chosen basis set determine the accuracy of the *ab initio* calculation.

Slater Type Orbitals

The Slater Type Orbitals (STO)[15] have the functional general form

$$\phi_{\xi,n,l,m}(r,\theta,\varphi) = NY_{l,m}(\theta,\varphi)r^{n-1}e^{-\xi r} \qquad 3.183$$

where N is the normalization constant, $Y_{l,m}$ are spherical harmonic functions and ξ is the nuclear effective charge. This type of basis functions does not present nodes in the radial part, but can be introduced using linear combination of these functions. However, two-electron integrals centred in three or four different atoms cannot be solved analytically using STO functions. This shortcoming limits their use to some semi-empirical methods (where those integrals are neglected) or density functional methods not including exact exchange (where the density is fitted to auxiliary functions).

Gaussian Type Orbitals

In order to overcome STO's drawbacks, Boys suggest the use of Gaussian type orbitals (GTO). These functions are suitable to solve multi centre integrals since the product of two Gaussian functions leads to another Gaussian function centred in a third different point. GTOs written in terms of Spherical and Cartesian coordinates present the form

$$\phi_{\xi,n,l,m}(r,\theta,\varphi) = NY_{l,m}(\theta,\varphi)r^{(2n-2-l)}e^{-\xi r^2} \qquad 3.184$$

$$\phi_{\xi,l_x,l_y,l_z}(x,y,z) = Nx^{l_x}\, y^{l_y}\, z^{l_z}e^{-\xi r^2} \qquad 3.185$$

where the sum of $l_x + l_y + l_z$ determines the type of orbital. GTO functions shows two main problems. The first of them is related to the fact that, in contrast to STO functions, GTOs do not properly represent the behaviour of the electron close to the nucleus. Furthermore, the probability of finding the electron falls too rapidly as the nucleus-electron distance.

Minimal Basis Set (Pople Basis Sets)

Combining the two above mentioned types of basis set, Pople and coworkers propose the STO-NG minimal basis set. This type of basis set uses a set of GTOs (N=3-6) to fit a STO function.

$$\phi_{STO-NG} = \sum_i a_i \varphi_{i,GTO} \qquad 3.186$$

The φ functions are called primitive GTOs (PGTOs), while ϕ are known as contracted GTOs (CGTOs). The degree of contraction is the number of PGTOs composing the CGTOs. Two different procedures can be employed in the contraction process. In the *segmented contraction*, a given set of PGTOs is portioned into smaller sets of functions that expand CGTOs through suitable coefficients. In this contraction scheme, each primitive is used in one contracted function. In contrast, in a *general contraction* all primitives enter all GTOs with different contraction coefficients.

The use of the STO-3G basis set represents an improvement with respect to the simple nGTO or STO basis sets. Although this basis set provides qualitative acceptable results, obtaining quantitative results requires the use of larger basis sets, since for example, this minimal basis sets are not able to properly describe multiple bonds. In these π-bonds the electron distribution is more diffuse than in a σ-bonds so the optimum exponents for describing this distribution along two different directions are not the same. This phenomenon, known as anisotropy, requires the use of larger basis set as the *split valence* basis set, which split the valence orbitals into different parts. For instance, the 6-311 is a triple split valence basis, which describe the core orbital with a contraction of six PGTOs and the valence is divided into three different parts, the inner one described by three PGTOs while the other two are represented by a single PGTO.

Polarization and diffuse functions

Although split valence basis sets represent an improvement to minimal basis sets, they are still unable to describe changes in the electronic clouds of atoms when they form a bond. In this situation, the electronic density of the atoms polarizes in the direction of the bond and the correct description of this effect requires the addition of higher angular momentum functions, known as *polarization functions*. Thus, *p-orbitals* are used for first period atoms, *d-orbitals* for second period atoms, *f-orbitals* for transition metals, etc.

Special bonding situations such as those occurring in anions or hydrogen bonded/van der Waals complexes require the use of diffuse functions which are characterized by very small exponents, which are able to describe charges far away from the nuclei. Diffuse functions are usually denoted by + indicating one set of diffuse *s*- and *p*- functions on heavy atoms or ++ indicating that in addition a diffuse *s*-function is added to hydrogen.

Atomic Natural Orbitals

The Atomic Natural Orbitals (ANO) basis sets contract a large set of PGTOs to a small set of CGTOs using natural orbitals from a correlated calculation usually at the CISD level. Natural orbital are those that diagonalize the density matrix, giving the orbital occupation numbers as eigenvalues. These occupation numbers are restricted to 0 or 2 in a RHF, where the ANOs[16] coincide with the canonical orbitals. However, when a correlated wavefunction is used, occupation numbers can take any value between 0 and 2.

One of the main advantages of this type of basis set is that they generate balanced basis sets. Furthermore, the smaller ANO basis set (ANO-S) gives good results since it uses the same number of PGTOs than in the larger ANO basis set (ANO-L). [17]

3.11 Beyond Born-Oppenheimer: Conical Intersections and Non Adiabatic Couplings.

So far we have obtained the potential energy surfaces by solving the electronic problem within the Born Oppenheimer Approximation and obtaining the correspondent uncoupled electronic (adiabatic) states. The reason why this approach leads to good results for several studies is that the non-considered nonadiabatic coupling terms (NACTs) depend on the mass ratio $(m_e/m_p)^{1/2}$, being expected to be two orders of magnitude smaller than the other magnitudes appearing in the electronic Schrödinger wave function. However, in situations where several electronic states are degenerated, those NACTs become extremely large and are necessary to be computed. Conical intersections are the most common concern since they are quite common for most systems and represent situations where adjacent states are coupled.

If we turn back to the first equations in this chapter,

$$\hat{H}_{tot} = \underbrace{\hat{T}_e + \hat{V}_{Ne} + \hat{V}_{ee} + \hat{V}_{NN}}_{\hat{H}_e} + \hat{T}_N \qquad 3.187$$

we can now expand more in detail the different terms, where the electronic Hamiltonian $\hat{H}_e$ is formed by

$$\hat{H}_e = \underbrace{-\frac{\hbar^2}{2m_e}\sum_i^{ne}\frac{\partial^2}{\partial x_i^2}}_{\hat{T}_e} + \frac{1}{4\pi\epsilon_0}\left(\underbrace{\frac{Z_A Z_B e^2}{r}}_{\hat{V}_{NN}} - \underbrace{\sum_i^{n_e}\frac{Z_A e^2}{D_{Ai}} - \sum_i^{n_e}\frac{Z_B e^2}{D_{Bi}}}_{\hat{V}_{Ne}} + \underbrace{\sum_i^{n_e}\sum_{i\neq j}^{n_e}\frac{e^2}{D_{ij}}}_{\hat{V}_{ee}}\right) \qquad 3.188$$

where n_e is the number of electrons, A and B represent the nuclei and i and j refer to the electrons. Z means the number of protons, m and e represent the mass and charge of the electron. And finally we denote D_{Ai} as the distance between the nuclei A and the electron I and D_{ij} is the distance between electrons I and j. If we also consider now the nuclei kinetic term

$$\hat{T}_N = -\sum_A \frac{\hbar^2}{2\mu}\frac{\partial^2}{\partial r^2} \qquad 3.189$$

where $\mu = m_A m_B/(m_A + m_B)$ is the reduced mass and r is the distance between them. If we considered now this term we can write something equivalent to equation 3.5 but for the total Hamiltonian and time dependent

$$\hat{H}\Psi\ (\mathrm{r},\mathrm{R},\mathrm{t}) = E\Psi(\mathrm{r},\mathrm{R},\mathrm{t}) \qquad 3.190$$

where the total wave function depend on the electron R position, the nuclei position r and the time and it can be written separating the electronic wave function and the nuclei wave function:

$$\Psi\ (\mathrm{r},\mathrm{R},\mathrm{t}) = \sum_{\alpha}^{N} |\Psi_\alpha^n(r,t)\rangle\, |\Psi_\alpha^e(r,R)\rangle \qquad 3.191$$

When if $\hat{H}_e$ is applied to the electronic wave function $|\Psi_\alpha^e(r,R)\rangle$ for each nuclear configurations the potential terms $V(r)$ are obtained using one of the ab intio methods described previously during this chapter. However, the result of applying this electronic Hamiltonian to the total wave function expressed as a combination of electronic and nucleic functions is

$$\hat{H}_e \sum_{\alpha}^{N} |\Psi_\alpha^n(r,t)\rangle\, |\Psi_\alpha^e(r,R)\rangle = \sum_{\alpha}^{N} |\Psi_\alpha^n(r,t)\rangle \hat{H}_e(r,R)\, |\Psi_\alpha^e(r,R)\rangle \qquad 3.192$$

since $\hat{H}_e$ present no derivatives respect to the coordinates in the nucleic wave function

$$\hat{H}_e \sum_{\alpha}^{N} |\Psi_\alpha^n(r,t)\rangle\, |\Psi_\alpha^e(r,R)\rangle = \sum_{\alpha}^{N} |\Psi_\alpha^e(r,R)\rangle V_\alpha(r) |\Psi_\alpha^n(r,t)\rangle \qquad 3.193$$

In order to obtain the total Hamiltonian acting onto the total wave function, we can evaluate now the effect of the kinetic term $\hat{T}_N$ with respect of the internuclear distance. If we first calculate the first derivative

$$\frac{\partial}{\partial r}\sum_{\alpha}^{N}|\Psi_{\alpha}^{n}(r,t)\rangle\,|\Psi_{\alpha}^{e}(r,R)\rangle=\sum_{\alpha}^{N}|\Psi_{\alpha}^{e}(r,R)\rangle\frac{\partial|\Psi_{\alpha}^{n}(r,t)\rangle}{\partial r}+ \qquad 3.194$$

$$+\sum_{\alpha}^{N}\frac{\partial|\Psi_{\alpha}^{e}(r,R)\rangle}{\partial r}|\Psi_{\alpha}^{n}(r,t)\rangle$$

And the second derivative

$$\frac{\partial^2}{\partial r^2}\sum_{\alpha}^{N}|\Psi_{\alpha}^{n}(r,t)\rangle\,|\Psi_{\alpha}^{e}(r,R)\rangle=\sum_{\alpha}^{N}|\Psi_{\alpha}^{e}(r,R)\rangle\frac{\partial^2|\Psi_{\alpha}^{n}(r,t)\rangle}{\partial r^2} \qquad 3.195$$

$$+\sum_{\alpha}^{N}\frac{\partial^2|\Psi_{\alpha}^{e}(r,R)\rangle}{\partial r^2}|\Psi_{\alpha}^{n}(r,t)\rangle\;+\sum_{\alpha}^{N}2\frac{\partial|\Psi_{\alpha}^{e}(r,R)\rangle}{\partial r}\frac{\partial|\Psi_{\alpha}^{n}(r,t)\rangle}{\partial r}$$

Lastly integrating respect to the electronic coordinates and taking into account that as said before

$$\hat{H}_e|\Psi_{\alpha}^{e}(r,R)\rangle=\;V(r)|\Psi_{\alpha}^{e}(r,R)\rangle \qquad 3.196$$

the expression for the total Hamiltonian can be written as

$$\left\langle\Psi_{\beta}^{e}(r,R)\middle|H\middle|\sum_{\alpha}^{N}|\Psi_{\alpha}^{n}(r,t)\rangle\,|\Psi_{\alpha}^{e}(r,R)\rangle\right\rangle=\underbrace{\overbrace{V_{\beta}(r)\Psi_{\beta}^{n}(r,t)}^{\hat{H}_e}-\overbrace{\frac{\hbar^2}{2\mu}\frac{\partial^2|\Psi_{\alpha}^{n}(r,t)\rangle}{\partial r^2}}^{\hat{T}_N}}_{Aprox\;BO}- \qquad 3.197$$

$$-\frac{\hbar^2}{2\mu}\sum_{\alpha}^{N}\left\langle\Psi_{\beta}^{e}(r,R)\middle|\frac{\partial^2}{\partial r^2}\middle|\Psi_{\alpha}^{e}(r,R)\right\rangle|\Psi_{\alpha}^{n}(r,t)\rangle-\frac{\hbar^2}{\mu}\sum_{\alpha}^{N}\left\langle\Psi_{\beta}^{e}(r,R)\middle|\frac{\partial}{\partial r}\middle|\Psi_{\alpha}^{e}(r,R)\right\rangle\frac{\partial}{\partial r}|\Psi_{\alpha}^{n}(r,t)\rangle$$

The **adiabatic approximation** considers only the diagonal terms of the Hamiltonian, being the out of diagonal elements negligible. Furthermore, the third and fourth terms in this equation are not included within the BO approximation, since the interaction of $\hat{T}_N$ with the electronic wave function are not considered. Then, the BO time dependent Schrödinger Equation for the electron movements are

$$\frac{\partial}{\partial t}\left|\Psi_\beta^n(r,t)\right\rangle = -\frac{i}{\hbar}\left(\frac{\hbar^2}{2\mu}\frac{\partial^2|\Psi_\alpha^n(r,t)\rangle}{\partial r^2} + V_\beta(r)\Psi_\beta^n(r,t)\right) \qquad 3.198$$

Then within the BO approximation, the potential energy surface V_β are obtained as a sum of the electronic potential and kinetic energy of a given state β plus the internuclear repulsion for each nuclei position.

Conical Intersections

As said before, the above equation cannot be used in regions where surface crossings take place, since the electrons are not able to adapt to the nuclei position and the wave function derivatives (third and fourth terms in eq 3.197) respect to the internuclear distance must be considered. Being the first derivative:

$$T_{\alpha\beta}^r(r) = \left\langle \Psi_\alpha^e(r,R)\left|\frac{\partial}{\partial r}\right|\Psi_\beta^e(r,R)\right\rangle \qquad 3.199$$

and the second one

$$T_{\alpha\beta}^{rr}(r) = \left\langle \Psi_\alpha^e(r,R)\left|\frac{\partial^2}{\partial r^2}\right|\Psi_\beta^e(r,R)\right\rangle \qquad 3.200$$

In those situations when a BO can no be used, those terms can not be despised and must be computed.

With this purpose the electronic time independent Schrödinger Equation in base of orthonormal electronic wave functions, which not depend on r

$$\frac{\partial}{\partial r}\left\langle \Psi_\beta^e(r,R)\middle|\Psi_\alpha^e(r,R)\right\rangle = 0 \qquad 3.201$$

then

$$\left\langle \frac{\partial \Psi_\beta^e(r,R)}{\partial r} \middle| \Psi_\alpha^e(r,R) \right\rangle + \left\langle \Psi_\beta^e(r,R) \middle| \frac{\partial \Psi_\alpha^e(r,R)}{\partial r} \right\rangle = 0 \qquad 3.202$$

$$\left\langle \frac{\partial \Psi_\beta^e(r,R)}{\partial r} \middle| \Psi_\alpha^e(r,R) \right\rangle = -\left\langle \Psi_\beta^e(r,R) \middle| \frac{\partial \Psi_\alpha^e(r,R)}{\partial r} \right\rangle \qquad 3.203$$

those equations can be rewritten as

$$2\left\langle \Psi_\alpha^e(r,R) \middle| \frac{\partial}{\partial r} \middle| \Psi_\alpha^e(r,R) \right\rangle = 2T_{\alpha\alpha}^r(r) = 0 \qquad for\ \alpha = \beta \qquad 3.204$$

$$T_{\alpha\beta}^r(r) = -T_{\beta\alpha}^r(r) \qquad for\ \alpha \neq \beta \qquad 3.205$$

Regarding the second derivative of the electronic wave function it can be written as a function of the first one using the unitary operator

$$\sum_\gamma^N \left|\Psi_\gamma^e(r,R)\right\rangle \left\langle \Psi_\gamma^e(r,R)\right| = 1 \qquad 3.206$$

then

$$\frac{\partial}{\partial r}\frac{\partial}{\partial r}|\Psi_\alpha^e(r,R)\rangle = \frac{\partial}{\partial r}\sum_\gamma^N \left|\Psi_\gamma^e(r,R)\right\rangle \underbrace{\left\langle \Psi_\gamma^e(r,R) \middle| \frac{\partial}{\partial r} \middle| \Psi_\gamma^e(r,R) \right\rangle}_{T_{\gamma\alpha}^r(r)} \qquad 3.207$$

$$= \frac{\partial}{\partial r}\sum_\gamma^N \left|\Psi_\gamma^e(r,R)\right\rangle T_{\gamma\alpha}^r(r)$$

$$= \sum_\gamma^N \frac{\partial \left|\Psi_\gamma^e(r,R)\right\rangle}{\partial r} T_{\gamma\alpha}^r(r) + \sum_\gamma^N \left|\Psi_\gamma^e(r,R)\right\rangle \frac{\partial T_{\gamma\alpha}^r(r)}{\partial r}$$

In order to obtain $T_{\beta\alpha}^r(r)$ we multiply the above expression by $\langle \Psi_\beta^e(r,R)|$

$$T_{\beta\alpha}^{rr}(r) = \sum_\gamma^N \underbrace{\left\langle \Psi_\beta^e(r,R) \middle| \frac{\partial}{\partial r} \middle| \Psi_\gamma^e(r,R) \right\rangle}_{T_{\beta\gamma}^r} T_{\gamma\alpha}^r(r) + \sum_\gamma^N \left\langle \Psi_\beta^e(r,R) \middle| \Psi_\gamma^e(r,R) \right\rangle \frac{\partial T_{\gamma\alpha}^r(r)}{\partial r} \qquad 3.208$$

Since the last term only survives for $\gamma = \beta$, it can be obtained that

$$T^{rr}_{\beta\alpha}(r) = \sum_{\gamma}^{N} T^{r}_{\beta\gamma}(r) T^{r}_{\gamma\alpha}(r) + \frac{\partial T^{r}_{\beta\alpha}(r)}{\partial r} \qquad 3.209$$

Then for those situations the derivatives of the electronic wave function respect to the internuclear distance is important and are not small compared to the potential V_β.

Another possible representation is the **diabatic** approach, where a position of the nuclei, r_0, is used for all the position of the electrons. Is the same to say that the electrons can now not be adapted to the nuclei position. The global wave function is now

$$\Psi\ (\mathrm{r}, \mathrm{R}, \mathrm{t}) = \sum_{\alpha}^{N} |\Psi^{n}_{\alpha}(r,t)\rangle\, |\Psi^{e}_{\alpha}(r_0, R)\rangle \qquad 3.210$$

The orthonormal condition is still valid for $r = r_0$ since the $|\Psi^{e}_{\alpha}(r_0, R)\rangle$ wave function is a function of the electronic Hamiltonian.

$$\left\langle \Psi^{e}_{\beta}(r_0, R) \middle| H_e(r = r_0) \middle| \Psi^{e}_{\alpha}(r_0, R) \right\rangle = E_i(r = r_0)\alpha\beta \qquad 3.211$$

If the same procedure as for the adiabatic approach is followed the expression for the total Hamiltonian integrated over the electronic coordinates

$$\left\langle \Psi^{e}_{\beta}(r_0, R) \middle| H \sum_{\alpha}^{N} |\Psi^{n}_{\alpha}(r,t)\rangle \middle| \Psi^{e}_{\alpha}(r_0, R) \right\rangle = \qquad 3.212$$

$$\left\langle \Psi^{e}_{\beta}(r_0, R) \middle| \hat{T}_N + H_e(r, R) \sum_{\alpha}^{N} |\Psi^{n}_{\alpha}(r,t)\rangle \middle| \Psi^{e}_{\alpha}(r_0, R) \right\rangle =$$

$$\left\langle \Psi^{e}_{\beta}(r_0, R) \middle| -\frac{\hbar^2}{2\mu}\frac{\partial^2}{\partial r^2} + H_e(r, R) \sum_{\alpha}^{N} |\Psi^{n}_{\alpha}(r,t)\rangle \middle| \Psi^{e}_{\alpha}(r_0, R) \right\rangle =$$

$$\sum_{\alpha}^{N}\left\{\left\langle\Psi_{\beta}^{e}(r_0,R)\middle|\Psi_{\alpha}^{e}(r_0,R)\right\rangle\left(-\frac{\hbar^2}{2\mu}\frac{\partial^2}{\partial r^2}\right)|\Psi_{\alpha}^{n}(r,t)\rangle\right.$$
$$\left.+\left\langle\Psi_{\beta}^{e}(r_0,R)\middle|H_e(r,R)\Psi_{\alpha}^{e}(r_0,R)\middle||\Psi_{\alpha}^{n}(r,t)\right\rangle\right\}=$$

$$=-\frac{\hbar^2}{2\mu}\frac{\partial^2}{\partial r^2}\left|\Psi_{\beta}^{n}(r,t)\right\rangle+\sum_{\alpha}^{N}H_{\beta\alpha}(r)|\Psi_{\alpha}^{n}(r,t)\rangle$$

Since for the first sum only the term with $\alpha=\beta$ survives.

The crossed terms $H_{\beta\alpha}(r)$

$$H_{\beta\alpha}(r)=\left\langle\Psi_{\beta}^{e}(r_0,R)\middle|H_e(r,R)\middle||\Psi_{\alpha}^{e}(r_0,R)\right\rangle \qquad 3.213$$

appear due to the different situation from the adiabatic approach. In this case, the electronic wave function is not a function for each r value, so those crossed terms are important. However, the kinetic crossing terms $T_{\beta\alpha}^{r}(r)$ and $T_{\beta\alpha}^{rr}(r)$ vanishes now since those electronic wave function are independent on the internuclear distance.

The diagonal $H_{\alpha\alpha}$ terms represent the diabatic potential, which make the time dependent Schrödinger equation easier to be solved, while the time independent version result easy to compute using the adiabatic potentials.

The selected representation for the dynamic simulations will be discussed within the next chapter, describing the pros and cons of each method.

The theoretical code used for CI optimization during this thesis is the one implemented in the MOLPRO package, for more details see Ref [18].

Spin Orbit Coupling

The importance of spin orbit couplings in molecules bearing heavy atoms has been already discussed in Chapter 2. So far, the nonrelativistic Hamiltonian has been considered, H^{nr}, but when spin-orbit coupling (SOC) is included the total Hamiltonian takes the form

$$\hat{H}=\hat{H}^{nr}+\hat{H}^{SO} \qquad 3.214$$

where $\hat{H}^{SO}$ is the spin orbit coupling operator. An expression for this operator can be derived based in the relativistic theory of Dirac.

Since an electron has two types of angular momenta, spin and orbital, it produces two magnetic moments. If the nucleus is considered as charge moving around the electron, then a magnetic field will be acting upon this particular electron. This magnetic field (B) interacts with the spin magnetic moment of the electron (μ) through the interaction energy equation (2.280) which correspond to the spin-orbit interaction term of the Hamiltonian

$$\hat{H}^{SO} = -\boldsymbol{\mu}\,\mathbf{B} \qquad 3.215$$

The expression for the magnetic field is

$$\boldsymbol{B} = -\frac{1}{mcr}\frac{dV}{dr}\boldsymbol{L} \qquad 3.216$$

where m is the mass of the electron and c the speed of light. $\boldsymbol{L}$ represents the orbital angular momenta and the force acting upon the electron is understood as the derivative of an isotropic potential, V.

The expression for the spin magnetic moment is

$$\boldsymbol{\mu} = -\frac{\mathrm{e}}{mc}\,\boldsymbol{S} \qquad 3.217$$

where **S** is the spin angular momenta. Substituting the two former equations into equation (2.280) we obtain the expression for the H^{SO}

$$\hat{H}^{SO} = \frac{\mathrm{e}}{2\,m^2c^2r}\frac{dV}{dr}\hat{\boldsymbol{L}}.\hat{\boldsymbol{S}} \qquad 3.218$$

The ½ factor is a relativistic correction regarding the movement of the electrons and $\hat{\boldsymbol{L}}.\hat{\boldsymbol{S}}$ is the product between orbital and spin angular momenta operators for the electron.

For a many electron system, where each electron, i, is influenced by a spherically averaged potential $V_i(r_i)$ calculated without the spin-orbit interaction, the $\hat{H}^{SO}$ operators takes the form

$$\hat{H}^{SO} = \sum_i \zeta_i(r_i)\ \hat{\boldsymbol{L}}_{\boldsymbol{i}}.\hat{\boldsymbol{S}}_i \qquad 3.219$$

with

$$\zeta_i(r_i) = \frac{\mathrm{e}}{2\, m^2 c^2 r_i} \frac{dV_i(r_i)}{dr_i} \qquad 3.220$$

and the total Hamiltonian for a many electron system becomes

$$\hat{H} = \sum_i \hat{H}^k(i) + \sum_{i<j} \frac{1}{r_{ij}} + \hat{H}^{SO} \qquad 3.221$$

To simplify the calculation of the SOC terms, MOLCAS[19] approximates the SO Hamiltonian by a one-electron effective Hamiltonian which also avoids the calculation of multi center integrals (Atomic Mean Field Approximation, AMFI.[20] Within this approach, the effective one electron representation of the matrix element of the SO operator between a pair of Slater determinants differing by a single valence spin orbital i/j takes the form

$$^{eff}\hat{H}_{ij}^{SO} = \langle i|H^{SO}(1)|j\rangle + \frac{1}{2}\sum_k n_k \left[\langle ik|H^{SO}(1,2)|jk\rangle - \langle ik|\square H^{SO}(1,2)|kj\rangle - \right. \qquad 3.222$$

$$\left. -\langle ki|H^{SO}(1,2)|jk\rangle\right]$$

where i, j, k denote spin orbital indices and n_k effective orbital occupation numbers. The mean field approach fixes the average occupation for all different pairs, n_k, instead of using occupations for each individual pair of Slater determinants.

In summary, the integrals describing the coupling between a singlet (A) and a triplet (B) state $\langle SM|\hat{H}^{SO}|S+1\ M\pm 1\rangle$ and $\langle SM|\hat{H}^{SO}|S+1\ M\rangle$, which are of interest for us, take the form

$$\langle 00|\hat{H}^{SO}|11\rangle = -\frac{\sqrt{2}}{2}\,(V^{AB}(x) + iV^{AB}(y) \qquad 3.223$$

$$\langle 00|\hat{H}^{SO}|10\rangle = V^{AB}(z) \qquad 3.224$$

$$\langle 00|\hat{H}^{SO}|1-1\rangle = -\frac{\sqrt{2}}{2}\,(-V^{AB}(x) + iV^{AB}(y) \qquad 3.225$$

where V^{AB} correspond to the Wigner-Eckart reduced matrix elements between the two spin states. We can observe that the singlet couples in the same way with between the two components of the triplet with M=1 and M=-1, although this terms can present different signs.

Bibliography

(1) Schrödinger, E. *Ann. Physik.* **1926**, *79*, 361.

(2) Hartree, D. R. *Proc. Cambridge Phil. Soc* **1928**, *24*, 89.

(3) Fock, V. Z. *Physik* **1930**, *61*, 126.

(4) Slater, J. C. *Phys. Rev.* **1930**, *35*, 210.

(5) Slater, J. C. *Phys. Rev.* **1929**, *34*, 1293.

(6) Condon, E. U. *Phys. Rev.* **1930**, *36*, 1121.

(7) Roothaan, C. C. J. *Rev. Mod. Phys.* **1960**, *32*, 179.

(8) Hall, G. G. *Proc. Roy. Soc.* **1951**, *A205*, 541.

(9) Pople, J. A.; Nesbet, R. K. *J. Chem. Phys.* **1954**, *22*, 571.

(10) Langhoff, S. R.; Davidson, E. R. *International Journal of Quantum Chemistry* **1974**, *8*, 61.

(11) Gdanitz, R. J.; Ahlrichs, R. *Chem. Phys. Lett.* **1988**, *143*, 413.

(12) Roos, B. O. *In Ab initio Methods in Quantum Chemistry II*

Lawley, K. P.Ed.; Wiley: Chichester **1987**.

(13) Andersson, K.; Malmqvist, P. Å.; Roos, B. O. *J. Chem. Phys.* **1992**, *96*, 1218.

(14) Finley, J.; Malmqvist, P. Å.; Roos, B. O.; Serrano-Andrés, L. *Chem. Phys. Lett.* **1998**, *288*, 299.

(15) Hehre, W. J.; Stewart, R. F.; Pople, J. A. *J. Chem. Phys.* **1969**, *51*, 2657.

(16) Pierloot, K.; Dumez, B.; Widmark, P. O.; Roos, B. O. *Theor. Chim. Acta* **1995**, *90*, 87.

(17) Widmark, P. O.; Malmqvist, P. Å.; Roos, B. O. *Theor. Chim. Acta* **1990**, *77*, 291.

(18) Werner, H.-J. *et al v. MOLPRO, a package of ab initio programs.*

(19) Aquilante, F. *et al J. Comput. Chem.* **2010**, *31*, 224.

(20) Christiansen, O.; Gauss, J.; Schimmelpfennig, B. *Phys. Chem. Chem. Phys.* **2000**, *2*, 965.

Chapter 4

Excited States Molecular Dynamics

The simulation of the mechanism that a given molecule follows as a function of time is crucial for the understanding of many chemical processes, especially in photochemical reactions. In this respect, molecular dynamic simulations can be used to obtain information about the timescales in which those processes take place, and also to predict the ratio between competing mechanisms. Most studies regarding photochemical reactions involve fast process where the electronic and nuclear dynamics are coupled, so the nonadiabatic (see Chapter 3) couplings must be calculated and BO Aproximation is not valid. Furthermore, some of the main goals of the excited state dynamic simulation is to get information about the time scales where internal conversion back to the ground state takes place in excited molecules and/or the lifetimes of triplet states, as they can be precursor of cytotoxicity (see Chapter 1). Since those processes occur close to conical intersections and crossings, it is quite interesting to understand what happens in the vicinity of those points of the PES where those state are degenerated. Semiclassical dynamics can arise some insight into those nonadiabatic transitions giving quite quantitative results and determining how those crossings influence the dynamic behaviour of the excited system. For our studies the key point of those calculations is to evaluate the competition between internal conversion to the ground state (being the main mechanism in conical bases) and intersystem crossing to the molecules' triplet state (which has turn out to be very important in thiobases).

Since for more accuracy respect to the experimental results performed for some thiobases, some of our studies have incorporated the whole nucleoside plus a given solvent. The treatment of such large system is not possible using quantum molecular dynamic itself and cheaper techniques must be employed. Then, the combination of molecular mechanics and quantum mechanics (QM/MM approach) is described in the second part of this Chapter.

4.1 Semiclassical dynamics

Semiclassical dynamics here after means that the nuclear (slow) motion is treated with the Newton equations (classical trajectories) while the electrons (fast motion) are treated quantum mechanically. Semiclassical dynamics treats the nuclei with trajectories that follow the Newton's equations, while for the electrons the time dependent Schrödinger equation (TDSE) must be solved. On the following, Q refers to the nuclear coordinates and q to the electronic ones. Defining Q(t) as a trajectory in the nuclear configuration space, the electronic Hamiltonian $\widehat{H}_{el}(Q)$, its eigenstates $\psi_K(q;Q)$ and eigenvalues $U_K(Q)$ are implicitly time dependent.

$$\widehat{H}_{el}\big(Q(t)\big)\big|\psi_K\big(Q(t)\big)\big\rangle = U_K\big(Q(t)\big)\big|\psi_K\big(Q(t)\big)\big\rangle \qquad 4.1$$

In this approximation, the TDSE is written for the electrons as (in atomic units $\hbar = 1$)

$$i\,\frac{\partial}{\partial t}|\Psi_{el}(t)\rangle = \widehat{H}_{el}|\Psi_{el}(t)\rangle \qquad 4.2$$

where the time dependent electronic wave function, $|\Psi_{el}(t)\rangle$ can be expanded as a linear combination of the adiabatic states, ψ

$$|\Psi_{el}(t)\rangle = \sum_L A_L(t)e^{-i\gamma_L(t)}\,|\psi_L(Q(t))\rangle \qquad 4.3$$

where

$$\gamma_L = \int_0^t U_L\big(Q(t')\big)dt' \qquad 4.4$$

In order to calculate the probability of finding the system in state L, $P_L(t) = |A_L(t)|^2$, the time dependent electronic wave function must be derived

$$\frac{\partial}{\partial t}|\Psi_{el}(t)\rangle = \sum_L e^{-i\gamma_L(t)}\left[\left(\dot{A}_L - i\gamma_L A_L\right)|\psi_L\rangle + A_L\left|\frac{d\psi_L}{dt}\right\rangle\right] \quad 4.5$$

Considering,

$$\frac{\partial \psi_L}{\partial t} = \frac{\partial \psi_L}{\partial Q}\frac{\partial Q}{\partial t} \quad 4.6$$

The above equation can be now written

$$\frac{\partial}{\partial t}|\Psi_{el}(t)\rangle = \sum_L e^{-i\gamma_L(t)}\left[\left(\dot{A}_L - i\gamma_L A_L\right)|\psi_L\rangle + A_L\sum_r\left|\frac{\partial \psi_L}{\partial Q_r}\right\rangle \dot{Q}_r\right] \quad 4.7$$

Multiplying from the left by $\langle\psi_K|$ and substituting into the TDSE

$$\dot{A}_K = -\sum_{L\neq K} A_L(t)e^{i(\gamma_K-\gamma_L)}\sum_r \dot{Q}_r\, G_{KL}^{(r)} \quad 4.8$$

$G_{KL}^{(\alpha)}$ is the dynamic coupling matrix element, and is defined as

$$G_{KL}^{(r)} = \left\langle\psi_K\left|\frac{\partial}{\partial Q_r}\right|\psi_L\right\rangle \quad 4.9$$

$$G_{KK}^{(r)} = 0 \quad 4.10$$

From the numerical interpretation of equation 4.8 the adiabatic populations are obtained. This probability is proportional to the scalar product of the nuclear velocity vector $\dot{Q}$ and the dynamic coupling and becomes important in regions where the coupling between states is large and the energy difference is small.

The above coupled equations are only possible to be solved analytically for simple cases and in most cases they are solved numerically by computing the electronic U_K and $G_{KL}^{(r)}$ at each time step or analytical representations of them are prepared as functions of Q coordinates.

Hellymann-Feynman formula can be used to solve the nonadiabatic couplings. Derivatives of the equation 4.1 are

$$\frac{\partial \widehat{H}_{el}}{\partial Q_r}|\psi_L\rangle + \widehat{H}_{el}\frac{\partial|\psi_L\rangle}{\partial Q_r} = \frac{\partial U_L}{\partial Q_r}|\psi_L\rangle + U_L\frac{\partial|\psi_L\rangle}{\partial Q_r} \qquad 4.11$$

Multiplying by $\langle\psi_L|$ and considering that $G_{KK}^{(r)} = 0$, the Hellymann-Feynman formula is obtained

$$\langle\psi_L|\frac{\partial \widehat{H}_{el}}{\partial Q_r}|\psi_L\rangle = \langle\psi_L|\frac{\partial U_L}{\partial Q_r}|\psi_L\rangle \qquad 4.12$$

$$\langle\psi_L|\frac{\partial \widehat{H}_{el}}{\partial Q_r}|\psi_L\rangle = \frac{\partial U_L}{\partial Q_r} \qquad 4.13$$

while if it is multiply by $\langle\psi_K|$ with $L \neq K$ a relation for the dynamics couplings is obtained

$$\langle\psi_K|\frac{\partial \widehat{H}_{el}}{\partial Q_r}|\psi_L\rangle + \widehat{H}_{el}\langle\psi_K|\frac{\partial}{\partial Q_r}|\psi_L\rangle = \langle\psi_K|\frac{\partial U_L}{\partial Q_r}\Big|\psi_L\rangle + U_L\langle\psi_K|\frac{\partial}{\partial Q_r}|\psi_L\rangle \qquad 4.14$$

$$\langle\psi_K|\frac{\partial}{\partial Q_r}|\psi_L\rangle = \frac{\langle\psi_K|\frac{\partial \widehat{H}_{el}}{\partial Q_r}|\psi_L\rangle}{U_L - U_K} \qquad 4.15$$

This formula evidences that the nonadiabatic couplings are larger when the PES are close in energy ($U_L - U_K$ small). The latest equation are only valid for exact eigenfunctions and the cannot be used to compute energy gradients but they can be applied when working with model Hamiltonians to represent analytical PES and couplings.

4.2 Nuclear trajectories

The atomic nuclei are then propagated by solving the Newton's equations. One of the most popular methods is the velocity Verlet algorithm, which defines the changes in the positions Q and velocities $\dot{Q}$ between t and t + Δt by using finite difference approximations. For a given potential energy function V(Q), the force F_α and the acceleration $\ddot{Q}$ (as a function of the mass m_α associated with the coordinate Q_α) can be defined

$$F_\alpha = -\frac{\partial V}{\partial Q_\alpha} \quad 4.16$$

$$\ddot{Q}_\alpha = \frac{F_\alpha}{m_\alpha} \quad 4.17$$

The basic idea of this algorithm is to write Taylor expansions for the position Q(t), one forward and one backward in time

Introducing a first approximation for the third derivatives

$$\dddot{Q}(t) = \frac{\ddot{Q}(t) - \ddot{Q}(t-\Delta t)}{\Delta t} + O(\Delta t^2) \quad 4.18$$

$$\dddot{Q}(t+\Delta t) = \frac{\ddot{Q}(t+\Delta t) - \ddot{Q}(t)}{\Delta t} + O(\Delta t^2) \quad 4.19$$

and substituting them into the expressions of $Q(t+\Delta t)$ and $\dot{Q}(t+\Delta t)$,

$$Q(t+\Delta t) = Q(t) + \Delta t\, \dot{Q}(t) + \Delta t^2 \left[\frac{2}{3}\ddot{Q}(t) - \frac{1}{6}\ddot{Q}(t-\Delta t)\right] + O(\Delta t^4) \quad 4.20$$

$$\dot{Q}(t+\Delta t) = \dot{Q}(t) + \Delta t \left[\frac{5}{6}\ddot{Q}(t) + \frac{1}{3}\ddot{Q}(t+\Delta t) - \frac{1}{6}\ddot{Q}(t-\Delta t)\right] + O(\Delta t^3) \quad 4.21$$

the equations defining the Verlet algorithm are found with an accuracy of order Δt^4 for each step.

4.3 Surface Hopping

Surface Hopping is a general methodology for dynamic propagation, in which the classical and quantum treatments for nuclei and electrons are combined. In surface hopping (SH) dynamics the system is propagated, at any time, on a single adiabatic potential energy surface defined by its population, although the probabilities of the rest of states may be different from zero. An increase in the probability of other state can result in a transition ("hop") between U_L and U_K surfaces. This situation is probable when a crossing region is reached, since changes on the abiabatic state populations can result in nonadiabatic transitions between different states. Those transitions are likely to occur near conical intersections and intersystem crossings points (because of spin orbit coupling). The branching of the population as a function of the probabilities values is introduced by stochastic algorithm; so many trajectories must be run in order to obtain reliable results. The appropriate number of trajectories as well as how they are generated will be discussed in following sections of this chapter (see section 4.4)

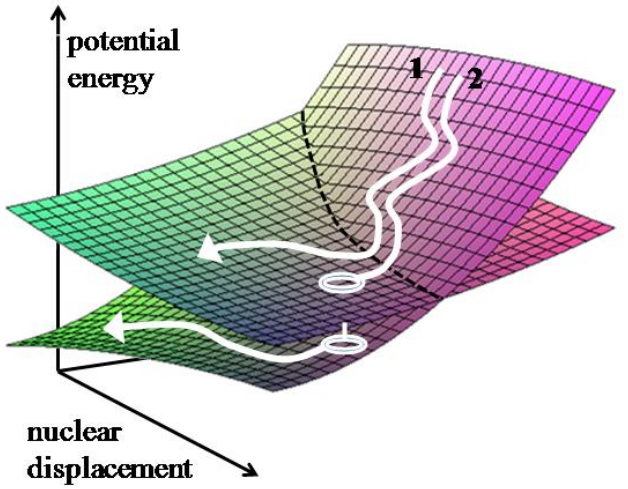

Figure 4.1. Surface Hopping scheme extracted from Ref.

In the Surface Hopping model the chemical system evolves on a PES and, at any time, the transition probabilities to the other PES are calculated. The main differences between the available SH models is how the transition probabilities are calculated. The most popular one is the Tully's[1] "fewest switches" algorithm, which provides accurate results for large molecular systems within reasonable computational cost. Since this is the method employed in the dynamics computed in this thesis, it will be discussed in the following.

Let's define $\mathrm{N}_k\ (t)$ as the number of trajectories found on q given surface U_K at a given time t. Then the fraction of the total trajectories (N_T) running on it is given by

$$\Pi_k\ (t) = \ \mathrm{N}_k\ (t)/\mathrm{N}_T \tag{4. 22}$$

For each trajectory, there is a given probability of running on this surface $\mathrm{P}_K(t)$, as well as for the rest of dynamic quantities, so it is more appropriate to define averaged probabilities

$$\overline{\mathrm{P}}_K(t) = \frac{1}{\mathrm{N}_T}\sum_{j=1}^{\mathrm{N}_T}\rho_{KK}^{(j)} \tag{4. 23}$$

where $\overline{\mathrm{P}}_K(t)$ is the averaged probability of the state $|\psi_K\rangle$ at any time t. Ideally Π_k and $\overline{\mathrm{P}}_K$ should be the same at a given time, then the SH algorithm is internally consistent if for each state and time the following equation is valid

$$\Pi_k = \overline{\mathrm{P}}_K \tag{4. 24}$$

The diagonal elements of the density matrix (state probabilities) are

$$\dot{\rho}_{KK}^{(j)} = -\sum_{L\neq K} 2\Re\left[A_L A_K^* e^{i(\gamma_K-\gamma_L)}\right]\sum_{\alpha}\dot{Q}_\alpha G_{KL}^{(\alpha)} = -\sum_{L\neq K} B_{KL}^{(j)} \tag{4. 25}$$

In order to achieve internal consistency hops at regular times randomly according to the probabilities $P_K^{(j)} = \rho_{KK}^{(j)}$. However this is totally unphysical, since it would mean that hops could take place in regions where the probabilities are negligible and many hop could occur, and the idea is to hop when probabilities change and to minimize the

number of hops. Then we should define a averaged transition probability,$\overline{T}_{k\to L} > 0$, within a small period of time Δt such that for each state K and time t

$$\Delta\Pi_k\,(t) = \overline{P}_K\,(t)\Delta t \qquad 4.\,26$$

Where

$$\Delta\Pi_k\,(t) = \Pi_k\,(t+\Delta t) - \Pi_k\,(t) \qquad 4.\,27$$

If the concept of averaged transition probability is introduced

$$\Delta\Pi_k = -\sum_K \Pi_k\,\overline{T}_{k\to L} + \sum_L \Pi_L \overline{T}_{L\to K} \qquad 4.\,28$$

If coherent propagation of the electronic density matrix is assumed, the derivative of the averaged state probabilities is

$$\overline{\dot{Pk}}\,(t)\Delta t = -\sum_{L\neq K} \bar{B}_{KL}\,\Delta t \qquad 4.\,29$$

Substituting the latest equation into the previous one

$$\overline{T}_{L\to K} = max\left\{0, \frac{\bar{B}_{KL}}{\Pi_k}\Delta t\right\} \qquad 4.\,30$$

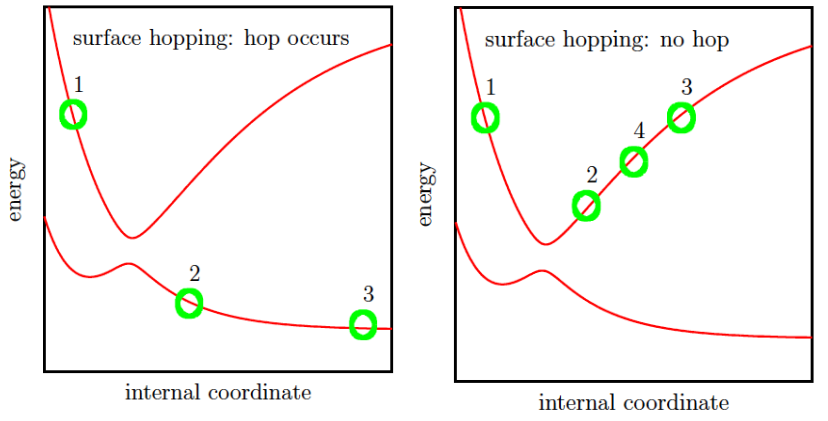

Figure 4.2. Surface Hopping scheme (REF). Upper panel shows a surface hopping scheme close to an avoided crossing which afterwards the system evolve in the lower PES. In the lower panel no hop takes place and the system oscillates in the upper PES.

This is known as the exact fewest transition probability. If this transition probability could be computed and used for all the trajectories, Π_k would coincide with $\overline{P}_K$ ate each time. However, treatment of averaged quantities is complicated and also implies that independent paths will affect each other. The Tully's approach for this transition probability is[1]

$$T(K \to L) = \frac{B_{KL}\Delta t}{P_K} \qquad 4.31$$

where the time derivative of the probability of finding the system in the state K can be expressed as a sum over all the states probabilities.

Starting from an ensemble of trajectories on a given PES, the transition probability, $T(K \to L)$, is evaluated at each time step, Δt.

Given those probabilities a (pseudo) random number ξ uniformly distributed in the interval [0,1] is generated and the hop between K and L surfaces take place if

$$\sum_{L=1}^{M-1} T(K \to L) < \xi \leq \sum_{L=1}^{M} T(K \to L) \qquad 4.32$$

We can now evaluate the expression for the change of Π_k within a time step

$$\Delta\Pi_k = \frac{\Delta t}{N_T} \sum_{L} \left[- \sum_{j \,\epsilon\, K} \frac{B_{KL}}{P_K} + \sum_{j \,\epsilon\, L} \frac{B_{LK}}{P_L} \right] \qquad 4.33$$

where $j \,\epsilon\, K$ means that only the trajectories running on K at t are considered.

After a jump from surface U_k to U_L the nuclear kinetic energy has to be changed in order to conserve the total energy. The kinetic energy must be rescaled by $\Delta \mathrm{T} = U_k - U_L$ after a hop. Then

$$\mathrm{T}' = T + U_k - U_L \qquad 4.34$$

This is usually done by adjusting the nuclear momenta along the nonadiabatic coupling vector $G_{KL}^{(\alpha)}$. In downward hops when $U_L - U_K > 0$ it should be possible to

alter the nuclear velocities in order to adjust the kinetic energy in the necessary way to ensure energy conservation. The same situation will be necessary for upward hops ($U_L - U_K < T$).

However, if the contrary situation takes place, that is $U_L - U_K < 0$ and/or $U_L - U_K > T$ for down and up hops respectively, it might happen that there is not enough energy to compensate the sudden variation of the potential energy. If that is the case the usual choice is to give up the hop. This "frustrated hops" is one of the discrepancy between Π_k and $\overline{P}_K$.

Another source of inconsistency between Π_k and $\overline{P}_K$ in surface hopping is connected with the lack of quantum decoherence. This phenomenon will be described in more detail in the section 4.6 and can be easily understood looking at Figure 4.2. When wavepackets are travelling on different surfaces and they get far from each other, the couplings between them are move away. Rather different quantum decoherence schemes has been implemented in view of use them with semiclassical treatments and can be very efficient on solving those problems of inconsistency (see sections).

Adiabatic vs Diabatic

Another important thing regarding Trully's surface hopping scheme is the selected representation for the potential description (recall Chapter 3, section 3.10). If a full quantum dynamics is performed then the result would be independent on the selected representation. If the adiabatic representation is selected the couplings are given by the nonadiabatic couplings but if the diabatic one is chosen instead, those couplings are zero, but they will be non-zero out of the diagonal elements of the electronic Hamiltonian. Both cases should give equivalent results for a full quantum dynamic calculation. However, this situation will change when TSH algorithm is used.

When classical trajectories plus SH scheme is used the results do strongly depend on the selected representation and in fact, this scheme only works fine within the adiabatic representation (that is why the above discussion has been performed using this approach). Why this different behaviour? Why does SH scheme only work under the adiabatic representation? Two main reasons:

(1) The "true" Potential Energy Surfaces (PES) are better described when adiabatic energies are used. That is because the PES computed adiabatically are well defined contrary to the diabatic energies which are ambiguously defines.

(2) The second reason implies the nonadiabatic couplings calculations. In the adiabatic representation those couplings are well localised. Then, localizing the surface hoppings is easier. However, in the diabatic representation the

nonadiabatic couplings are deslocalized, and as a consequence, the trajectory can hop very often, more than desirable.

Further reasons regarding how the spin orbit couplings are calculated in the two different representations can be also used to choose the more appropriate scheme, (see section 4.7 on this chapter)

4.4 Initial Conditions Sampling

As said before, surface hopping methods requires running a great number of trajectories in order to get relevant results. How many trajectories are really needed? This number depends on several things. First, on the process under study, if for instance one in interested on the quantum yield for a given electronic state, normally more than 50 trajectories are needed to obtain a statistically reliable averaged population. For instance, if N_T are run and the probability of the studied event is P, the average (x) and its standard deviation (σ) for the interesting even are

$$x = N_T P \qquad 4.35$$

$$\sigma = \sqrt{N_T P(1-P)} \qquad 4.36$$

The relative error is then

$$\sigma/x = \sqrt{(1-P)/x} = \sqrt{P(1-P)/N_T} \qquad 4.37$$

It can be demonstrated using the above equations, that for a very probable event, let say 50% of quantum yield and running 500 trajectories, the expected error is 2%. However if we are expecting to obtain results for a less likely process let say 10% for the same number of trajectories similar errors are found but for lower probabilities. Then it will be safer to increase the number of trajectories. Then, why not to run always thousands of trajectories?

The mots limiting factor when deciding the appropriate number of trajectories to run is the computational cost. That is because the selected method for computing the electronic structure determines the complexity of the calculation and as a consequence the computational time. If a single trajectory is able to run for a given time in less than few days lots of trajectories can be run, but when, on the contrary, the same time propagation takes several weeks to be completed the number of trajectories must be limited to few hundreds or even less. When analytical surfaces are calculated, thousands of trajectories are usually selected. On the other hand, when the surfaces are obtained using semiempirical methods (see section 4.5 on this Chapter) usually few hundred (200-400) of trajectories are required. However, this number decreases dramatically when ab initio methods are employed and in those cases less than 100

trajectories are usually run. Then a compromise between the accuracy and the computational demanding must be reached.

Another reason for running so many trajectories is that the initial conditions must describe the initial state under study. As said in Chapter 2, the most important event in photochemistry is light absorption so the sampling of the initial conditions must take into account both the coordinates (Q) and the momenta (P) describing the initial ground state and the exciting light. The quantum harmonic oscillator can be used to sample the coordinates and momenta according to a Wigner distribution. Also finite temperature effects can be used to do the same according to Boltzamann's distribution.

Wigner distribution

If normal coordinates are defined:

$$Q_\sigma = \sum_\sigma L_{r\sigma}\sqrt{m_r}\,\Delta Q_r \qquad 4.38$$

where ΔQ_r is the cartesian displacement with respect to the equilibrium geometry of the initial state and $L_{r\sigma}$ is an orthonormal matrix which is obtained diagonalizing the Hessian matrix of the ground state PES. The cartesian displacements are easily obtained by inverting the above equation

$$\Delta Q_r = m^{-1/2}\sum_\sigma L_{r\sigma}\,Q_\sigma \qquad 4.39$$

Similar equations can be written for the Cartesian velocities $\dot{Q}_\alpha$ and the momenta P_α. In the vibrational ground state, the distributions for the normal coordinates and momenta are Gaussian functions

$$W(Q_r) = \sqrt{\frac{\omega_r}{\pi}}\,e^{-\omega_r Q_r^2} \qquad 4.40$$

$$W(P_r) = \frac{1}{\sqrt{\pi\omega_r}}\,e^{-P_r^2/\omega_r} \qquad 4.41$$

Imposing the above distributions in a classical system, two independent distributions of potential and kinetic energy are generated. If the potential is harmonic, the total

energy averages to the zero point energy (ZPE), $\omega_\sigma/2$ for each normal mode. The ZPE increases with the size of the molecule, which is not a problem in quantum wavepacket dynamics since it remains at least equal to $\omega_\sigma/2$. However, in classical calculations, the ZPE can concentrate along a single trajectory allowing the system to overcome energy barriers that would not be possible without this extra energy. A solution to this problem is to keep the highest frequency modes (C-H, N-H, O-H ….) frozen during the sampling procedure.

Once a starting set of geometries has been produced, the excited state from where the simulation takes place must also be chosen. If more than one state are in the requested energy interval, its population is proportional to the respective contributions to the absorption spectra, in other words, proportional to its transition dipole moment. In this way, the dynamic simulation starts with a set of different geometries, and from different excited states.

Boltzamann distribution

For large systems there is no possibility to sample using the Wigner distribution because of several reasons. First, usually the computing of the frequencies for such large systems is too expensive. Although they could be calculated there will be such a number of very low frequencies that using the harmonic approximation could be risky, since for frequencies with it is also important to take into account the vibrational thermal excitation and the anharmonicity of the potential. Then for those medium to large systems the Boltzamann distribution sampling is preferred. In order to perform this kind of distribution a Brownian trajectory starting from the equilibrium geometry can be performed for a long enough time and using a thermostat. In our studied QM/MM case (see Chapter 7) this trajectory was run during 50 ps and the Bussi-Parrinello thermostat was used.

Independently on the used distribution for the sampling, the procedure to select the trajectories to be run as a function of excitation probabilities, that is, the square of the transition dipole moment, is

(1) A set of points (Q_i, P_i) is selected following the Wigner or the thermal trajectory.

(2) The number of trajectories to be launched from the starting point (Q_i, P_i) depends on the computed transition probabilities for the considered excited state and that they are included within an energy window. Why to use an energy window? Instead of using only a given excitation energy a given interval is used

$$\Delta E \pm \Delta\Delta E/2 \qquad 4.42$$

This means that a given trajectory is selected only if

$$\Delta E - \Delta\Delta E/2 \leq U_k - U_0 \leq \Delta E + \Delta\Delta E/2 \qquad 4.43$$

where $U_k - U_0$ defines the transition energy. If this condition is not satisfied no trajectory is launched from this point. If a small $\Delta\Delta E$ is used, almost all trajectories will be rejected, so it only can be used if lots of starting points are available.

(3) If the above condition is satisfied, the transition energies (ΔE_1) and dipoles (μ_i) are computed for the selected point.

(4) If one or more states satisfy the condition in state (2) one is chosen by an stochastic algorithm with state probability proportional to μ_i^2. Then several trajectories can be launched from the same point starting from different states. The maximum number of trajectories that can be started from a given point (Q_i, P_i) is computed by

$$\mu_i^2 \Big/ \mu_{ref}^2 \qquad 4.44$$

within a given N_{max}

(5) Finally, a given trajectory starting on a given state from a given point is launched if

$$\mu_i^2 < x_j N_{max} \mu_{ref}^2 \qquad 4.45$$

being x_j a random number between 0 and 1.

4.5 Semiempirical methods

As said in the previous section, PES are easily computed using semiempirical methods (SE) so they can be an alternative to *ab initio* methods for the treatment of molecules of large size, and/or when a great number of trajectories must be simulated. They are called semiempirical because they use semiempirical parameters to reproduce experimental or higher-level calculations data. This parametrization joined to other several approximations considered in SE methods make them much cheaper, from the computational point of view.

SE methods are similar to ab initio approaches in the sense they used the same SCF procedures (RHF, UHF, CI, etc…). However, important differences between both methods are found relative to:

(1) *Valence electrons*. In a SE calculation only the valence electrons are taken into account. Core electrons are treated as a part of the atomic nuclei. Therefore, only basis functions for the valence electrons are needed. Moreover, SE methods use minimal basis sets.

(2) *The integrals*. The core and the two-electron integrals are not explicitly calculated, what cuts out the main effort in *ab initio* calculations. Some of these integrals are considered to be zero (depending on the SE method) and the rest are evaluated in an empirical way.

(3) *The basis functions*. Atomic basis functions are assumed to be orthonormal. The only exception are the one electron-two center integrals.

The zero-differential-overlap (ZDO) approximation is the basis of the semiempirical methods and consists on setting all the products of atomic orbitals $\mu_A \nu_B$ to be zero and the overlap integral $S_{\mu\nu} = \delta_{\mu\nu}$ (where δ is the Kronecker delta). In other words, it neglects the product of functions on different atoms and reduces the overlap matrix S to a unit matrix. Furthermore, at this approach all the three- and four-center two electron integrals vanish. The remaining integrals are introduced as parameters, which values are taken from higher-level calculations or experimental data. The different semiempirical methods are classified according to the approximations made for the one- and two-electron integrals.

In the neglect of diatomic differential overlap (NDDO) method there are no further approximation that those considered for the ZDO approach. It considers all the two-electron integrals $(\mu\nu|\sigma\lambda)$ but forcing μ and ν to be on the same atomic center and σ and λ to be in the same atomic center too (but these two atomic centers can be different).

The MNDO[2] model is based on the NDDO approximation and it employs a real atomic minimum basis for the valence electrons. The molecular orbitals (MO) are obtained solving the SCF equations where the superposition of atomic orbitals is neglected. For a closed-shell system

$$\boldsymbol{FC} = \boldsymbol{C}\epsilon \qquad 4.46$$

where $\boldsymbol{F}$ is the Fock matrix, ϵ is the diagonal matrix of the MO energies and $\boldsymbol{C}$ is an orthogonal matrix. The Fock matrix for two given A and B atoms can be written as

$$F_{\mu_A\nu_A} = h_{\mu_A\nu_A} + \sum_{\lambda A,\sigma A} P_{\lambda A,\sigma A}\left[\langle \mu_A\nu_A|\lambda_A\sigma_A\rangle - \frac{1}{2}\langle \mu_A\lambda_A|\nu_A\sigma_A\rangle\right] + \sum_{B}\sum_{\lambda B,\sigma B} P_{\lambda B,\sigma B}\langle \mu_A\nu_A|\lambda_B\sigma_B\rangle \quad 4.47$$

$$F_{\mu_A\nu_B} = h_{\mu_A\nu_B} - \frac{1}{2}\sum_{\lambda A,\sigma B} P_{\lambda A,\sigma B}\langle \mu_A\lambda_A|\nu_B\sigma_B\rangle \quad 4.48$$

where $h_{\mu\nu}$ and $P_{\mu\nu}$ are the one-electron Hamiltonian matrix and the density matrix elements. Then the total energy can be obtained as the sum of the electronic energy E_{HF} and the nucleus-nucleus repulsion energy E_{AB}^{core}

$$E_{HF} = \frac{1}{2}\sum_{\mu\nu} P_{\mu\nu}(h_{\mu\nu} + F_{\mu\nu}) \quad 4.49$$

$$E_{tot} = E_{HF} + \sum_{A<B} E_{AB}^{core} \quad 4.50$$

The following interactions and parameters are included in the MNDO model

(1) One-center one-electron integrals

$$h_{\mu_A\nu_A} = U_\mu\delta_{\mu_A\nu_A} - \sum_{B\neq A} Z_B(\mu_A\nu_A|s_Bs_B) \quad 4.51$$

where U_μ is the semiempirical parameter, which represents the energy of the χ_μ orbital in the A atom. The second term is an approximation of the core-electron attraction, where Z_B is the charge of the B core and $s_B$is an s-type orbital centered on B.

(2) Two center one-electron integrals

$$h_{\mu\nu} = \frac{1}{2}S_{\mu\nu}(U_\mu + U_\nu) \quad 4.52$$

where U are the semiempirical parameters for a given atom and orbital and S represents the overlap between the two orbitals.

(3) One-center two-electron repulsion integrals $(\mu_A \nu_A|\sigma_A \lambda_A)$ are represented by five atomic parameters based on s and p orbitals.

(4) Two-center two-electron repulsion integrals $(\mu_A \nu_A|\sigma_B \lambda_B)$ are taken into account through another semiempirical parameter (atomic orbital exponent) depending on the atom and the orbital.

(5) Two-center core-core repulsions

$$E_{AB}^{core} = E_{AB}^{electr} + E_{AB}^{effective} \qquad 4.53$$

$$E_{AB}^{electr} = Z_A Z_B (s_A s_A|s_B s_B) \qquad 4.54$$

The $E_{AB}^{effective}$ term is the Pauli exchange repulsion and contains four parameters more.

The Austin Method 1 (AM1)[3] was developed at the University of Texas at Austin by Dewar, Zoebisch, Healy, and Stewart in 1985. The main achievement of AM1 is to overcome core-core repulsion problems of NDDO model. Gaussian functions centered at internuclear points are added to obtain a better description of these repulsions.

The nuclear repulsion energy of two nuclei A and B is calculated as

$$V_N(A,B) = Z_A Z_B (s_A s_A|s_B s_B) + \frac{Z_A Z_B}{r_{AB}} \sum_{i=1}^{4} \left[a_{A,i} e^{-b_{A,i}(r_{AB}-c_{A,i})^2} + a_{B,i} e^{-b_{B,i}(r_{AB}-c_{B,i})^2} \right] \qquad 4.55$$

where Z is the charge of the atomic core, r is the interatomic distance, $(s_A s_A|s_B s_B)$ represent the repulsion between electrons in the same center and a, b and c are the Gaussian functions centered at various distances. AM1 is one of the most widely used SE methods, giving satisfactory results for geometries, energies and dipole moment calculations.

The MNDO model and its standard applications (AM1, PM3, PM5) have been parameterized with respect to the ground state properties. Then those methods are able to reproduce ground state properties and their equilibrium geometries. For the studied projects during this thesis, which always include excites states and often geometries completely different from the equilibrium geometry **ad hoc reparameterization** is often necessary (see next section).

Furthermore, our cases are frequently dominated by state mixing which are better described by CI interaction since HF do not lead correctly with this situation (recall section 3.7 in Chapter 3). For this reason the group in Pisa has developed a semiempirical CI approach based on SCF molecular orbitals with **floating occupation numbers (FOMO-CI)**

Floating occupation numbers

Certain chemical problems such as bond-breaking and excited states require the use of multireference methods, as CASSCF, for their correct description. However, this approach is at the same time expensive and not compatible for semiempirical scheme. A cheaper and effective alternative is to run a floating (or fractional) occupation number SCF calculation followed by a CI calculation. M. Persico and co-workers[4,5] have implemented this procedure in the MOPAC program.[6]

This method describes the population of each orbital as a Gaussian function (along the energy axis ε) centered at the corresponding Fock eigenvalue. For the i-th orbital with ε_i energy its population is described by

$$f_i(\varepsilon) = \frac{\sqrt{2}}{\sqrt{\pi}\omega}\, e^{-(\varepsilon-\varepsilon_i)^2/(2\omega^2)} \qquad 4.56$$

where ω, the orbital energy width, is an arbitrary parameter. The electronic $f_i(\varepsilon)$s functions are such that

$$\int_{-\infty}^{+\infty} f_i(\varepsilon)\, d\varepsilon = 2 \qquad 4.57$$

The occupation number are evaluated as

$$O_i = \int_{-\infty}^{\varepsilon_F} f_i(\varepsilon)\, d\varepsilon \qquad 4.58$$

where ε_F, the Fermi level, is define imposing the sum of the occupation numbers to be equal the total number of electrons N

$$N = \sum_i \int_{-\infty}^{\varepsilon_F} f_i(\varepsilon)\, d\varepsilon \qquad 4.59$$

Virtual orbitals with a high energy will have $O_i = 0$, while for low lying orbitals with $\varepsilon_F - \varepsilon_i \gg \omega$ the occupation number will be close to 2. In the MOPAC program fractional occupation numbers are limited to the active orbitals involved in the CI.

This procedure yields a set of well-behaved MOs, even in the case of degeneracy. However, the SCF energy does not have physical meaning and a subsequent CI calculation must be performed.

Reparameterization

The optimization of semiempirical parameters for C, N, S, O and H atoms has been carried out starting from the standard AM1 parameters. Geometrical parameters, vertical excitation and adiabatic energies (target values) are requested to be well reproduced as criteria for the optimization procedure. Specific targets used in the parametrization procedure are detailed in the results chapter. The optimization is performed minimizing the value of the F(P) function[7]

$$F(P) = \left[\sum_i \left(\frac{V_{s,i}(P) - V_{t,i}}{V_{t,i}}\right)^2 W_i\right]\left[\sum_i W_i\right]^{-1} \qquad 4.60$$

where $V_{t,i}$ are target values, $V_{s,i}\,(P)$ semiempirical computed values (which depend on the semiempirical parameters P) and W_i are the weights of the targets. This function is calculated for the initial set of parameters P, resulting the error between the computed values and the target ones. The parameters are modified in order to minimize this error. Once the function is converged, the minimum error is achieved and the set of parameters is the optimized one.

For the 6-Thioguanine case, the only geometries not correctly reproduced after the parametrization are those of the S_1 and T_2 excited states where the S atom is deviated from the plane of the thiopurine ring. In fact, we found the SCCC semiempirical dihedral to be almost equal to 180º, while the target value is around 150º.

In order to solve this issue, the following correction function was added

$$U_{cos}(\theta, \boldsymbol{\theta_0}) = C\left[cos\left(\frac{\theta - \boldsymbol{\theta_0}}{A}\right) - 1\right] e^{-B(\theta - \boldsymbol{\theta_0})^2} \qquad 4.61$$

θ represents the dihedral value, and $\boldsymbol{\theta_0} = 180º$. A, B and C are adjustable parameters, which are also optimized. For

$$A = 0.0431481481 \quad B = 0.0003600000 \quad C = 0.0308799012$$

a good description of S_1 and T_2 excited states equilibrium geometries

For 4-thiothymine no further considerations were necessary, but instead starting the parameterization from the default AM1 values, the previously obatined values for 6-TG where employed.

For both systems an error ~10% was obtained which is not meaningful due to the large values requested in the parameterization procedure.

4.6 Quantum Decoherence

The lack of quantum decoherence is probably one of the main drawbacks of mixed quantum/classical description of nonadiabatic molecular dynamics. The decoherence of an open quantum system is the decay of the off diagonal elements of the reduced density matrix due to its interaction with the environment. Two main physical effects are responsible for quantum decoherence. The first (so-called pure dephasing) is due to the fluctuations of the energy difference between the states of the system. The second term arise from the overlap of the nuclear wavepackets connected to different electronic states. The first effect is taken into account by most mixed quantum classical approaches, also by surface hopping. However, the second effect cannot be directly taken into account since it strictly depends on the nuclear wavefunction, which are treated classically. Several procedures have been implements in order to introduce quantum decoherence in semiclassical approaches.

The correction proposed by Truhlar and co-workers is the following. At each time step the coefficients determining the transition probabilities are evaluated. However these coefficients are multiplied by a scaling factor

$$C'_K = C_k e^{-\Delta t/\tau_{KM}} \qquad 4.62$$

where M and K are two different states. This scaling factor ($e^{-\Delta t/\tau_{KM}}$) is related with the kinetic energy through

$$\tau_{KM} = \frac{\hbar}{|E_K - E_M|}\left(1 + \frac{C}{E_{kin}}\right) \qquad 4.63$$

where E_{kin} is the nuclear kinetic energy and C is a constant, usually set to 0.1 hartree. This correction of the expansion coefficients tends to equate populations to distributions, cancelling the coherence effects. When the energy difference between the two states M and K is large, the transition probability between them becomes small. However, when this correction is negligible when the energy gap between those states is small, then the probabilities are large and the surface hopping algorithm must not be corrected.

Overlap Decoherence Correction (ODC)

This new correction has been developed by Granucci and Persico to include the quantum decoherence effects which are neglected by standard surface hopping algorithms. With this purpose, this correction besides considering representative points in the current adiabatic potential energy surface, it also introduces representative point in the other PES which put some probability on it. To do that, Gaussian wavepackets of a given width (σ) are associated at each representative point (see Figure 4.3) and their time evolution is evaluated. Recall Figure 4.3, at time equal to 0 (t_0) the A states carries all the probability. After some time t_1 the state B increases its probability and a Gaussian wavepacket is introduced in B. This wavepacket evolves faster since its available energy is larger. At time equal to t_2 if there is still some probability on B another wavepacket is added, if the overlap between them is small the wavepackets on B are annihilated and their probability is attributed to A.

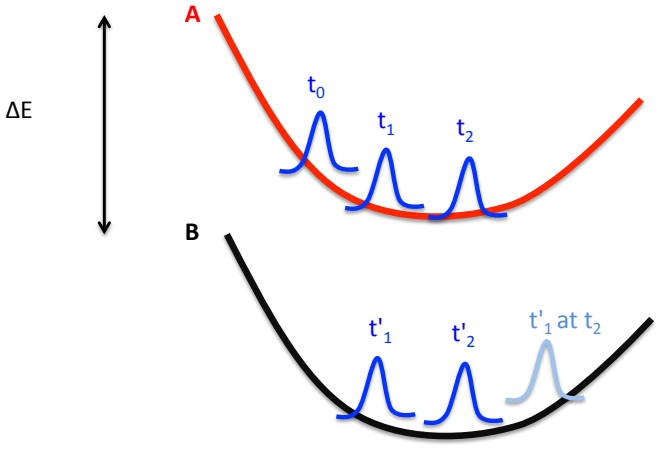

Figure 4.3. Overlap Decoherence Correction scheme.

As a summary, the ODC approach is the following:

(1) A wavepacket is associated with the leading representative point propagating on the current state (A).

(2) Every timesteps, if the probability of any state, B for instance, (different from A) has increased a new representative point is created on that state along with its wavepacket.

(3) The time evolution of the wavepackets is computed in a simplified way in order to not perform further electronic structure calculations.

(4) The overlap between any wavepacket and the leading one is evaluated (t_1' and t_1' at t_2). If it drops under a given threshold (S) the leading one is eliminated and the corresponding probability is attributed to the current state.

(5) The representative points and their Gaussian wavepackets can also be eliminated if the probability has increased with time. In those cases, starting from the last added wavepacket, the previous ones are supressed until the probability is equal to the one presented some time before.

(6) When a surface hopping occurs, a new leading wavepacket is created and all the existing ones on that PES are eliminated.

This new algorithm implies no further computational efforts and only depends on two new parameters, the Gaussians width and the overlap threshold. The ODC scheme has been tested in four different systems given quite accurate results and it was found to be robust with respect to the overlap threshold, and to give similar results for a different Gaussian widths ranging from 0.5 to 5.

4.7 Spin Orbit Coupling and Surface Hopping

As said before (see Chapter 3, section 3.10) the total Hamiltonian

$$\hat{H}_{tot} = \hat{H}_{el} + \hat{H}_{SO} \qquad 4.64$$

The spin orbit term is usually small compared to the electronic Hamiltonian. Introducing this term into the surface hopping scheme is not an easy task since the spin orbit couplings split the multiplets increasing the number of states. Furthermore,

the eigenstates of $\widehat{H}_{tot}$ are complex and present nonzero diagonal nonadiabatic couplings.

When states of different spin are included in the dynamics simulation, equation 4.35 must be generalized according to[8]

$$T(\beta \rightarrow \alpha) = \frac{2\Re\left\{c_\alpha(t)c_\beta^*(t)\left[\frac{i}{\hbar}H_{\beta\alpha}[\vec{R}(t)] + K_{\beta\alpha}[\vec{R}(t)]\right]\right\}}{c_\beta^*(t)c_\beta(t)}\Delta t \qquad 4.65$$

where $H_{\beta\alpha}$ represents the effective Hamiltonian, whose diagonal elements are the different potentials and the off diagonal elements correspond to the diabatic couplings, and $K_{\beta\alpha}$ is related to the nonadiabatic couplings between states. Two different approaches can be used to simulate SOC dynamics. The diabatic representation includes the SOC in the potential part of the Hamiltonian. In contrast, in the adiabatic representation, which is the one in our simulations, the SOC is included in the kinetic part of the Hamiltonian. In this case, first the eigenvalues of the electronic Hamiltonian and the couplings, $K_{\beta\alpha}$, are calculated separately. Afterwards, the full matrix is diagonalized. Further details are given in the followin.

Diabatic approach

The surface hopping is performed with the eigenstates $|\psi_L\rangle$ and eigenvalues E_K of the electronic Hamiltonian, $\widehat{H}_{el}$. The matrix elements

$$\langle\psi_K|\widehat{H}_{SO}|\psi_M\rangle \qquad 4.66$$

are then treated as residual couplings. The use of this approach in surface hopping scheme present several drawbacks. This approach will work if SOC are small and effective only close to degeneracy regions. However, there are many systems where those couplings have been found to be important also far from those crossing regions.

Further problems regarding axis rotations can be present under this scheme. In this approach the singlet and triplet are not mixed during the dynamics and their singlet and triplet feature are conserved during it. If a rotation of the axis frame takes place, the three component of the triplet will be mixed within this rotation. This rotation should not affect the dynamics, since the singlet triplet probability should be invariant to rotation, however for the SH this is only possible if the triplet state is treated such that is not possible to distinguish between the three component. However this is an approximation, since each multiplet should be considered as a singlet state.

Let's consider then the adiabatic approach.

Adiabatic approach

In this approximation, rotation invariant is not a problem since the singlet and triplet states are mixed and treated as spin-mixed eigenstates of $\widehat{H}_{tot}$. However, other problems arises when this approach is selected to run the dynamics.

In this case the nuclei evolve on a potential energy surface where the spin-orbit interaction is also considered, and then, the Newton equations of motion for the nuclei must be integrated. The main problem is that the analytical gradients of the energy for the spin-mixed wavefunctions must be calculated. This analytical gradients evaluation is the most complicated issue for the adiabatic approach. However, Granucci and Persico have developed a procedure, which allows the computing of that gradients for semiempirical CI wavefucntions.

For a given current state K, with

$$\widehat{H}_{tot}|\psi_K\rangle = U_K|\psi_K\rangle \qquad 4.67$$

then,

$$U_K = E_K^{el} + E_K^{SO} \qquad 4.68$$

where,

$$E_K^{el} = \langle\psi_K|\widehat{H}_{el}|\psi_K\rangle \qquad 4.69$$

and,

$$E_K^{SO} = \langle\psi_K|\widehat{H}_{SO}|\psi_K\rangle \qquad 4.70$$

Then the gradients of the spin-mixed states are

$$\frac{\partial U_K}{\partial Q} = \frac{\partial E_K^{el}}{\partial Q} + \frac{\partial E_K^{SO}}{\partial Q} \qquad 4.71$$

Although the difficulty to compute this gradients is the main drawback of working within the adiabatic approach, this is the most recommended way to perform the nonadiabatic dynamics. Specially, for systems where spin-orbit coupling terms are very important, the diabatic approximation is not recommended at all.

Then, for both systems 6-Thioguanine and 4-Thiothymine the dynamic simulations have been performed under the adiabatic approach.

4.8 QM/MM Method

When the system under study requires the inclusion of the solvent for an accurate description of its main photochemical behaviour and/or where the system itself is quite large, the above semiclassical dynamic simulations are not affordable. Computationally less demanding methods are then necessary. Molecular Mechanical (MM) methods enable to perform molecular dynamics in huge chemical and biological systems, up to thousand of atoms. Unfortunately, those methods are based on molecular mechanical force field, which are not able to describe changes in the electronic structure of the system. Again, for describing excited states, bond forming and/or breaking, quantum mechanical (QM) methods are required. So, QM are needed for the correct treatment of the system but they are computationally too expensive and MM are able to treat with large system but not with electronic excitation. What is the solution?

A natural solution to this problem is to combine the QM and the MM, the well-known QM/MM approaches. This powerful hybrid method allows the study of huge systems at reasonable computational cost but being also able to conserve the desirable accuracy. Then in QM/MM methods the most relevant and/or complex part of the system is treated quantum mechanically, while the rest of the molecular and/or the solvent are described within molecular mechanical force fields (see Figure 4.4).

Besides its extensive use in the study of organic and inorganic chemical reactions, QM/MM has been widely use in the study of biological systems, giving successful results for simulating enzymatic reactions, molecular docking, protein's fluorescence studies ...etc. Thereby, QM/MM has gained importance in the last 20 years since it present a theoretical alternative for the study of biological systems being able to accurate describe the biorelevant processes within an affordable computational cost.

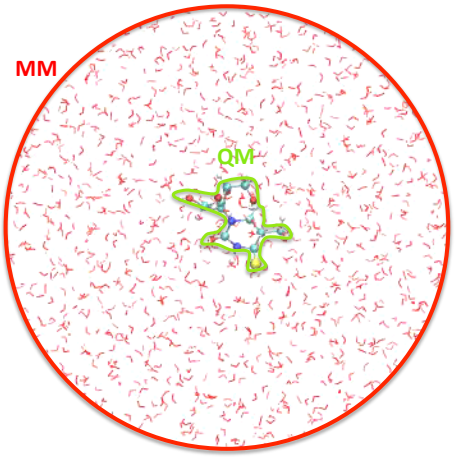

Figure 4.4. QM/MM scheme where the relevant part of the system is treated with quantum mechanic methods and the solvent (H_2O in this case) is described using molecular mechanical force fields.

The main procedure for the QM/MM approach is summarized below. The electronic Hamiltonian is divided into three terms, one specific for the QM subsystem,, one represented by the force field,, and the third one related with the interaction between the QM and MM subsystems:

$$\hat{H}_{el} = \hat{H}_{QM} + \hat{H}_{MM} + \hat{H}_{QM/MM} \qquad 4.72$$

The total energy can also by divided

$$U_K = U_{QM} + U_{MM} + U_{QM/MM} \qquad 4.73$$

where U_{MM} can be identified with $\hat{H}_{MM}$ while U_{QM} and $U_{QM/MM}$ are the expectation values from $\hat{H}_{QM}$ and $\hat{H}_{QM/MM}$ respectively.

The total energy can be expressed as

$$U_K = \langle \psi_K | \hat{H}_{QM} + \hat{H}_{QM/MM} | \psi_K \rangle + U_{MM} \qquad 4.74$$

The $\hat{H}_{QM}$ part takes the form adopted in the semiempirical methods.

Force Field: $\hat{H}_{MM}$

U_{MM} is obtained by a classical force field and it contains the interaction terms between the linked atoms as well as purely electrostatic and repulsion/dispersion interactions between pairs of non bonded MM atoms. A general force field form is

$$U_{MM}(\vec{R}_1, \vec{R}_2, \dots, \vec{R}_N) = \sum_{ibonds=1}^{Nbonds} U_{bond}(i_{bonds}, |\vec{R}_a - \vec{R}_b|) \qquad 4.75$$

$$+ \sum_{iang=1}^{Nang} U_{ang}(i_{ang}, |\vec{R}_a, \vec{R}_b, \vec{R}_c|)$$

$$+ \sum_{idihe=1}^{Ndihe} U_{dihe}(i_{dihe}, |\vec{R}_a, \vec{R}_b, \vec{R}_c, \vec{R}_d|)$$

$$+ \sum_{i=1}^{N-1} \sum_{j>i}^{N} U_{pairs}(i, j, |\vec{R}_a - \vec{R}_b|)$$

where U_{bond}, U_{ang}, U_{dihe} and U_{pairs} are the interaction terms depending on the bond length, the angles, the dihedral angles and on the distances between non bonded atoms, respectively. The four summations in the above equation run on N_{bond}, N_{ang} and N_{dihe} which are the number of the three kind of interactions. Finally the i_{bonds}, i_{ang} and i_{dihe} indexes specify which atoms a,b or c are involved, meanwhile, i and j represent two non bonded atoms. The U_{pairs} interactions, as said, before, include repulsion/dispersion and Coulombic terms related with atomic charges.

In our studies the model OPLS/AA[9] force field has been used as starting point. This is one of the most commonly used force fields (Optimized Potential for Liquid Simulations) force field, developed by William L. Jorgensen at Purdue University and later at Yale University.

The functional form for this force field is the following:

$$U_{MM} = U_{bonds} + U_{angles} + U_{dihedrals} + U_{nonbonded} \qquad 4.76$$

Bond stretching and the angle bending are defined as harmonic potentials, since they are very strong and fluctuate only slightly around their equilibrium values at room temperature

$$U_{bonds} = \sum_{bonds} k_r(r - r_0)^2 \quad 4.77$$

$$U_{angles} = \sum_{angles} k_\theta\,(\theta - \theta_0)^2 \quad 4.78$$

Torsions are described by a cosine expansion and can take any value within 360º depending on the height of the barrier between the low energy conformations.

$$U_{dihedrals} = \sum_{n=1}^{4} \frac{C_n}{2}[1 + \cos(n\delta)] \quad 4.79$$

And finally the nonbonded interactions are only taken into account for atoms three or more bonds apart. They are described as Coulomb and Lennard Jones two-body interaction terms. The Lennard Jones potential is a combination of attractive van der Waals forces due to dipole-dipole interactions and empirical repulsive forces due to Pauli repulsion.

$$U_{nonbonded} = \sum_{i<j} \left\{ \frac{q_i q_j}{r_{ij}^2} + 4\varepsilon_{ij} \left[\left(\frac{\sigma_{ij}}{r_{ij}} \right)^{12} - \left(\frac{\sigma_{ij}}{r_{ij}} \right)^{6} \right] \right\} f_{ij} \quad 4.80$$

where f_{ij} is a scaling factor, which is equal to 0.5 for 1-4 atoms and 1 otherwise.

Other Force Field approaches as AMBER[10] (Assisted Model Building and Energy Refinement), originally developed by Peter Kollman's group at the University of California San Francisco do not highly differ from the OPLS one.

Electrostatic Interaction: $\hat{H}_{QM/MM}$

This term contains all the coupling terms between the QM and the MM portions, which can be of three different kinds

$$\hat{H}_{QM/MM} = \hat{H}_{QM/MM}^{Coul} + \hat{H}_{QM/MM}^{vdW} + \hat{H}_{QM/MM}^{CA} \quad 4.81$$

Within the QM/MM approach used on these studies the electrostatic term contains the Coulomb interaction between the QM cores and electrons with the MM atomic charges

$$\hat{H}_{QM/MM}^{Coul} = \sum_{\alpha,m} \frac{q_\alpha q_m}{R_{\alpha m}} - \sum_{i,m} \frac{q_m}{R_{im}} \quad 4.82$$

where i is the number of electrons, α are the QM nuclei and m are the MM atoms. The core charge of the QM atom α, is q_α, while q_m is the atomic charge of the MM atom, m. $R_{\alpha m}$ and R_{im} are the distances between the QM electron or nuclei and the MM atom.

The Van der Waals interactions between the QM and MM atoms are

$$\hat{H}_{QM/MM}^{vdW} = 4 \sum_{\alpha,m} \varepsilon_{\alpha m} \left[\left(\frac{\sigma_{\alpha m}}{R_{\alpha m}} \right)^{12} - \left(\frac{\sigma_{\alpha m}}{R_{\alpha m}} \right)^{6} \right] \quad 4.83$$

where $\varepsilon_{\alpha m}$ and $\sigma_{\alpha m}$ are the Lennard-Jones parameters for the α QM atom interacting with the m MM atom, and are described by

$$\varepsilon_{\alpha m} = \sqrt{\varepsilon_\alpha \varepsilon_m} \quad 4.84$$

$$\sigma_{\alpha m} = \sqrt{\sigma_\alpha \sigma_m} \quad 4.85$$

The $\hat{H}_{QM/MM}^{vdW}$ and the first term in the $\hat{H}_{QM/MM}^{Coul}$ are included into the total energy expression and they are not state specific, but they can influence the PES and the dynamics of the system. The second term in the $\hat{H}_{QM/MM}^{Coul}$ expression is added to the $\hat{H}_{QM}$ part to perform the electronic wavefunction and energies calculations and is treated in the same way that electron-nucleus electrostatic interactions inside the QM region. This term must be added before diagonalizing the Hamiltonian in order to achieve state-specific electronic energies.

The last term, $\hat{H}_{QM/MM}^{CA}$ involves the connection atom (CA). Since the QM/MM calculation is performed under a real system the QM part has to be complete, no dangling bonds are permitted. As easy way to solve this problem is to use a CA, that is, to finish the bond with an artificial atom, which act as a link between the QM and the MM part and is also used to saturate the QM part, in other words, an artificial atom is introduced in the bond defining the two parts. This atom uses to be hydrogen and this theory is the well-known linking atom approach (see Figure 4.5).
Further approaches have been proposed in order to avoid ambiguities in the treatment of the interactions involving this atom. The one used during this thesis and explained above, was first described by Antes and Thiel[11] and replaces a carbon atom of the system by an hydrogenoid atom with one s atomic orbital. Its electron interacts quantum-mechanically with the rest of the AM part while the interaction with the MM

part is ensured by mechanical and electrostatic embedding. The approached implemented by Persico et al[12] only differs in the treatment of the electronic interaction between the connection atom and the MM part, as well as in the parameterization.
Then the $\hat{H}^{CA}_{QM/MM}$ involves MM contributions that involve the CA, at least one MM atom and possibly one or two QM atoms.

The PES depends on the distances, angles and dihedral angles, which involve covalent bonds around the QM/MM boundary and those dependences are reflected in the $\hat{H}^{CA}_{QM/MM}$ term. The connection atom has a fractional charge, contrary to the rest of atoms

$$q_{CA} = Q + 1 - \sum_{m} q_m \qquad 4.86$$

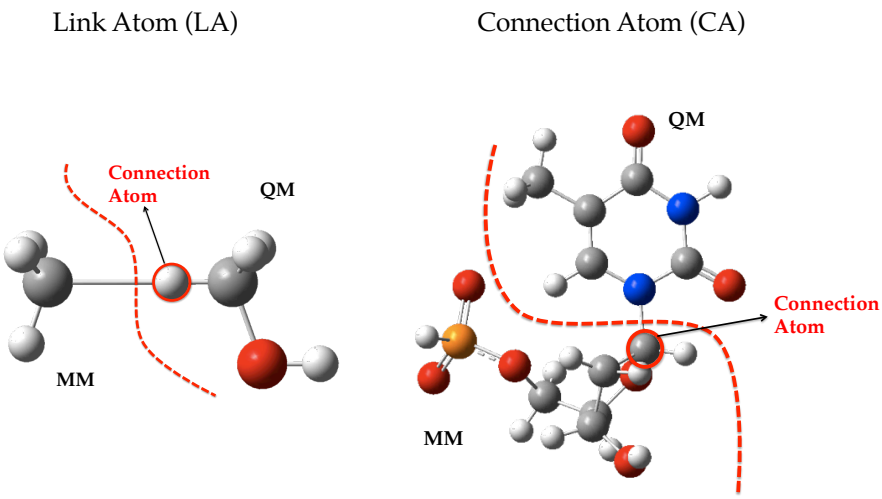

Figure 4.5. Illustration of the linking atom (left) and connection atom (right) scheme. The most relevant part of the system from an electronic point of view is treated with QM and the rest of the molecule is described with MM.

Each MM atom presents an attributed q_m as prescribed by the used force field, but preserving the total charge, Q, of the QM/MM system. Usually this total charge is equal to zero, however, the QM and MM subsystems are charged. In a practical way, the charge of the CA, q_{CA}, is determined in view of the charges of the MM groups directly bonded to it. If q_{CA} is overestimated (for instance if the CA is a carbon atom replaced by a hydrogen, the q_{CA} exceeds 1), it induces a polarization in the next QM bond. Furthermore, the CA also interacts with the MM part through the electronic density (see $\hat{H}^{Coul}_{QM/MM}$ expression) and also through q_{CA}. This excess of charge must be fixed and it is better to treat it within the MM part, then all interactions of the CA are with MM atoms are included (from second neighbours on). These interactions are

usually proportional to $q_{CA} + q_{el}$ where $q_{el} \approx -1$ is the CA electronic charge. Therefore, a core charge $q'_{CA} = 1$, which cancels q_{el} and annihilates the total interaction, is used when computing the $\widehat{H}^{CA}_{QM/MM}$ electrostatic terms.

The semiempirical parameters for the connection atom as for the QM atoms must be optimized. The main issue of this parameterization is that, an atom containing only 1 electron must reproduce the geometry and electronic structure of the substituted one. Then, as done before for the AM1 parameters, the best option is to list several properties of a full QM calculation and try to reproduce them with a QM/MM calculatio

The above conjugated semiempirical QM/MM multistate method using the connection atom approach to treat covalent bonds linking the QM and MM parts, can be used to effectively treat with excited states and bond breaking in the QM part.

4.9 SHARC Method

The SHARC (Surface-Hopping-in-Adiabatic-Representation-including-arbitrary-Couplings) method has been implemented in the group of Prof. González[13] to provide a semiclassical description of the coupled electronic and nuclear motion in complex molecular systems. SHARC also follows the time evolution of the system using a mix of quantum and classical dynamics, where the electrons are treated quantum mechanically and the nuclei classically. Equation 4.69 defines the transition probability for a hop using the time dependent coefficients of the electronic wave function. The SOC terms are also treated within the adiabatic approach, the coupling terms are moved to the $K(R\,(t))$, which evaluates the change of the electronic basis functions with time

$$K_{\alpha\beta}(R(t)) = \left\langle \phi_\beta(R(t);r) \middle| \frac{\partial}{\partial t} \middle| \phi_\alpha(R(t);r) \right\rangle \qquad 4.87$$

Then the $H^d(R(t),t)$ matrix is diagonalized, and afterwards, the $K(R\,(t))$ matrix is recalculated, leading to localized couplings in geometries where the electronic states are (nearly) degenerated.

In order to obtain the matrix that diagonalize the Hamiltonian, the electronic wave function is expanded as a linear combination of basis sets

$$\left|\phi_{\beta}^{d}(R(t);r,t)\right\rangle = \sum_{\alpha} U_{\beta\alpha}(R(t),t)|\phi_{\alpha}^{a}(R(t);r)\rangle \qquad 4.88$$

The $U_{\beta\alpha}$ matrix is a unitary matrix that diagonalizes the Hamiltonian, $H^{d}(R(t),t)$ matrix at every time t. In this basis the elements of the adiabatic Hamiltonian matrix, $H^{d}(R(t),t)$, are defined as

$$H_{\beta\alpha}^{a}(R(t),t) = V_{\alpha}^{a}(R(t),t)\delta_{\beta\alpha} \qquad 4.89$$

being the $V_{\alpha}^{a}(R(t),t)$ the diagonal elements of the adiabatic Hamiltonian.

The nonadiabatic couplings are obtained as the derivatives of the $|\phi_{\alpha}^{a}(R(t);r)\rangle$

$$K_{\beta\alpha}^{a}(R(t),t) = \left\langle \phi_{\beta}^{a}(R(t);r,t)\middle|\frac{\partial}{\partial t}\middle|\phi_{\alpha}^{a}(R(t);r,t)\right\rangle \qquad 4.90$$

$$= K_{\beta\alpha}^{\phi}(R(t),t) + K_{\beta\alpha}^{U}(R(t),t)$$

where $K_{\beta\alpha}^{\phi}(R(t),t)$ are the non adiabatic couplings in the original basis, and $K_{\beta\alpha}^{U}(R(t),t)$ are the ones induced by the rotation matrix U.

$$K_{\beta\alpha}^{\phi}(R(t),t) = \sum_{\lambda\gamma} U_{\lambda\beta}^{*}(R(t),t)K_{\lambda\gamma}\big(R(t)\big)U_{\lambda\alpha}(R(t),t) \qquad 4.91$$

and

$$K_{\beta\alpha}^{U}(R(t),t) = \sum_{\lambda} U_{\lambda\beta}^{*}(R(t),t)\frac{\partial}{\partial t}U_{\lambda\alpha}(R(t),t) \qquad 4.92$$

To obtain the new potentials $V_{\alpha}^{a}(R(t),t)$ and the nonadiabatic coupling elements $K_{\beta\alpha}^{a}(R(t),t)$, the matrix $H^{d}(R(t),t)$ is diagonalized at distances R and $R+\Delta R$. The gradient of the potential and the gradient of the $U(R(t),t)$ matrix are evaluated and the new matrices are used to calculate the nonadiabatic dynamics.

Bibliography

(1) Tully, J. C. *J. Chem. Phys.* **1990**, *93*, 1061.

(2) Dewar, M. J. S.; Thiel, W. *J. Am. Chem. Soc.* **1977**, *99*, 4899.

(3) Dewar, M. J. S.; Zoebisch, E. G.; Healy, E. F.; Stewart, J. P. *J. Am. Chem. Soc.* **1985**, *107*, 3902.

(4) Granucci, G.; Persico, M.; Toniolo, A. *J. Chem. Phys.* **2001**, *114*, 10608.

(5) Granucci, G.; Toniolo, A. *Chem. Phys. Lett* **2000**, *325*, 79.

(6) Stewart, J. P. *MOPAC 2000, Fujitsu Limited* **1999**, *Tokyo, Japan*.

(7) Alexandrova, A. N.; Tully, J. C.; Granucci, G. *J. Phys. Chem. B* **2010**, *114*, 12116.

(8) Granucci, G.; Persico, M. *J. Comput. Chem.* **2011**, *32*, 2690.

(9) Jorgensen, W. L.; Tirado-Rives, J. *J. Am. Chem. Soc.* **1988**, *110*, 1657.

(10) Cornell, W. D.; Cieplak, P.; Bayly, C. I.; Gould, I. R.; Merz, K. M.; Ferguson, D. M.; Spellmeyer, D. C.; Fox, T.; Caldwell, J. W.; Kollman, P. A. *Journal of the American Chemical Society* **1995**, *117*, 5179.

(11) Antes, i.; Thiel, W. *J. Phys. Chem. A* **1999**, *103*, 9290.

(12) Ciminelli, C.; Granucci, G.; Persico, M. *J. Chem. Phys* **2005**, *123*, 174317.

(13) Richter, M.; Marquetand, P.; González-Vázquez, J.; Sola, I.; González, L. *J. Chem. Theory Comput.* **2011**, *7*, 1253.

Chapter 5

Endoperoxides' Photochemistry

A detailed overview of the photophysics and photochemistry of endoperoxides is given within this Chapter. With this purpose, interpretation about the absorption properties and relaxation mechanism connected to the photophysics and photochemistry of these systems, anthracene-9,10-endoperoxide (APO) and cyclohexadieneendoperoxide (CHDEPO), has been collected and compared with previous theoretical and/or experimental studies. [1-5]

As already mentioned in Chapter 1, two main processes were found to govern endoperoxides' photochemistry: O-O homolysis and cycloreversion, being the latter responsible for $^1O_2$ generation of great importance in many areas (see Chapter 1). The evolution in real time is also analysed by performing semiclassical molecular dynamics simulations for the smaller endoperoxide CHDEPO.

All the results described in this Chapter are collected in Publications I, II and III.

5.1 Absorption Spectra

The main features of the computed CASPT2 and CASSCF absorption spectra of CHDEPO and APO are summarized in Table 5.1. Otherwise specified, the discussion will be done considering the more reliable CASPT2 results although a carefull comparison with the CASSCF predictions will be also done along the following sections.

CHDEPO absorption spectrum was calculated at MS-CASPT2//CASSCF(14,12)/ANO-L level of theory [2] over 3, 4, 2 and 5 roots of A_1, A_2, B_1, and B_2 symmetries, respectively (Table 5.1). The 14 electrons in 12 orbitals active space is specified in Scheme 1a and space contains $2\pi_{CC}$, π_{OO}, π^*_{OO}, σ_{OO}, $2\sigma_{CO}$ occupied orbitals and the $2\pi^*_{CC}$, σ^*_{OO}, $2\sigma^*_{CO}$ virtual ones. If not specified, CASPT2 energies are referred. The lower energy region of the spectrum is characterised by two transitions, S_1 and S_3 at CASPT2 and S_1 and S_2 at CASSCF, showing a mixed $\pi^*_{OO}\sigma^*_{OO}$ + $\pi^*_{OO}\pi^*_{CC}$ character. On basis of the small differences in the CI coefficients obtained for both configurations in both states, at CASPT2 level of theory, Corral et al. assign the $\pi^*_{OO}\pi^*_{CC}$ character to the S_1 and the $\pi^*_{OO}\sigma^*_{OO}$ character to the S_3 peaking respectively at 3.59 and 4.63 eV. These two states are flanking at CASPT2 level a dark $\pi^*_{CC}\pi^*_{CC}$ state at 4.39 eV. The oscillator strengths of both states are in the same order of magnitude, being the one of the S_3 twice the S_1. Since both states (S_1 and S_3) are likely to be populated depending on the excitation wavelength, both are going to be considered during our following study to explain CHDEPO deexcitation mechanisms.

CHDEPO

		(CASSCF) MS-CASPT2			
		Main Config.	CI Coeff.	ΔE (eV)	*f*
(S_1)	S_1	$\pi^*_{OO}\pi^*_{CC(b2)}$ $\pi^*_{OO}\sigma^*_{OO}$	(-0.63) -0.73 (0.67) 0.56	(5.35) 3.59	0.003
(S_3)	S_2	$\pi_{CC(b1)}\pi^*_{CC(b2)}$	(-0.87) -0.82	(7.31) 4.39	0.000
(S_2)	S_3	$\pi^*_{OO}\sigma^*_{OO}$ $\pi^*_{OO}\pi^*_{CC(b2)}$	(0.61) 0.71 (0.67) 0.56	(6.15) 4.63	0.006

APO

		MS-CASPT2			
		Main Config.	CI Coeff.	ΔE (eV)	*f*
(S_1)	S_1	$\pi^*_{OO}\sigma^*_{OO}$ $\pi^*_{OO}\pi^*_{CC(b2)}$	(0.83) 0.60 (0.28) 0.60	(5.79) 3.85	0.000
(S_8)	S_2	$\pi^*_{OO}\pi^*_{CC(a1)}$	(-0.70) -0.85	(8.66) 4.25	0.000
(S_3)	S_3	$\pi_{CC(b1)}\pi^*_{CC(a1)}$	(-0.58) -0.55	(6.23) 4.34	0.003
(S_2)	S_4	$\pi_{CC(b2)}\pi^*_{CC(b2)}$ $\pi_{CC(b1)}\pi^*_{CC(b1)}$	(0.51) 0.55 (0.48) 0.47	(6.07) 4.47	0.000
(S_{16})	S_5	$\pi^*_{OO}\pi^*_{CC(b1)}$	(0.73) 0.77	(9.59) 4.59	0.017

Table 5.1. CASSCF and MS-CASPT2 excitation energies (in eV), main configuration interaction (CI) coefficients and oscillator strengths f, for the low lying excited states of CHDEPO and APO extracted from Refs [2,3].

A much more complicated scenario was found for **APO** in the same energy range using the MS-CASPT2//CASSCF(14,12)/ANO-S protocol for the calculation of electronic energies and oscillator strengths, Table 5.1. The calculations were performed using state-average (SA) procedure over 7, 4, 6, and 6 roots for the symmetries A_1, B_1, B_2, and A_2, respectively. A total number of 5 electronic states were calculated below 4.60 eV. Three of them S_1 ($\pi^*_{OO}\sigma^*_{OO}$), S_2 ($\pi^*_{OO}\pi^*_{CC(a1)}$) and S_4 ($\pi^*_{CC}\pi^*_{CC}$), however, present negligible oscillator strength values. The S_3 ($\pi^*_{CC}\pi^*_{CC}$) was found to weakly absorb and the most intense absorption in this regions was calculated for the S_5 ($\pi^*_{OO}\pi^*_{CC(b1)}$) peaking at 4.59 eV. It is important to note here, that the CASSCF and CASPT2 spectra are extremely different, for instance, the spectroscopic state S_5 mentioned before goes up to ~9.5 eV, corresponding to the S_{16} state at CASSCF level of theory. Both states S_3 ($\pi^*_{CC}\pi^*_{CC}$) (because it is the spectroscopic state within the low-lying states) and S_5 ($\pi^*_{OO}\pi^*_{CC(b1)}$) (since it presents the most intense absorption) will be considered to explain the main pathways responsible for excited APO deactivation. As said above, there are huge discrepancies between CASSCF and CASPT2 on describing the S_5 state but also with other states as the S_2, which is also rise up in energy at CASSCF level. Those differences were reported in Ref [3] and will be also considered far from the FC region, computing CASPT2 energies at all the optimized CASSCF critical points.

In view of the very computing demanding of the CASPT2 calculations in APO, a thorough study was undertaken. This study include a wide range of GGA, meta-GGA, hybrid, double hybrid, long range corrected functionals. The obtained results are collected in Publication I and point out that, although generalization to other systems might be dangerous, functionals with an amount of exact exchange between 30-35% seem to be promising candidates for the prediction of the low-energy region of the UV spectra of endoperoxides.

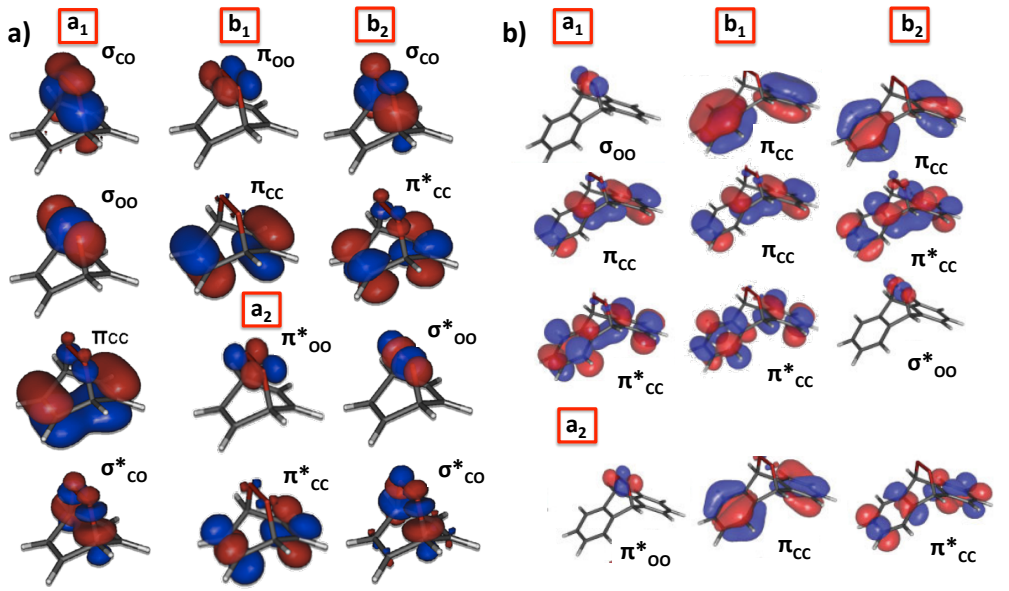

Scheme 5.1. CASSCF optimized molecular orbitals included in the (14,12) active space for the ground state of a) CHDEPO and b) APO, extracted from Refs [2,3].

5.2 CHDEPO Deactivation Pathways

Accordingly to the CASPT2 absorption spectrum calculated for this system, two electronic states (S_1 and S_2) below 5 eV, with oscillator strength different from zero, are susceptible to be populated after irradiation within this energy range. CASSCF Minimum Energy Paths (MEPs) starting from the FC region and following S_1 and S_2 states were calculated using the at (14,12) active space (see section 5.1 and Scheme 5.1) and the 6-31G* basis set.

MEP calculation from the $\pi^*_{OO}\sigma^*_{OO}$ excited state. O-O Homolysis

This MEP, MEP_{FC1}, was computed considering a state average over the first four singlet roots and following the gradient of the first electronic excited state S_1 $\pi^*_{OO}\sigma^*_{OO}$, recall CASSCF state ordering in Table 5.1. Structurally, the relaxation of this electronic state translates in the weakening of the O-O bond in the first steps of the MEP (O-O distance of 1.781) and its final dissociation (O-O distance of 2.749) when the system reaches a point if the PES where the 4 considered roots become almost degenerated (less than 3kcal/mol of energy difference) in energy, see Figure 5.1.

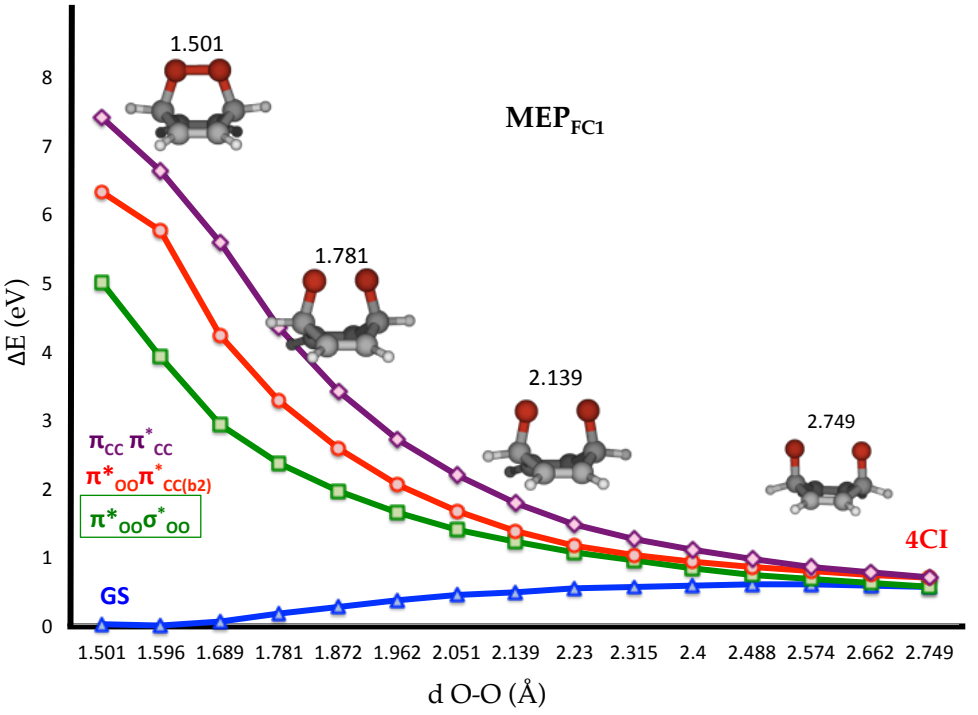

Figure 5.1. Minimum Energy Path from the FC region following the second excited state (π^*_{OO} σ^*_{OO}) gradient towards the high degeneracy region, 4CI, calculated at SA4-CASSCF(14,12)/6-31G*. Snapshots at representative points of the MEP are presented together with their O-O distance. Energies in eV and distance in Angstroms.

This degeneracy point was previously reported in Ref. [4] and arises from the degeneracy of the ground state ($\pi_{OO}^{(2)}$ $\pi^*_{OO}{}^{(2)}$ $\sigma^*_{OO}{}^{(0)}$), the singlet excited states ($\pi_{OO}^{(1)}$ $\pi^*_{OO}{}^{(2)}$ $\sigma^*_{OO}{}^{(1)}$ and $\pi_{OO}^{(2)}$ $\pi^*_{OO}{}^{(1)}$ $\sigma^*_{OO}{}^{(1)}$) and a double excitation ($\pi_{OO}^{(1)}$ $\pi^*_{OO}{}^{(1)}$ $\sigma^*_{OO}{}^{(2)}$). The nine-dimensional branching space of this 4CI is represented in Figure 5.2 and its defined by the gradient difference g_{01}, g_{02} and g_{03} vectors and the derivative coupling ones: h_{01}, h_{02}, h_{03}, h_{12}, h_{13}, h_{23}.

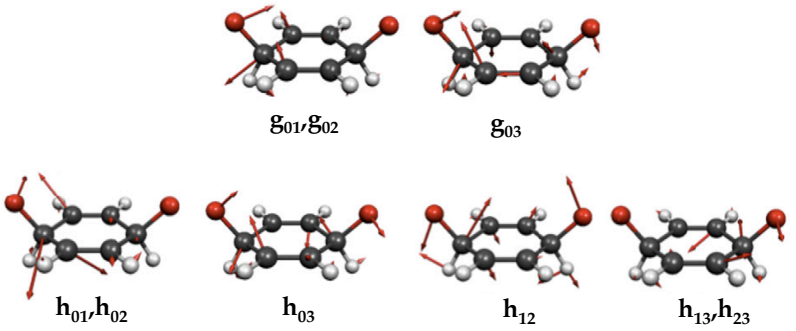

Figure 5.2. Gradient difference (g) and derivative coupling (h) vectors at the four state degeneracy point in CHDEPO. Adapted from Ref [4].

As detached from MEP_{FC1} in Figure 5.1, no energy barrier needs to be surmounted to access this point of the PES, being directly accessible from the FC region. Thereby, deactivation through this 4CI is expected to bring very efficiently population of excited CHDEPO molecules back to the ground state. **The shape of the potential energy profiles point to a very favourable formation of O-O homolysis products upon the population of the $\pi^*_{OO}\sigma^*_{OO}$ state**. However, alternative pathways starting from other electronic states absorbing in the same region need also to be considered, both statically and dynamically, to have an idea of the real distribution of products. The further evolution of the system once arrived to the 4CI point will be further discussed in Section 5.4

MEP calculation from the $\pi^*_{OO}\pi^*_{CC(b2)}$ excited state. Cycloreversion

Deactivation from the $\pi^*_{OO}\pi^*_{CC(b2)}$ excited state, MEP_{FC2}, was studied considering three singlet roots and following the gradient for the second excited state S_2 (recall CASSCF state ordering in Table 5.1). Results are presented in Figure 5.3. According to our calculations, CHDEPO would evolve directly to a conical intersection with the ground state, after crossing with the low-lying state S_1 $\pi^*_{OO}\sigma^*_{OO}$. Along the relaxation, the global MEP coordinate governed by the C-O distance, starts increasing immediately from the FC value (1.472 Å) until its almost dissociation (~3 Å) at the point where the $\pi^*_{OO}\pi^*_{CC(b2)}$ crosses with the ground state. Again, the system evolves barrierless from the FC region towards conical intersection (CI) with the ground state, that is, no minimum was found along this calculation.

Starting from the CI and following the gradient of the $\pi^*_{OO}\pi^*_{CC}$ state a minimum was found on this potential. This minimum $\pi^*_{OO}\pi^*_{CC}$, Min_{SW}, is characterized by a slight elongation of the remaining C-O bond. Obviously, in view of the resemblance of the

geometry of this minimum, where one of the two C-O bonds is already broken to the cycloreversion products, relaxation from this state was considered a precursor of singlet oxygen generation leading simultaneously to benzene as side products.

The elongation of the remaining C-O bond is expected to raise the energy of the system. Thus, we undertook the search of a transition state (TS) separating this minimum, Min_{SW}, with another one where both CO bonds are broken, Min_{O2}. This search was however hindered because of the weevil shape of the PES in the vicinity of this stationary point along the C-O stretching coordinate, bringing the system to any of the two minima flanking the TS. The protocol for the location of the TS consisted, first, of the mapping of the PES in this particular region, performing a relaxed scan calculation along the C-O stretching coordinate. In order to simplify the optimization and to prevent the evolution of the system to undesired products, the O-O distance was to constrained to its value at the Min_{SW} (1.350 Å). A maximum in the potential energy was found for C-O distances between 1.75 and 2.0 Å. Finally, for a C-O distance of 1.9 Å a TS structure was optimized with an imaginary frequency corresponding to the stretching of the second C-O bond. To confirm the connection of this TS with Min_{SW} and the final photoproducts (benzene and $^1O_2$) MEP calculations were as well undertaken. Interestingly, the MEP in the forward direction led to a weakly van der Waals complex between benzene and the oxygen molecule, where the ground state and the first excited state are degenerated.

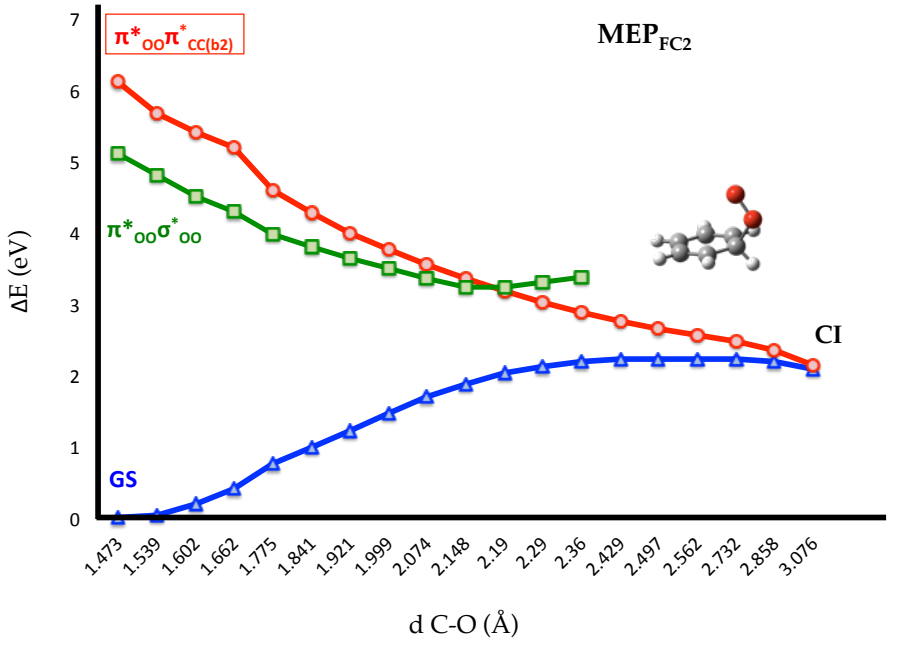

Figure 5.3. Minimum Energy Path from the FC region following the second excited state ($\pi^*_{OO}\pi^*_{CC}$) gradient towards a degeneracy point (CI) with the ground state, calculated at SA4-CASSCF(14,12)/6-31G*. Energies in eV and distance in angstroms.

A global picture for the cycloreversion pathway is depicted in Figure 5.4, where final energies were refined at MS-CASPT2//CASSCF(14,12)/ANO-S level of theory. Our calculations reveal a very **favourable deactivation path from the FC region** with no

energy barrier towards the ground state. Once in the Min_{SW}, the system needs to surmount a barrier of 0.3 eV, **to produce singlet oxygen**. Considering the starting energy of the system, the existence of this barrier should not prevent the observation of cycloreversion products.

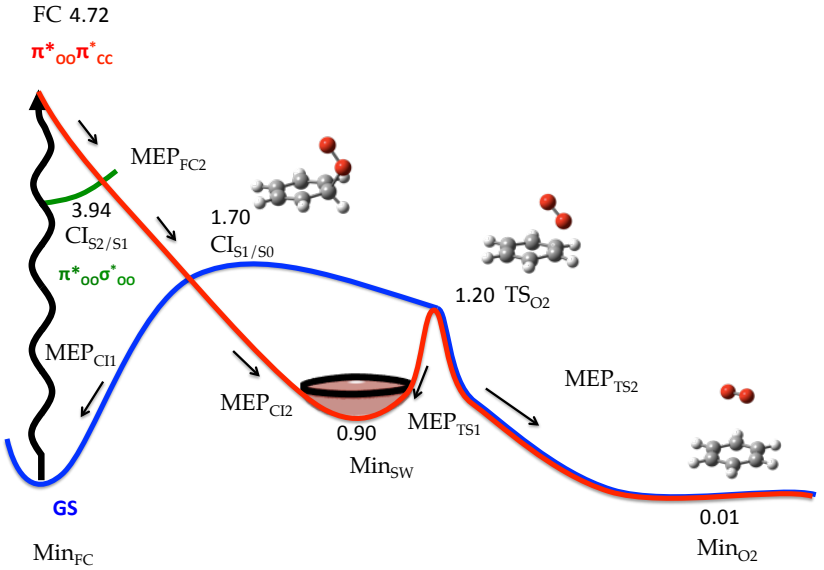

Figure 5.4. Global deactivation mechanism of CHDEPO after excitation to the $\pi^*_{OO}\pi^*_{CC}$ state. Energies (in eV) calculated at MS-CASPT2//SA4-CASSCF(14,12)/ANO-S level of theory relative to the FC ground state.

Nevertheless, all this statement are done based on static calculations and dynamic simulations can help on stablishing a more realistic photoproduct distribution and also can predict timescales for the different pathways. Those dynamic results are presented below.

5.3 CHDEPO Molecular Dynamics

Although static calculations can be very useful in the interpretation of the deactivation of a particular excited system or even compulsory for the assessment of the theoretical protocol to be used in subsequent molecular dynamic simulations or for constructing reliable PES, a more complete understanding of a photochemical problem can be achieved after being analysed from a time resolve perspective. The photoreactivity of endoperoxides can be actually considered as a very interesting problem to be analysed from a dynamic point of view where two competing deactivation mechanism () leading to very different photoproducts are formed. Taking into account the difficulties inherent to the large size of APO, its complicated electronic structure and the similarities in the deactivation mechanism found for both systems, the smaller endoperoxide CHDEPO was taken as model to analyse the deactivation of endoperoxides. For this, SHARC program was used (see Chapter 4).

The theoretical protocol used for the dynamics was the same previously described for the computing of the deactivation mechanism. In particular, the large active composed of 14 electrons in 12 orbitals, combined with relativistic basis set (ANO-RCC contracted as 3s2p for H and 4s3p2d for C and O) were employed throughout the dynamics. Although other active spaces were tested, all the orbitals included in the 14,12 were found to be essential for describing both O-O homolysis and C-O bond cleavage. Regarding the basis set, the above mentioned basis was found to correctly describe spin-orbit coupling effects and to be large enough for the correct description of dissociation processes. The dynamics was performed using CASSCF(14,12/ANO-RCC level of theory state average over 4 singlets + 4 triplet roots, which are the smallest number of states needed for describing the 8 fold CI (4CI singlets +4CI triplets). MOLCAS package was used for the energies, gradients, and spin orbit coupling calculations, while SHARC (surface-hopping-adiabatic-representation-including-arbitrary-couplings) was used for dynamic propagation.

A Wigner harmonic distribution for the ground state was used to generate 1000 initial conditions. Single point CASSCF and MS-CASPT2 calculations on top of these geometries were performed to simulate the absorption spectrum of CHDEPO (Figure 5.5). CASSCF spectrum presents a main band centered around ~6 eV corresponding to the S_2 ($\pi^*_{OO}\sigma^*_{OO}$ computed statically at 6.15 eV, with oscillator strength of 0.006) state (see Table 5.1) and another one, much less intense, at ~5 eV ascribed to S_1 ($\pi^*_{OO}\pi^*_{CC(b2)}$ computed statically at 5.35 eV, with oscillator strength of 0.003) (see Table 5.1). The simulated MS-CASPT2 spectrum present sthe same shape, with the intense band between 4-5 eV (the S_3 $\pi^*_{OO}\sigma^*_{OO}$ at 4.63 eV) and a less intense absorption below 4eV (S_1 $\pi^*_{OO}\pi^*_{CC(b2)}$ at 3.59). Although both spectra share same shape and characteristics, the CASSCF spectrum is significantly displaced to higher energies compared to the CASPT2. This excess of initial available energy can be problematic during the dynamic simulations leading the system to undesired high-energy regions of the PES. With this aim, the CASSCF spectrum was scaled by a 0.75 factor (see ^{SC}CASSCF in Figure 5.5) in order to overlap with the CASPT2 spectrums. The performance of this scaling factor far from the FC region was tested by computing CASSCF and CASPT2 single points at different points of the most important pathways (see supporting information of Paper II). Although the 0.75 scaling factor fits well close to the FC region, once a degeneracy region (either 4CI in Figure 5.1 or CI in Figure 5.4) both CASSCF and CASPT2 start to be very similar, being necessary to eliminate this factor. Then, SHARC was asked to stop when the S_0 potential was reached and to continue without any scaling factor.

Other possible problems, as an excess of velocities on the hydrogen atoms which could lead to undesired products were avoided by substituting the H by deuterium within the initial conditions settings and within the trajectories propagation. Using oscillator strengths and excitation energies the set of initial conditions was selected from the whole set of 1000 geometries. Within this conditions 78 initial condition were selected, 51 of them starting on the second excited state (S_2) and the remaining 27 conditions starting on the S_3 excited state.

The results of the singlet/triplet dynamics simulations propagated for a time of 100 fs are shown in Figure 5.6. For these simulations 8 electronic states (4 singlets and 4

triplets) were considered. The population is initially distributed into the S_2 and S_3 states.

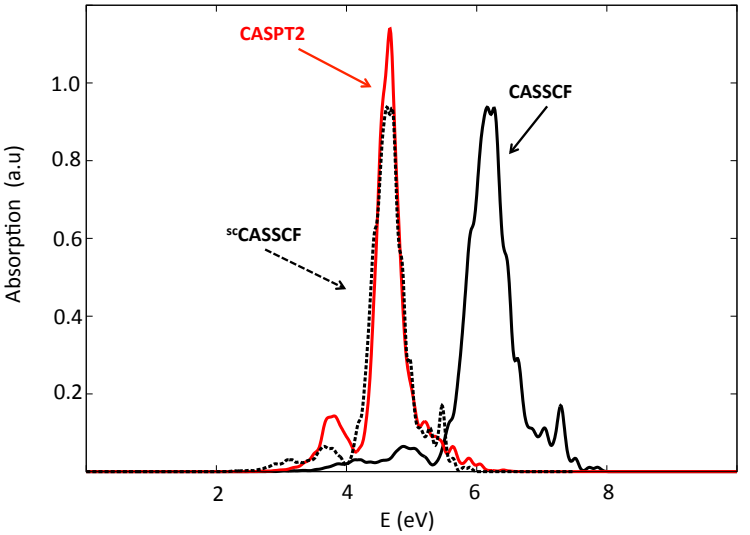

Figure 5.5. Simulated absorption spectra for CHDEPO. Black solid line corresponds to the spectrum obtained using S4-CASSCF(14,12)/ANO-RCC level of theory, while red solid line represents the results obtained with MS-CASPT2. Black dotted line is the CASSCF spectrum scaled (^{sc}CASSCF) in order to fit with the CASPT2 result.

Accordingly to our simulations, the population of both states decays rapidly in favor of the S_1 and S_0 states that accumulate the largest fraction of population within the first 20 fs. From this moment and until the end of the simulation, 60% of the total population is equally distributed between the 4 singlet states, whereas the remaining 40% is distributed between the 4 triplet states in an equitable way. This ultrafast decay is in agreement with the two computed MEPs in section 5.2, MEP_{FC1} or MEP_{FC2}, showing profiles starting from the FC region and that rapidly evolve to a conical intersection with the ground state and/or with other low-lying states.

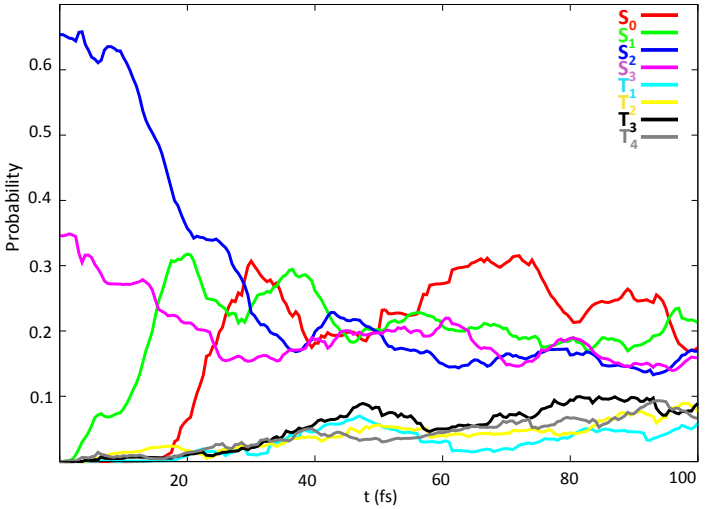

Figure 5.6. Time evolution of the average quantum amplitude of included singlet (S_0 in red, S_1 in green, S_2 dark blue, S_3 in pink) and triplet (T_1 in light blue, T_2 in yellow, T_3 in black, T_4 in grey) states.

Although, the final distribution of population between singlet and triplets is compatible with wavepacket arriving at the 8 fold degeneracy region and therefore indicative of the important role of O-O homolysis in the photochemistry of this endoperoxide, in order to distinguish between both mechanisms (cycloreversion and O-O homolysis), an analysis of the geometries can be very helpful. In particular, the evolution in time of the distance between the O_2 and benzene ($d_{benz\text{-}OO}$) centers of mass was chosen as a representative parameter for this purpose, see Figure 5.7. In fact, for trajectories leading to O-O homolysis this distance decreases until it reaches the value of zero, corresponding to the situation where the O-O distance is maximum and the C-O bonds are coplanar to the rest of the ring. A further increase of this distance could be connected with either a large value of the OCC bending bringing together the 2H atoms or alternatively to the return of he system to the original geometry.

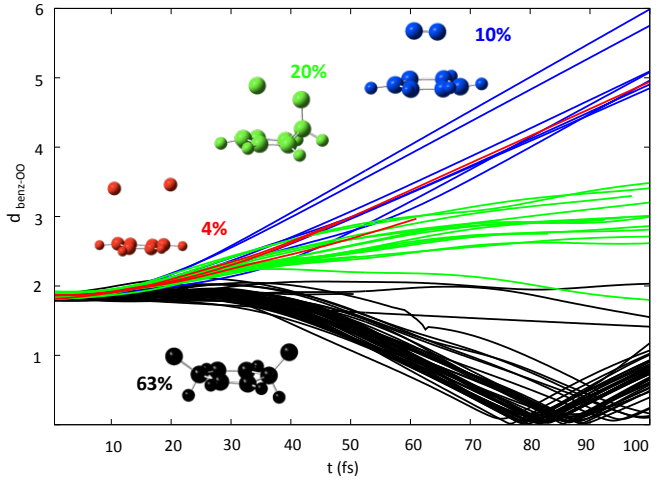

Figure 5.7. Time evolution of the $d_{benz\text{-}OO}$ distance for different groups of trajectories. In black trajectories connected to O-O homolysis, in blue the ones producing $B+{}^1O_2$ and other products in red and green. Percentages for the different products are as well specified

In the case of trajectories leading to cycloreversion a progressive increase of this distance is expected, consistent with the dissociative of the two C-O bonds and $^1O_2$ release.

According to Figure 5.7 most of the trajectories (63%) would undergo O-O homolysis (the MEP_{FC1} pathway in Figure 5.1), that is, and oscillating trend for the $d_{benz\text{-}OO}$ distance. The second most important group of trajectories (20%), evolve breaking simultaneously the C-O bond and the endoperoxide bridge, and therefore do not correspond with none of the most probable deactivation mechanism for endoperoxides. Singlet oxygen generation is registered for 10% of the run trajectories, where an almost linear increase in the $d_{benz\text{-}OO}$ distance observed with time. The remaining trajectories (4%) lead to other side products such as atomic oxygens and benzene which are expected to be connected with very high energy profiles. We ascribe the generation of these photoproducts to the failure of the quantum chemical employed methodology, lacking from dynamic correlation, in the prediction of these potential energy profiles. However, in view of the structural evolution of the system for the trajectories depicted in Figure 5.7 in red ad green and the PES in Figure 1.4

showing larger barriers to revert to the GS than to achieve $^1O_2$ generation we ascribe these trajectories to cycloreversion. Therefore, the final ratio of O-O homolysis and cycloreversion trajectories would amount 63% and ~30% in line with experimental findings for the larger endoperoxide APO.[1]

Two representative trajectories will be discussed exemplifying O-O homolysis (Figure 5.8) and cycloreversion (5.10).

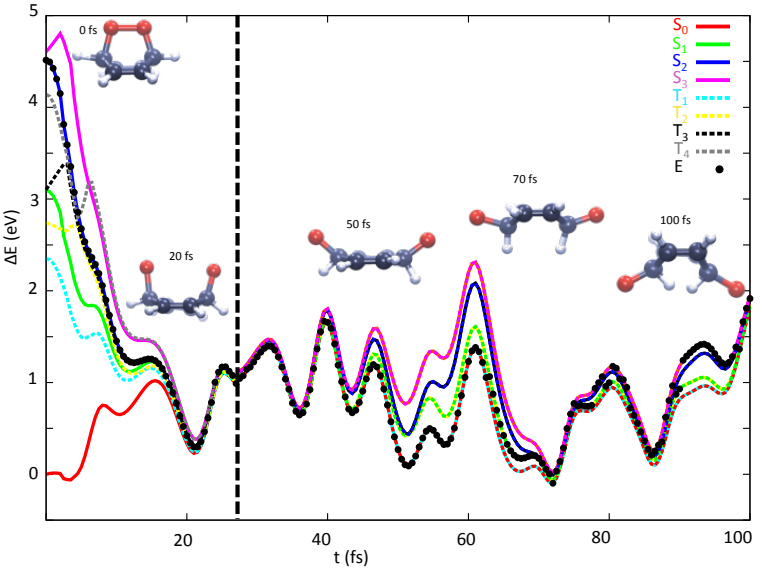

Figure 5.8. Time evolution of a representative trajectories leading to O-O homolysis products. Singlet states are represented as solid lines, being S_0 in red, S_1 in green, S_2 in blue and S_3 in pink, while triplet states are in dotted lines in light blue T_1, yellow T_2, black T_3 and grey T_4. The current potential energy of the system is represented un black dots. Vertical dotted line in black indicates the time step at which the trajectory reaches S_0 and therefore the scaling is switched off.

The left hand side of the Figure 5.8 reminds very much the shape of the MEP_{FC1} calculated for the O-O homolysis mechanism. Interestingly, the 8 fold degeneracy region is reach only 20fs after the beginning of the simulation. The geometry at this point of the simulation is also quite similar to the one optimized for the 4CI[4], and the system reaches the S_0 some fs after. The system remains on the degeneracy region for 20 fs more, and afterwards the electronic states become non-degenerated. In the following, the O-O distance increases until the C-O bonds become coplanar with the benzene ring and a further increase of the OCC angle is observed concomitant with the distortion of the ring planarity and the approach of the H bonds.

Although the geometry at the final time of propagation shows a quite short H-H distance suggesting the formation of H_2, none of the propagated trajectories evolves to $BQ+H_2$. We attribute this to a combination of dynamic effects and the non complete used active space (see paper II for further details). We observe the generation of H_2 for a trajectory run from new initial conditions generated with H instead of D, snapshots for this trajectory are represented in Figure 5.9

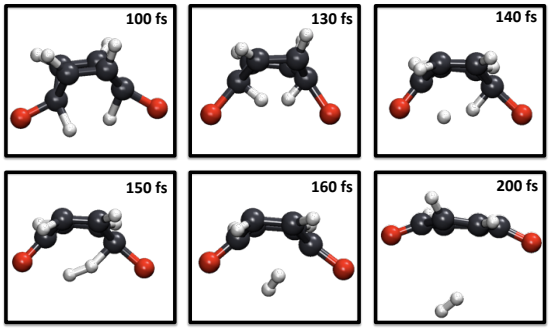

Figure 5.9. Representative snapshots of a given trajectory leading to H_2 + BQ products.

The second representative trajectory undergoing cycloreversion is represented in Figure 5.10. Similarly to the trajectory represented in Figure 5.8, the evolution of the potential energy along the trajectory reminds the MEP calculated quantum chemically, MEP_{FC2} (Figure 5.3). In fact, from the initially populated state S_2 the system decays barrierless to a CI with the immediately lower excited state S_1 at t=15 fs. Only 10 fs after CHDEPO encounters a new internal conversion funnel to the GS, where two minima are separated by and energy barrier, being ascribed to Min_{SW} (t=50 fs), Min_{O2} (t=75 fs) and the TS (t=70 fs) respectively. The final products at t=100 fs clearly resembles benzene and $^1O_2$.

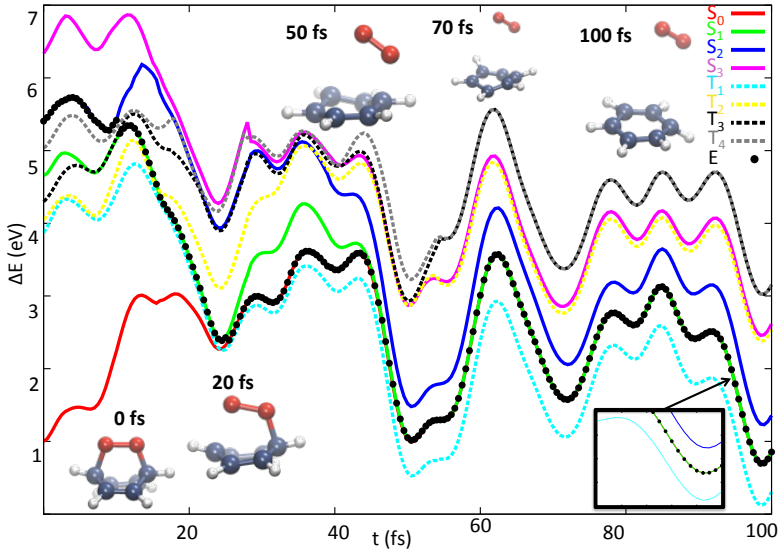

Figure 5.10. Time evolution of a representative trajectories undergoing cycloreversion. Singlet states are represented as solid lines, being S_0 in red, S_1 in green, S_2 in blue and S_3 in pink, while triplet states are in dotted lines in light blue T_1, yellow T_2, black T_3 and grey T_4. The potential energy at each time is indicated as black points. Representative snapshots at indicated times are also presented. Zoom of the last part of the simulation is represented in the inset.

Summary

Two main aspects could be responsible for **O-O homolysis** ~60% being **more favored than** cycloreversion ~30% (**singlet oxygen generation**) in **CHDEPO** deactivation mechanism:

(1) No energy barriers were found to be present along the O-O homolitic clevage coordinates, while small energy barriers are required to disscociate the second C-O bond.
(2) Along the MEP_{FC2}, the $\pi^*_{OO}\pi^*_{CC}$ state crosses the low-lying $\pi^*_{OO}\sigma^*_{OO}$, which could translates into a transfer of population between these states.

5.4 APO Deactivation Pathways

Similar to CHDEPO the absorption spectrum of APO endoperoxide (see Table 5.1) showed two electronic state with non zero oscillator strength, $\pi^*_{CC}\pi^*_{CC}$ and $\pi^*_{OO}\pi^*_{CC(b1)}$. Minimum energy pathways of them performed in the present and previous works will be analysed in this section.

MEP calculation from the $\pi^*_{OO}\sigma^*_{OO}$ excited state. O-O Homolysis

O-O dissociation mechanism in APO was studied in detail in Ref. [5] using MS-CASPT2/CASSCF calculations. Similarly to CHDEPO, the minimum energy path following the $\pi^*_{OO}\sigma^*_{OO}$ state leads directly and barrierlessly to a four state degeneracy region. The four-fold CI involves the degeneracy of the same states as previously described for CHDEPO. Triplet states were also taken into account in this work, and consistently the four triplet analogues of the singlet electronic states taking part in the 4CI were also calculated within the same energy range difference of 1.5 kcal/mol. This highly degenerated crossing is expected to translate into high probability of decaying to the ground state in ultrafast time scale.

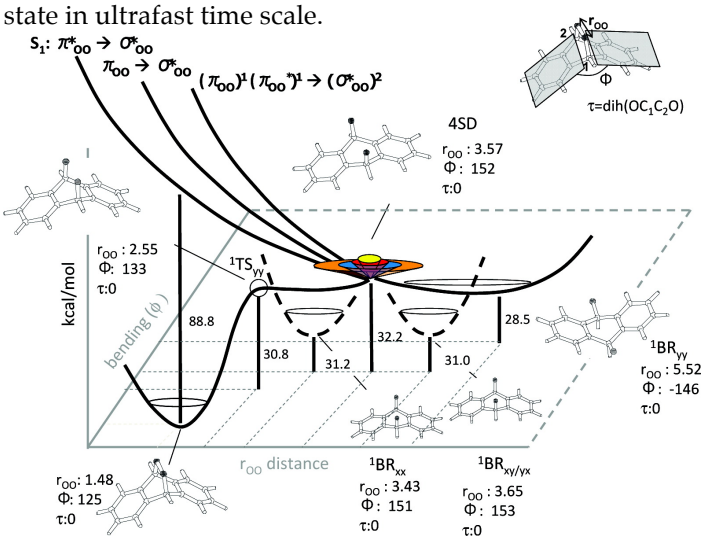

Figure 5.11. Pathways leading to O-O homolysis in APO through the eight-fold (four singlet plus four triplet) degeneracy regions calculated at MS-CASPT2/CASSCF. Extracted from Ref [5].

MEP calculation from the $\pi^*_{CC}\pi^*_{CC}$ and $\pi^*_{OO}\pi^*_{CC(b1)}$ excited states. Cycloreversion

In a first stage, deactivation from the $\pi^*_{CC}\pi^*_{CC}$ state (S_3 state in FC at CASPT2 level of theory, Table 5.1) was investigated. Taking into account that similar CI and Min_{SW} as the optimized for CHDEPO were also reported for APO, a preliminary overview for the deactivation of the $\pi^*_{CC}\pi^*_{CC}$ state and its role in cycloreversion was obtained by a LICC calculation between FC and Min_{SW}, Figure 5.12.

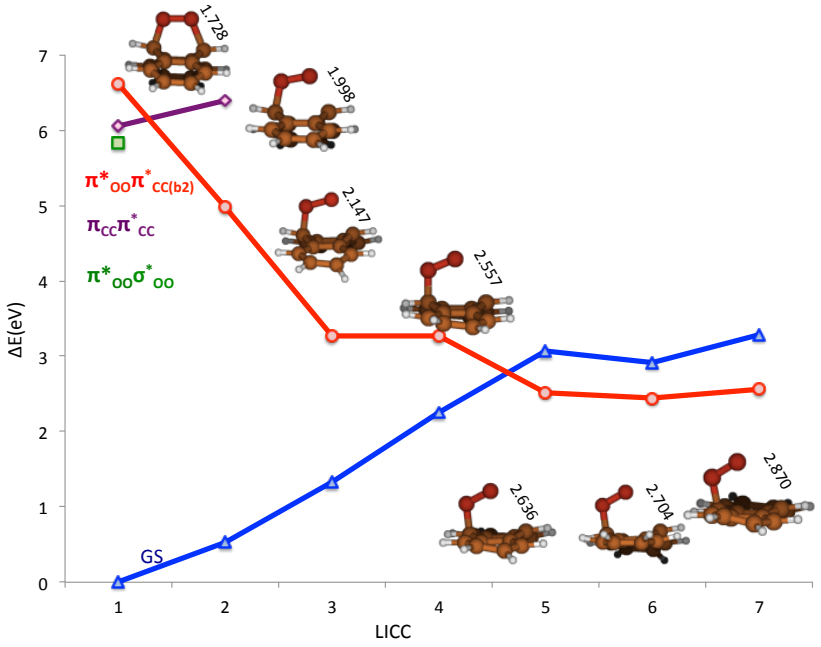

Figure 5.12. Linear Interpolation Cartesian Coordinates (LICC) calculation between FC and Min_{SW} geometry calculated at S4-CASSCF(14,12)/ANO-S level of theory.

According to the LICC calculation the spectroscopic $\pi^*_{CC}\pi^*_{CC}$ state would cross the higher $\pi^*_{OO}\pi^*_{CC(b2)}$ state relatively close to the FC region through the CI_1 and although is not seen in the LICC (due to the number of roots considered in the calculation), not far from this region the first FC excited state $\pi^*_{OO}\sigma^*_{OO}$ state would also cross the $\pi^*_{OO}\pi^*_{CC(b2)}$ state through CI_2. Both minimum energy crossing points were optimized and refined at MS-CASPT2/CASSCF energy level. The two crossings (CI_1 and CI_2) together with the conical intersection analogue to one found for CHDEPO that involves the $\pi^*_{OO}\pi^*_{CC(b2)}$ and the ground state would define the $PATH_1$ or in other words the initial part of the cycloreversion mechanism summarized in Figure 5.13. Once in Min_{SW} the same procedure as the one described for CHDEPO was followed to locate the TS, to connect it with the second minima, Min_{O2}, and to calculate the final energies.

An overview of the cycloreversion mechanism undergone by APO after absorption is the following. Population transfer is expected from the $\pi^*_{CC}\pi^*_{CC}$ state to the $\pi^*_{OO}\pi^*_{CC(b2)}$ excited state throughs the CI_1 crossing lying close to the FC region at 5.41 eV. Once in the reactive $\pi^*_{OO}\pi^*_{CC(b2)}$ state, leading to dissociation of the first C-O bond,

there is a chance that a small fraction of the molecules reach the $\pi^*_{OO}\sigma^*_{OO}$ state, connected to O-O homolysis processes through the CI_2 (at 5.25 eV). Finally, the population would reach the ground state populating either the initial FC minimum or Min_{SW}. Dissociation of the remaining C-O bond requires the system to increase its energy by 2 eV (40 kcal/mol) reaching another minimum on the same potential, Min_{O2}. This minimum where 1O2 and anthracene are weakly bound through Van der Waals interactions was found to be very stable thanks to the recovery of the aromaticity of the anthracene moiety.

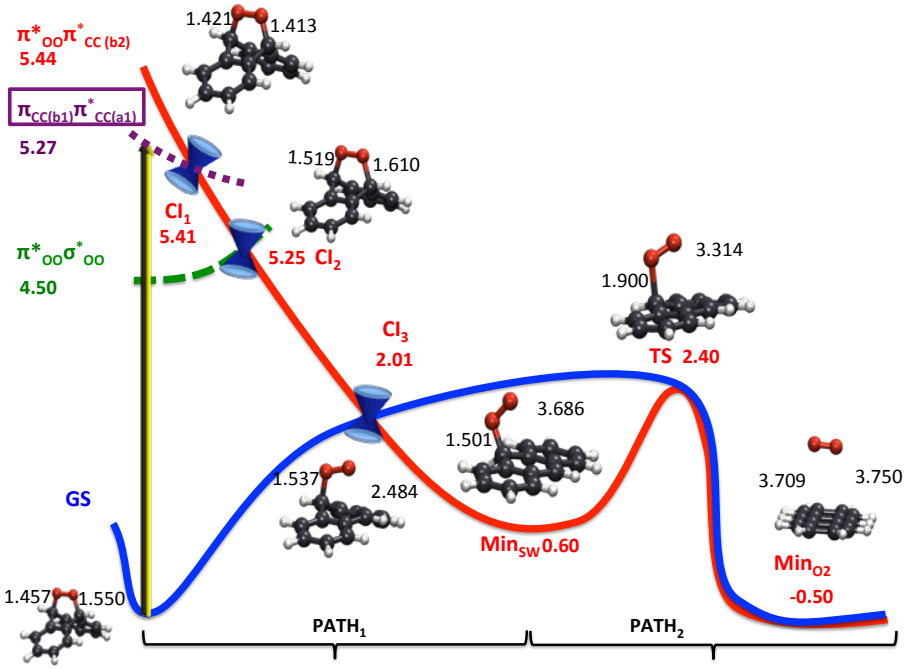

Figure 5.13. Global deactivation mechanism of APO after excitation to the $\pi_{CC}\pi^*_{CC}$ state, connecting FC region with Min_{O2}. Energies calculated at MS-CASPT2/SA5-CASSCF(14,12)/ANO-S level of theory and expressed in eV and relative to the ground state at FC region. C-O distances are indicated in Angstroms.

From Figure 5.13, we can conclude that once in Min_{SW} both endoperoxides show very similar mechanism to produce singlet oxygen ($PATH_2$), although still there are some differences that deserve to be discussed. For instance, the energy barrier from Min_{SW} connected to the dissociation of the second C-O bond is significantly higher for APO (2eV vs 0.4 eV on CHDEPO). However, it should be noticed that the initial energy accumulated by the system upon absorption is also greater in the larger endoperoxide. In principle, **upon inspection of both profiles ($PATH_1$ and $PATH_2$) of APO $^1O_2$ is expected from the population of $\pi^*_{CC}\pi^*_{CC}$ state.**

Relaxation pathways were also investigated for the $\pi^*_{OO}\pi^*_{CC(b1)}$ state. Many difficulties were found when investigating these pathways. As already mentioned in section 5.1, this state is not well reproduced at CASSCF level that overestimates its energy.

Therefore, at CASSCF level this state was found to be preceded by several other $\pi^*_{OO}\pi^*_{CC}$ and $\pi_{CC}\pi^*_{CC}$ states, being the S_{16}. In order to better handle the very large number of roots necessary to investigate the deactivation mechanism from this state we have reduced the active space, removing π_{CC} orbitals and allowing then the localization of the $\pi^*_{OO}\pi^*_{CC(b1)}$ state within the first number of roots. Unfortunately, it was not possible to reduce also the number of π^*_{CC} orbitals, since the necessary $\pi^*_{CC(b1)}$ was found to be strongly correlated to the rest. Then, the new active space was reduced to 4 electrons in 7 orbitals ($\pi^*_{OO,}$ $\pi_{CC(b1)}$, $\pi^*_{CC(a1)}$, $\pi^*_{CC(b2)}$, $\pi^*_{CC(b1)}$, $\pi^*_{CC(a2)}$, σ^*_{OO}) for the MEP calculation.

This MEP was only considered as a first approach to locate the crossings of the $\pi^*_{OO}\pi^*_{CC(b1)}$ state with low-lying states but no important conclusion can be extracted from it due to the very bad description of CASSCF for this state and the small active space considered. The computed MEP at SA10-CASSCF/ANO-S level of theory starting at the FC geometry and relaxing the last root corresponding to the spectroscopic state, $\pi^*_{OO}\pi^*_{CC(b1)}$. Due to the large number of roots considered, the MEP calculation was stopped every time it reached a degeneracy region between the spectroscopic state and any low-lying state. A new MEP calculation following the appropriate character ($\pi^*_{OO}\pi^*_{CC(b1)}$) gradient was then performed.

The most relevant crossing points founded along the MEP were further optimized as minimum energy crossing points and then their energies were refined using MS-CASPT2 and the larger 12,11 active space (see Figure 5.14). From those energies it can be extracted, that after excitation (at 6.33 eV) the spectroscopic state $\pi^*_{OO}\pi^*_{CC(b1)}$ evolves towards a conical intersection with one of the low-lying states, $\pi_{CC(b1)}\pi^*_{CC\,(b1)}$, placed at 5.90 eV ($S_4$ at the FC). The $\pi^*_{OO}\pi^*_{CC\,(b1)}$ state gradient would further drive the system towards other two degeneracy regions with the $\pi_{CC(b1)}\pi^*_{CC\,(a1)}$ (5.56 eV) and $\pi^*_{OO}\pi^*_{CC\,(a1)}$ (5.28 eV) states. The first two crossings do not require large distortions of the molecule and compared to FC geometry they present strengthened of the C-O and O-O bonds, being the $\pi^*_{OO}\pi^*_{CC\,(b1)}$/ $\pi_{CC(b1)}\pi^*_{CC\,(a1)}$ conical intersection geometry the most sensitive to these changes. However, the $\pi^*_{OO}\pi^*_{CC\,(b1)}$/ $\pi^*_{OO}\pi^*_{CC\,(a1)}$ degeneracy point changes the previous described trend, presenting larger CO distances.

From this region on, the system evolve barrierless through a degeneracy region between the spectroscopic and the $\pi^*_{OO}\pi^*_{CC\,(b2)}$ state (see Figure 5.14). Although the appropriate character is followed along the MEPs, this state (S_2) becomes a mixture of different $\pi^*_{OO}\pi^*_{CC}$ excitations holding $\pi^*_{OO}\pi^*_{CC\ (b1)}$ and $\pi^*_{OO}\pi^*_{CC\ (b2)}$ characters. Thereby, the reached conical intersection at the end of the minimum energy path shares similar geometries (one of the CO bonds is already dissociated) and energies with the one described above in $PATH_1$. Then, also very high in energy states can be responsible for C-O homolisys and in further steps of singlet oxygen generation and can no be discarded to play a role in deactivation mechanisms of APO.

Summary

For **APO** photochemistry a main aspect indicates that, at least, **cycloreversion will effectively compete with O-O homolysis**:

(1) Two spectroscopic states lead to cycloreversion photoproducts instead of being connected to O-O homolysis.

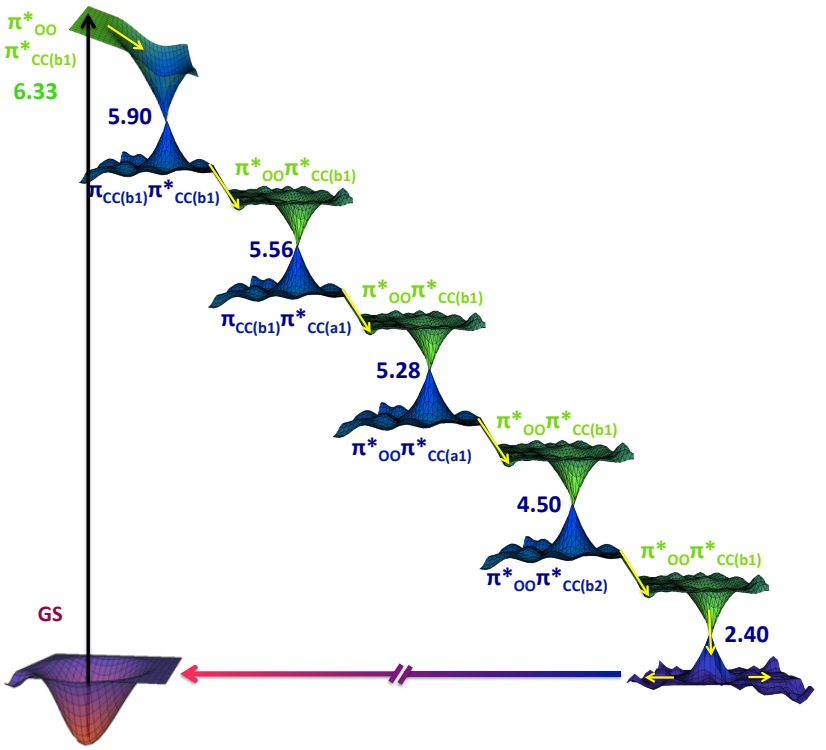

Figure 5.14. Deactivation mechanism from the FC region of APO along the high in energy spectroscopic state $\pi^*_{OO}\pi^*_{CC(b1)}$. Energies in eV calculated at MS-CASPT2//CASSCF(12,11)/ANO-L level of theory.

5.5 Conclusions

Based on MEPs, the two important deactivation mechanisms (O-O homolysis and cycloreversion) in CHDEPO and APO endoperoxides do not reveal the presence of minima or energy barriers in the way to the ground state. Despite, low energy barriers were found onwards for the generation of singlet oxygen and H_2, respectively, they are not expected to prevent the formation of these photoproducts. According to out dynamic simulations in CHDEPO, O-O homolysis is preferred for the relaxation of this system. This result can be ascribed to the presence of very efficient conical intersection along the MEP from the $\pi^*_{OO}\pi^*_{CC}$ state connected with cycloreversion, responsible for the deviating population, to the $\pi^*_{OO}\sigma^*_{OO}$ state connected to O-O

homolysis. The yields obtain during this dynamics reveal a ratio of ~60%:~30% for O-O homolysis and cycloreversion. Since similar pathways were found for APO we expect similar ratio for this competing mechanisms in the larger endoperoxide, being in good agreement with recent experimental results.[1]

Bibliography

(1) Lauer, A.; Dobryakov, A. L.; Kovalenko, S. A.; Fidder, H.; Heyne, K. *Phys. Chem. Chem. Phys.* **2011**, *12*, 8723.

(2) Corral, I.; González, L. *Chem. Phys. Lett.* **2007**, *446*, 262.

(3) Corral, I.; González, L. *J. Comput. Chem.* **2008**, *29*, 1982.

(4) Corral, I.; González, L. *Chem. Phys. Lett.* **2010**, *499*, 21.

(5) Mollenhauer, D.; Corral, I.; González, L. *J. Phys. Chem. Lett.* **2010**, *1*, 1036.

Chapter 6

Purines Photochemistry

Although very similar, structurally speaking, to canonical guanine and adenine nucleobases, purine and 9-methylpurine bases (see scheme 6.1) are characterized by unusual photophysical behaviour with high triplet quantum yield contrary to ultrafast ground state recovery registered for the canonical nucleobases. The in detail study of the deactivation mechanism of these systems and their comparison with the canonical nucleobases (and other interesting bases as 2-aminopurine) is key to understand the influence of peripheral substituents in the heterocyclic skeleton. With this aim, absorption spectra and minimum energy paths (MEPs) were computed, and the main stationary points of the singlet and triplet manifold were localized. Results obtained for this study together with experimental results (carry out by Pr. Crespo group) and dynamics calculations (performed in Pr. González group) are presented in Paper IV.

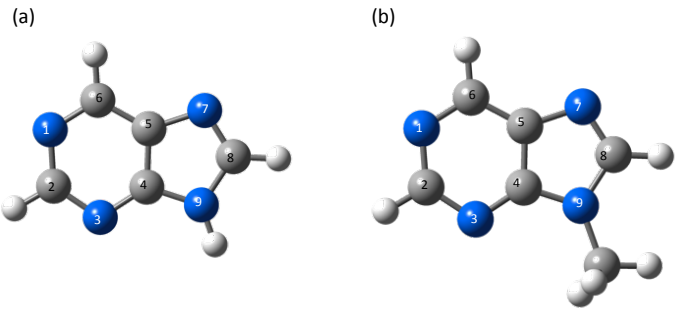

Scheme 6.1 Atom labelling of purine (a) and 9-methylpurine (b).

6.1 Absorption Spectra

Tables 6.1 compiles MS-CASPT2//SA-CASSCF(16,12)/ANO-L singlet and triplet vertical transition energies and oscillator strengths for purine (P) and 9-methylpurine (9MP) bases. The (16,12) active space includes the whole set of π orbitals (5 bonding and 4 anti-bonding) and 3 lone-pairs sitting on the nitrogen atoms 1, 3 and 7 (Scheme 6.1). For both bases, the lowest-lying singlet excited state (ca. 4.05 eV) is of nπ* nature, whereas the first bright state corresponds to the S_2, absorbing around 4.68 eV and shows ππ* (L_a) character (accordingly to Platt's nomenclature [1]). In the region between 4.8- 5.0 eV peaks the next bright state also of ππ* (L_b) nature (S_4 in P and S_3 in 9MP). In the same region of the spectrum, we find less intense nπ* absorptions (S_3 in P and S_4 in 9MP). Two triplet states, 1 nπ* (T_2) and 1 ππ* (T_1), were computed below the S_2 excited state in P, whereas another ππ* (T_3) was also located below the S_2 excited state in 9MP.

	CASSCF(16,12)/ANO-L			MS-CASPT2		
State	Main Config.	CI Coeff.	ΔE	CI Coeff.	ΔE	f
			Purine			
S_1	$n_1\pi^*_{CC}$	-0.84	5.24	0.86	4.05	0.0038
S_2	$\pi_{CC}\pi^*_{CC}(L_a)$	0.64	5.20	0.60	4.68	0.0724
S_3	$n_1\pi^*_{CC}$	0.80	6.18	-0.86	4.94	0.0027
S_4	$\pi_{CC}\pi^*_{CC}(L_b)$	-0.72	6.88	0.67	5.02	0.0306
T_1	$\pi_{CC}\pi^*_{CC}$	-0.63	3.95	0.78	3.76	-
T_2	$n_1\pi^*_{CC}$	0.81	4.92	-0.81	3.92	-
T_3	$\pi_{CC}\pi^*_{CC}$	0.48	5.14	-0.75	4.71	-
T_4	$n_1\pi^*_{CC}$	-0.78	5.68	0.81	4.72	-
			9-Mehylpurine			
S_1	$n_1\pi^*_{CCa}$	0.84	5.24	0.86	4.05	0.0036
S_2	$\pi_{CC}\pi^*_{CC}(L_a)$	-0.68	5.17	0.68	4.69	0.0609
S_3	$\pi_{CC}\pi^*_{CC}(L_b)$	0.77	6.59	-0.76	4.85	0.0384
S_3	$n_1\pi^*_{CC}$	0.64	6.20	-0.82	4.96	0.0018
T_1	$\pi_{CC}\pi^*_{CC}$	-0.77	3.93	-0.87	3.67	-
T_2	$n_1\pi^*_{CC}$	-0.83	4.94	0.85	3.94	-
T_3	$\pi_{CC}\pi^*_{CC}$	0.68	5.10	0.87	4.43	-
T_4	$n_1\pi^*_{CC}$	-0.80	5.68	-0.83	4.75	-

Table 6.1 Singlet and triplet vertical absorption energies (in eV), main contributions to the wave functions and oscillator strengths of Purine and 9-MethylPurine calculated at CASSCF(16,12)/ANO-L and MS-CASPT2//CASSCF levels of theory using IPEA shift 0.0.

Interestingly, contrary to what observed for other systems considered along this thesis, it is worth noting here that the absorption spectrum of these systems is very sensitive to the IPEA shift introduced in the CASPT2 calculations. In fact, a better agreement with the experiment results of Prof. Crespo is achieved avoiding the used of this shift. In fact, the calculated absorption spectra (without IPEA shift, Table 6.1) for P and 9MP perfectly match the one recorded by Prof. Crespo, see Figure 6.1. From this Figure 6.1 we can conclude that the low-lying $\pi\pi^*$ (L_a) and $\pi\pi^*$ (L_b) states are responsible the first band, placed at 265 nm, but also $n\pi^*$ states can contribute to it in a lesser extent. A very intense $\pi\pi^*$ state is responsible for the second band (not shown in Table 6.1), peaking at below 200nm.

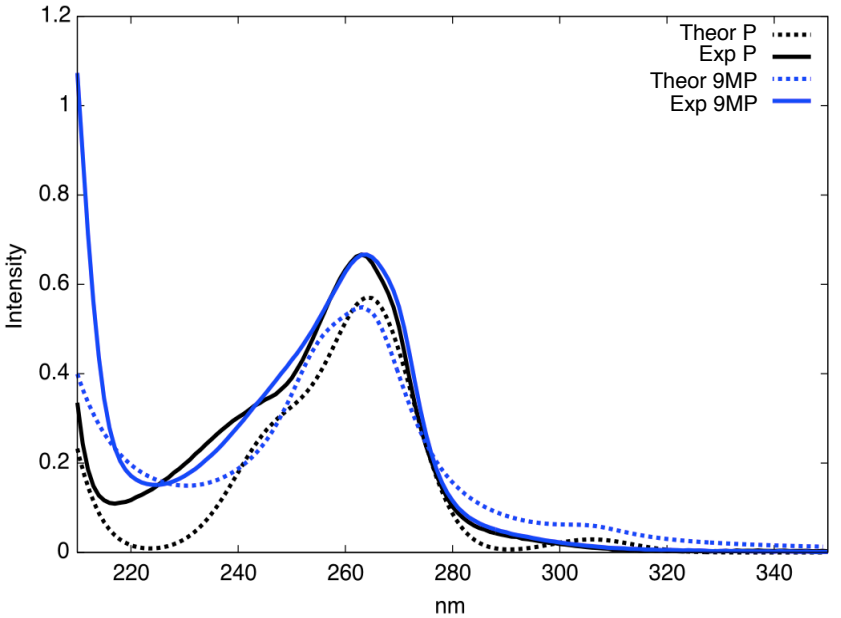

Figure 6.1 Theoretical (dashed lines) and Experimental (in acetonitrile, solid lines) absorption spectra of P (black) and 9mP (blue).

The only difference between the absorption spectrum of P and 9MP is the different state ordering of the S3 and S4 states at CASPT2 level, but since those state are close in energy we can conclude that both bases share the main absorption trends. In fact, for both bases P and 9MP the first state presenting the largest oscillator strength $\pi\pi^*$ (L_a) was considered as the spectroscopic state and the main responsible for energy absorption at least at the wavelength considered in the spectrum.

These similarities/differences between P and 9MP can be extended to other bases as adenine (A) and 2aminopurine, using the absorption spectra calculated by Serrano-Andrés[2] and already mentioned within Chapter 1. The absorption spectra of adenine A, and P/9MP are in fact very similar except for the state ordering of the two $\pi\pi^*$ states, L_a and L_b, which are inverted in A, recall Table 1.1. However, since both states are close in energy in A (5.35 and 5.16 eV) and the oscillator strength for $\pi\pi^*$ (L_a) was calculated to be 100 times larger, this state is has been considered as the spectroscopic state in the literature for this system. For 2-aminopurine, however, the ordering of

both ππ* states is the same as for P. Again for this system, the ππ* (L_a) has been traditionally considered to be the spectroscopic state since although the oscillator strength has been computed to be half of the other ππ* (L_b) state, the calculated energy gap (of 1 eV) is now large. These differences in the absorption spectra of these systems can have an effect in their photophysics and/or photochemistry leading to different deactivation schemes. Assuming that adenine, 2-aminopurine, P and 9P have in common the spectroscopic initial ππ* (L_a) state some considerations can be taken into account. For adenine two low-lying states must be crossed before reaching the ground state while for 2-aminopurine this state is the lowest one. An intermediate situation is found for 9P since only one state separated the spectroscopic and the ground state. Further insight into the deactivation mechanism of these three systems will be gained upon comparison of the computed MEPs from the ππ* (L_a) state.

6.2 Singlet Deactivation Mechanism

In a first stage the deactivation mechanism from the S_2 ππ* (L_a) was considered for both P and 9MP bases. Since almost no differences were found between them, only results for 9MP are presented here (see supporting information of Paper IV for more details).

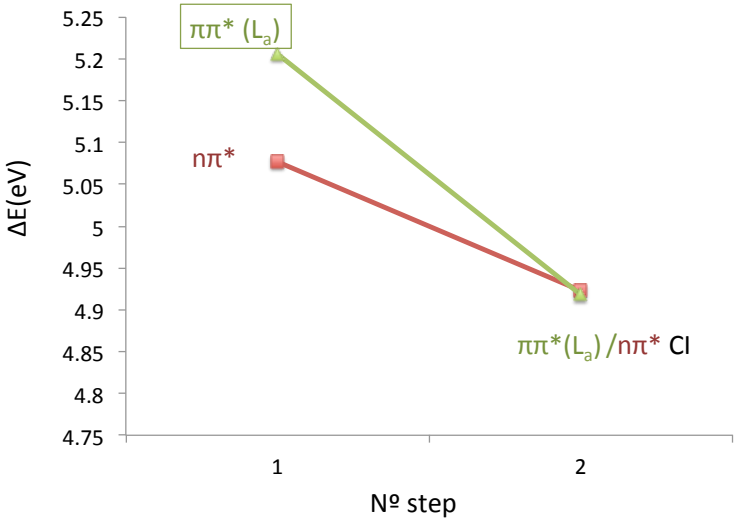

Figure 6.2 CASSCF(16,12)/ANO-S Minimum energy path from the FC region following the S_2 ππ* (L_a) gradient.

The CASSCF (16,12)/ANO-S minimum energy path starting from the FC region following the S_2 ππ* (L_a) state reveals the existence of a conical intersection with the low-lying S_1 nπ* state not far away from the FC region, Figure 6.2. From this CI two MEPs were followed considering gradients of the ππ* (L_a) and nπ* states, problems were found during the first one since the topology of the PES seems to increase the energy in this region, while the second MEP ends up in a minimum in the second potential showing nπ* character, see Figure 6.3.

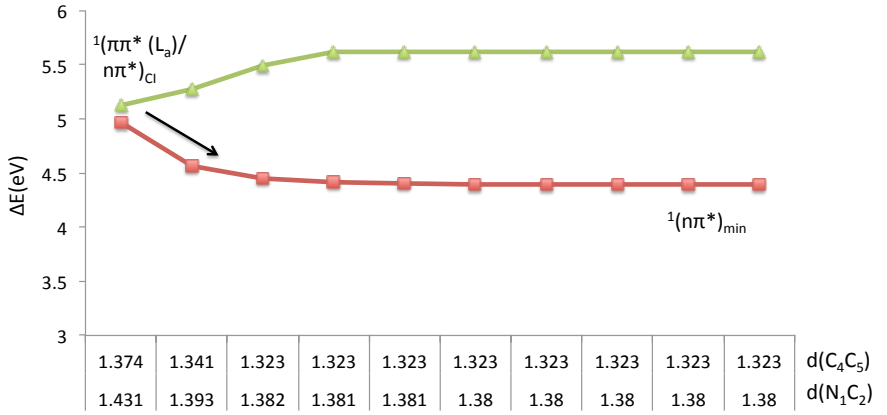

Figure 6.3. CASSCF(16,12)/ANO-S Minimum energy path starting from the ππ* (L_a)/nπ* degeneracy point following the S_1 nπ* gradient.

We have investigated the way the system further deactivates to the ground state once the system reaches the S_1 potential. For this, conical intersection between this state and the ground state was optimized and subsequent MEPs followed it were performed towards both the ground state and the nπ* minimum, see Figure 6.4.

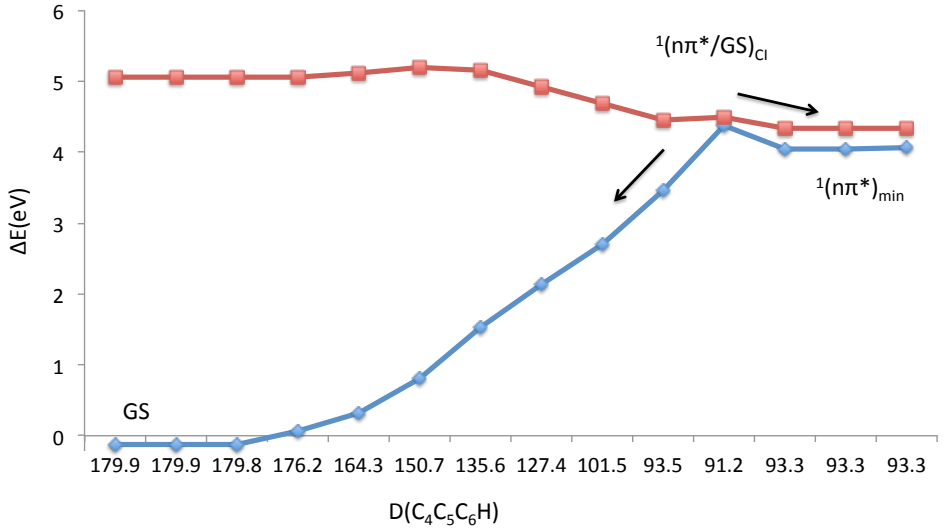

Figure 6.4. CASSCF(16,12)/ANO-S Minimum energy path starting from the nπ*/GS degeneracy following the S_1 nπ* and the GS gradients.

For completeness a conical intersection between the ππ* (L_a) and the ground state was also optimized. Starting from this CI structure, further MEPs were performed to ensure the connection between this point and the respective minima. The MEP from the CI following the gradient of the first root is depicted in Figure 6.5. The examination of this Figure reveals that the GS is reached barrierlessly from the CI. The MEP following the gradient of the second root trying to connect this CI and the ππ*

(L_a) minimum never convergence due to energy increase. A transition state between the minimum and the CI was then optimized.

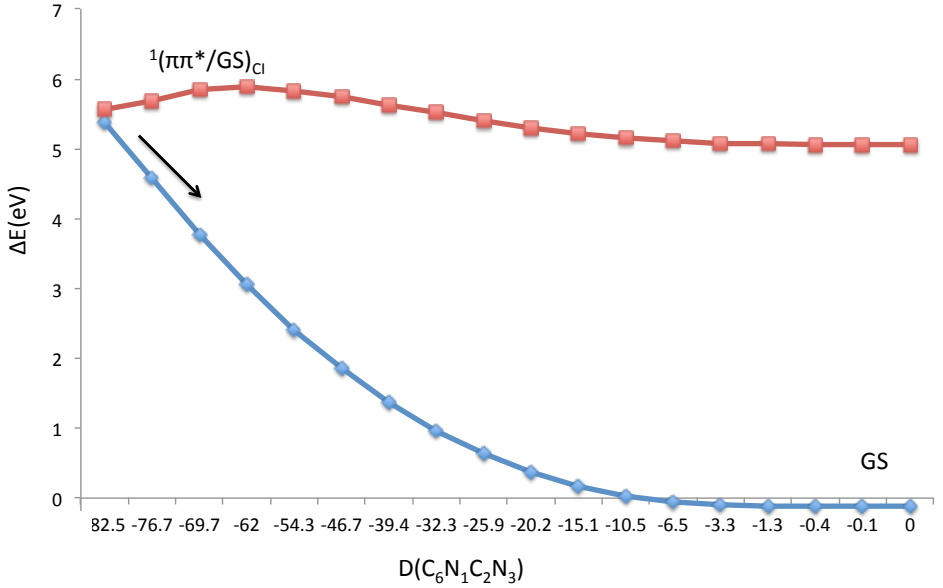

Figure 6.5. CASSCF(16,12)/ANO-S Minimum energy path starting from the ππ*/GS degeneracy point following the S_0.

For the sake of better comparison with A and 2AP, where alternative deactivation mechanism were found from the S_3 ππ* (L_b) state, the deactivation mechanism starting from this state was also investigated. The MEP from the FC region following the gradient of the S_3 ππ* (L_b) reaches a minimum on this potential. In order to connect this minimum with the mechanism explained above, a conical intersection with the low-lying S_2 ππ* (L_a) was optimized. Once this conical is reached the system could, a priori, evolve following any of the previously described mechanisms.
During this section, the main deactivation pathways along the singlet manifold have been described. Additionally, alternative mechanisms leading to triplet state population have been also investigated and will be detailed in the next section.

Finally, a global picture containing both singlet and triplet deactivation paths, is presented in section 6.4, as well as, a comparative with the previously calculated mechanisms for adenine, guanine and 2-aminopurine in section 6.5.

6.3 Triplet Deactivation Mechanism

Since two main minima presenting ππ* (L_a) and nπ* character are likely to be populated accordingly to MEPs explained in the previous section, additional funnels (singlet/triplet minimum energy crossing points) allowing the exchange of population reaching this minima with the triplet manifold were located. According to El-Sayed[3] rules greater probability for intersystem crossing is expected between singlet and triplet states presenting different characters. Thus $^1\pi\pi^*(L_a)/^3n\pi^*$ and $^1n\pi^*/^3\pi\pi^*$ ISC points were optimized. In the following, singlet multiplicity will be indicated using 1 as superscript while 3 will be used for triplets.

Interestingly, the optimized $^1n\pi^*/^3\pi\pi^*$ ISC point was calculated to be very close to the $^1n\pi^*$ minimum whereas $^1\pi\pi^*(L_a)/^3n\pi^*$ was found to be very close to the $^1\pi\pi^*(L_a)/^1n\pi^*$ IC funnel. Spin orbit coupling terms computed at these points of the PES amounts to 10-20 cm^{-1}, indicating a non-negligible probability of populating the triplet manifold at these regions. Further MEPs were computed from the intersystem crossing points following singlet and triplet gradients (see Figures 6.6a and 6.6b) connecting singlet minima and the conical intersection $^3\pi\pi/^3n\pi^*$ in the triplet manifold, respectively. MEPs from this $^3\pi\pi/^3n\pi^*$ CI reached the corresponding triplet $^3\pi\pi^*$ and $^3n\pi^*$ minima (see Figure 6.6c). Both minima and the CI were further optimized. Deactivation from the triplet manifold to the ground state was also considered by locating the $^3n\pi^*/GS$ conical intersection.

All stationary points of the singlet and triplet manifolds and interstate crossing points have been gathered together providing an overview of all possible deactivations mechanisms of excited purines in next section by computing MS-CASPT2 energies.

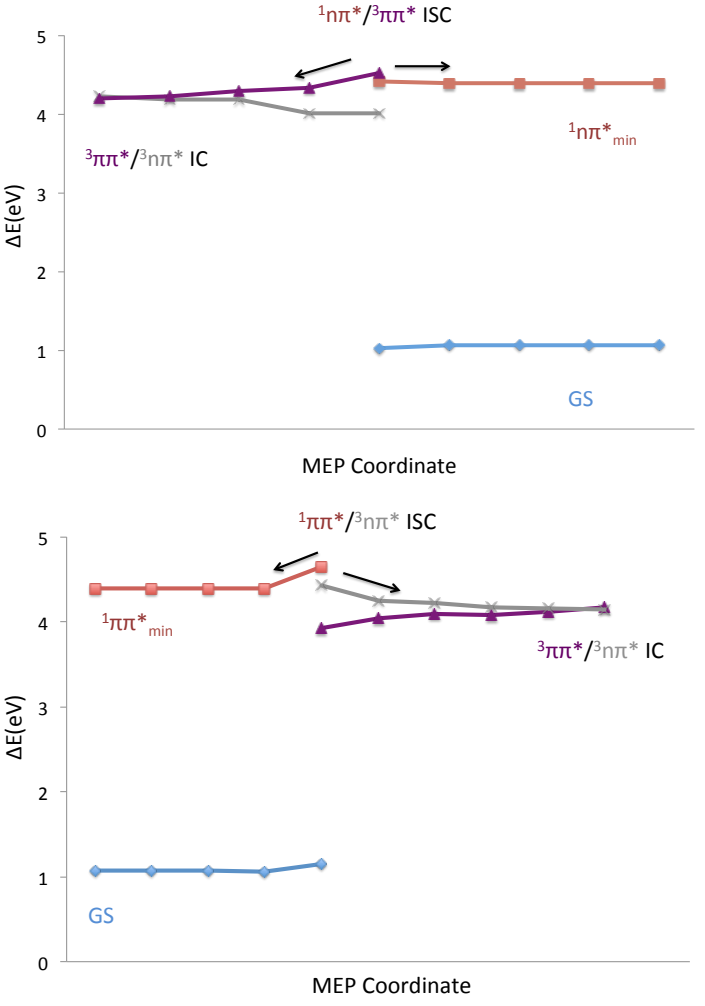

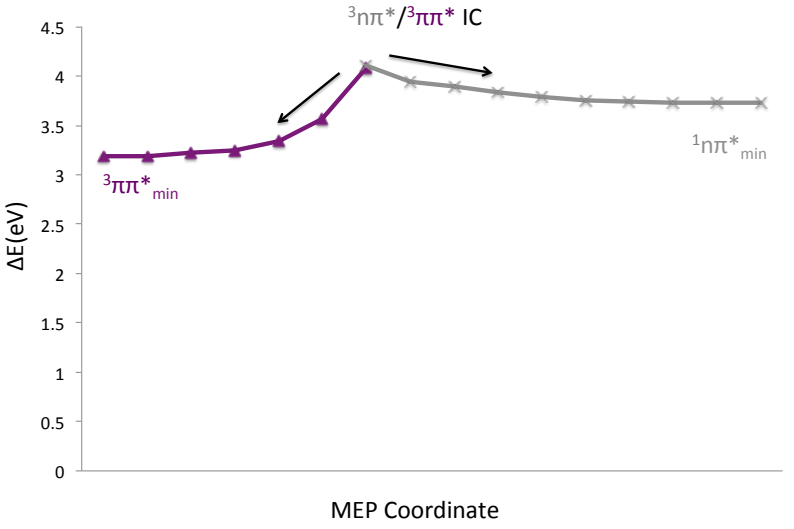

Figure 6.6. CASSCF(16,12)/ANO-S Minimum energy paths from the $^1n\pi/^3\pi\pi^*$, $^1\pi\pi/^3n\pi^*$ and the $^3n\pi/^3\pi\pi$ respectively.

6.4 Global Deactivation Mechanism

The global picture for the deactivation of excited 9MP is shown in Figure 6.7. The energies presented are calculated at MS-CASPT2//CASSCF(16,12)/ANO-L theory level. For those CI where the inclusion of dynamic correlation leads to an increase of the energy gap between the considered states, a further refinement was performed taken into account the gradient difference vector. These refined CASPT2 CIs, specially the ones involving the ground state, increased significantly their energy with respect to CASSCF level of theory, in order words, the decay of the population to the ground state is favoured at CASSCF level, while it is prevented by the existence of energy barriers at CASPT2 level. Other problems were found along the construction of new pictures for the deactivation mechanism of 9MP dynamic correlation. In fact, the $\pi\pi^*$ (L_a) minimum optimized at CASSCF level on the first excited potential, switched to the third root at CASPT2 level of theory. In order to obtain a more reliable picture including dynamic correlation around this region of the PES we reoptimized at CASPT2 level this minimum using a smaller active space (see supporting information Paper IV).

According to the more reliable CASPT2 results, deactivation from excited 9MP along the S_2 $\pi\pi^*$ (L_a) state will progress as follows. The system will arrive barrierless to a minimum on the S_2 potential (or would evolve directly to the CI with the S_1 $n\pi^*$ state at CASSCF level), which, is very close to the S_2 $\pi\pi^*$ (L_a)/S_1 $n\pi^*$ CI (4.42 and 4.48 eV). In summary, both CASSCF and CASPT2 methodologies provide very similar pictures in which the S_1 $n\pi^*$ minimum is easily accessed. The remaining population on the S_1 $\pi\pi^*$ (L_a) can evolve following two different ways, (1) transferring population into the triplet manifold via intersystem crossing (S_1 $\pi\pi^*$ (L_a)/ T_2 $n\pi^*$ at 4.49 eV) or (2) deactivating to the ground state by internal conversion (S_1 $\pi\pi^*$ (L_a)/GS at 4.70 eV). The occurrence of a transition state along the second pathway and the large structural changes that the molecules must experience (out-of-plane movement of the N_1 atom,

leading to a large distortion of the C_6-N_1-C_2-N_3 dihedral) compared to the close in energy and geometry that the minimum and the ISC are, would clearly favour either the transfer of population to the triplet manifold or to alternatively to the S_1 $n\pi^*$ minimum.

Once in the S_1 $n\pi^*$ minimum (3.80 eV) the system would need to increase its energy (due to large geometry distortions produced by the out-of-plane movement of the C_6-H bond perpendicularly to the purine skeleton) by ~0.6 eV to reach the ground state IC funnel (S_1 $n\pi^*$/GS at 4.38 eV) or can as well populate the triplet manifold through an ISC region very close to it (S_1 $n\pi^*/T_2$ $\pi\pi^*$ at 3.70 eV). Again, triplet population is expected to be more favoured due to the absence of energy barriers to reach the ISC funnel.

Once in the triplet manifold both triplet minima are connected through T_2 $n\pi^*/T_1$ $\pi\pi^*$ CI. Although at "long" times the more stable minimum T_1 $\pi\pi^*$ is expected to carry the largest population, both minima could a priori be populated. From the most stable triplet minimum T_1 $\pi\pi^*$, deactivation to the ground state was found to play negligible role, since the corresponding conical intersection was found to appear at very high energies (~2 eV higher than the minimum), and it is not represented in Figure 6.7.

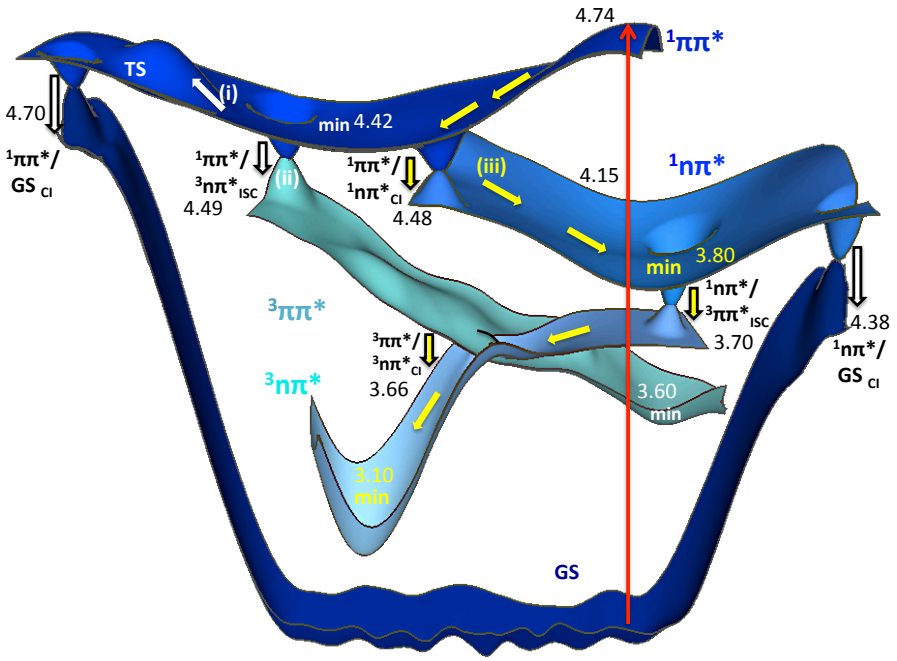

Figure 6.7. MS-CASPT2//CASSCF(16,12)/ANO-L Deactivation mechanisms computed for 9-methylpurine. Singlet states in solid lines (S_0 in blue, S_1 in brown, S_2 in green, S_3 in black) and triplet states in dashed lines (T_1 in purple and T_2 in grey). Energies in eV relative to the S_0 energy at the FC minimum.

In summary, the most favourable deactivation mechanism scheme based on static quantum chemical calculations would be the following: S_2 $\pi\pi^*$ (L_a)--->S_1 $n\pi^*$---> T_1 $\pi\pi^*$ (Path 1 in Figure 6.8), but other possible paths as S_2 $\pi\pi^*$ (L_a)--->T_2 $n\pi^{**}$---> T_1 $\pi\pi^*$ could not be discarded (Path 2 in Figure 6.8), without dynamic studies. From the S_2

$\pi\pi^*$ (L_a) potential, population can directly populate the triplets via ISC ($^1\pi\pi^*(L_a)/^3n\pi^*$) or alternatively evolve along the singlet manifold and reach the S_1 potential. In the proximity of the S_1 $n\pi^*$ minimum the most probable deactivation pathway is again to undergo ISC ($^1n\pi^*/^3\pi\pi^*$) to the triplet manifold, where the population would finally reach the most stable T_1 $\pi\pi^*$ minimum.

If 9MP is however excited to the higher bright state $\pi\pi^*(L_b)$ would involve an additional internal conversion funnel to decay from the $\pi\pi^*(L_b)$ minimum localized along the MEP (Path 3 in Figure 6.8).

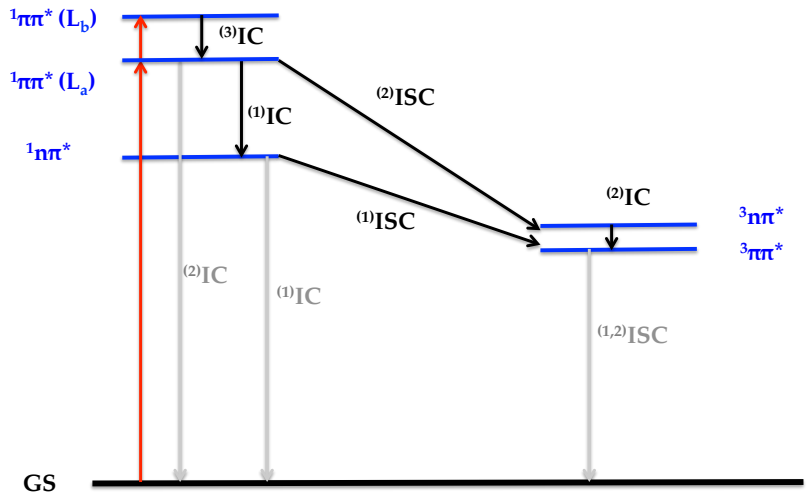

Figure 6.8. Possible deactivation mechanism for the excited 9MP base.

Further details regarding structures, MEPs and/or the energetics of the deactivation pathways can be found in Paper IV and its supporting information.

6.5 Comparison with other nucleobases: adenine, 2-aminopurine and guanine

In the following, the influence of the substitution of the purine skeleton with a NH2 or C=O groups and its position will be analysed through the comparison of the photophysics of adenine (A), 2aminopurine (2AP) and guanine (G) with that of P or 9MP. For this purpose, the works of Serrano-Andrés[2,4] will be taken as reference.

Adenine (6-aminopurine)[5]

As already discussed in section 6.1, the S_3 $\pi\pi^*$ (L_a) excited state has been traditionally considered in the literature as the spectroscopic state. The MEPs calculated by the group of Serrano-Andrés evolve barrierless towards a conical intersection with the ground state, after crossing the low-lying excited S_2 $\pi\pi^*$ (L_b) and S_1 $n\pi^*$ states. There is no evidence for the existence of minima along this path according to these calculations. Thereby, the excess of energy absorbed by the system upon population of

the S_3 $\pi\pi^*$ (L_a) state is transferred on the way to the ground state in an ultrafast timescale through internal conversion process. If the S_2 $\pi\pi^*$ (L_b) state is alternatively populated either directly or via internal conversion from the S_3 $\pi\pi^*$ (L_a) spectroscopic states, the system will evolve towards a minimum on this potential, but it can also cross with the low-lying S_1 $n\pi^*$ state. From the S_1 $n\pi^*$ state, the system decay to the ground state is prevented by energy barriers due to the presence of a transition state. Then a **minor** alternative relaxation **mechanism** involving **S_1 $n\pi^*$** state has been postulated as responsible for the **longer-lived species** and **slower decays** to the ground state.

2-aminopurine[2]

The spectroscopic state of 2-aminopurine presents the same $\pi\pi^*$ (L_a) character but in this case it corresponds to the first excited state S_1. The MEP, starting from the spectroscopic state at the FC equilibrium geometry, ends in a minimum separated from the CI with the ground state by a transition state placed 0.2 eV (~5kcal/mol) above this minimum. Due to the high energy of the $\pi\pi^*$ (L_b) state, this state is believed to play a negligible role in the photophysics of 2-aminopurine, being only important when exciting at short wavelengths. The use of short wavelength can allow the indirect population of the low-lying state $n\pi^*$, however deactivation from this state is also considered of minor importance due to the existence of low energy barriers (~2kcal/mol) separating the minimum and the CI with the ground state. In conclusion, the occurrence of moderate energy barriers on the way to the ground state from the $\pi\pi^*$ (L_a) state is compatible with the non radiative decay observed for 2AP and with the slower deactivation (nanosecond) compared to A. Recent experiments report for this system[6] that fluorescence (30%) from the spectroscopic $\pi\pi^*$ (L_a) minimum is as important as internal conversion (30%) supporting the above statement. However, these experiments bring attention to the importance of ISC for this system for which they recorded 40% of quantum yield.

Then, different behaviour was found depending on the substituted position with NH_2 group.

Guanine (6-oxo-2-aminopurine)[4]

The state ordering calculated for guanine (G, S_1 $\pi\pi^*$ (L_a) at 4. 93 eV) was found to be very similar to the one of 2AP (S_1 $\pi\pi^*$ (L_a) at 4. 33 eV) even if the two nucleobases have the purine heterocycle substituted with different groups. Although the absorption spectrum of guanine (G) was found to be closer to 2AP, the deactivation pathways calculated for this system resemble more to the computed for A. The MEP from the spectroscopic state was found to be barrierless towards the conical intersection with the ground state showing no minimum along it. The shape of this pathway is responsible for the ultrashort decay observed experimentally and of the same order to the ones of adenine (~150 femtoseconds). Also as for adenine alternative slower mechanism involving $n\pi^*$ state are also possible. The slightly shorter times of G are consistent with the smaller number of roots connected to the spectroscopic state, which avoids the additional crossings characteristic of A.

Thereby, addition of an oxo group to 2-aminopurine seems to avoid the presence of minimum along the spectroscopic state minimum and to favour even more the deactivation to the ground state compare to 6-aminopurine (adenine).

Comparison with purines

From the comparison of all the bases studied here and in previous works it is possible to conclude that the nature and position of the substituent influences both the shape of the absorption spectrum and the deactivation mechanism altering completely the photophysics of these systems. In principle, we could classify these systems into two main groups; (1) the first characterized by steep MEPs leading direct and barrierless to internal conversion funnels to the GS (canonical bases G and A) and considered then photostable and (2) the second with MEPs showing one or several barriers on the way to these funnels (2AP and P), which are not photostable and present important triplet yields. The height and position of these energy barriers together with the existence and efficiency of ISC funnels in the proximity of the minima separated from the GS CIs by a transition state will regulate the ISC vs photostability ratio.

An in depth study on how the electronic effects induced by peripheral substitution model the deactivation mechanism of these systems in is progress in our group.

6.6 Excited states Dynamics: Ab initio Simulations and Ultrafast Femtosecond Experiments

Ab initio Dynamic Simulations

Due to the significantly different topology of the CASSCF and CASPT2 PES, semiclassical dynamic simulations performed within the first level of theory for purine base found the decay to the ground state to be the main mechanism. These dynamic simulations were performed by Clemens Rauer et al. in the group of Pr. Leticia González using CASSCF (12,9)/def-2svp level of theory. Unfortunately using CASPT2 gradients during the dynamics is nowadays unaffordable. During the first 200 fs of simulation it can be observed that all the initial population is placed in the S_2 stat and decays very fast to the fist excited state (see Figure 6.9). Then, this population is transferred from the S_1 to the ground state until a time equal to 1000 fs when the number of trajectories running on the S0 is more than the one evolving on the excited states. This is explained as the absence of energy barrier from neither of the singlet minima towards its correspondent conical intersection with the ground state. Since ground state population take place quit fast, there is not enough time for triplet population to take place from these singlet minima. Thereby, the main mechanism proposed according to this results after light absorption is the S_2->S_1->S_0 with intersystem crossing to triplet states occurring with minor rates.

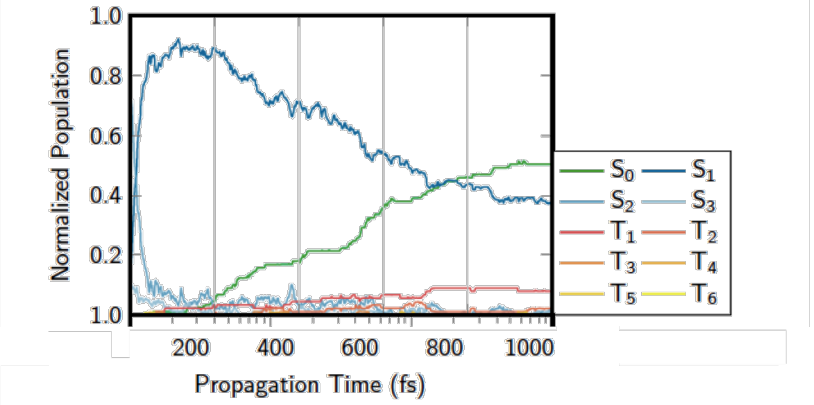

Figure 6.9. Time evolution of the state coefficients for purine.

Ultrafast Femtosecond Dynamic Experiments for P and 9MP

Femtosecond broadband transient absorption experiments were performed in parallel by the group of Prof. Crespo-Hernandez (Case Western Reserve University in Cleveland) to investigate the excited-state dynamics 9MP and purine free base P in solution (see Figure 6.10). Excitation of 9MP in aqueous solutions at 266 nm results in ultrafast internal conversion of the initially excited state to the vibrationally-excited $S_1(n\pi^*)$ state. After vibrational and conformational relaxation, which occurs in a time scale of hundreds of picoseconds, the relaxed $S_1(n\pi^*)$ state in 9MP then decays in hundreds of picoseconds (τ_3) to populate a long-lived transient absorption species that has an absorption maximum at 406 nm with a shoulder at ~580 nm in acetonitrile and at absorption maximum at 412 nm with a shoulder at ~570 nm in aqueous buffer solution (Fig. 6.10).

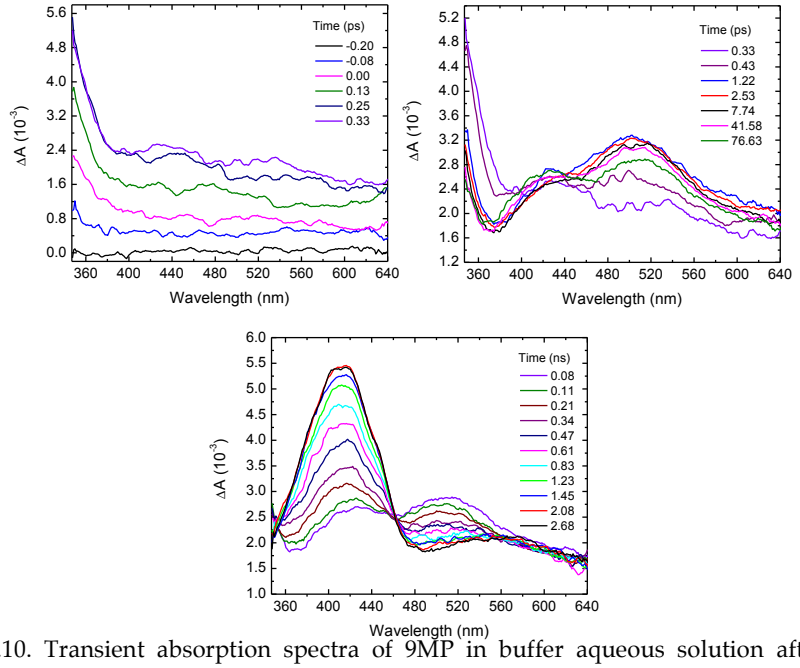

Figure 6.10. Transient absorption spectra of 9MP in buffer aqueous solution after 266 nm excitation

This transient absorption species does not decay within the three nanoseconds time window of the instrument and it is assigned to the lowest-energy triplet state in 9MP. Analogous experiments in polar aprotic and nonpolar solvents for 9MP show an almost twofold decrease in the intersystem crossing lifetime, suggesting that a solvent-dependent energy barrier must separate the S_1 minimum from the singlet-to-triplet crossing region

6.7 Conclusions

The effect of substituting the purine skeleton of DNA/RNA nucleobases has been investigates comparing the absorption spectrum and the photophysics of purine with that of adenine, guanine and 2aminopurine. Our results show that both the nature and the position of the substitution affect the absorption properties and the relaxation mechanism of these systems, altering their intrinsic reactivity. In fact, high level multiconfigurational ab initio calculations including dynamic correlation predict for P and 9MP the existence of energy barriers separating the singlet minima from IC funnels to the GS. The occurrence of effective ISC in the proximity of these minima would favour the population of the triplet manifold. The amino substitution in position 2 decreases the energy barrier for accessing to the GS and therefore smaller singlet/triplet yields are obtained. Furthermore, amino substitution in position 6 (adenine) or oxo in position 2 (guanine) produce the vanishing of these barriers leading to barrierless PES from the FC to the GS conferring these nucleobases their stability properties.

Bibliography

(1) Platt, J. R. *J. Chem. Phys.* **1949**, *17*, 484.

(2) Serrano-Andrés, L.; Merchán, M.; Borin, A. C. *Proceedings of the National Academy of Sciences* **2006**, *103*, 8691.

(3) El-Sayed, M. A. *J. Chem. Phys.* **1963**, *38*, 2834.

(4) Serrano-Andrés, L.; Merchán, M.; Borin, A. C. *J. Am. Chem. Soc* **2008**, *130*, 2477.

(5) Serrano-Andrés, L.; Merchán, M.; Borin, A. C. *Chem. Eur. J.* **2006**, *12*, 6559.

(6) Reichardt, C.; Wen, C.; Vogt, R.; Crespo-Hernández, C. E. *Photochem. Photobiol. Sci* **2013**, *12*, 1341.

Chapter 7

Thiobases Photochemistry

The effect of carbonyl-by-thiocarbonyl substitution in the spectroscopy of canonical DNA and RNA nucleobases will be described throughout this chapter. In this chapter we will examine the absorption spectra and deactivation mechanism of the purine nucleobase 6-thioguanine (6TG) and pyrimidines 4-thiothymine (4TT), 2-thiocytosine (2TC) and 4-thiouracil (4TU). The results for 4TU nucleobase described in the following are part of the Master Thesis of Kathy Chen in which I participated.

Further functionalization with a second sulphur atom was also considered to investigate the effect of an extra heavy atom in the calculated spin orbit coupling and thus in the intersystem crossing rates. With this aim, a similar protocol as the one described above for the rest of thiobases was undertaken for the doubled substituted 2,4-thiothymine.

Semiempirical semiclassical dynamic simulations for two representative thiobases (a purine and a pyrimidine) were also carried out to elucidate the actual deactivation mechanism and intersystem crossing rates.

Static and dynamic results for 6-Thioguanine are compiled in Papers V and VI respectively, while drafts for the publications containing the results obtained for 4TT and 2TC (in collaboration with the group of Prof. Leticia González) are under preparation.

7.1 Absorption Spectra

The computed absorption spectra for 6TG, 4TT, 4TU and 2TC bases are summarized in Table 7.1.

	6TG MS-CASPT2/CASSCF(14,12)/ANO-L			2TC MS-CASPT2/CASSCF(14,10)/ANO-L		
	Main Config.	CI Coeff.	ΔE (f)	Main Config	CI Coeff.	ΔE (f)
S_1	$n_s\pi^*_{CS}$	0.91	3.36 (0.000)	$n_s\pi^*_{CS}$	-0.90	3.62 (0.000)
S_2	$\pi_{CC}\pi^*_{CS}$	0.83	4.05 (0.535)	$\pi_{CC}\pi^*_{CC}$	-0.85	3.86 (0.054)
S_3	$\pi_{CC}\pi^*_{CC}$	0.86	4.90 (0.144)	$n_S\pi^*_{CC}$	-0.88	4.04 (0.000)
S_4	$n_S\pi^*_{CC}$	-0.80	5.07 (0.007)	$\pi_{CC}\pi^*_{CS}$	0.84	4.67 (0.740)
	4TT MS-CASPT2/CASSCF(14,10)/ANO-L			4TU MS-CASPT2/CASSCF(14,10)/ANO-L		
S_1	$n_S\pi^*_{CS}$	-0.94	3.12 (0.000)	$n_S\pi^*_{CS}$	0.86	3.04 (0.000)
S_2	$\pi_{CC}\pi^*_{CS}$	-0.87	4.26 (0.591)	$\pi_{CC}\pi^*_{CS}$	0.87	4.13 (0.500)
S_3	$\pi_{CS}\pi^*_{CS}$	-0.87	4.85 (0.134)	$\pi_{CS}\pi^*_{CS}$	0.77	4.87 (0.170)
S_4	$n_S\pi^*_{CC}$	0.71	5.91 (0.000)	$n_S\pi^*_{CC}$	0.67	5.46 (0.002)
S_5	$\pi_{CC}\pi^*_{CC}$	0.62	6.20 (0.173)	$\pi_{CC}\pi^*_{CC}$	0.54	5.52 (0.210)

Table 7.1 Singlet vertical absorption energies (in eV), main contributions to the wave functions and oscillator strengths of the studied thiobases 6TG (6-Thioguanine), 2TC (2-thiocytosine), 4TT (4-thiothymine) and 4TU (4-thiouracil) calculated at the MS-CASPT2//CASSCF levels of theory using the active space and basis set specified for each case.

The four thiobases spectra have in common a first dark excited state, presenting $n_S\pi^*_{CS}$ character and placed around 3-3.6 eV. Above in energy we find the first bright $\pi\pi^*$ excitation which involves the same orbitals for 6TG, 4TT and 4TU while slightly different orbitals for 2TC. The energy difference between the S_1 and S_2 states increases in the order 2TC (0.24 eV) < 6TG (0.69 eV) < 4TU (1.09 eV) < 4TT (1.14 eV) and can play a role during the deactivation mechanism of these bases. Higher energy regions of the spectra are characterised by one or several bright $\pi\pi^*$ excitations preceded or followed by other $n\pi^*$ states. For all the thiobases examined, the S_2 has been considered as the spectroscopic state, since for all the systems except 2TC, it correspond to the lowest lying electronic excited state carrying the largest oscillator strength.

For more details regarding active space and/or other technical issues see attached supporting information of the corresponding papers.

Triplet states were also considered for the four thiobases since evaluating intersystem crossing rates in these bases is one of the main aims of this thesis. Triplet vertical energies relative to the ground state at the FC equilibrium geometry are collected in Table 7.2 for 6TG, 2TC, 4TT and 4TU bases.

	6TG MS-CASPT2/CASSCF(14,12)/ANO-L			2TC MS-CASPT2/CASSCF(14,10)/ANO-L		
	Main Config.	CI Coeff.	ΔE	Main Config	CI Coeff.	ΔE
T_1	$\pi_{CC}\pi^*_{CS}$	-0.86	3.10	$\pi_{CC}\pi^*_{CS}$	0.86	3.42
T_2	$n_S\pi^*_{CS}$	-0.91	3.31	$\pi_{CC}\pi^*_{CC}$	-0.85	3.54
T_3	$\pi_{CC}\pi^*_{CC}$	-0.86	4.24	$n_S\pi^*_{CS}$	-0.88	3.59
T_4	$\pi_{CS}\pi^*_{CS}$	-0.72	5.05	$n_S\pi^*_{CC}$	0.83	4.05
	4TT MS-CASPT2/CASSCF(14,10)/ANO-L			4TU MS-CASPT2/CASSCF(14,10)/ANO-L		
T_1	$\pi_{CC}\pi^*_{CS}$	-0.77	2.97	$\pi_{CC}\pi^*_{CS}$	0.66	2.89
T_2	$n_S\pi^*_{CS}$	-0.93	3.03	$n_S\pi^*_{CS}$	0.84	2.99
T_3	$\pi_{CS}\pi^*_{CS}$	0.74	4.11	$\pi_{CS}\pi^*_{CS}$	0.47	4.27
T_4	$\pi_{CC}\pi^*_{CC}$	0.75	5.24	$\pi_{CC}\pi^*_{CC}$	0.48	5.15

Table 7.2 Triplet vertical absorption energies (in eV) and main contributions to the wave functions of the studied thiobases 6TG (6-Thioguanine), 2TC (2-thiocytosine), 4TT (4-thiothymine) and 4TU (4-thiouracil) calculated at the MS-CASPT2//CASSCF levels of theory using the active space and basis set specified for each case.

Two triplet states were found to be below in energy (3.10 and 3.31 eV) than the spectroscopic (4.05 eV) state, S_2, for 6TG, with $\pi\pi^*$ and $n\pi^*$ characters respectively and also for 4TU. For the rest of the bases, 2TC and 4TT, one additional $\pi\pi^*$ triplet state was also located below the S_2 spectroscopic state. ISC with any of these lower lying triplet states is in principle possible. However, according to El-Sayed rules (see Chapter 2) the most probable transition would require a change in the character of the singlet and triplet transition involved, so since the spectroscopic state presents $\pi\pi^*$ character, the most efficient ISCF expected with a triplet $n\pi^*$ state. The singlet ($\pi\pi^*$)/triplet ($n\pi^*$) energy gap follows the order: 2TC (0.27) < 6TG (0.7) < 4TU (1.14) < 4TT (1.23) eV.

Although these calculations only reveal information about the behaviour of the excited singlet and triplet states at the FC region some trends were found for the four computed thiobases giving place to some interesting questions?

(1) The S_2 excited state was found to be the main spectroscopic state (at least at low energy regions) for all of them.
(2) The energy gap between S_2 and S_1 ranges from 0.2 (2TC) to 1.2 eV (4TT), being the main differences between the singlet absorption spectra of the studied bases. Is then internal conversion more accessible in 2TC and 6TG than in 4TT?
(3) Energy differences between the spectroscopic state and the interesting triplet state follow the same pattern described above. Although small energy difference is not the only factor defining intersystem crossing probability, could also this trend give us an idea of how close are the singlet/triplet

crossings from the FC region? Are then intersystem crossing points more accessible in 2TC and 6TG than in 4TT?

To answer the above raised questions and to detail the deactivation mechanism from the excited states further calculations, as minimum energy paths, conical intersections and minimum singlet/triplet crossing points optimizations, are required.

7.2 Singlet Deactivation Mechanism

Two main possible scenarios were found when computing the minimum energy paths from the FC region along the spectroscopic S_2 state: (a) the occurrence of a degeneracy region with the low-lying S_1 state accessed barrierlessly (Type A) (b) the existence of a minimum on the S_2 potential from which the system need to sourmont an energy barrier to access the CI the lower lying state (Type B) (see Figure 7.1). The first case was found for 6TG and 2TC bases whereas the second situation is characteristic of 4TT and 4TU.

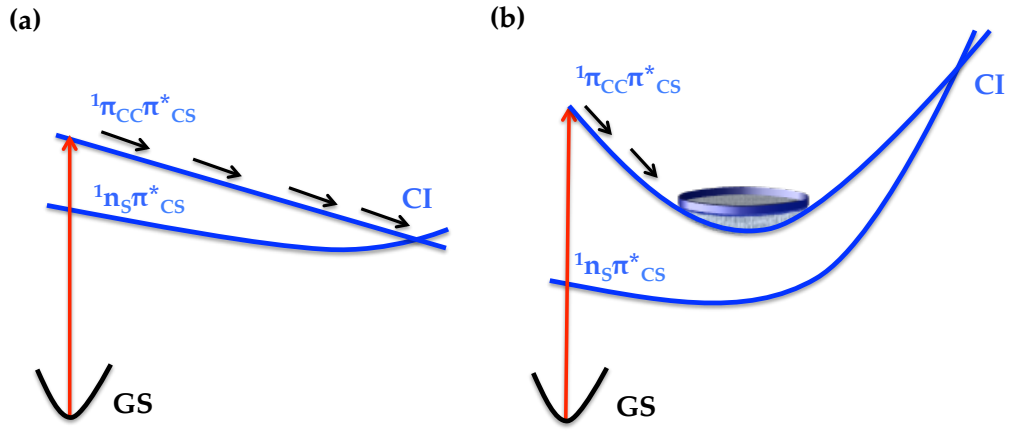

Figure 7.1 Scheme of the two possible scenarios for the singlet deactivation mechanism of the thiobases along its spectroscopic state: (a) evolving barrierless towards a conical intersection (CI) with low-lying states or (b) reaching a minimum on this potential.

Type A: 6TG and 2TC

Both 2TC and 6TG presenting the smallest the S_2-S_1 energy difference at the FC region (0.42 and 0.69 eV) show the S_2/S_1 CI relatively close to the FC region and reaching the MEP the degeneracy region in few steps. Starting from the CI two minima on the S_1 potential were optimized presenting $n_S\pi^*_{CS}$ and $\pi_{CC}\pi^*_{CS}$ respectively for both 6TG and 2TC (see paper V). Although both of them are likely to be populated, the $n_S\pi^*_{CS}$ minimum is the most stable one and is expected to accumulated the largest population (see section 7.5). Then, for these bases, after excitation to the spectroscopic state, the

population should remain on the $n_S\pi^*_{CS}$ minimum for a brief period of time ultrafast populating the first excited state (see section 7.5).

Starting from the S_1 $n_S\pi^*_{CS}$ minimum, deactivation to the ground state is not likely to occur due to the large energy gap between this minimum and the corresponding conical intersection with the ground state (see paper V). Arriving to this CI involves important geometrical changes, which move the C-S bond out of the plane. Since, from the S_1 $\pi_{CC}\pi^*_{CS}$ minimum the amount of energy required to revert to the ground state is smaller, this path is proposed as a more plausible deactivation funnel.

Other alternative mechanisms starting from the above minima involving triplet manifold will be considered in the following section.

Type B: 4TT and 4TU

As already mentioned in section 7.1, for these bases a large S_2-S_1 energy gap of ~1.1 eV was found. The minimum energy path from the FC region reaches a $\pi_{CC}\pi^*_{CS}$ minimum on the second excited state. From this minimum the conical intersection was optimized and was located 1.5 eV above the minimum, even higher than the initial absorption energy of the spectroscopic state. This CI is connected with a $n_S\pi^*_{CS}$ minimum on the S_1 potential. Therefore, contrary to the ultrafast decay to the S_1 expected for type A bases, 4TT and 4TU molecules will remain trapped in the S_2 $\pi_{CC}\pi^*_{CS}$ minimum for larger periods of time. In fact, fluorescence was experimentally recorded for these species (see section 7.5).

Despite the different profiles above expñained for type A and B bases, decay to the ground state was also found to play a minor role compared to alternative pathways (see next section) in type B bases too.

This classification of the thiobases has been done on the sole base of static calculations and results obtained from MEP and CI optimizations, and further complementary time resolved studies would help providing a more general and complete overview. Information from experiments and dynamic simulations will be detailed in section 7.5. However, two main ideas can be concluded from the above described pathways:

- Type A thiobases: 6TG and 2TC are expected to experience ultrafast internal conversion from the spectroscopic state S_2 $\pi_{CC}\pi^*_{CS}$ to the first excited state $n_S\pi^*_{CS}$.
- Type B thiobases: 4TT and 4TU are expected to slowly transfer the population from the spectroscopic state S_2 $\pi_{CC}\pi^*_{CS}$ to low-lying excited states.
- Both Type A and Type B thiobases present high energy barriers to deactivate to the ground state from the corresponding singlet minima.

7.3 Mechanisms for Triplet Population

As anticipated in the previous section, from the S_2 $\pi_{CC}\pi^*_{CS}$ state the most probable intersystem crossing funnel for the transfer of population to the triplets. The $n_S\pi^*_{CS}$ triplet is the T_2 (at the FC region) for 6TG, 4TU and 4TT (recall table 7.2), and although it corresponds to the T_3 for 2TC it is almost degenerated with T_2 and even becomes T_2 at the CASSCF level and/or smaller number of roots are specified. Onwards, spin is specified as a superscript before the state character.

Then, the first possibility to transfer population to the triplet manifold is through the $^1\pi_{CC}\pi^*_{CS}/^3n_S\pi^*_{CS}$ crossing (ISC_1, see Figure 7.2). This ISC_1 has been located close to the singlet $^1\pi_{CC}\pi^*_{CS}/^1n_S\pi^*_{CS}$ CI and as a consequence, is energetically accessible during the deactivation mechanism of Type A bases but is quite far from the singlet minimum in Type B bases (see Figure 7.2). Due to the location and large SOCs computed at ISC_1, its is expected to compete with further deactivation along the singlet manifold for the considered bases, keeping in mind that internal conversion is expected to take place faster than intersystem crossing.

Which is the real efficiency of this intersystem crossing funnels? Can it compete with S_2->S_1 internal conversion? These questions can be answered through the analysis of the results obtained during the dynamic simulations performed for bases corresponding to both types (Type A 6TG and Type B 4TT), see section 7.5.

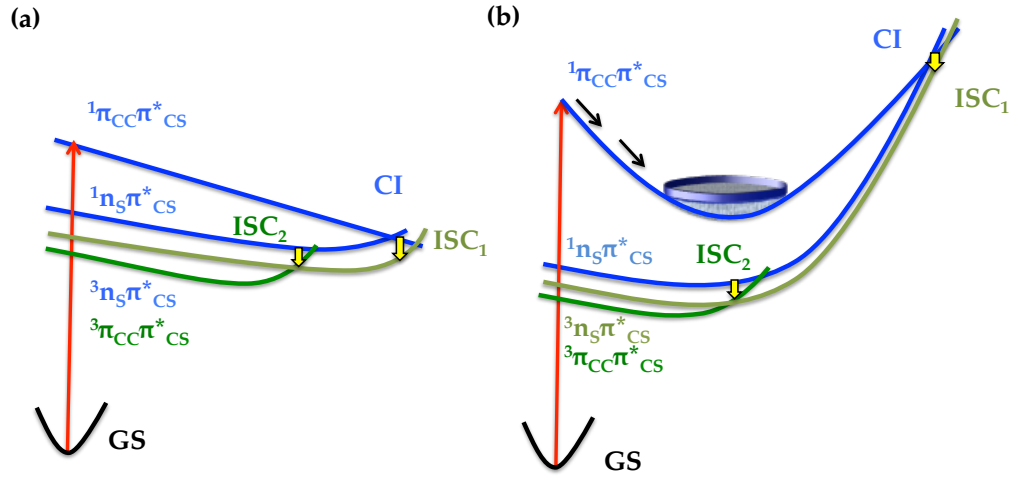

Figure 7.2 Scheme for the two possible scenarios allowing for the population of the triplet manifold in thiobases: (a) Type A bases: 6TG and 2TC (b) Type B bases 4TT and 4TU.

Once the triplet $^3n_S\pi^*_{CS}$ state is reached, a minimum with this character can be found being also very similar to the corresponding singlet minimum. In fact, for 6TG for instance, in this region the three states $^1n_S\pi^*_{CS}$, $^3n_S\pi^*_{CS}$ and $^3\pi_{CC}\pi^*_{CS}$ are degenerated

and the molecules reaching the $^3n_S\pi^*_{CS}$ minimum are immediately able to convert to the lowest $^3\pi_{CC}\pi^*_{CS}$ one.

Although direct population of the S_1 $n_S\pi^*_{CS}$ state is unlikely due to its low oscillator strength, it can be reached by internal conversion from the spectroscopic state (specially in Type A bases) and, thus, a second intersystem crossing mechanism from (ISC_2, see Figure 7.2) can also be considered.

From the S_1 $n_S\pi^*_{CS}$ minimum, a singlet/triplet minimum energy crossing point between this singlet and the $^3\pi_{CC}\pi^*_{CS}$ state was calculated. The optimized structure for the ISC_2 was found to be very close to the mentioned minimum, both in energy and geometry. Large SOCs obtained for this ISC_2 together with the proximity to the singlet minimum turn this region of the PES in principle excellent funnel for triplet population. Once in the $^3\pi_{CC}\pi^*_{CS}$ state, a minimum on the first excited triplet state is found, and it is the most stable one, being then the most likely to be populated. If the first ISC1 takes place and it is the $^3n_S\pi^*_{CS}$ minimum the one that it is reached, as said before, it can convert to the most stable $^3\pi_{CC}\pi^*_{CS}$ one through a CI existing between them.

From any of the optimized triplet minima, deactivation to the ground state was also found to be not very favourable due to large energy difference between them and the intersystem crossings connecting to the ground state.

Further details on the triplet deactivation mechanisms can be found in the corresponding papers and from the results of the dynamic simulations. However, some conclusions can be extracted from these static calculations:

(1) Intersystem crossing from the S_2 $^1\pi_{CC}\pi^*_{CS}$ spectroscopic state to the $^3n_S\pi^*_{CS}$ triplet state, ISC_1, is expected to be fast in Type A bases and slow for B bases, however, in both bases it will compete with IC to the S_1.

(2) Although intersystem crossing from the S_1 $^1n_S\pi^*_{CS}$ state to the $^3\pi_{CC}\pi^*_{CS}$ state, ISC_2, is energetically accessible in both kind of bases, the rate determining step is internal conversion to the S_1 since it cannot be populated directly by light absorption. Then, ISC_2 strongly depends on the efficiency of IC to the S_1, expected to be fast for Type A bases and slower for B ones.

(3) In conclusion, both ISC (1 and 2) are expected to take place ultrafast for Type A bases while due to the existence of high energy barriers should be slower in Type B systems. However, it should be taken into account that we can say nothing until now about yields for triplet population, and slow it does not mean that they cannot be reached in type B thiobases.

(4) Non-radiative decay from the triplet state to the ground state requires overcoming of large energy barriers.

7.4 Global Deactivation Mechanism

The global deactivation mechanism based on quantum chemical static calculations for the thiobases 6TG, 2TC, 4TT and 4TU is depicted in Figure 7.3.

For **Type A** thiobases (6TG and 2TC) S_2 would decay in an **ultrafast time scale** to S_1, as suggested by barrierless minimum energy paths connecting the FC region with the conical intersection between the spectroscopic state and S_1. Then ISC to the triplet manifold would take place via ISC_2 and after internal conversion, the most stable T_1 $^3\pi_{CC}\pi^*_{CS}$ minimum is reached. Molecules are expected to be trapped on it time enough to experience Type II singlet oxygen production reactions: **S_2->S_1->T_2/T_1**. An alternative mechanism, where triplet states are directly populated from the S_2 can also play a role as it is predicted as energetically favourable from a static point of view.

Type B thiobases (4TT and 4TU) present similar decay pictures except for the minimum found in the spectroscopic state potential and which is expected to slow down internal conversion and ISC_1 **S_2->S_1->T_2/T_1**. However, since SOC are not negligible at this minimum region it might be the case that ISC_2 occurs before than IC to the S_1 takes place, **S_2->T_2->T_1.**

As said several times through this discussion, dynamic simulations will shed some light into mechanisms competition and the time scales and rates in which ISC takes place.

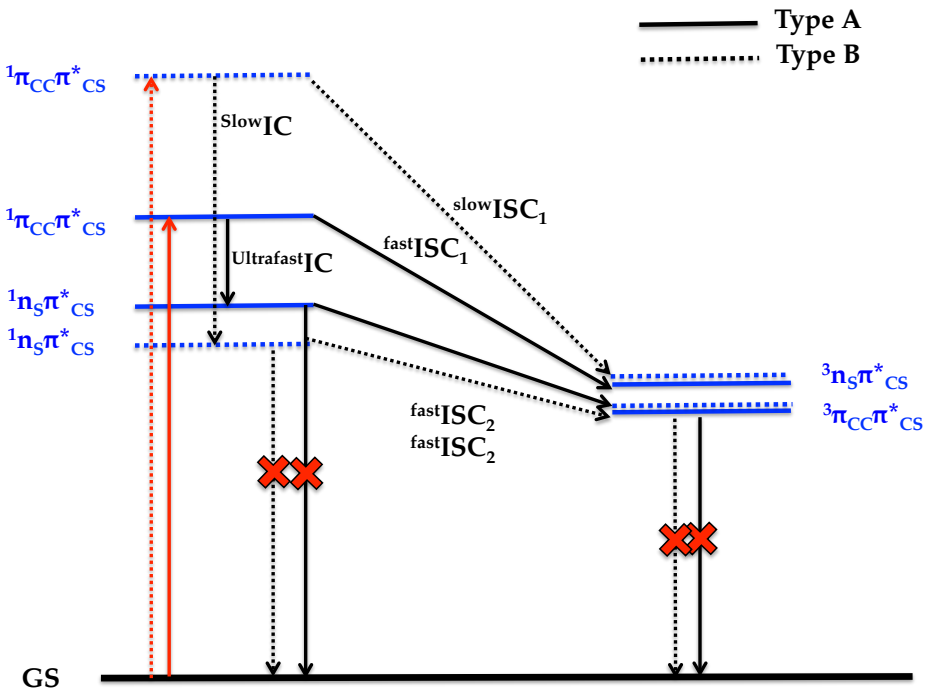

Figure 7.3 Most probable singlet and triplet deactivation mechanisms after light absorption (red arrow) for Type A bases (solid lines) and Type B bases (dotted lines). ISC = intersystem crossings and IC= internal conversion.

7.5 Excited state Dynamics: Semiclassical Simulations and Ultrafast Femtosecond Experiments.

Semiclassical dynamics using the surface hopping algorithm and semiempirical methods (see Chapter 4) were performed for two of the four studied thiobases. Results from Ultrafast Femtosecond Experiments performed by the group of Prof. Carlos Crespo-Hernández will also be discussed in this section.

Type A: 6TG

Singlet and Singlet/triplet dynamic simulations were performed for 6TG in gas phase and the results are collected in paper VI.

Both simulations reveal that after light absorption, the spectroscopic S_2 $^1\pi_{CC}\pi^*_{CS}$ state is populated and decays ultrafast to the lower state S_1 $^1n_S\pi^*_{CS}$ state, being both populations equal within the first 50 fs (see Figure 7.4). This fast decay is consistent with the CI found between both states close to the FC region by the static ab initio calculations in Type A bases. An analysis of the geometries obtained at the end fo the simulations reveals that the system is mainly populating the S_1 $^1n_S\pi^*_{CS}$ minimum, and no significant decay to the ground state takes place during the first 10 ps. Those results are also in concordance with the most probable mechanism for Type A bases predicted in base of the static calculations (see Figure 7.3)

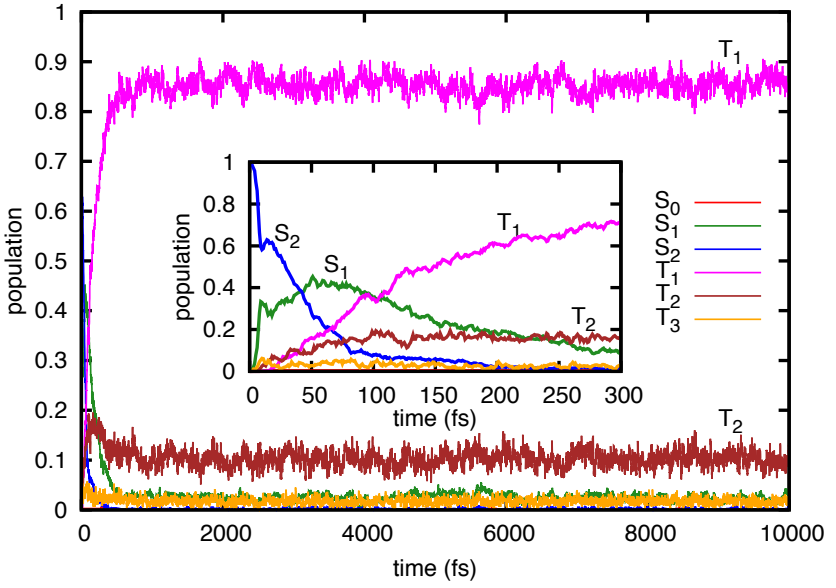

Figure 7.4 . Population of the spin-diabatic states as a function of time from 0 to 10000 fs in 6TG semiclassical dynamic simulations.

From the S_1 $^1n_S\pi^*_{CS}$ minimum, in a second stage, the triplet states are populated (see Figure 7.4), via the ISC_2 funnel for most of the trajectories (see paper VI for further details). From ~100fs on, the first triplet state appears as the most populated state, being the computed lifetime for triplet population to ~170 fs (see Figure 7.4). Along

these trajectories hops between the first two triplet states and the first singlet state were observed, in agreement with the degeneracy region between the $^1n_S\pi^*_{CS}$, $^3n_S\pi^*_{CS}$ and $^3\pi_{CC}\pi^*_{CS}$ states described in the previous section for 6TG. The obtained averaged geometries at the final time of the simulations agreed with the one optimized with the ab initio calculations for the most stable $^3\pi_{CC}\pi^*_{CS}$ minimum.

From the populated $^3\pi_{CC}\pi^*_{CS}$ minimum out singlet/triplet dynamics, do not register enough number of hops to the ground state in order to predict an accurate time for ground state population, due to the large energy difference between this minimum and the CI allowing the transfer of population to the ground state. However, during the singlet only dynamics few hops were registered from the S_1 $^1n_S\pi^*_{CS}$ minimum to the ground state. Half of the geometries obtained at the time of these hops did not match with any of the previous optimized CI connecting either S_1 $^1n_S\pi^*_{CS}$ or $^1\pi_{CC}\pi^*_{CS}$ minima with the ground state. This new CI crossing structure was considered and reoptimized, involving higher excited states at the FC region, which were not considered during the first stage of the 6TG study, complementing the previous picture obtained from the static calculations.

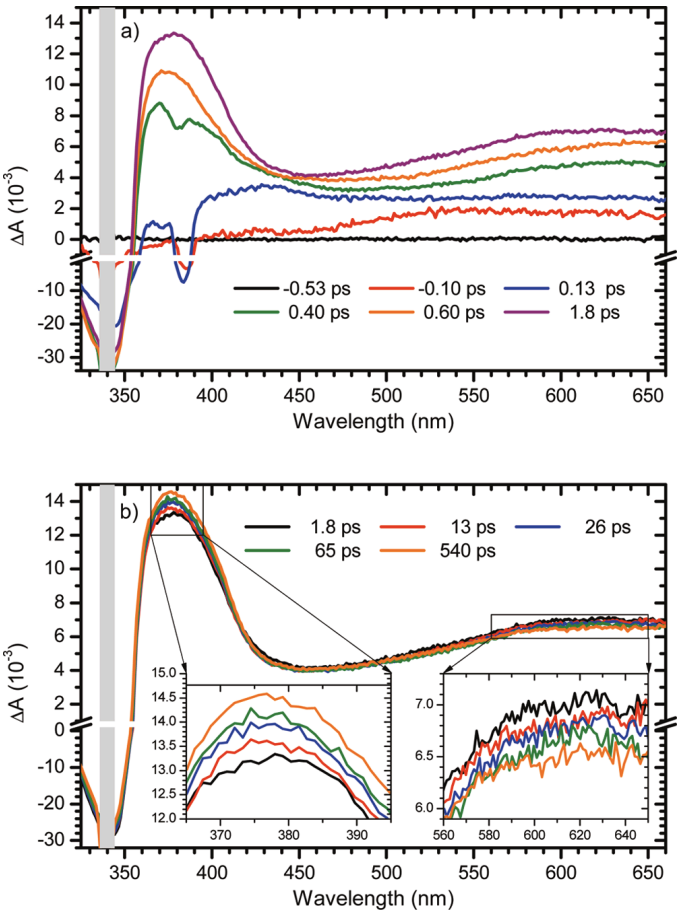

Figure 7.5. Femtosecond transient absorption spectra for 6TG in aqueous buffer solution ph=7 after 340 nm. Upper panel: early time delays and lower panel: time delays from 1.8 to 540 ps. Adapted from Refs [3,4].

In conclsuion, the most probable deactivation mechanism found during the singlet/triplet dynamics is: $S_2\ ^1\pi_{CC}\pi^*_{CS}$ -> $S_1\ ^1n_S\pi^*_{CS}$ -> $T_1\ ^3\pi_{CC}\pi^*_{CS}$, being the time for ISC of ~170 fs and the triplet yield ~0.9.

Our simulated lifetimes (gas phase) are in good agreement with the transient absorption experiments performed by Prof. Crespo-Hernández et al (see Figure 7.5) in aqueous solutions that recorded times of ~300 fs for triplet population (band at ~350 nm). Also agreement was found regarding triplet yields between our simulations (0.9) and experimental results (0.8±0.2).

Type B: 4TT

QM/MM singlet/triplet dynamic simulations were performed for 4TT including in this case solvent effects. The QM subsystem (4-thiothymine) was described using a reparameterized AM1 semiempirical Hamiltonian (reparameterized with our QC results described in previous sections), where the molecular orbitals were obtained from a closed shell calculation using the floating occupation number method. Within this orbital set a multi electron configuration interaction with a complete active space of 8 electrons and 6 orbitals was performed. The MM subsystem was represented by the OPLS-AA force field (ribose) and the TIP3P model (water).

For 4TT our dynamic simulations reveal that after light absorption, the $S_2\ ^1\pi_{CC}\pi^*_{CS}$ spectroscopic state is populated and slowly decays within the first picoseconds (see Figure 7.6). This gradual decay of the S_2 state is in good agreement with the very stable minimum found in gas phase static calculations for Type B bases in this potential, showing high energy IC and ISC funnels. As the S_2 state decays, S_1, T_2 and T_1 states population start to increase, the later state carrying 50% of the population after 6 ps.

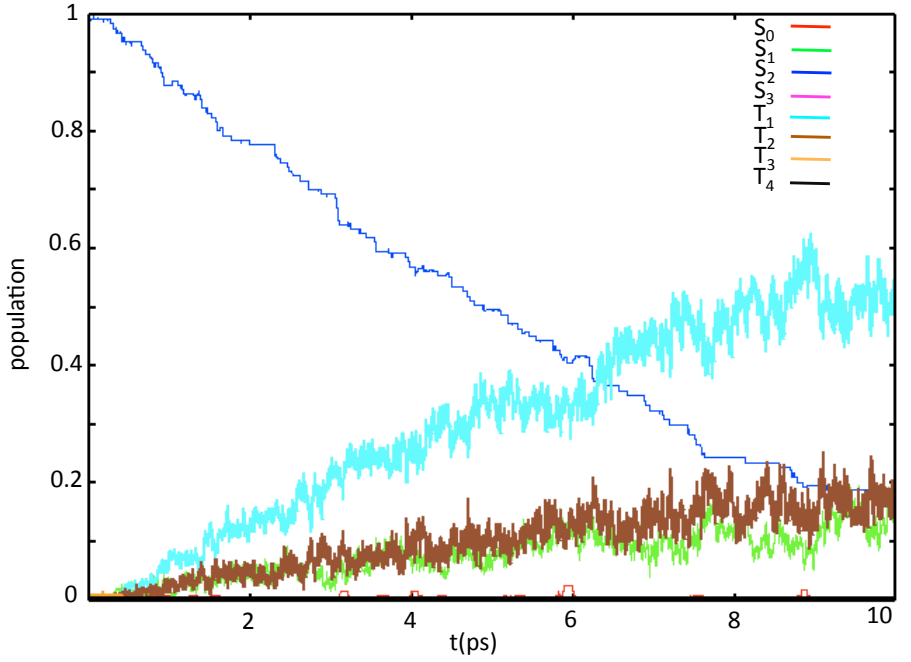

Figure 7.6 .Population of the spin-diabatic states as a function of time from 0 to 10 ps in 4TT semiclassical dynamic simulations.

From an analysis of the hops experienced by 4TT from the S_2 state it can be concluded that this state transfers 75% of its population to S_1 state, whereas the remaining 25% goes to the triplet manifold (either T_1 or T_2). Although percentages for the S_2->T population transfer are slightly larger than for 6TG (90% S_2->S_1 vs 10% S_2-T), they also confirm that for regions where 2 singlets and 1 triplet states (S_2, S_1 and T_2) are almost degenerated IC is preferred despite large SOC values computed in these regions.

The population reaching the S_1 $^1n_S\pi^*_{CS}$ state, is rapidly transfered to the triplet manifold (see Figure 7.6), indicated that the ISC_2 is the main funnel for triplet population, during the dynamic simulations, although as already discussed some hops also take place through ISC_1. In fact, the population of the S_1 state does not increase significantly with the decay of S_2 (as for 6TG) but it remains more or less constant from 6 ps until the end of the simulation. From ~6 ps on, the first triplet state is the most populated state, being the computed lifetime for triplet population is of ~3.7 ps (see Figure 7.6) and ISC expected to be completed after 10 ps. Assuming that the remaining population in S_2 will decay to the triplet manifold, a triplet yield of ~0.8 is expected. Not enough population of the ground state is registered at the final time of the propagation to predict an accurate lifetime for this process. This is compatible with the large energy difference between computed both the S_1 or T_1 minima and the CI allowing the recovery of the ground state.

These results are in agreement with the most probable mechanism for Type B bases predicted on the basis of the static calculations (see Figure 7.3), showing slower ISC compared to Type A bases and not IC to the ground state for the propagated time.

Excited state dynamic experiments performed for 4TT by Harada et al.[1,2] exciting at ~260 nm show that singlet-triplet ISC takes place within a time of approximately 10 ps. However, Crespo et al.[3,4] femtosecond transient absorption experiments in aqueos solution and acetonitrile obtain triplet lifetimes within the femtosecond scale (~300 fs). These later results significantly differ from the lifetimes extracted from our simulations, and also from the potential energy gas phase static profiles.

In view of the above experimental results, further static and dynamic calculations (in progress) are in progress giving special attention to the solvent role in the deactivation mechanism of 4TT.

7.6 Solvent Effects

Taking into account the results obtained by our previous dynamic studies, it can be said that for the thiobases studies ISC takes place from the $^1n_S\pi^*_{CS}$ state. Since Crespo et al measured ISC in the femtosecond scale, S_2->S_1 internal conversion necessarily needs to occur in the same times. This would, however, imply that our optimized S_2 $^1\pi_{CC}\pi^*_{CS}$ minimum and the $^1\pi_{CC}\pi^*_{CS}/^1n_S\pi^*_{CS}$ CI are not correctly described, in view of the large energy gap between them (~1.5 eV) that is incompatible with the S_2-S_1 internal conversion funnel occurring in this ultrafast scale. Since previous studies suggested that explicit water molecules can be essential for direct comparison with the experiment in natural DNA bases[5] and since our PCM calculations showed no

significant effect, some solvent molecules (water and acetonitrile) have been then considered. Thereby, taking into account these solvent molecules selected points of the PES (FC equilibrium geometry, the S_2 $^1\pi_{CC}\pi^*_{CS}$ minimum and the S_2/S_1 CI) were reoptimized (at CASSCF(12,9)/6-31g* level of theory), see Figure 7.7.

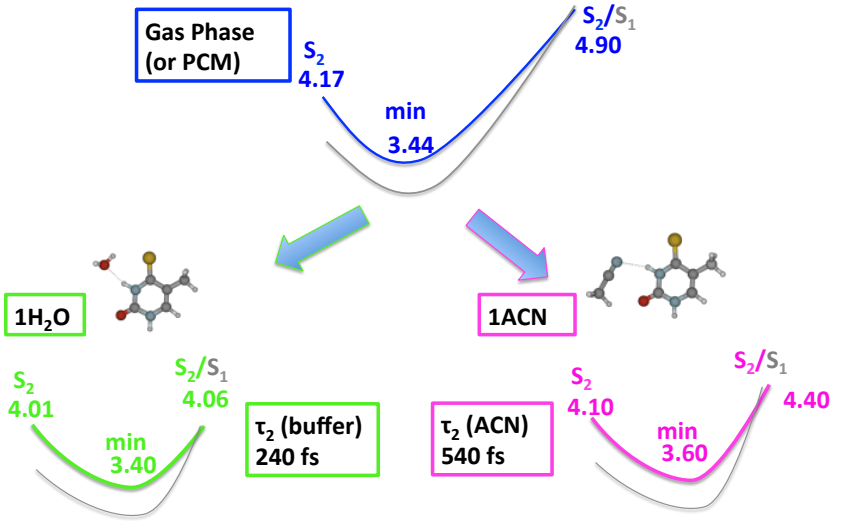

Figure 7.7 .CASPT2 energies (in eV), relative to the ground state at the FC geometry) calculated at the optimized critical points in gas phase (blue) including one water molecule (green) and one acetonitrile molecule (pink). Experimental recorded lifetimes are also included for comparison.

When one water molecule was included into the optimization of the S_2 $^1\pi_{CC}\pi^*_{CS}$ minimum and the $^1\pi_{CC}\pi^*_{CS}/^1n_S\pi^*_{CS}$ CI, we register for both geometries an increase in the C-S distance respect to the FC equilibrium bond, being almost dissociated at the position of the CI. Interestingly, the energy gap between the minimum and the CI is significantly reduced, from 1.5 to 0.6 eV (in green in Figure 7.7), compared to the one calculated in gas phase (blue curves in Figure 7.7). Although an important energy difference still exists between the minimum and the CI, it is possible to overcome this smaller energy barrier in shorter time scales and still can explain the experimentally observed fluorescence in 4TT. For acetonitrile (pink situation in Figure 7.7) an intermediate case between gas phase and water is found. The energy barrier separating the S_2 $^1\pi_{CC}\pi^*_{CS}$ minimum and the IC funnel is now ~0.8 eV, which should explain the longer lifetime experimentally measured for the S_2 state, 540 fs compared to the one recorded in water, 240 fs. Although, further water molecules (up to 7 molecules) have been included to better mimic the first solvation layer and point charges were considered for the simulation of the bulk water, the minimum energy gap between the S_2 minimum and the $^1\pi_{CC}\pi^*_{CS}/^1n_S\pi^*_{CS}$ CI was found for the single water molecule calculations (0.5-0.6 ev).

The effect of the ribose into the calculations was also tested, both after including it explicitly into the QM part and substituting it by a methyl group. However, none of these attempts succeed in decreasing this energy gap suggesting that the role of the ribose is not the key point determining the ultrafast IC in 4TT.

Although our QM/MM dynamics simulations do include solvent effects in the MM part, the semiempirical Hamiltonian used to describe the QM part was reparameterized with our gas phase CASPT2 calculations. Further simulations using AM1 values reparameterized with the new calculations including water molecules are in progress. Interestingly, the energy of the S_2 $^1\pi_{CC}\pi^*_{CS}$ minimum relative to the GS minimum is not dramatically affected by the inclusion of solvent molecules, whereas the $^1\pi_{CC}\pi^*_{CS}/^1n_S\pi^*_{CS}$ CI is strongly affected by solvents effect decreasing its energy in 0.9 eV on going from gas phase to solution.

Solvent effects could be, then, essential for the interpretation of experimental results performed in solution.

7.7 Comparison with canonical DNA Bases

The absorption spectra and deactivation mechanism for thiobases extracted from our combined theoretical/experimental studies will be compared with the well-known photochemical behaviour of the canonical bases in this section.

Three main differences can be found between canonical DNA and thiosubstitued bases regarding their absorption energy region, their photostability and their intersystem crossing rates.

(1) Absorption Energy Region: UVB/C vs UVA.

As already mentioned in Chapter 1, canonical DNA bases absorb (4.5-5.5 eV see Chapter 1)[6] in the UVB-UVC (4.00-12 eV) region of the electro magnetic spectrum while their thio-analogues present the maximum of absorption (3.80-4.20 eV see Table 7.1) in the UVA region (3.00-4.00 eV).

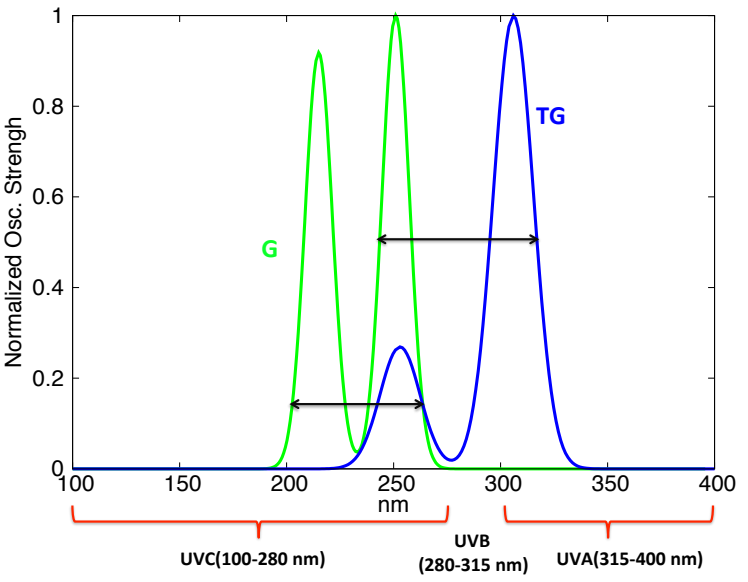

Figure 7.8 Simulated Absorption Spectra from Guanine (Ref 6) and Thioguanine Bases.

UVA radiation has normally been considered as harmless since canonical DNA bases do not absorb in this region. However, the shift experienced by the absorption spectrum from the UVB/C to the UVA on moving from canonical DNA bases to their thio- substituted counterparts (see Figure 7.8) can lead to the excitation of these nucleobases and trigger photochemical reactions in patients where thiobases have been incorporated into their DNA.

(2) Deactivation Mechanism: Photostability vs Phototoxicity.

As described in Chapter 1, deactivation pathways of excited canonical **DNA bases** lead directly to a conical intersection with the ground state. The absence of minima or energy barriers along these pathways explain the **photostability** properties of these bases since the excited bases very easily revert to their ground state through these efficient funnels.

Quite the reverse, in the case of **thiobases**, the computed large energy barrier separating any of the populated singlet and/or triplet minima from their respective conical intersection with the ground state prevent the molecule to rapidly recover their ground state, remaining on the excited state longer times. In fact, the **phototoxicity** for these bases can be ascribed to the long enough lifetimes of these triplet intermediates and their energy relative to the ground state which is transferred to environmental molecular oxygen producing singlet oxygen (see Chapter 1) leading then to DNA damage.

(3) Intersystem crossing rates: Low vs High triplet yields.

Both the modest SOC computed at the ISC found along the deactivation pathway of **DNA nucleobases** and for the remoteness of other ISC from the regions of the PES likely to be visited by the wave packets explain the **low triplet yield** reported both theoretically and experimentally for these bases. [6-8]

Contrary, in case of thiobases, efficient funnels for intersystem crossing have been located in the vicinity of populated singlet minima along the minimum energy paths of these bases. The large SOC enhanced by the heavy atom effect and the high degeneracy between singlet and triplet manifolds at these parts of the PES, point to a very efficient transfer of population between them. In fact, our dynamic simulations show close to unity triplet yields for thiobases in agreement with the intersystem crossing rates measured experimentally.

Oxygen-by-Sulfur substitution leads to dramatic changes into the photochemistry of DNA nucleobases altering their photostability and conferring them potential cytotoxic properties.

Bibliography

(1) Harada, Y.; Okabe, C.; Kobayashi, T.; Suzuki, T.; Ichimura, T.; Nishi, N.; Xu, Y.-Z. *J. Phys. Chem. Lett.* **2010**, *1*, 480.

(2) Harada, Y.; Suzuki, T.; Ichimura, T.; Xu, Y.-Z. *J. Phys. Chem. B* **2007**, *111*, 5518.

(3) Reichardt, C.; Crespo-Hernández, C. E. *J. Phys. Chem. Lett.* **2010**, *1*, 2239.

(4) Reichardt, C.; Crespo-Hernández, C. E. *Chem. Commun.* **2010**, *46*, 5963.

(5) Karunakaran, V.; Kleinermanns, K.; Improta, R.; Kovalenko, S. A. *J. Am. Chem. Soc.* **2009**, *131*, 5839.

(6) González-Luque, R.; Climent, T.; González-Ramírez, I.; Merchán, M.; Serrano-Andrés, L. *J. Chem. Theory Comput.* **2010**, *6*, 2103.

(7) Mai, S.; Marquetand, P.; Richter, M.; González-Vázquez, J.; González, L. *Chem. Phys. Chem.* **2013**, *14*, 2920.

(8) Nikogosyan, D. N.; Angelov, D. A.; Oraevsky, A. A. *Photochem. and Photobiol.* **1982**, *35*, 231.

Conclusions

Throughout this thesis ab-initio methods and mixed quantum classical dynamics simulations were used to investigate the photophysics and/or photochemistry of relevant chromophores precursors of $^1O_2$ and other ROS of two main classes aromatic endoperoxides and thiobases derivatives.

In the case of endoperoxides, our final goal was to provide insight into how singlet oxygen generation competes with other possible mechanism, i. e. O-O homolysis. The studies of the deactivation mechanism of the two considered endoperoxides (APO and CHDEPO) reveal that both systems evolve barrierless from the FC region along the considered state ($\pi\pi^*$ for cycloreversion and $\pi\sigma^*$ for O-O homolysis) towards the ground state. Thereby, both mechanisms (O-O homolysis and cycloreversion) present conical intersection with the ground state easily accessible from the FC region. In case of O-O homolysis, a degeneracy region involving the first 4 singlets and 4 triplets is reached and is characterized by the rupture of the O-O bond. For cycloreversion a conical S_1/S_0 intersection is found where the first C-O bond is broken. For both mechanisms, these degeneracy points with the GS are connected with minima in this potential. In a second step a transition state needs to be surmounted to reach the final photoproducts (H_2 and $^1O_2$). Thereby, both mechanisms are probable from excited endoperoxides. Dynamic simulations in the small endoperoxide CHDEPO provided relevant information about the competition between these deactivation paths, giving a distribution of ~60%:~30% for O-O homolysis and cycloreversion. In summary, the present study highlights the importance of obtaining a time resolved picture of a photochemical process to discern the relative importance of different competing channels.

For the other type of photosensitizers, thiobases, we have investigated Type II mechanisms, responsible for their toxicity in cellular environments. Thiobaes are UVA chromophores and its photoreactivity can be attributed to the S_2 excited state. The competition between the deactivation through the singlet and the triplet manifolds governs the photochemistry of these systems.

Nevertheless, the important energy barriers connecting intermediate singlet minima with conical intersection funnels for the decay to the ground state along the singlet manifold, favor the decay of excited thiobases through the triplet PES. Population transfer into the triplet manifold takes place via two different regions of the PES, where Spin Orbit Coupling (SOC) terms were calculated to be important. The triplet minima accumulate enough energy so as to transfer it to the ground state oxygen molecules, producing $^1O_2$.

Our quantum chemical predictions were assessed by performing semiclassical dynamics simulations and considered the competition between singlet and triplet decay introducing SOC. Singlet/triplet dynamics reveal that the population of the triplet manifold takes place in an ultrafast time scale for 6TG, whereas it is slower in case of 4TT. In conclusion, the topology of thiobases' PES favors the population of triplet state minima, while prevents deactivation to the ground state via the singlet or triplet manifold due to the size of the energy barriers connecting these deactivation funnels. From the comparison of these results with the photophysics of the canonical nucleobase, we conclude that oxygen-by-sulfur substitution leads to a great stabilization of the calculated low-lying electronic excitations. This substitution results in the shift of the absorption maximum of the spectra from UVC (canonical DNA nucleobases) to UVA (in thiobases). This substitution is also responsible for the cytotoxic properties of thiobases, which contrast with the photostability of DNA nucleobases, attributed to the barrierless deactivation from the spectroscopic state S_1 to the S_1/S_0 conical intersection.

The effect of substituents of different nature and lying at different positions of the heterocycle in the photophysical properties of the purine free base was studied by comparing our calculations on free base purine with previous results obtained for other substituted bases. These calculations reveal that purine bases deactivates barrierless from the S_2 spectroscopic state to a minimum in the first excited state. From this singlet minimum, injection of population to the triplet manifold was found to be likely to occur, whereas deactivation to the ground state by internal conversion should play a second role due to the presence of energy barriers. Then, the mechanism predicted for purine is very different to the barrierless paths to the ground state found calculated, for instance, in guanine and adenine. In fact, the behavior of purine is more similar to the paths described for 2-aminopurine. In this system, the substitution of position 2 with an amino group introduces an energy barrier preventing the decay to the GS. These results highlight that both the nature and position of the substituents in the heterocyclic skeleton common to all nucleobases are key factors determining the deactivation of excited nucleobase derivatives.

All the results presented in this thesis are collected in publications attached in Appendix I, whereas further publications not directly connected to the subject of this thesis work and in collaboration with organic experimental groups are compiled in Appendix II.

Conclusiones

En esta tesis métodos ab initio y simulaciones de dinámica semiclásica han sido empleadas para investigar la fotofísica y/o la fotoquímica de cromóforos relevantes precursores de $^1O_2$ y otros especias reactivas de dos clases principales endoperóxidos aromáticos y tiobases.

En el caso de los endoperóxidos, nuestro objetivo final es proveer información acerca de cómo la generación de oxigeno singlete compite con otros mecanismos posibles, por ejemplo O-O homolisis. Los estudios sobre los mecanismos de desactivación en los dos endoperóxidos considerados (APO y CHDEPO) muestran que ambos sistemas evolucionan sin barreras desde la región FC siguiendo el estado específico ($\pi\pi^*$ en cycloreversion y $\pi\sigma^*$ en O-O homolysis) y hacia el estado fundamental. De este modo, ambos mecanismos (O-O homolisis y cicloreversión) presentan intersecciones cónicas con el estado fundamental fácilmente accesibles desde la región FC. En el caso de la O-O homolisis un punto de degeneración entre los 4 primeros singletes y los 4 primeros tripletes es alcanzado, caracterizado por la ruptura del enlace O-O. En el caso de la cicloreversión una intersección cónica S_1/S_0 se encontró, donde uno de los enlaces C-O ya esta roto. En los dos mecanismos estos puntos de degeneración con el GS están conectados con mínimos en el mismo potencial. En un segundo paso, un estado de transición separa dichos mínimos de los productos finales (H_2 y $^1O_2$). Así, los dos mecanismos son probable desde endoperóxidos excitados. Simulaciones dinámicas en el endoperóxidos pequeño CHDEPO han revelado importante información acerca de la competencia de los caminos de desactivación, dando una distribución de productos ~60%:~30% para la O-O homolisis y la cicloreversión. En conclusión, este estudio señala la importancia de llevar a cabo simulaciones dinámicas para obtener una visión resuelta en el tiempo y para discernir entre a priori mecanismos igualmente probables.

Para el otro tipo de fotosensibilizadores, tiobases, hemos investigado mecanismos de Tipo II responsables de su toxicidad en ambientes celulares. Las tiobases son cromóforos UVA y su fotoreactividad es atribuida al estado excitado S_2. La competición entre la desactivación a través de estados singlete y triplete gobierna la fotoquímica de estos sistemas.

Sin embargo, las importantes barreras de energía que conectan los mínimos singlete con las intersecciones cónicas para decaer al estado fundamental, favorecen el decaimiento de estas bases a través de las superficies triplete. La población de estados triplete tienen lugar a través de dos puntos diferentes donde grandes términos de acoplamiento spin-órbita fueros calculados. Los mínimos triplete poblados acumular energía suficiente para transferir al oxígeno molecular y producir, $^1O_2$.

Nuestras predicciones en base a cálculos químico cuánticos fueron corroborados llevando a cabo simulaciones dinámicas semiclásicas considerando la competición entre el decaimiento singlete y triplete introduciendo acoplamientos spin-órbita. Esta dinámica reveló que la población de los estados tripletes tiene lugar de formar ultrarrápida en la 6TG mientras que es más lenta en la 4TT. En conclusión, la topología de las PES en las tiobases favorecen la población de los mínimos tripletes, mientras que previene la desactivación hacia el estado fundamental via estados singlete o triplete debido a las altas barreras de energía que conectan esos canales. Comparando estos resultados con la fotoquímica de las bases cánonicas, se puede concluir que la sustitución de oxígeno por azufre conduce a una gran estabilización de las excitaciones de baja energía. Esta sustitución resulta en un desplazamiento de los máximos del espectro de absorción desde la región UVC (canonical DNA nucleobases) hacia la UVA (tiobases). Esta sustitución es también responsable de las propiedades citotóxicas en contraste con la fotoestabilidad de las DNA nucleobases, atribuida a los caminos de desactivación sin barrera de energía desde el estado espectroscópico S_1 hasta la cónica S_1/S_0.

Los efectos de los sustituyentes de diferente naturaleza y en diferentes posiciones en las propiedades fotofísicas de la base libre purina ha sido estudiada comparando nuestros cálculos sobre los mecanismos de desactivación en la purina con estudios previos en otras bases. Estos cálculos revelaron que la base purina desactiva sin barreras de energía desde el estado espectroscópico S_2 hacia un mínimo en el primer estado excitado. Desde este mínimo, se encontró que la inyección de población a los estados triplete era probable, mientras que la desactivación hacia el estado fundamental debe jugar un papel secundario debido a la presencia de barreras de energía para alcanzar las intersecciones cónicas. Asi, el mecanismo mas favorable predicho para la base purina es contrario al mecanismo sin barreras para llegar al estado fundamental encontrado para otras bases, como por ejemplo, en guanina y adenina. De hecho, el comportamiento de la purina es similar al descrito para la 2aminipurina, donde la sustitución en la posición 2 con un grupo amino introduce barreas de energía para decaer al GS. Estos resultados, subrayan que ambas la naturaleza y posición de los sustituyentes en el esqueleto del heterociclo son factores clave que determinan el decaimiento de los derivados de nucleobases excitados.

Los resultados presentados en esta tesis están recogidos en las publicaciones contenidas en el Apéndice I, mientras que otras publicaciones no directamente conectadas con el objeto de la tesis y en colaboración con grupos experimentales orgánicos están contenidos en el Apéndice II.

Appendix A

Published Articles Resulting from this Thesis Work

Article I

Can TD-DFT predict excited states in endoperoxides?

Computational and Theoretical Chemistry 975 (2011) 13–19

Article II

Time-resolved insight into photosensitized generation of singlet oxygen in endoperoxides

Submitted to *Chemical Science*

Article III

Towards understanding the photoinduced singlet oxygen generation mechanism in anthracene endoperoxide.

Submitted to *J. Phys. Chem. Lett*

Article V

An ab initio mechanism for efficient population of triplet states in cytotoxic sulfur substituted DNA bases: the case of 6-thioguaninew

Chem. Commun., 2012, **48**, 2134–2136

Article VI

Competing ultrafast intersystem crossing and internal conversion: a time resolved picture for the deactivation of 6-thioguanine

Chem. Sci., 2014, 5, 1336.

Appendix B

Other Articles Published During this Thesis Period

Article VII

Versatile Bottom-up Approach to Stapled p-Conjugated Helical Scaffolds: Synthesis and Chiroptical Properties of Cyclic o-Phenylene Ethynylene Oligomers

Angew. Chem. Int. Ed. 2012, 51, 13036 –13040

Article VIII

An Insight into the Mechanism of the Axial Ligand Exchange Reaction in Boron Subphthalocyanine Macrocycles

J. Am. Chem. Soc. accepted

SYNOPSIS TOC